Cohesive soil erosion by a low pressure vertically impinging jet

R.W.F. Janmaat

Delft University of Technology

TU Delft Delft University of Technology

Boskalis

Challenge the future

Cohesive soil erosion by a low pressure vertically impinging jet

Mass flow excavation

by

R.W.F. Janmaat

to obtain the degree of Master of Science
at the Delft University of Technology.

Student number: 4317823
Project duration: April 1, 2019 – May, 2020
Thesis committee:
Prof. dr. ir. C. van Rhee, TU Delft, chair
Dr. ir. G. H. Keetels, TU Delft, supervisor
Dr. ir. A. J. Nobel, Boskalis
Dr. A. Askarinejad, TU Delft

Boskalis

TU Delft Delft University of Technology

Preface

This study continues on the research performed by Bob Kerssens, who unfortunately passed away before completing his research.

This report forms the closure of my Master of Science program in Hydraulic engineering at the Delft University of Technology.

Boskalis allowed me to put both my practical and theoretical skills to the test, by offering me a challenging graduation project, for which I am grateful. A special thanks goes to Arno for his support, guidance and insights he gave me during this project. Furthermore would like to thank Geert Keetels, Cees van Rhee and Amin Askarinejad for their time and knowledge.

I would like to thank the colleagues at the R&D department for their help and making me feel a part of the team. Moreover, I thank my fellow graduates at Boskalis for their moral support during our lunch and coffee breaks.

Finally, I would like to thank my parents, my family and friends for helping me to forget this thesis outside office hours.

R.W.F. Janmaat
Delft, May 2020

Summary

In this study, the excavation process of a low pressure vertical impinging jet in cohesive soil has been investigated. Based on literature and experimental research, different soil failure mechanisms have been investigated. The main result of this study is a relation between the main jet and soil parameters, and the scour rate development.

In dredging activities, submerged hydraulic jets are widely used for different purposes. Mass flow excavation is a hydraulic, low pressure, subsea excavation method whereby a large volume flow is applied to the seabed through which the seabed is eroded, and the soil is transported. A mass flow excavator operates at a pressure of about 0.5 bar and can have a nozzle diameter between 0.5-1.5 m. The mass flow excavator operates at a standoff distance of more than six times the nozzle diameter.
The erosion process of a cohesive soil by impinging jets depends on many variables(e.g., jet flow velocity, standoff distance, grain size, undrained shear strength). The erosion processes, especially for dynamic pressures (in this study called the stagnation pressure, p_{stag}) of lower than two times the undrained shear strength (su), are not fully understood. It is still unknown what the influence of different soil and jet parameters are. As a result, it is still unknown what the expected scour rate will be during a mass flow excavation process of cohesive soils.
The goal of the research is to quantify and be able to predict the production of a mass flow jet on cohesive soils. For this purpose, the relevant parameters of cohesive soil erosion have to be investigated, and fluid velocity profiles of the jet have to be related to clay bed failure mechanisms. Special attention is put on the effect of the consolidation coefficient (c_v) on the erosion process.

A stationary experimental setup was used to measure the scour volume and depth over time due to fully developed low-pressure jets. In 20 individual jet tests, a range of standoff distances (distance from the nozzle to the bed SOD = 150 - 300 mm), stagnation pressures ($p_{stag,0}$ = 0.4-1.4su), and consolidation coefficients (c_v = 2.25·10^{-8} - 3.42·10^{-7}) was tested. All tests were executed with a constant nozzle diameter (D_n = 20 mm), and a constant undrained shear strength (su ≈10 kPa). Together with data obtained in previous research in which the nozzle diameter and the undrained shear strength are varied, a broad dataset is obtained.
From the obtained data, it can be concluded that the consolidation coefficient does have an influence on the scour rate. It has been found that the erosion speed is mainly influenced by the ratio of p_{stag}/su, independent of the standoff distance and nozzle diameter.

The dataset is used to assess whether the erosion process is drained or undrained, and which failure mechanisms occur. The test results were inconclusive on whether the process is drained or undrained. However, it can be concluded that there is a possibility of undrained failure (mass erosion), especially at stagnation pressures larger than 1 ·p_{stag}/su, due to pressure fluctuations. At lower p_{stag}/su ratios, it is more likely that the erosion process is drained.

Existing empirical relations to predict the scour rate are tested against the dataset. These relations did not provide satisfactory results as large deviations between the calculated, and the observed depth are present. The dependency on the hard to determine critical shear stress for erosion (τ_{cr}) makes these relations less practical.
It was attempted to relate the scour rate to the bed shear stress exerted by the jet. The calculated bed shear stress was coupled to the bed swelling theory to obtain scour rates. However, this did not result in satisfactory results between the observed and calculated scour rates.
Subsequently, an empirical relation is derived based on the stagnation pressure, undrained shear strength, and consolidation coefficient. This empirical relation is able to predict the scour depth development mostly within a 35% margin of error. A linear relation between the radius of the jet on the soil, the scour depth Z_c and the scour volume V is found.

List of Symbols

Roman letters

A	Area	m^2
a	Empirical estimation coefficient	-
A_c	Activity	-
b	Empirical estimation coefficient	-
c	Cohesion	N/m^2
c_v	Vertical consolidation coefficient	m^2/s
D	Diameter	m
D_{50}	Median particle diameter	m
E	Erosion rate	$kg/m^2/s$
g	Gravitational constant	m/s^2
h	Drainage length	m
h_e	Erosion depth	m
h_r	Fictious height of the radial jet	m
h_{sw}	Swelling depth	m
I	Momentum flux	N
i	Pressure gradient	Pa/m
k	Experimental constant	-
k_s	Equivalent roughness height	m
k_w	Hydraulic (water) conductivity	m/s
l	length scale	-
LI	Liquidity index	%
LL	Liquid limit	%
M	Erosion rate parameter	$kg/m^2/s$
m	mass	kg
m_v	Vertical compressibility	m^2/N
n	Porosity	-
n_{fr}	Fractal dimension	-
p	Pressure	N/m^2
p_{frac}	Fracture initiation pressure	N/m^2
PC	Percentage of clay	%
Pe_w	Péclet number for pore water dissipation	-
PI	Plasticity index	%
PL	Plastic limit	%
Q	Flow rate	m^3/s
q_z	Specific discharge	m/s
R	Radius	m
r	Radial distance to centerline of the jet	m
S	Degree of saturation	-
s	Axial jet distance, measured along the jet centerline	m
SOD	Standoff distance	m
su	Undrained shear strength	N/m^2
T	Dimensionless time-scale	-
t	Time	s
T_c	Dimensionless time scale	-
U	Degree of consolidation	-
u	Velocity	m/s
V	Volume	m^3
w	Water content	-

X	Shear stress parameter	N/m^2
z	Distance in z-direction	m
Z_c	Jet cavity depth	m

Greek letters

α_e	Erosion coefficient	-
α_h	Erosion coefficient	-
$\alpha_{1,2,3}$	Bed shear stress coefficients	-
α_{mom}	Entrainment coefficient	-
β	Slope of measured consolidation	-
Δ	Difference between two values of a parameter	-
δ	Boundary layer height	m
ϵ	Strain	-
κ	Kármán constant	-
μ	Dynamic viscosity	N s/m^2
μ_n	Nozzle discharge coefficient	-
ϕ_s	Solid volume concentration	-
ρ	Density	kg/m^3
σ	Total stress	N/m^2
$\sigma_{1,2,3}$	Principal stresses	N/m^2
τ	Shea stresses	N/m^2
φ	Internal friction angle	grad

Subscripts

0	At nozzle exit or initially
bl	Boundary layer
cr	Critical
dr	Flow development region
f	failure
j	Jet
mc	Micro-crack
n	Nozzle
rem	Remoulded
s	Solids
sw	Swelling
u	Uniform
v	Vertical
$void$	Void space (pores)
w	Water
zi	Zone of impingement

Superscripts

$'$	Effective (soil pressure)

Contents

1 Introduction

1.1. Background

Building and maintaining infrastructure in wet areas is becoming more critical, with the increasing use of offshore areas. To be able to build offshore and subsea structures often, the seabed needs to be prepared.

Subsea excavation can be mechanical, e.g., backhoe, TSHD, trencher, or hydraulic through high or low-pressure jets.

Mass flow Excavation is a hydraulic, low pressure, subsea excavation method whereby a large volume flow is applied to the seabed through which the seabed is fluidized, and the soil is transported. This excavation method can be used for various applications, such as de-burial of assets, seabed levelling, or trenching.

The advantages of mass flow excavation with respect to other methods are, that it is a non-contact method, that can be applied to a wide range of seabed conditions, and allows for the creation of tight curvatures for trenches.

A mass flow excavator operates at a pressure of about 0.5 bar and can have a nozzle diameter between 0.5-1.5 m. The mass flow excavator operates at a standoff distance of more than six times the nozzle diameter.

Although the erosion process by a mass flow excavator in granular soils is quite well understood, not much is known of the erosion process in cohesive soils. It is relevant to understand the erosion process, the governing hydraulic and soil parameters, and the related erosion rates, to be able to predict the production during the mass flow jetting.

In a previous study by Kerssens [19] (2017), the erosion behaviour of cohesive soils by low-pressure jets was investigated for two types of cohesive soil samples. Kerssens observed production for stagnation pressures (p_{stag}) lower than two times the undrained shear strength (su). The stagnation pressure is defined as a normal load in the main direction of the jet flow due to the mass flow of the jet. According to classical soil mechanics, a cohesive soil does not fail below two times the undrained shear strength.

Kerssens observed significant differences in the production between the two types of cohesive soil samples at the same ratio of p_{stag}/su. It is suggested that this could be due to the influence of the consolidation coefficient c_v on the erosion process.

In this document, the erosion of cohesive soils using low-pressure jets is investigated. By improving the knowledge of this process, the use of this tool can be optimized.

1.2. Problem Definition

The erosion process of a cohesive soil by impinging jets is complex and depends on many variables (e.g., jet flow velocity, standoff distance, grain size, undrained shear strength).
The erosion processes, especially for $p_{stag}/su < 2$, are not fully understood. It is still unknown what the influence of the consolidation coefficient c_v and other soil parameters are in this excavation process.
As a result, it is still unknown what the expected production will be during a mass flow excavation process of cohesive soils. Because the expected production is unknown, the assessment of the mass flow excavation viability in these soils is uncertain.

1.3. Research objective

The goal of the research is to quantify and be able to predict the production of a mass flow jet on cohesive soils. For this purpose, the relevant parameters of cohesive soil erosion have to be investigated, and fluid velocity profiles of the jet have to be related to clay bed failure mechanisms.

- **Main research question**
  - How and to what extent can the production of the mass flow jet in cohesive soils at $p_{stag}/su < 2$ be estimated?
- **Sub questions**
  1. How does the erosion rate develop over time during jetting, and can this be related to an erosion mechanism?
  2. What influence do the ratio p_{stag}/su, nozzle diameter, and standoff distance have on the erosion process?
  3. Does the vertical consolidation coefficient cv have a influence erosion process at $p_{stag}/su < 2$?

1.4. Scope

This graduation project will focus on the cohesive soil erosion process by a low-pressure jet. Data for support of the research will be obtained by experiments using a test setup at Boskalis, as well as by data obtained from a literature review. Only cohesive soil erosion will be considered, which means that granular soil erosion will be excluded. The tests will be performed with a stationary jet with respect to the soil samples. Only a fully developed jet flow will be considered. Only uniform artificially created soil samples will be tested. This way, the influence of individual parameters on soil erosion can be evaluated by excluding soil variability's occurring in natural soils.
The parameters varied in this study are:

- Ratio of p_{stag}/su (by altering the jet pressure)
- Standoff distance SOD
- Consolidation coefficient c_v

The undrained shear strength is kept constant at approximately 10 kPa. The nozzle diameter in this study is kept constant at 20 mm. The effect of the nozzle diameter on the erosion process will be investigated using the data of the erosion tests performed by Kerssens [19] (2017). As in this study, only one nozzle diameter is tested, it should be noted that when the standoff distance SOD is altered, also the ratio of SOD/D_n changes. In table 1.1, the range of the tested variables is given. Also, the range of the variables of the data obtained from other studies is included and annotated with an asterisk.

Table 1.1: Range of test variables used in this study and range of variables of the total data set annotated with asterisk
*) considered data from other studies

Variable		Range
Undrianed shear strength su	[kPa]	7.96-12.29
		2.81-61.50*
Diameter nozzle D_n	[mm]	20
		3.18-40*
Standoff distance SOD	[mm]	147-298
		40.00-280*
Stagnation pressure $p_{stag,0}$	[kPa]	4.00-17.50
		1.57-144*
Flowspeed at nozzle u_0	[m/s]	3.46-8.44
		1.06-25.9*
Consolidation coefficient c_v	[m^2/s]	2.25E-08-3.42E-07
		1.00E-08-2.00E-07*
$p_{stag,0}/su$	[-]	0.42-1.46
		0.26-7.57*
SOD/D_n	[-]	7.35-14.9
		7-30*

1.5. Outline

In chapter 2, a literature study is performed. This chapter is divided into four main parts. In the first part, the cohesive soil characteristics are elaborated. In the second part, the jet development and characteristics are explained. In the third part, four different failure mechanisms and their workings are explained. In the last part of this chapter, previous similar studies of erosion of cohesive soils by low-pressure jets are elaborated.

Chapter 3 explains how the jetting test setup works and how the soil samples are prepared and consolidated. In this chapter, the soil sample characteristics of this study, but also of the other studies used in the analysis, are given.

The experiments performed in this study are elaborated in chapter 4. In this chapter, the test matrix is given. The test procedure is explained, and the measurements before, during, and after the tests are given. Following up, the interpretation of the test report is given. Lastly, the repeatability of the tests is analyzed.

In chapter 5, the results of the tests are presented. First, the results of the consolidation tests are analyzed. A summary table of the configuration of the performed tests and the results is given in section 5.3. This is followed by a scour depth analysis. In the scour depth result analysis, the effects of the individual jet parameters on the scour depth development are explained.

Following up, in chapter 6, an analysis of the possible erosion process given. The existing scour relations are tested against the obtained dataset. Also, the calculation method for the stagnation pressure is verified. In the last part of this chapter, an empirical relation for the scour rate and scour volume of vertical impinging jets in a cohesive soil is given based on the test data.

Lastly, in chapter 7, the conclusions of the results and analysis are given and discussed. Followed up by recommendations.

2

Literature Study

2.1. Introduction

The scour process of cohesive soils due to impinging jets is complex, because a lot of different soil and jet parameters have an influence. The erosion process depends on the jet characteristics and soil parameters such as the particle size distribution, clay fraction, undrained shear strength, permeability, compressibility, consolidation coefficient, density and moisture content (Fell et al. [10], 2013).

The supporting theories for the cohesive soil erosion by jets are explained in this chapter. The chapter is subdivided into three sections.

In the first section, soil characteristics are elaborated. In this section, individual parameters influencing the erosion discussed. Secondly, the jet flow is described; this is needed to understand the erosion forcing mechanism. In the third section, the erosion process is described; this is the interaction of the fluid with the bed. Lastly relevant previous work in erosion by low pressure jets is discussed.

2.2. Cohesive soil characteristics

Cohesive soils mainly consist of a clay, silt, and sand fraction, in which the clay particles are mainly responsible for the cohesive behavior. In this study, fully saturated soils will be considered.

Cohesive soils are characterised by low permeability, high compressibility, plastic behaviour, and swelling properties. The combination of high compressibility and low permeability results in an initial undrained response of the soil upon loading.

2.2.1. Classification

Soils can be classified on basis of their particle size distributions, as is presented in table 2.1.

Soil Type	Grain Size range [mm]
Gravel	>2.0 till ≤63
Sand	>0.063 till ≤2.0
Silt	>0.002 till ≤0.063
Clay	≤0.002

Table 2.1: Grain size distribution

Clay and silt should not be differentiated based on particle size alone, since the more important physical properties of silt and clay are only related indirectly to particle size (PIANC [30], 1984). Therefore, clay types are usually classified based on strength and plasticity. The strength of clay is defined as the undrained shear resistance su, which will be further discussed in chapter 2.2.2. Plasticity is the property a substance has when deformed continuously under a finite force, the shape will be maintained when the force is removed or reduced. Andrade et al. [1] (2011).

Clay commonly occurs in nature as a mixed soil. Soil mixtures will result in different soil-properties. Sandy soils start to exhibit cohesive properties with a clay particle content as low as 10% by weight (van der Schrieck [37], 2016). Soils behaving as clay are of interest for this investigation.

Clay minerals are characterised by their small particle size (as described in 2.2.1), flat shape, net negative electrical charge, and a large specific surface which interacts with pore water. This characterisation results in the cohesive behaviour of the soil.
The three most common clay types are kaolinite, illite, and montmorillonite. Kaolinite is a non-swelling mineral with relatively large particles, which results in a small specific surface. Montmorillonite, on the other hand, is a highly plastic, swelling clay with a large specific surface. This high specific surface results in a larger ability to bind water.

For fine soils, the consistency determines the ease at which it can be handled. The consistency is dependent on the water content (w) of the soil. The water content is defined as the ratio of the mass of water (W_w) to the mass of solids (W_s):

$$w = W_w/W_s \tag{2.1}$$

A cohesive soil can be in a solid, plastic or liquid state; these states are distinguished by the consistency limits, also denoted as the Atterberg limits. The state depends on the water content. The liquid limit (LL) is the water content of a clay at the transition between the plastic and liquid state. The transition from the liquid to the plastic state of the soil is denoted as the liquid limit (LL). The plastic limit (PL) is the transition in water content from the plastic to the solid-state. The difference in water content between the liquid and plastic limit is called the plasticity index:

$$PI = LL - PL \tag{2.2}$$

The plasticity index is a measure of the amount of water bounded within the sediment at specific stress or strength levels.

Soils consist of particles, water and air. The ratio of the volume of the pores (V_{void}) and the volume of the soil (V) is the porosity:

$$n = V_{void}/V \tag{2.3}$$

The saturation (S) of a soil is defined as the ratio of the water volume to the volume of pores:

$$S = V_w/V_{void} \tag{2.4}$$

Where S=1 represents a fully saturated soil. In this research, only fully saturated soils will be considered.

The type and the amount of clay-particles of clay-particles influence the plasticity. The activity (A_c) of a soil is used to separate these quantities:

$$A_c = \frac{PI}{\% < 2\mu m} \tag{2.5}$$

In which $\% < 2\mu m$ is the clay content. The activity of Kaolinite is usually low, around 0.4, where for Montmorillonite it can go up to around 7. The higher the activity the more the properties, such as exchangeable cations and pore fluid composition, of the soil are susceptible to change (Mitchell and Soga [24], 2005).

The consistencies of different cohesive soils can be compared using the liquidity index (LI):

$$LI = \frac{w - PL}{PI} \tag{2.6}$$

A soil can be regarded as a fluid when $LI > 1$ and the soil can be regarded as a non-plastic granular solid when $LI < 0$.

Remoulding a undisturbed sample of cohesive soil results in a reduction in the undrained shear strength. This reduction is dependent on the sensitivity of the soil. Wroth and Wood [45] (1978) found

that the undrained shear strength of a cohesive soil at the remoulded state correlates well with the liquidity index as follows:

$$su_{rem} = 170 \exp^{-4.6LI} \tag{2.7}$$

2.2.2. Stress states in cohesive soil

The stress in a soil in a certain point can be related to the rotation of the plane to the principal directions. The principal directions are the directions in which the shear stresses are minimal or zero, and the normal stresses are maximal or minimal. The maximum principal stress is denoted as σ_1, and the minimum principal stress is σ_3. The intermediate principal stress is denoted by σ_2.
The Mohr-Coulomb circle defines the normal stress and the shear stress on a certain plane. The maximum mobilized shear stress before failure (assuming that this is also the shear stress during the failure) τ_f in a cohesive soil body is:

$$\tau_f = c + \sigma' \tan \varphi. \tag{2.8}$$

In which τ_f= critical shear stress for shear failure, σ'= the normal effective stress to the shear plane, c cohesion, and φ= internal friction angle. The effective stress is the total stress acting on a plane minus the pore pressure:

$$\sigma' = \sigma - p_w \tag{2.9}$$

This failure criterion is visualised in the Mohr circle as the straight line making an angle φ with the horizontal axis.

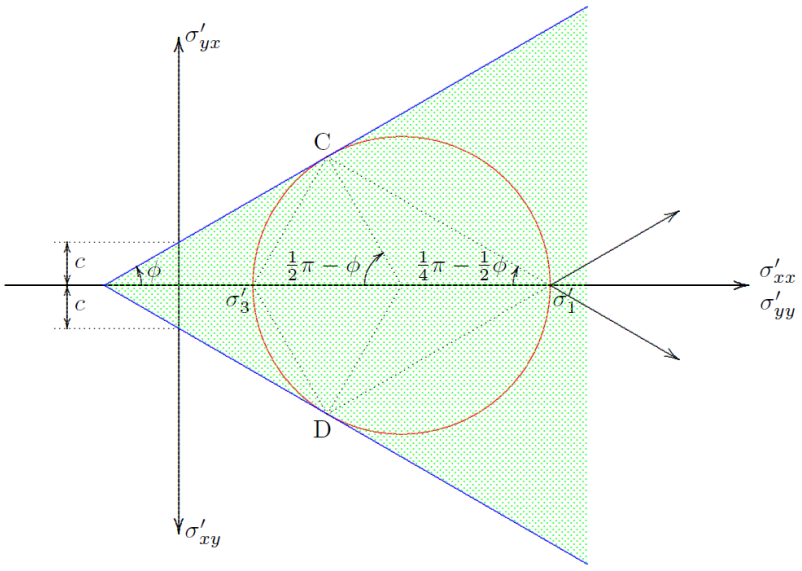

Figure 2.1: Mohr-Coulomb failure Criterion (Verruijt [40], 2012)

Failure of the soil will occur when the Mohr circle touches the Coulomb envelope, indicated in figure 2.1 as point 'C' and 'D'.

Undrained Behavior in Soils

Undrained behaviour in soils occurs when a load is applied quickly, and the permeability of the soil is relatively low. After the load is applied only the pore water pressure is increased by the same increment as the load increase, the effective stress does not increase, because there is no time for the pore water to flow out of the soil. Cohesive soils have a relatively low permeability, and relatively high compressibility, which results in undrained behaviour when loads are applied. If there is a possibility for drainage, and sufficient time for the soil to drain, the pore pressures will be reduced, and the effective stress will increase.

For clay soils, the critical shear stress is often defined as the undrained shear strength or su. The undrained shear strength can be determined by considering the total stresses. The undrained shear strength is determined as one half of the maximum shear stress, expressed in total stresses:

$$su = \frac{1}{2}(\sigma_1 - \sigma_3) \tag{2.10}$$

The undrained shear strength can be determined by considering the total stresses of an undrained triaxial undrained test. In the undrained triaxial test the the total stress increment is equal to the pore pressure increment on a short loading period, as no consolidation can occur. The undrained failure of cohesive soils can be described as c is equal to su and the $tan(\varphi)$ in figure 2.1 is equal to 0. The Mohr circles for total stresses is illustrated in figure 2.2, in which can be seen that the undrained shear strength is half the subtracted principal stresses.

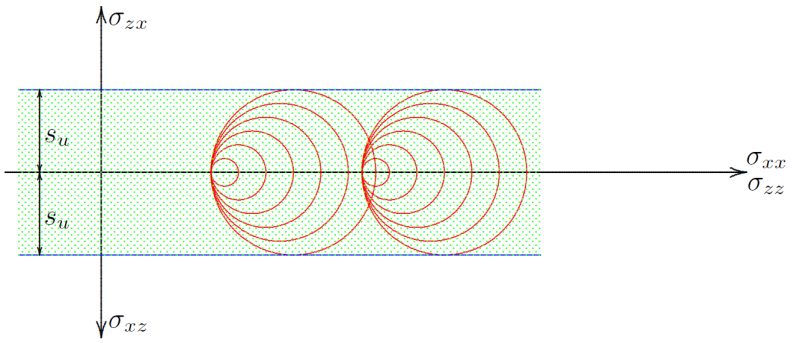

Figure 2.2: Mohr-Coulomb for total stresses (Verruijt [40], 2012)

In figure 2.2 the total stress of two undrained triaxal test is given, in which σ_1 is gradually increased and σ_3 is kept constant but is increased in the second test. The mid point of the circle moves with $\sigma_1 + \sigma_3/2$, the circles become bigger as $\sigma_3 - \sigma_1$ becomes bigger. Between the two tests the effective stresses are practically the same magnitude and only the the total stresses increase in magnitude.

2.2.3. Compressibility

The compressibility of a soil is the ratio of strain occurring over an effective stress increment:

$$m_v = \frac{\epsilon}{\Delta\sigma'} \tag{2.11}$$

Where m_v is the compressibility coefficient and ϵ is the occurring strain. In this formula a linear stress-strain relation is assumed.

2.2.4. Permeability

The permeability coefficient k_w, also hydraulic conductivity, represents the resistance at which a fluid can flow through a porous medium. It relates the discharge trough a porous medium to both the fluid properties and the applied pressure gradient from a head difference. The permeability is a function of the porosity and particle size distribution. Since the grain size of clayey soils is small, the permeability of this type of soil is also small.

The hydraulic conductivity k_w can be determined using Darcy's law:

$$q_z = -k_w i \tag{2.12}$$

In which q_z is the specific discharge and i the pressure drop over a given distance($\frac{dh}{dl}$).

The velocity of this erosion process depends mainly on the permeability of the soil and the flow velocity of the jet; the lower the water permeability, the slower the erosion process for the same jet velocity (van Rhee [39], 2010).

The hydraulic conductivity can also be determined using the coefficient of consolidation c_v. The relation of the consolidation coefficient to the hydraulic conductivity is elaborated in chapter 2.2.5.

2.2.5. Consolidation

Consolidation refers to the process by which soils change volume in response to a change in pressure; this applies to both swelling and compaction (Terzaghi [35], 1943). The mathematical equation for the one dimensional consolidation is given as follows:

$$\frac{\partial p}{\partial t} = c_v \frac{\partial^2 p}{\partial z^2} \tag{2.13}$$

As mentioned before, deformations in undrained situations generate pore water pressure gradients. The combination of the compressibility m_v with the permeability k_w leads to the coefficient of pore water dissipation, or consolidation coefficient c_v:

$$c_v = \frac{k_w}{m_v} \frac{1}{\rho_w g} \tag{2.14}$$

c_v can characterize the dissipation of pore water pressure gradients both during swelling (negative gradients) as during consolidation. For cohesive soils, the compressibility m_v is relatively large and the hydraulic conductivity k_w is relatively small, resulting in a small consolidation coefficient c_v.

The relatively slow soil response on a stress change results in pore water pressure gradients. The dissipation of these gradients is characterised by c_v, this holds for consolidation or swelling, resulting in compression or extension, respectively.
Unloading of the soil results in swelling due to the pore volume increase. Swelling is accompanied by negative pore water pressure gradients, which results in an inward pore water flow. The opposite holds for consolidation.
The time scale for consolidation T_c of a soil with a drainage length h follows from equation 2.13:

$$T_c = \frac{h^2}{c_v} \tag{2.15}$$

This is only valid for larger time scales (usually $c_v t/h^2 > 2$)(Verruijt [40], 2012). If the time parameter $c_v t/h^2$ becomes smaller, the degree of consolidation U can be assumed to be as follows:

$$U = \frac{\Delta h - \Delta h_0}{\Delta h_\infty - \Delta h_0} \approx \frac{2}{\sqrt{\pi}} \sqrt{\frac{c_v t}{h^2}} \tag{2.16}$$

In which Δh_∞ is the deformation of the sample when at the end of the consolidation process, Δh_0 the deformation directly after application of the load. This equation describes the response of the soil on short time scales.

Determining the consolidation coefficient

The coefficient of consolidation (c_v) can be determined from the data obtained in a consolidation test, for example, an oedometer test. In this study oedometer tests are performed to determine the consolidation coefficient. The oedometer consolidation test setup is given in figure 2.3.

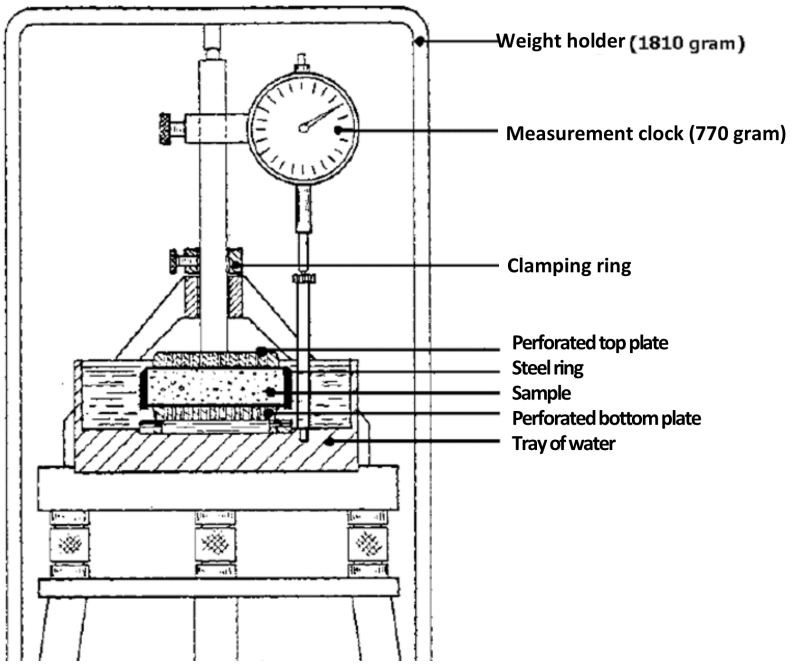

Figure 2.3: Oedometer test setup (from CTB2000 Oedometer test book)

There are several methods to calculate the consolidation coefficient from the data of a consolidation test. In this study, the average of three different calculation methods is taken as the coefficient of consolidation of a particular soil.

The first method is the Log(t)-method. The measured deformation of the sample is plotted against the logarithm of time for this method, see figure 2.4. In this method, the consolidation coefficient is calculated as follows:

$$c_v = 0.197 * \frac{h^2}{t_{50\%}} \tag{2.17}$$

In which h[m] is the height of the sample if only one side is drained. If both sides of the sample are drained, height needs to be divided by 2. $t_{50\%}$ is the time needed to reach a degree of consolidation of 0.5, see figure 2.4. 0.197 is a time factor derived from the differential equation of one dimensional consolidation (derived in Verruijt [40], (2012)).

The degree of consolidation is determined from the final deformation Δh_∞ minus the initial deformation Δh_0. Δh_∞ is taken as the intersection point of the steepest possible tangent and the straight line asymptote for a large time value. This point is defined as the maximum value of the primary consolidation phase. The consolidation that is occurring after this point is denoted as secondary consolidation.

The initial deformation Δh_0 can be determined by assuming that in the beginning of the consolidation process, the degree of consolidation increases proportional with $\sqrt{t}$. Therefore the deformation between $t = 0$ and $t = t_1$ is the same as $t = t_1$ and $t = 4t_1$.

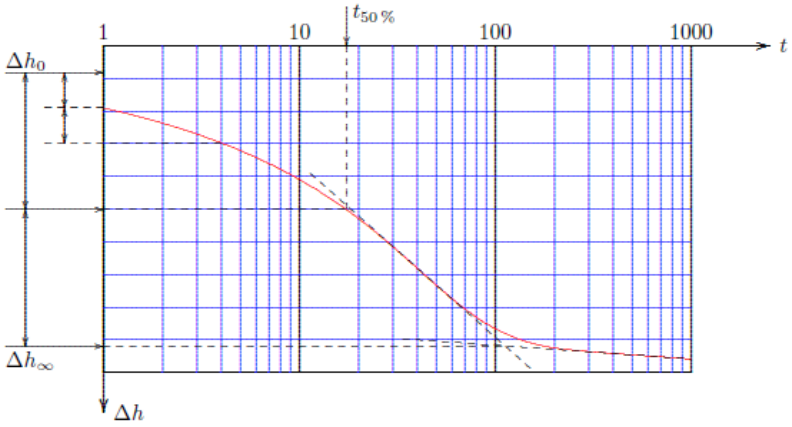

Figure 2.4: Log(t)-method (Verruijt [40], 2012)

The second method is the $sqrt(t)$-method. In this method the measured deformation of the sample is plotted against the root of the time t.

In this method Δh_0 is determined as the intersection point of the straight tangent to the curve with the axis $\sqrt{(t)}$=0, see figure 2.5. $\Delta h_{90\%}$ is determined by plotting a line which is 15% smaller than the tangent of the measurement data, the intersection point with the measurement curve is $\Delta h_{90\%}$. The corresponding time factor value for a degree of consolidation of 0.9 is 0.848. The consolidation coefficient can then be calculated as follows:

$$c_v = 0.848 \frac{h^2}{t_{90\%}} \tag{2.18}$$

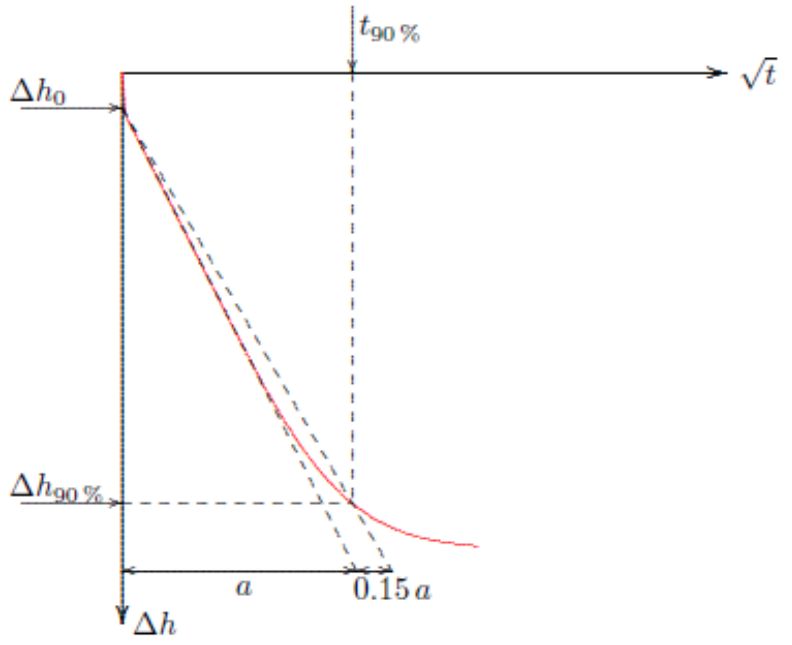

Figure 18.2: $\sqrt{t}$-method.

Figure 2.5: $\sqrt{t}$-method (Verruijt [40], 2012)

The last method is the method of calculating the consolidation coefficient is derived by Asaoka [3] (1978). Asoaka proposed that the measured consolidation at z_i, z_{i+1}, z_{i+2} etc., at points of time t,

$t + \Delta t$, $t + 2\Delta t$ could be approximated as follows:

$$z_{i+1} = \beta z_i + \beta_1 \tag{2.19}$$

The derived relation between the slope of the measured consolidation and the actual consolidation can be used to calculate the coefficient of consolidation:

$$c_v = -\ln(\beta)\frac{4h^2}{\pi^2 \Delta t} \tag{2.20}$$

In which β is the slope of of the measured consolidation at t, and Δt is the time step taken between the points for calculating the slope.

All the methods are an approximation of the consolidation value. Errors between the different methods are usually in the order of 10% to 20% (Verruijt [40], 2012). Dykstra and Joling [9] (2001) and Nobel [27] (2013) both reported larger values for the Asoaka method in relation to the other methods. Verruijt [40] (2012) suggests that the errors occur due to the incorrect assumption of a linear relationship between stress and strain. Measurement errors could also lead to an incorrect value of c_v, due to the fact that the consolidation usually is relatively small.

Typical values of the consolidation coefficient for different clay minerals

As mentioned in chapter 2.2.1, different clay minerals have different soil mechanical properties. That also holds for the consolidation coefficient. University. [36] (1951) found the typical ranges given in table 2.2, for the consolidation coefficient per clay mineral. In the same study, it was also found that the individual minerals do not influence the coefficient of consolidation proportionally to the amounts present.

Clay Mineral	Consolidation coefficient range [m^2/s]		
montmorillonite	$6.0 \cdot 10^{-10}$	to	$3.0 \cdot 10^{-9}$
illite	$3.0 \cdot 10^{-9}$	to	$2.4 \cdot 10^{-8}$
kaolinite	$1.2 \cdot 10^{-7}$	to	$9.0 \cdot 10^{-7}$

Table 2.2: Typical ranges of the consolidation coefficient per clay mineral (from University. [36] (1951))

2.2.6. Relations of soil parameters

Some of the typically obtained soil parameters can be related to each-other. It is hypothesised in this study that the soil parameters influencing the scour of a cohesive soil by a low pressure jet, is predominantly dependent on the consolidation coefficient and the undrained shear strength. The consolidation coefficient is in turn a function of the permeability and the compressibility. In table 2.3 the typically obtained soil parameters and their relation to some of the other soil parameters is given. In general the more clay in a soil, the higher the plasticity, the greater the compressibility and the lower the hydraulic conductivity (Mitchell and Soga [24]. 2005). In Mitchell and Soga [24] (2005), it can also be found that the liquidity index correlates well with the with the compressibility and the (undrained shear) strength. Winterwerp and Van Kesteren [44] (2004) also found that the liquidity index could be correlated to the permeability. The water content can be related to the undrained shear strength. As the water content rises, also the void ratio becomes larger, which reduces the apparent cohesion, and therefore the strength. The percentage of clay in the soil influences the permeability and the compressibility. As the clay percentage becomes higher the less permeable the soil generally becomes, and the higher the compressibility.

Table 2.3: Typically obtained soil properties and the relation to other soil parameters

Typically obtained properties	Related to
Plasticity index PI	Permeability k_w and compressibility m_v
Liquid limit LL	Consolidation coefficient c_v
Liquidity index LI	Undrained shear strength su, compressibility m_v and permeability k_w
Water content w	Undrained shear strength su
Percentage clay/silt/sand	Permeability k_w and compressibility m_v
Mean grain size D_{50}	Clay percentage
Soil swell potential	Compressibility m_v
Soil void ratio	Undrained shear strength su, compressibility m_v and permeability k_w
Undrained shear strength	-

As given in table 2.3 a lot of the typically obtained parameters can directly or indirectly be correlated to the undrained shear strength or the consolidation coefficient, via the influence of the parameter on the permeability and compressibility.

2.3. Jet characteristics

To be able to assess the erosion forces exerted by the jet flow on the soil body, first, the jet flow to the bed and near the bed has to be described. In the following subsections, the flow development of the jet, the impinging jet and the radial wall jet are described. Subsequently, the pressures and shear forces exerted by the jet flow on the soil can be determined.

2.3.1. Jet development

Water flowing from a jet-nozzle into a body of water will mix with the stagnant water. This mixing starts after the water jet leaves the nozzle. Due to the turbulence created by the mixing, stagnant water will be entrained in the jet flow, and the jet flow will grow larger, which is called the plane turbulent free jet. The free jet can be divided into two different regions. The first region is called the Flow development region, which is close to the nozzle. The jet leaving the nozzle is assumed to have a uniform velocity. The turbulence penetrates inward, towards the jet-centerline, which results in a smaller region of unhindered with the axial distance from the jet. This region is called the potential core, depicted in figure 2.6 with the dashed lines.
The second region is called the region of fully developed flow. In this region, the turbulence has penetrated the jet axis, which means that the mixing layer is fully developed, as can be seen in figure 2.6.

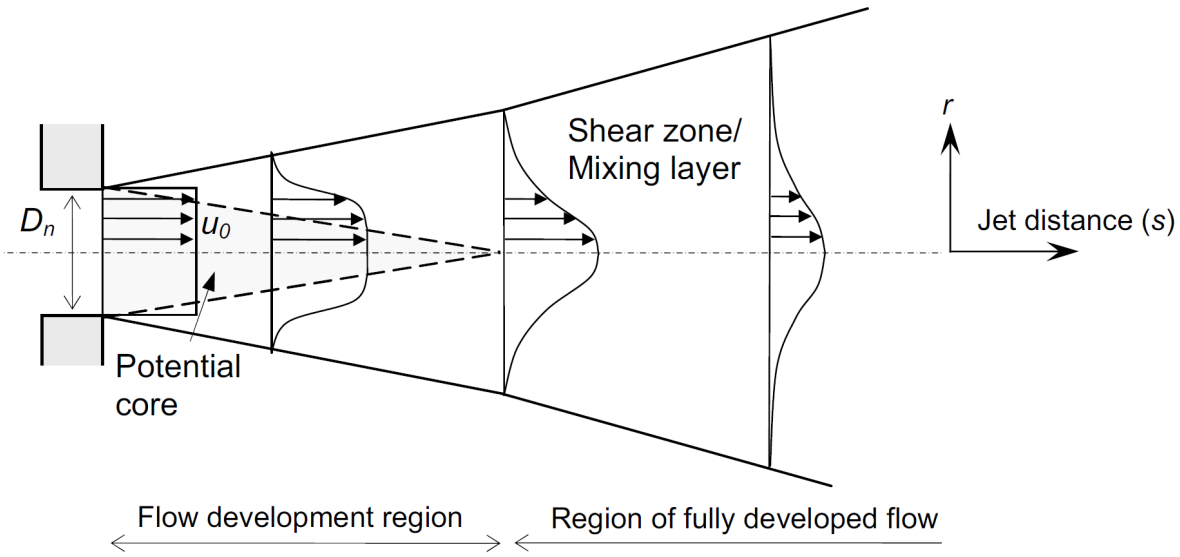

Figure 2.6: Plane turbulent free jet definition sketch (Nobel [27], 2013)

In the region of fully developed flow, the velocity profile is Gaussian. The flow speed in this region can be described according to the following formula:

$$u_j(s,r) = \sqrt{\frac{k_1}{2}} u_0 \frac{D_n}{s} \exp\left(k_2 \frac{r^2}{s^2}\right) \tag{2.21}$$

In which u_j is the flow speed at a axial jet distance s and radial distance r, u_0 is the jet velocity at the nozzle, and k_1 and k_2 are empirical constants. k_1=77±2 and k_2=87.3 ±5 averaged based on expermiments by Fischer et al. (1979).
To calculate the distance of the start of the region of fully developed flow from the nozzle the jet flow can be approximated by neglecting momentum loss to the ambient such that $I = I_0$(Rajaratnam [32], 1976):

$$I(s) = \rho_w 2\pi \int_0^\infty u_j(s,r)^2 r \cdot dr = I_0 \tag{2.22}$$

Where I_0 is the momentum flux at the nozzle exit:

$$I_0 = \rho_w Q_0 u_0 \tag{2.23}$$

in which Q_0 is the flow rate at the nozzle exit

$$Q_0 = \mu_n \frac{1}{4} \pi D_n^2 u_0 \tag{2.24}$$

where μ_n is the nozzle discharge coefficient. Assuming a discharge coefficient of 1, and substituting equation 2.21, 2.23 and 2.24 into Equation 2.22 it follows that k_1 and k_2 must be equal for momentum preservation. Therefore, a value for k_1 and k_2 of 77 is used. The region of fully developed flow starts where the centerline jet velocity is equal to the initial velocity at the nozzle: $u_j(s = s_{dr}, 0) = u_0$. From this it follows that the region of fully developed flow starts at:

$$s_{dr} = \sqrt{\frac{k_1}{2}} * D_n \approx 6.2 D_n \tag{2.25}$$

In other words, the length of the development region is approximately 6.2 times the nozzle diameter. Other researchers proposed another value of the start of the fully developed region(Moore and Masch Jr [25], 1962, Beltaos and Rajaratnam [5], 1977, (Rajaratnam [32], 1976) . The difference in the proposed

distance is likely due to the difference in the jet parameters and the jet geometry, such as k_1, k_2, and the nozzle discharge coefficient μ_n. The jet parameters k_1 and k_2 in this study are based on the assumption of momentum preservation. Only the fully developed jet flow will be considered, which means that the standoff distances during the test are larger than $6.2D_n$.
Equation 2.21 needs to be integrated to calculate the volume of entrained water in the fully developed region as a function of the distance:

$$Q(s) = Q_0\sqrt{\frac{8}{k}\frac{s}{D_n}} \quad \text{for} \quad s \geq s_{dr} \tag{2.26}$$

The flow rate increases linearly with the distance. The entrainment per unit length can be obtained by differentiating Equation 2.26:

$$\frac{dQ}{ds} = \alpha_{nom}\pi D_n u_0 \quad \text{for} \quad s \geq s_{dr} \tag{2.27}$$

In which α_{mom} is the entrainment coefficient, which can be calculated as follows:

$$\alpha_{mom} = \frac{1}{\sqrt{2k}} \approx 0.081 \quad \text{for} \quad s \geq s_{dr} \tag{2.28}$$

The entertainment coefficient is constant in the region of fully developed flow.
The differential equations for conservation of the momentum flux is given as:

$$\frac{dI}{ds} = \frac{d\left(\rho_w Q u_u\right)}{ds} = 0 \tag{2.29}$$

Equation 2.27 and 2.29 can be rewritten as follows:

$$\frac{du_u}{ds} = -\frac{dQ}{ds}\frac{1}{\pi r_u^2} = -2\alpha_{\text{mom}}\frac{u_u}{r_u} \tag{2.30}$$

$$\frac{dr_u}{ds} = \frac{du_u}{ds}\frac{r_u}{u_u} = \frac{dQ}{ds}\frac{1}{\pi r_u u_u} = 2\alpha_{\text{mom}} \tag{2.31}$$

Where u_u is the uniform flow velocity and $r_u = D_j/2$ is the fictitious jet radius. Equations 2.30 and 2.31 can be analytically solved assuming a constant entrainment coefficient. Using the boundary conditions: $u_u(0) = u_0$ and $r_u(0) = D_n/2$, the following equations can be derived:

$$u_u(s) = \frac{1}{2}\sqrt{\frac{k}{2}}u_0\frac{D_n}{s} \quad \text{for} \quad s \geq s_{dr} \tag{2.32}$$

$$r_u(s) = \sqrt{\frac{2}{k}}s \quad \text{for} \quad s \geq s_{dr} \tag{2.33}$$

This means that the approach of assuming an uniform flow velocity, results in half the flow velocity at $r = 0$ with respect to a Gaussian distribution of the flow velocity (equation 2.21).

2.3.2. Impingement zone

At the point where free jet impinges on a surface, the jet flow diverges, and a radial wall jet will develop. The radial wall jet velocities need to be known to be able to predict the shear stresses exerted on the bed by the jet flow To calculate these velocities first, the flow inside the impingement zone needs to be defined. The shear stresses and the impingement pressure can, in turn, be related to the soil erosion by the jet.

The radial wall flow can be described using the following set of differential equations set up by Nobel [27] (2013):

$$\frac{dQ_r}{dr} = 2\pi r u_{u,r}\alpha_{\text{mom},rw} \tag{2.34}$$

$$\frac{du_{u,r}}{dr} = -\frac{dQ_r}{dr}\frac{\rho_w u_{u,r}}{\rho_w Q_r} = -\frac{\alpha_{\text{mom},rw}u_{u,r}}{h_r} \tag{2.35}$$

$$\frac{dh_r}{dr} = -\frac{du_{u,r}}{dr}\frac{2h_r}{u_{u,r}} - \frac{h_r}{r} = 2\alpha_{\mathrm{mom},rw} - \frac{h_r}{r} \tag{2.36}$$

In which h_r is the fictitious height of the radial jet and $\alpha_{mom,rw}$ is the entrainment coefficient of the radial wall jet. Poreh et al. [31] (1967) found that the entrainment coefficient is about 0.128. In equations 2.34, 2.35 and 2.36 it is assumed that the effect of the entrainment of solid particles and the effect of the bed shear stresses on the flow are negligible.
To define the boundary conditions for equations 2.34 to 2.36 a zone of impingement is defined, see figure 2.7. as is depicted in figure 2.7. In this zone, it is assumed that the jet flow is fully deflected.

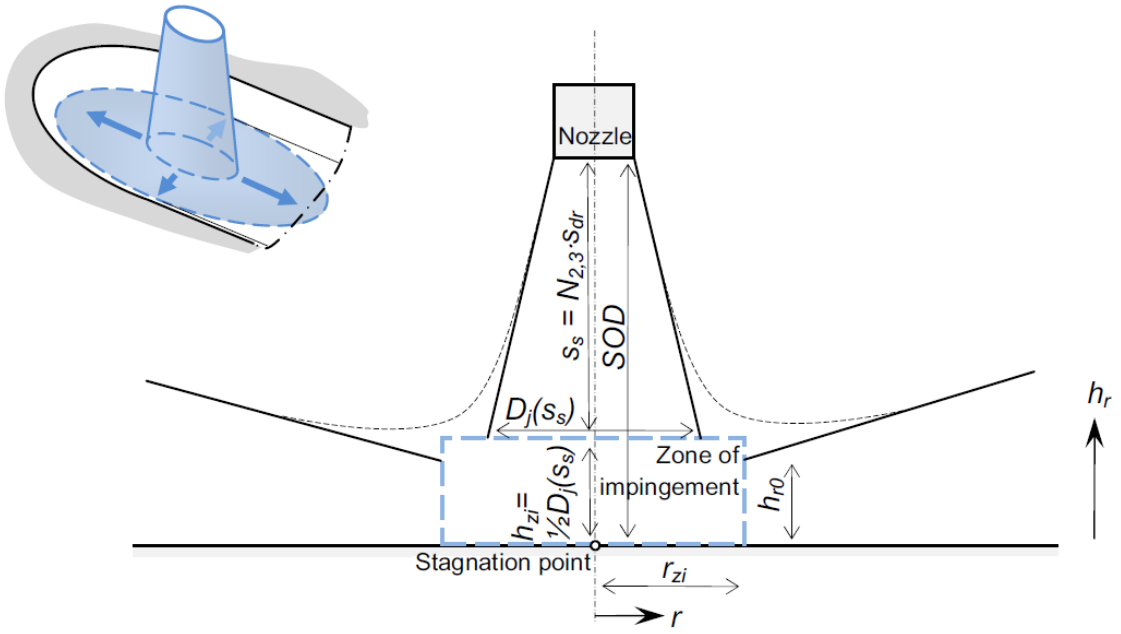

Figure 2.7: Definitions radial dispersing jet flow (Nobel [27], 2013)

The height of this zone h_{zi} is half the fictitious diameter at the top of the impingement zone $D_j(s_s)$. The fictitious diameter $D_j(s_s)$ can be calculated using equation 2.33 assuming $s = s_s$.

A base diameter of $\sqrt{2}D_j(s_s)$ needs to be assumed to compensate for the vertical momentum flux of the jet. This is used to calculate the height (h_{zi}) and the radius (r_{zi}) of the impingement zone and the jet velocity on top of the zone of impingement:

$$u_{zi} = \frac{1}{2N_3}u_0 \quad \text{for} \quad SOD \geq D_n(1+\sqrt{k/2}) \tag{2.37}$$

$$h_{zi} = D_n N_3 \quad \text{for} \quad SOD \geq D_n(1+\sqrt{k/2}) \tag{2.38}$$

$$r_{zi} = \sqrt{2}D_n N_3 \quad \text{for} \quad SOD \geq D_n(1+\sqrt{k/2}) \tag{2.39}$$

$$N_3 = \frac{SOD}{D_n(1+\sqrt{\frac{k}{2}})} \quad \text{for} \quad SOD \geq D_n(1+\sqrt{k/2}) \tag{2.40}$$

The stagnation pressure can be calculated on the basis of the Bernoulli principle. The stagnation pressure is a function of the axial jet velocity. The constant uniform stagnation pressure can be calculated as follows:

$$p_{stag,u} = \frac{1}{2}\rho_w u_u(s)^2 \tag{2.41}$$

In which $u_u(s)$ can be calculated with equation 2.32. The pressure will form shear surfaces in the soil; consequently, the soil will fail along these surfaces when the stagnation pressure exceeds the shear resistance of the surface.

2.3.3. Radial wall Jet

The flow leaving the zone of impingement in the radial direction (Q_{r0}) is assumed to be equal to the flow rate that enters at the top side:

$$Q_{r0} = Q_{ss} = u_u(s_s)\frac{1}{4}\pi D_j(s_s)^2 \tag{2.42}$$

In which $u_u(s_s)$ can be calculated using equation 2.37 because $u_u(s_s) = u_{zi}$. The radial uniform jet velocity can be derived from the horizontal radial momentum flux:

$$u_{u,r} = \frac{I_r}{\rho_w Q_r} = \frac{f_2 I}{\rho_w Q_r} \tag{2.43}$$

In which I_r is the momentum flux and Q_r flow rate in radial direction and f_2 is an empirical constant. The vertical momentum flux is not fully converted in to a horizontal momentum flux. Momentum flux losses are associated with the direction change. About 30% of the momentum flux is lost in the impingement zone, therefore $f_2 \approx 0.7$.

At the edge of the impingement zone ($r = r_{zi}$) the following equations can be derived:

$$u_{u,r0} = \frac{1}{2}\frac{f_2}{N_3}u_0 \quad \text{for} \quad SOD \geq D_n(1+\sqrt{k/2}) \tag{2.44}$$

$$h_{r0} = \frac{1}{\sqrt{8}}\frac{N_3}{f_2}D_n \quad \text{for} \quad SOD \geq D_n(1+\sqrt{k/2}) \tag{2.45}$$

Where $u_{u,r0}$ is the initial radial jet velocity and h_{r0} is the flow height at $r = r_{zi}$. Using these initial conditions equations 2.34 to 2.36 can be solved which results in the following equations:

$$u_{u,r}(r) = u_0\sqrt{\frac{f_2 D_n^2}{8f_1\alpha_{\text{mom}}r^2 + 4\left(N_3 D_n\right)^2\left(\frac{1}{f_2} - 4f_1\alpha_{\text{mom}}\right)}} \quad \text{for} \quad SOD \geq D_n(1+\sqrt{k/2}), r > r_{zi} \tag{2.46}$$

$$h_r(r) = f_1\alpha_{\text{mom}}r + \frac{\left(N_3 D_n\right)^2\left(\frac{1}{f_2} - 4f_1\alpha_{\text{mom}}\right)}{2r} \quad SOD \geq D_n(1+\sqrt{k/2}), r > r_{zi} \tag{2.47}$$

Where $u_{u,r}(r)$ and $h_r(r)$ are the radial jet velocity and radial jet flow height as a function of the radial distance and f_1 is an empirical constant of 1.5.

The effect of the stand off distance decreases with the radial distance. The effect of the stand off distance is negligible for radial distances larger than $12D_n$ (Nobel [27], 2013, Poreh et al. [31], 1967).

The radial jet velocity decreases with the radial distance of the jet centre line due to entrainment of both water and soil. The entrainment of the radial flow of an impinging jet is about 1.5 times higher than the entrainment of a free jet (f_1) (Nobel [27], 2013).

The boundary layer development between the soil and the jet flow can be approximated by the boundary layer development of a boundary layer on a rough plane in a uniform flow. The shear stresses that are exerted on the soil are in the order of a few percents of the stagnation pressure.

2.3.4. Bed shear stress

A boundary layer is formed at the interface between the jet and the soil. At a solid boundary, the jet will have zero velocity relative to the boundary, as stated in the no-slip condition. This condition results in a velocity gradient and related shear stresses perpendicular to the soil. At the beginning of the radial wall jet, the thickness of the boundary layer is negligible, which results in high bed shear stresses. The bed shear stress as a function of the radial distance from the jet-centerline is given in figure 2.8. Near the jet-centerline, where the jet impinges on the surface, the bed shear stress is almost zero. The maximum bed shear stress occurs at the point where the radiall jet velocity is maximum, which is at the edge of the impingement zone.

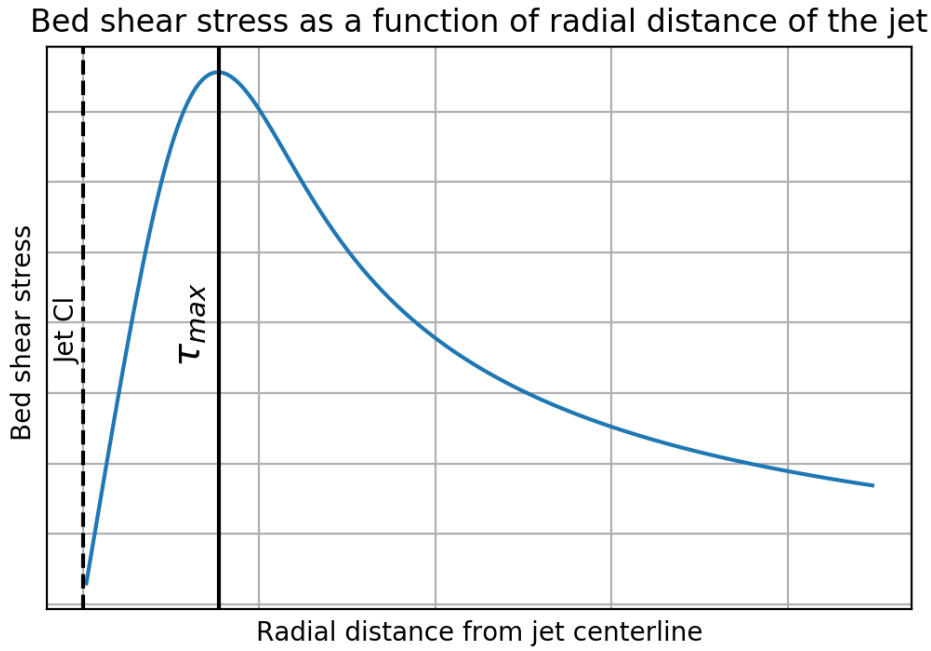

Figure 2.8: Bed shear stress development on a flat bed as a function of the radial distance from the jet-centerline.

The bed shear stress resulting from a impinging jet is elaborated in this section.

Rough bed

The bed shear stresses imposed by the radial wall jet can be approximated by the wall shear stresses of a uniform flow on a rough plate (Nobel [27], 2013).

The bed shear stresses can then be calculated using the following equation:

$$\tau_b = c_f \frac{1}{2} \rho_w u_{m,bl}^2 \tag{2.48}$$

In which c_f is the friction coefficient and $u_{m,bl}$ is the maximum velocity at the edge of the boundary layer.

An upper limit for the friction coefficient can be found by applying a rough plate approximation for the boundary layer development. The relative roughness height influences the maximum velocity at the edge of the boundary layer, as found by Rajaratnam [32] (1976). This variation can be approximated as follows:

$$\frac{u_{m,bl}}{u_{u,r0}} = K_1 - 0.54 \log\left(\frac{r}{k_s}\right) \tag{2.49}$$

In which $u_{u,r0}$ is the initial radial wall jet velocity, which can be calculated using equation 2.44, r is the distance to the jet (to $r0$), and K_1 is an empirical constant approximated by the empirical equation:

$$K_1 = -0.29 \ln\left(\frac{k_s}{h_{r0}}\right) + 1.13 \tag{2.50}$$

In which h_{r0} is the initial height of the radial wall jet, as defined in equation 2.45. And k_s is the equivalent roughness height, which is in the order of $5D_{50} - 1D_{90}$. Rajaratnam [32] (1976) found that the maximum velocity at the edge of the boundary layer varies with the relative roughness height.

The velocity profile in a boundary layer is assumed to be logarithmic, to calculate the bed shear stress at the edge of the boundary layer the boundary layer height needs to be known. In the relation setup by Rajaratnam [32] (1976), the boundary layer thickness is defined as δ=0.026*r.

$$u_{bl}(\delta) = \frac{u_*}{\kappa} \ln \frac{\delta}{h_0} \tag{2.51}$$

In which u_* is the bed shear velocity defined as $\sqrt{\tau_b/\rho_m}$, κ is the Kármán constant, which is approximately 0.41, and h_0 is an integration constant to set the velocity somewhere near the bed at zero. Equation 2.51 can be rewritten to obtain the bed shear stress:

$$\tau_b = \left(\frac{u_{m,bl}}{ln(\delta/h_0)}\kappa\right)^2 \rho_m \tag{2.52}$$

The friction coefficient can subsequently be calculated by substituting the velocity at the edge of the boundary layer $u_{m,bl}$ and the obtained bed shear stress from equation 2.52, in equation 2.48.

Stochastic bed shear stress

The instantaneous bed shear stress varies due to turbulence. The turbulent motion is stochastic and can be approximated by a probability density distribution for the bed shear stress. Van Prooijen and Winterwerp [38] (2010) developed a distribution for the bed shear based on the bed shear stress measurements of Obi et al. [28] (1996). The developed distribution is given in figure 2.9 as the red line. An analytical parameterised expression is developed, which is only dependent on the mean bed shear stress. A third-order polynomial fits this parameterised function. This function is given and further discussed in section 2.4.2.

The probability density function of the bed shear stress is given by Van Prooijen and Winterwerp [38] (2010) as:

$$r\,(T_b) = \frac{\alpha_1}{2\sqrt{2\pi T_b^*}} \exp\left[-\frac{1}{2}(\sqrt{T_b^*} - \alpha_3)^2\right] \tag{2.53}$$

In which

$$T_b = \frac{\tau_b}{\rho_w \sigma^2} \tag{2.54}$$

With $T_b^* = \alpha T_b - \alpha_2 \alpha_3^2$. Where T_b is the dimensionless bed shear stress and α_1 and α_2 and α_3 are fit parameters. α_3 is equal to the dimensionless mean velocity: μ_u/σ_u. In which μ_u and σ_u represent the mean value and the standard deviation of the distribution respectively. These fit parameters are tuned to fit the measurement data obtained by Obi et al. [28] (1996). The values for the fit parameters that gave the best fit are as follows: α_1=1.75; α_2=0.83; and α_3=3.1

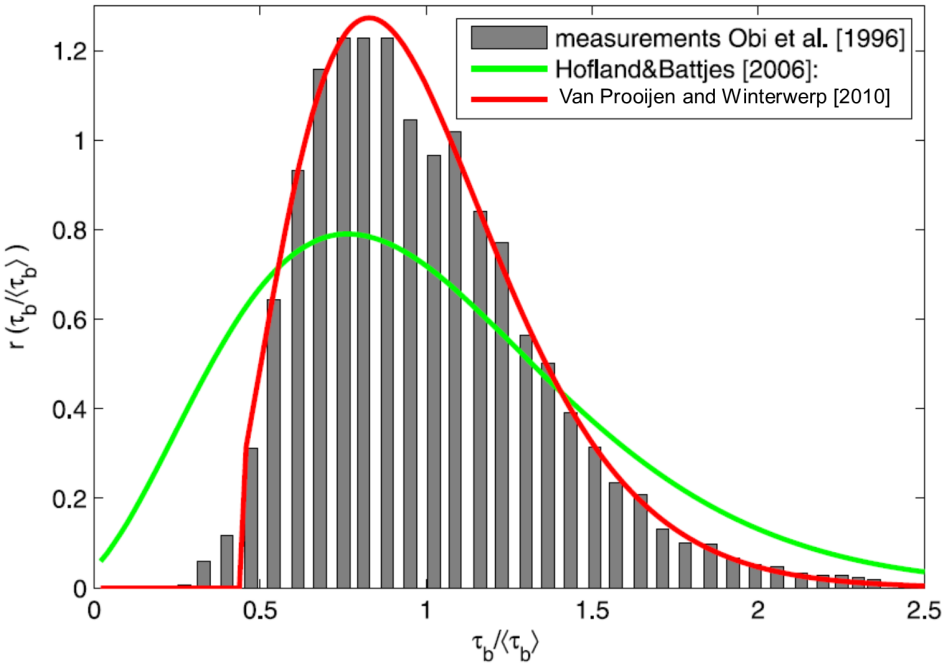

Figure 2.9: Measurements of the bed shear stress normalized by the mean bed shear stress (Obi et al. [28], 1996), the fitted relation of Hofland and Battjes [14] (2006) and the modified relation by Van Prooijen and Winterwerp [38] (2010).

2.3.5. Scaling of scour depth results

The stagnation pressure is defined in equation 2.41 and with the flow velocity as defined in equation 2.32. Combining these equations results in the following equation:

$$p_{stag} = \frac{1}{2}\rho\frac{k}{2}u_0^2\frac{D_n^2}{s^2} \tag{2.55}$$

In equation 2.55 the distance of the jet to the soil surface is increasing during the duration of the test. Therefore $s = SOD + Z_c$, in which Z_c is the scour hole depth . As the stagnation pressure is changing throughout the test, it is preferred to take the constant jetting pressure defined as $p_{jet} = \frac{1}{2}\rho u_0^2$. Rewriting this equation results in equation 2.56.

$$p_{stag} = p_{jet} \cdot \frac{k}{2} \cdot \left(\frac{D_n}{SOD + Z_c}\right)^2 \tag{2.56}$$

Assuming that the stagnation pressure must be a factor (N_c) times su, equation 2.56 can be rewritten to:

$$p_{stag} = N_c \cdot su \tag{2.57}$$

From equation 2.56 and 2.57 follows:

$$N_c \cdot su = p_{jet} \cdot \frac{k}{2} \cdot \left(\frac{D_n}{SOD + Z_c}\right)^2 \tag{2.58}$$

Equation 2.58 can also be written as:

$$\frac{SOD + Z_c}{D_n} = f \cdot \sqrt{\frac{p_{jet}}{su}} \tag{2.59}$$

In which $f = \sqrt{\frac{k}{2N_c}}$. This means that the square root of p_{jet}/su is proportional to the actual distance from the jet to the soil surface, divided by the nozzle diameter, as given in equation 2.60.

$$\frac{(SOD + Z_c)}{D_n} \propto \sqrt{p_{jet/su}} \tag{2.60}$$

Writing the equation in this manner has the advantage that both sides are dimensionless. Furthermore, the varying standoff distance and nozzle diameter are scaled according to the relative jet pressure.

2.4. Failure mechanisms

Other researchers have investigated the erosion processes of cohesive soils by submerged jets. Erosion of a cohesive soil has been classified into four modes by Winterwerp and Van Kesteren [44] (2004), this classification scheme is modified by Jacobs [16] (2011) and has a close resemblance with the classification scheme presented by Mazurek [22] (2001). The four different cohesive soil erosion modes are entrainment, floc erosion, surface erosion and mass erosion. In figure 2.10 the erosion modes are visualised. These erosion types are elaborated in the next section.

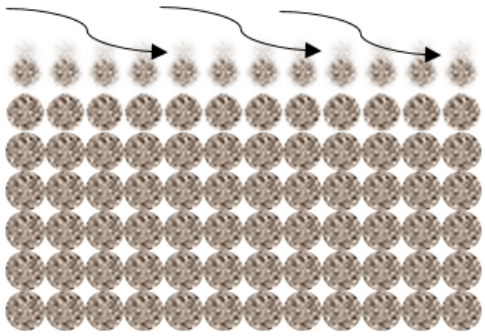

(a) Entrainment

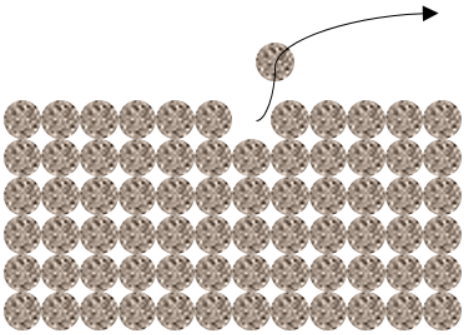

(b) floc erosion

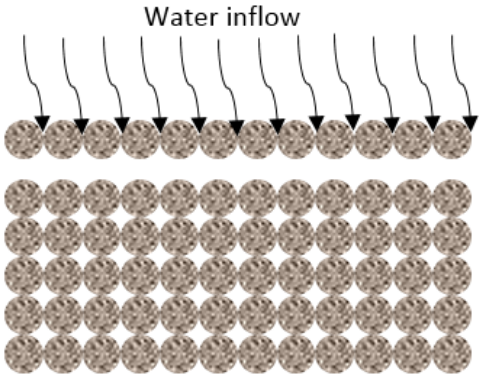

(c) Surface erosion

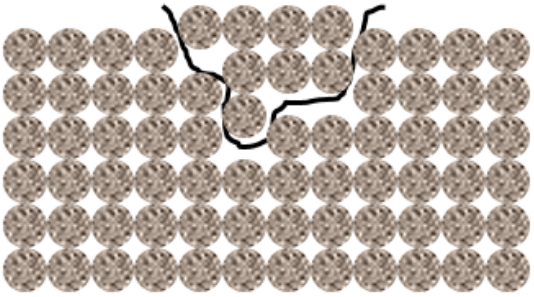

(d) Mass erosion

Figure 2.10: Four different erosion types graphically explained

2.4.1. Entrainment

Entrainment is when the bed behaves as a viscous fluid, the stress at the interface between the fluid mud layer and the overlying water column exceeds the yield strength of the mud, see figure 2.10a.

2.4.2. Floc and surface erosion

Floc and surface erosion are considered as a drained erosion process. An excess stress equation often used to describe surface and floc erosion. Ariathurai [2](1974) presented a parameterized excess stress erosion formula based on erosion experiments by Partheniades [29] (1965):

$$E = M\left(\frac{\tau_b - \tau_{cr}}{\tau_{cr}}\right) \text{ for } \tau_b > \tau_{cr} \tag{2.61}$$

In which E is the erosion rate in $kg/m^2/s$, M is an erosion parameter, τ_b the turbulent-mean bed shear stress, and τ_{cr} a critical shear stress for erosion.

Several researchers such as Smerdon and Beasley [33] (1959), Whitehouse et al. [42] (2000) and Winterwerp et al. [43] (2012) developed empirical relations for the critical shear stress of cohesive soils. They related the critical shear stress to different soil parameters such as the plasticity index PI, the density of the bed ρ_b, and the dispersion ratio D_r.
Dunn [8] (1959) and Hollick [15] (1976) used submerged vertical impinging jets to approximate the critical shear stress of a soil, who also related it to soil parameters. Dunn found that the plasticity index and the undrained shear strength were the dominant soil parameters influencing the soil erosion.

Floc erosion

Floc erosion is depicted in figure 2.10b. Flocs are a individual or a collection of clay particles with a cohesion of a few millimeters. Mazurek [22] (2001) quantified flocs as thin elements of soil, 1-3 mm diameter, max 0.5 mm thick. The threshold for floc erosion to occur is $\tau_b \tilde{\geq} \tau_{cr}$. Floc erosion is defined as the erosion of individual flocs are disrupted from the bed when the flow-induced peak stresses $\hat{\tau}_b$

exceed the local bed strength. Therefore, floc erosion is related to the stochastic characters of the floc strength and flow condition. Floc erosion is the dominant erosion type at low bed shear stresses.

Surface erosion

Surface erosion, figure 2.10c occurs when the mean flow-induced stresses are significantly larger than the critical shear stress τ_{cr}. Surface erosion is a continuous drained process. A combination of shear force, uplift forces and their fluctuations act to remove the soil particles and start the erosion process. The threshold for surface erosion occurs for $\bar{\tau}_b = \tau_{cr}$, where τ_{cr} drained shear strength. For surface erosion to occur, the water content has to increase. As water flows in to the pores the water content increases and decreases the strength of the bed. This process is called swelling. Also during the erosion process, the bed becomes over-consolidated when above lying layers are removed, which increases the swelling rate.

The depth of the swelling front is a function of the swelling properties of the sediment and can be described as a diffusion process. The depth of the swelling front can be defined by equation 2.62.

$$h_{sw} = \sqrt{\pi c_v t} \tag{2.62}$$

In which h_{sw} is defined as the depth at which the water pressure starts to dissipate. Between the top of the bed and a distance of h_{sw} in the bed the pore water pressure converges to the water pressure at the top of the bed, deeper in the bed the pore water pressure equals the pore water pressure at $t = 0$.

The swelling rate is proportional to the ratio between the consolidation coefficient c_v and the depth below the soil surface h_{sw} and is given as the time derivative of the location of the swelling front:

$$\frac{dh_{sw}}{dt} = \frac{\sqrt{\pi c_v}}{2\sqrt{t}} \tag{2.63}$$

$$\sqrt{t} = \frac{h_{sw}}{\sqrt{\pi c_v}} \tag{2.64}$$

$$v_{sw} = \frac{dh_{sw}}{dt} = \frac{\pi c_v}{2h_{sw}} \approx \frac{c_v}{h_{sw}} \tag{2.65}$$

Where v_{sw} is the propagation velocity of a swelling front at a depth h_{sw}, see figure 2.11.

In the top layer, the strength is assumed to decrease from the swelling front depth to the surface linearly. At the swelling front depth, the strength is equal to the undrained shear strength su. At the surface, the strength is equal to the residual strength τ_{cr}, which reflects the shear strength at zero effective stress (coherence of the flocs to the bed). The value of τ_{cr} can be referred to as the actual critical shear stress for erosion. Empirical relations can be used to determine this value.

The thickness of the layer that can be eroded by the bed shear stress τ_b induced by the flow, assuming a linear distribution of the strength of the bed, can be described as follows:

$$h_e = h_{sw}\frac{\tau_b - \tau_{cr}}{su - \tau_{cr}} \approx h_{sw}\frac{\tau_b - \tau_{cr}}{su} \quad \text{for} \quad su >> \tau_{cr} \tag{2.66}$$

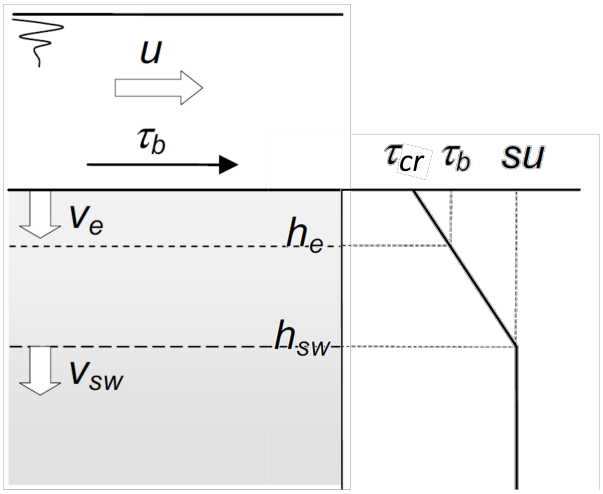

Figure 2.11: Surface erosion definition of the different parameters and the strength distribution in a swelling bed, diagram is not to scale (after Nobel [27] (2013))

Winterwerp and Van Kesteren [44] (2004) state that the swelling depth h_{sw} scales with the size of the bed-forming flocs. Furthermore, the swelling depth should at least be an order of magnitude larger than the size of the primary particles (flocculi) D_f.

The minimum thickness of the erosion layer scales with the median diameter of the particles in the soil D_{50} according to Winterwerp and Van Kesteren [44] (2004) and Jacobs [16] (2011). A correction is applied for the initial pore water n_0 at the top layer:

$$h_e = \frac{10D_{50}}{1 - n_0} \tag{2.67}$$

Assuming that the bed shear stresses are equal to the bed strength at h_e for erosion, the swelling depth will decrease for an increasing bed shear stress τ_b. For a continuously eroding bed, the erosion velocity must be equal to the swelling rate: $v_e = v_{sw}$. Substituting equation 2.66 and 2.67 into equation 2.65, results in the equation for the erosion velocity:

$$\frac{10D_{50}}{1 - n_0} = h_{sw}\frac{\tau_b - \tau_{cr}}{su - \tau_{cr}} \tag{2.68}$$

$$h_{sw} = \frac{10D_{50}(su - \tau_{cr})}{(1 - n_0)(\tau_b - \tau_{cr})} \tag{2.69}$$

$$v_{sw} = \frac{c_v(1 - n_0)(\tau_b - \tau_{cr})}{10D_{50}(su - \tau_{cr})} \quad \text{for} \quad su >> \tau_{cr} \tag{2.70}$$

$$v_{sw} = v_e = \frac{c_v\phi_s}{10D_{50}}\frac{\tau_b - \tau_{cr}}{su} \tag{2.71}$$

Where ϕ_s the volume concentration of the sediment bed at the onset of swelling (which is equal to $1 - n_0$). From equation 2.71 Winterwerp and Van Kesteren [44] (2004) derived the following equation for the erosion rate parameter M_e

Winterwerp and Van Kesteren [44] defined the erodibility parameter M for floc and surface erosion in equation 2.61, from equation 2.71:

$$M_E = \frac{c_v\phi_s\rho_{dry}}{10D_{50}su} \tag{2.72}$$

Where ρ_{dry} the dry bed density. Using this formulation M is decomposed in diagnostic parameters which can be obtained from standard tests.

Jacobs [16] (2011) derived a formulation for the surface erosion rate which is to a large extend based on the formulation proposed by Winterwerp and Van Kesteren [44] (2004):

$$M_S = \frac{c_{v,s}\rho_{dry}}{D_{50}\phi^{1/(n_{fr}-3)}su} \tag{2.73}$$

In which n_{fr} is the fractal dimension, which is between 2.6< n_{fr} <2.8 within the bed (Winterwerp and Van Kesteren [44], 2004). Both Winterwerp and Van Kesteren [44] (2004) and Jacobs [16] (2011) found that for surface erosion, the erosion rate is dependent on the undrained sediment strength, and limited by the dissipation rate of the pore water pressure, which can be approximated using the coefficient of consolidation which is described in chapter 2.2.5.
Winterwerp et al. [43] (2012) altered equation 2.72, with in stead of taking $10D_{50}$ a erosion factor $\alpha_e \cdot D_{50}$ is assumed, in which α_e is defined as:

$$\alpha_e \equiv \frac{\pi\alpha_h}{2} \quad \text{in which} \quad \alpha_h \approx \frac{h_e\phi_s}{D_{50}} \tag{2.74}$$

In which h_e is the erosion layer thickness as defined in equation 2.67.

To have a smooth transition between no erosion to linear erosion (equation 2.71), Van Prooijen and Winterwerp [38] (2010) developed a parmeterised equation which takes into account the stochastic nature of bed shear stress fluctuations and relates it to the mean bed shear stress, as discussed in section 2.3.4, this function is given as follows:

$$\frac{E}{M\tau_{cr}} = \begin{cases} 0 & \text{if } \frac{\langle\tau_b\rangle}{\tau_{cr}} < 0.52 \\ a_1\left(\frac{\langle\tau_b\rangle}{\tau_{cr}}\right)^3 + a_2\left(\frac{\langle\tau_b\rangle}{\tau_{cr}}\right)^2 + a_3\left(\frac{\langle\tau_b\rangle}{\tau_{cr}}\right) + a_4 & \\ \left(\frac{\langle\tau_b\rangle}{\tau_{cr}} - 1\right) & \text{if } \frac{\langle\tau_b\rangle}{\tau_{cr}} > 1.7 \end{cases} \tag{2.75}$$

In which $\langle\tau_b\rangle$ is the turbulent mean bed shear stress. The following parameters have been found by Van Prooijen and Winterwerp [38] (2010): α_1=-0.144; α_2=0.904; α_3=-0.823; α_4=0.204.

The theoretical maximum surface erosion velocity occurs at $\tau_b = su$ where $h_{sw} = he$:

$$v_{e,max} = \frac{c_v\phi_s}{10D_{50}} \tag{2.76}$$

As explained in this chapter the process of swelling and pore water pressure dissipation can be described using the consolidation coefficient. To test whether the erosion process is drained or undrained, e.g. if the erosion is occurring in combination with pore pressure gradients, the Péclet number for pore water pressure dissipation Pe_w can be investigated, which is defined as:

$$Pe_w = \frac{vl}{c_v} \tag{2.77}$$

In which v is a velocity scale, and l is a length scale. Taking for the velocity scale, the erosion speed v_e and for the length scale the depth of the swelling front h_{sw}, which can be defined as $10 \cdot D_f$. Equation 2.77 can than be expressed as follows:

$$Pe_w = \frac{v_e h_{sw}}{c_v} \tag{2.78}$$

Winterwerp and Van Kesteren [44] (2004), state that for $Pe_w < 1$ the erosion process is fully drained. The process can be considered undrained if $Pe_w > 10$.

Critical bed shear stress

Soil particles can only be removed when the exerted stresses exceed the bonding stresses of the soil, which keeps it in the bed. This strength is known as the critical shear stress for erosion. The critical shear stress relates to the drained strength of the soil. Several different empirical relations exist to

approximate the critical shear stress based on bulk soil parameters. Winterwerp and Van Kesteren [44] (2004) found that the strength and swell can be related to the plasticity index PI. Winterwerp et al. [43] (2012) found a relation between the critical shear strength and plasticity index, based on a formulation developed by Smerdon and Beasley [33] (1959):

$$\tau_{cr} = 0.7PI^{0.2} \tag{2.79}$$

Winterwerp et al. [43] (2012) found that that equation 2.79 gives a relatively good fit for soils with a PI larger than 7%.

2.4.3. Mass erosion

Mass erosion is the undrained disruption of chunks of material. Mass erosion (figure 2.10d) occurs when the scale of the flow-induced deformations of the sediment bed is larger than the scale at which pore water pressure gradients dissipate, therefore mass erosion is an undrained process. The threshold is given by:

$$p_{stag} > 2 \sim 5su \tag{2.80}$$

Other researchers observed mass erosion(Winterwerp et al. [43], 2012, Mazurek [22], 2001, Nobel [27], 2013, Kerssens [19], 2017, Moore and Masch Jr [25], 1962). The threshold mass erosion is based on the bearing capacity of the soil. Whereas the other thresholds of erosion are based on the critical bed shear stress is the threshold for mass erosion based on the stagnation pressure of the jet exerted on the soil.

2.4.4. Fracturing

A fifth failure mechanism called fracturing. Fracturing is the failure of macro-cracks. These macro-cracks are formed by the coalescence of micro-cracks that are present in the soil (Nobel [27], 2013). Fracturing has much resemblance with mass erosion, as it is visually observed as the removal of large chunks of soil. Mazurek [22] (2001) divided mass erosion into two classes, one due to disturbances in the clay (in this study called fracturing), and one that is not associated with disturbances in the clay structure, but due to high bed shear stresses and pressures on the soil (called mass erosion in this study).
Fracturing could occur under an impinging jet in the stagnation zone as depicted in figure 2.12.

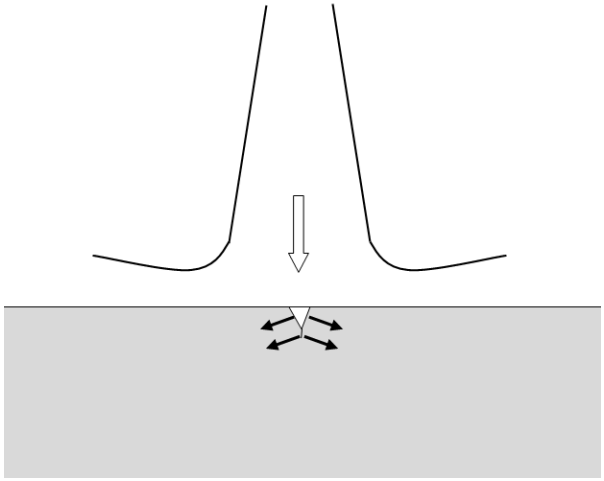

Figure 2.12: Tensile stresses (black arrows) induced by a vertically impinging jet on a soil surface

According to Marchi et al. [21] (2013), the fracturing of clay in undrained conditions occurs by a rapid increase in the fluid injection pressure at crack tips. Fracture initiation can be either due to tensile or shear stresses. Tensile cracks are generated when the minor principal effective stresses σ_3' become equal to the negative value of the tensile strength $\sigma_{t,f}'$, as can be seen in figure 2.13 (a). Undrained shear failure (figure 2.13) can occur in soft clays before it reaches tensile failure, according to Soga et al. [34] (2005). Soga et al. [34] (2005) suggests that an increase in the plastic shear failure zone

develops an unstable state around the cavity, as a reaction on the increased cavity pressure, which leads to localized micro-scale fractures where the injected fluid can infiltrate. At a certain stress level, micro-cracks in the plastic zone coalescence to macro-cracks. The jet flow can enter the microscopic macro-cracks leading to local tensile stresses at the crack tips, eventually resulting in tensile failure. According to Marchi et al. [21], the occurrence of tensile or shear failure can be related to the liquidity index LI. For a positive value of LI, which means that the soil is in a plastic state, shear failure is more likely to occur than tensile failure at the onset of fracture. A negative value of the liquidity index implies that the soil is in a semi-solid state, as mentioned in section 2.2.1. In these conditions, permanent deformation occurs under increasing hydraulic pressure and will crack; this corresponds to tensile failure. Since the soil samples tested in this study all have a positive Liquidity index, fracturing due to shear failure is more likely to occur. Marchi et al. [21] (2013) derived that fracturing due to shear failure could initiate at a pressure equal to the undrained shear strength if the initial principal stress is equal to zero:

$$p_{frac} \approx su \tag{2.81}$$

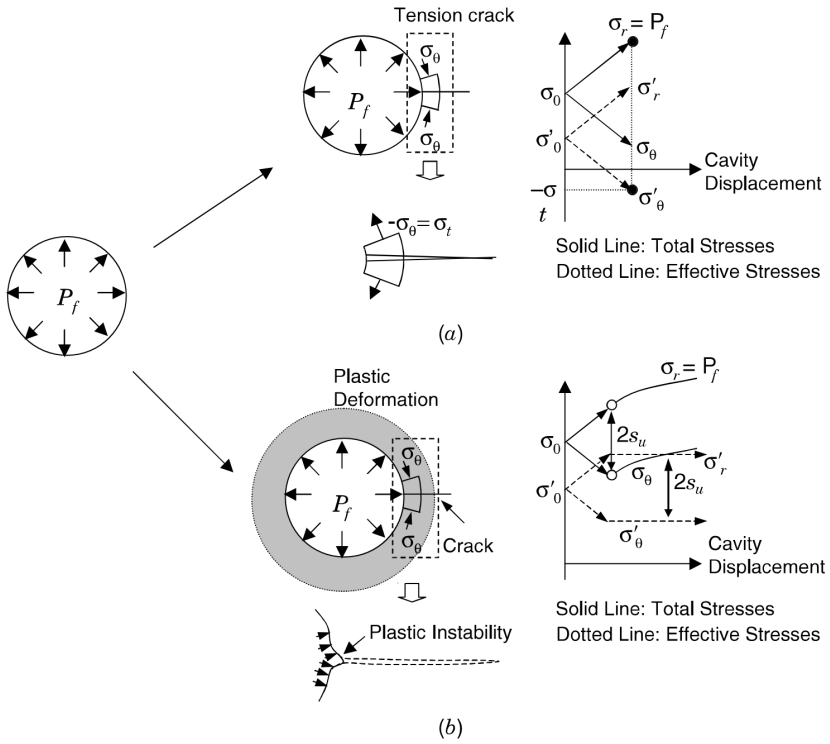

Figure 2.13: Fracture mechanisms caused by increased fluid pressure in cavities: tensile fracture (a) and shear failure (b) both in undrained conditions (Mitchell and Soga [24], 2005)

Key factors for determining the fracturing pressure in clayey soils are the confining pressure, undrained shear strength, and the tensile strength (Marchi et al. [21]).

Internal fracturing

The internal-cracks are formed by discontinuities in the soil skeleton, for example, larger particles such as stones. Coalescence of micro-cracks occurs under shear failure in the undisturbed material between the cracks (Winterwerp and Van Kesteren [44], 2004). The coalescence mechanism can be seen in figure 2.14.

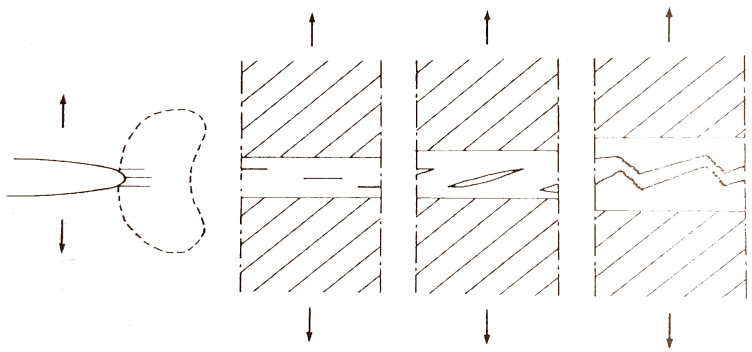

Figure 2.14: Crack propagation and coalescence in cohesive soils (Winterwerp and Van Kesteren [44], 2004)

Other researchers have observed that due to the stress concentrations between the cracks, the soil fails at stresses that are much smaller than the undrained shear strength (Mitchell and Soga [24], 2005, Winterwerp and Van Kesteren [44], 2004). Barron [4] (1948) stated that crack propagation of microcracks is dependent on the crack size, drainage length, and the consolidation coefficient.
The fracturing behaviour of cohesive soils can be described using linear elastic fracture mechanisms. Water over-pressure in a crack leads to This theory states This theory states that water over-pressure in a crack leads to stresses around the edges of the crack. These stresses around the edge of the crack are equal to the tensile stress due to the tensile loading.

Loading a saturated soil with tensile stress $\Delta\sigma_t$, a pressure drop inside a micro-crack is initially generated which is equal to the tensile strength, as can be seen in figure 2.15(a) and (b). The black framework in (b) is an infinitesimal control volume to express the stress state for a point within the crack. Directly after loading no stress concentrations around the edges of the crack occur. However, in the pores surrounding the crack, the pore water pressure only drops with $1/3\Delta\sigma_t$, as can be seen in figure 2.15 (c). The deviation between the water pressure inside the crack and the surrounding pores (of $2/3\Delta\sigma_t$) results in the pore-water flow towards the cracks. Due to the flow towards the cracks the water pressure inside the crack increases. The increased water pressure inside the crack results in stress concentrations around the cracks. The black framework in (c) is an infinitesimal volume to express the stress state in a point within the soil outside of the crack. In this point both water and solid material is present. There are both pore water pressures and effective pressures present, as in equation 2.9. In this description both compression and dilation are both neglected.

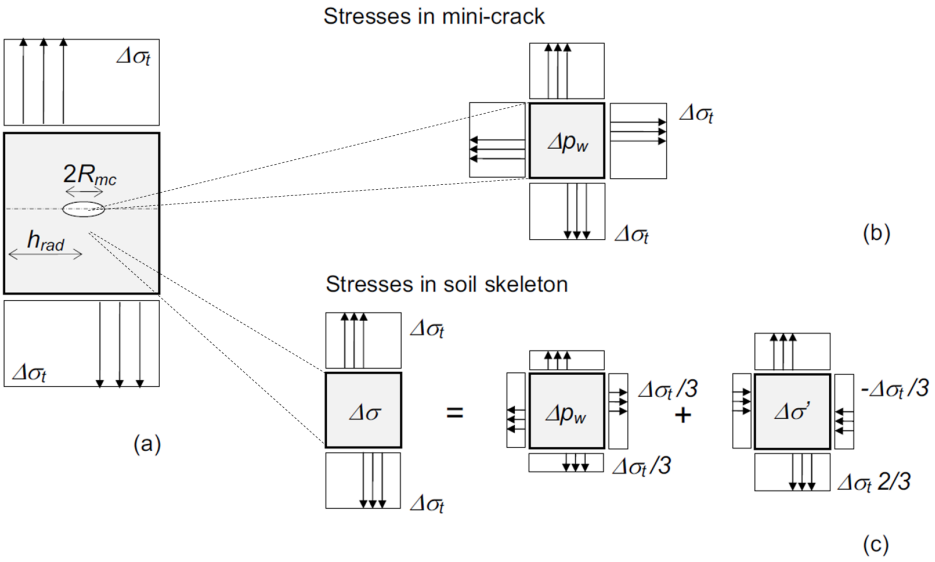

Figure 2.15: Fracturing process: (a): Schematic representation and definitions of fracturing. (b) Pressure in micro-crack at t=t_0 (directly after loading). (c) Stresses in the soil skeleton directly after loading. (Nobel [27], 2013)

The fracturing of a soil is a time-dependent process. The main soil parameters governing the fracturing process are the coefficient of consolidation c_v and the crack size inside the soil. Barron [4] (1948) developed a theory to predict the pore water pressure development inside a penny shaped crack (p_{wmc}) over time. The normalized water pressure development given as $\frac{\Delta p_{w,mc}}{\Delta \sigma_t}$ is given in the following function:

$$\frac{\Delta p_{w,mc}}{\Delta \sigma_t} = \frac{1}{3} + \frac{2}{3} e^{\frac{-8T_{mc}}{b_{mc}}} \tag{2.82}$$

In which T_{mc} is a dimensionless times scale and b_{mc} is a shape factor given in the equations below:

$$T_{mc} = \frac{c_v t}{(2h_{rad})^2} \tag{2.83}$$

$$b_{mc} = \frac{n_{mc}^2}{n_{mc}^2 - 1} \ln(n_{mc}) - \frac{3n_{mc}^2 - 1}{4n_{mc}^2} \tag{2.84}$$

$$n_{mc} = \frac{h_{rad}}{R_{mc}} \tag{2.85}$$

In which h_{rad} is the drainage length and R_{mc} is the radius of a penny-shaped crack.
Plotting the the normalized water pressure development inside the crack as a function of time, as can be seen in figure 2.16.The dimensionless water pressure levels asymptotically towards $1/3$. Nobel [27] (2013) suggests that the dissipation up till 10% results in a minimal stress concentration and can therefore be neglected. The critical time of loading can be calculated using equations 2.82-2.85. This can be used to assess whether fracturing is a possible erosion mechanism occurring with mass flow jetting.

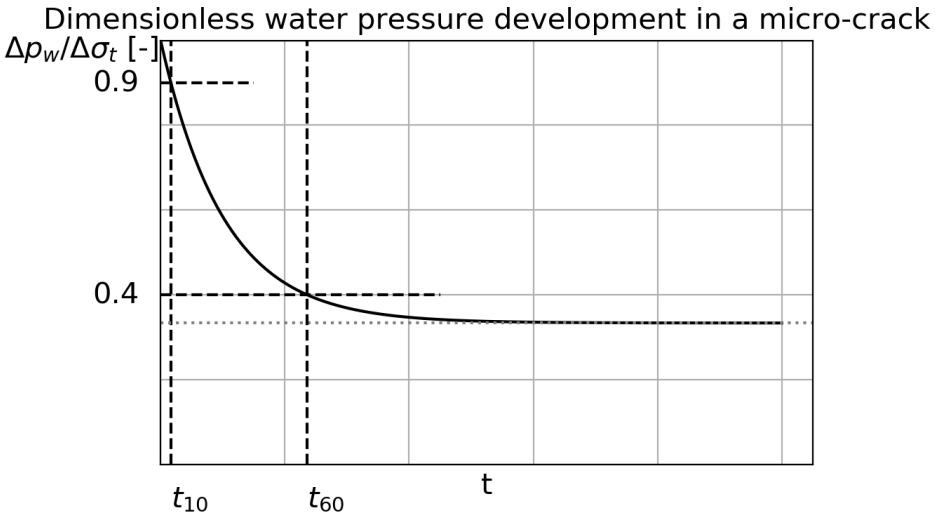

Figure 2.16: Water pressure development in a a micro-crack as a function of the time

2.4.5. Natural variation

Natural variations inside soils have a big influence on the erosion behaviour of cohesive soils. As described earlier in section 2.4.4, disturbances in the soil make that fracturing can occur easier. Variation in the soil also changes essential soil parameters such as, the undrained shear strength su, the permeability k_s, compressibility m_v and therefore the consolidation value c_v, which turn also influence the onset of mass erosion, flock and surface erosion.

Kamphuis [18] (1990) reported that when sandy seams are present in clay samples that separation occurs along with the fractures and sandy planes. Mass erosion type of behaviour would occur in some parts, and in other parts, where the sample was more homogeneous, significant less erosion would occur. He also noted that when a sample was damaged, erosion would occur at shear stresses which were lower than the critical shear stress. Mazurek [22] (2001) found that the creation of a disturbance in a clay soil could cause the development of mass erosion.
Kerssens [19] (2017) did several tests with natural clays with varying amounts of homogeneity. He found that the natural clays would exhibit mass erosion and fracturing behaviour at stagnation pressures lower than 1 su, whereas more homogeneous plastic clays would start to fail in the same way at 2-3 times the undrained shear strength. Kerssens [19] (2017) also found out that clay samples that were created using a vacuum executer would fracture along the weaker planes present in the sample due to this production method.
Therefore it can be concluded that natural variation has a significant influence on the erosion behaviour of clay beds. However, in this study, only artificial clay is used and investigated. This is done to properly investigate the effect of the consolidation coefficient (c_v). Also, the relative influences of the different types of erosion are not known yet, using artificial clay will make it significantly harder to analyse this effect.

2.5. Previous work in erosion by low pressure jets

Most of the studies researching the erodibility of cohesive soils are executed using a parallel flow over a soil surface and relating that to shear stresses exerted on the soil, which has resemblance with the radial wall jet as described in chapter 2.3.3. This type of study has been done by Winterwerp and Van Kesteren [44] (2004) and Jacobs [16] (2011). The resulting formula's describe surface and floc erosion (equation 2.72, 2.73). However, these formulae tend to deviate when a mass erosion and fracturing process is occurring. Furthermore, the penetration depth of a jet is hard to describe using these formulae.
Researchers, however, have investigated the erosion of cohesive soils using turbulent jets. Some relevant studies are discussed in this chapter. A relevant term for the developed models is the critical shear stress for erosion, which is first discussed.

2.5.1. Hedges (1990)
Hedges [13] (1990) investigated the scour of clays with a vertically inclined submerged turbulent jet. Hedges analysed the effects of the time duration of scour impingement, standoff distance and shear strength of the clay. Hedges reported the scoured volume at different time intervals. Hedges did not report the penetration depth of the jet.
Hedges found a linear relationship between the scour volume, and the time of impingement, however, this was only based on three data points with a total test duration of 15 minutes. Furthermore, he found a relationship between the undrained shear strength and the erosion velocity and volume. Lastly, he found decreased scour with increasing jet height.

2.5.2. Mazurek (2001)
Mazurek [22] (2001) investigated scour of cohesive soils by submerged circular turbulent impinging jets. The test apparatus used by Mazurek has a close resemblance with the test setup used in this study. Mazurek varied the nozzle diameter, standoff distance and jetting velocity. Only one clay mixture was used in the tests. Mazurek derived equations based on the excess shear stress as presented in equation 2.61 and using experimental fitted parameters to predict the maximum equilibrium erosion depth, the equilibrium erosion depth at the jet centre-line, and the equilibrium erosion volume by a submerged impinging jet. In this formula, the erosion parameter M is an empirical fitted parameter. The critical bed shear stress is the only parameter relating to the soil in these equations. The critical bed shear stress is derived from jet test data. The formula obtained by calibration for the maximum equilibrium scour depth is as follows:

$$\frac{Z_{c,max}}{SOD} = 0.19 \cdot \left(\frac{X - X_{cr}}{X_{cr}} \right)^{0.74} \tag{2.86}$$

In which $Z_{c,max}$ is the equilibrium maximum scour depth,X_{cr} is the critical shear stress derived from the data (approximately $0.16X$), and X is the shear stress on the soil surface defined as:

$$X = \rho_w u_0^2 \cdot \frac{D_n}{SOD}^2 \tag{2.87}$$

Note that no soil parameters are included in X_{cr}.

2.5.3. Hanson (2004)
Hanson and Cook [12] (2004) developed a Jet erosion apparatus to find a value for the critical shear stress τ_c and the erosion parameter M of equation 2.61 based on the eroded depth by the apparatus as a function of time. To apply this formula and find the soil erosion rate, JET erosion tests need to be executed. This method of measuring the cohesive soil erodibility and classifying the soil is widely used in the USA. A disadvantage of this method is that for each soil, a JET test needs to be performed to determine the critical shear stress and erosion parameter. Soil parameters such as undrained shear strength and the Atterberg limits are often not reported in the studies applying this method.

2.5.4. Kerssens (2017)
Kerssens [19] (2017) used a preliminary version of the present setup. Kerssens investigated the different cohesive soil failure mechanisms. He used two different clay mixtures with a wide range of undrained shear strength. At different jet velocities and nozzle diameters, the scour volume was observed over time. In this study, the depth development of the scour hole is not measured; however, the final depth of the scour hole is reported. In his study, Kerssens left the ratio of the standoff distance over the nozzle diameter constant. In his study, the erosion speed is related to the bed shear stress exerted by the impinging jet. His erosion rates predictions were calculated using the formula's developed by Winterwerp et al. [43] (2012), with the erosion parameter M_E as defined in equation 2.72.

2.5.5. Dong (2019)
Dong et al. [7] (2019) designed an experimental apparatus to study the scouring of cohesive beds by vertical submerged jets. Dong investigated the critical shear stress for the onset of scour as well as the scour hole dimensions. In the tests of Dong, the cohesive beds had different water contents. Varying

the water content also varied the undrained shear strength of the samples used. Dong tested with a constant nozzle diameter and varied the jet speed and standoff distance. Like Mazurek [22], Dong developed an equation for predicting the scour hole dimensions based on the excess shear stress equation. However, dong also included the nozzle diameter, time and water content in his equation. By including the time in his equation, Dong can predict the scour hole development over time, whereas Mazurek only derived an equation for the equilibrium depth. The equation for the depth development of the scour hole over time derived by Dong is as follows:

$$\frac{Z_c}{SOD} = 0.27 \cdot \left(\ln \frac{t\mu}{\rho D_n^2}\right)^{0.507} \cdot \left(\frac{w}{LL}\right)^{1.993} \cdot \left(\frac{\tau - \tau_{cr}}{\tau_{cr}}\right)^{0.704} \tag{2.88}$$

In which μ is the dynamic viscosity of the fluid Dong found that the dimensionless scour depth logarithmically varies with the scour duration $ln(t\mu/\rho D_n^2)$, which is based on the results of Moore and Masch Jr [25](1962).
The role of the dynamic viscosity of the fluid in this equation is not clear.

2.5.6. National Academies of Sciences, Engineering and Medicine (2019)

Briaud et al. [6] (2019) published a comprehensive summary report on the relationship between erodibility and properties of soils. In this study, data was collected from a range of different laboratory and in situ- (jet) erosion tests. Although not all the tests are directly comparable to the tests performed in this study, the relationships in the parameters found to influence the erosion can be used.
In this study a list of typically obtained soil properties that influence the erosion resistance is given some of these soil parameters can be related to other soil properties, to reduce the number of soil parameters that need to be accounted for, in table 2.3 these relations are given.

In this study, two statistical approaches, a deterministic frequentist regression and a probabilistic interference were carried out to find the best correlations between the erosion forces and the soil parameters influencing the erodibility. Different models are created for the different types of tests, based on the erosion test data that was used to develop them. The jet erosion test (JET) discussed in chapter 2.5.3 has the most similarities with the test setup used in this study.
The proposed equation for the critical shear stress t_{cr} based on the JET data is given as:

$$\tau_{cr} = -0.248 \cdot PC - 1.23 \cdot \rho_{situ} + 0.21 \cdot w_c + 0.07 \cdot su - 36.89 \cdot D_{50} + 31.82 \tag{2.89}$$

In which PC is the percentage of clay, and w_c is the water content in the soil. However, this equation still has a R^2 value of only 0.50, which is a low correlation.
Some general observations in this study are listed below:

- The erosion resistance increases with a decreasing D_{50} (for $D_{50} < 0.3$mm).
- An increase in the clay percentage leads to an increase of the erosion resistance.
- An increase in the plasticity index PI leads to an increase in the erosion resistance.
- An increase in the plastic limit PL leads to an increase of the erosion resistance.
- The undrained shear strength su and the wet unit weight ρ are directly proportional to the erosion resistance.
- The water content w_c alone does not give a good correlation to the erosion resistance alone. However, it leads to an decrease in the soil resistance for finely graded soils.

3

Experimental test setup

3.1. Introduction

A test setup is designed to assess the relative influences of the different types of cohesive soil failure mechanisms on the erosion rate for different stagnation pressures. By using different types of clay mixtures as test samples, the consolidation coefficient c_v is varied. By varying the consolidation coefficient, the effect of this coefficient can be assessed.

In the first paragraph, the test-setup is described. This includes the specifications of the sensors and the pump. Secondly, the different measurements that are done before, during and after the tests are described. Lastly, the preparation of the clay is described.

3.2. Test setup

The test setup used in this study is based on the test setup used by Kerssens [19] (2017), which is comparable to the setup of Mazurek [22] (2001). Kerssens also did tests to assess cohesive soil erodibility by low-pressure jets. The results of that study will also be included in this study.

Some adjustments are made to the test setup designed by Kerssens, to be able to do continuous weight measurements and to do depth measurements.

In figure 3.1 the test setup with all the different components indicated can be seen. The test setup consists of an aluminium measurement frame that is hoisted into a perspex cylinder, which has a length of 2.5 meters. A clay sample (LxBxH = 450x450x200 mm) is hanged off in three threaded rods which are connected to s-type load sensors. Because the sample is hanging free in the threaded rods, the weight of the sample can continuously be measured. Retainers are installed, giving the sample a few millimetres of space to move, but make sure the sample is not moving too much.

The threaded rods can be adjusted in length. By doing so, the standoff distance to the jet nozzle can be altered.

The depth measurement rod is a device which can measure the depth of the eroded hole without having to take the sample out of the water. The rod can be moved and turned to find the maximum hole depth in the sample. After the depth measurement, the rod can be moved as to not interfere with the jet.

Two pressure sensors (relative to ATM) are installed in the test setup. One pressure sensor is connected to the water supply tube to measure the flow pressure. The other pressure sensor is located on the aluminium frame to determine the water level in the perspex cylinder.

The water supply tube is connected, via a flexible hose to an electrical centrifugal pump. An electromagnetic flow-meter is present between the water supply tube and the pump. The revolutions of the pump can be adjusted, and by doing so, the jetting pressure and flows-peed can be adjusted. The pump is connected to a large water reservoir to which also the water outlet valve is connected; therefore, water recirculates from the perspex cylinder to the water reservoir and back.

An air release valve is located at the top op of the water supply tube. This is to make sure no bubbles will go trough the nozzle and by that interfere with the erosion process.

The water standpipe acts as an overflow, thereby a constant water level in the perspex cylinder is maintained. The nozzle of the jet is designed in such a way to minimize contraction losses. In figure

3.2, a picture of the test setup is given. Some extra pictures of the test setup, including annotations can be found in appendix E.3.

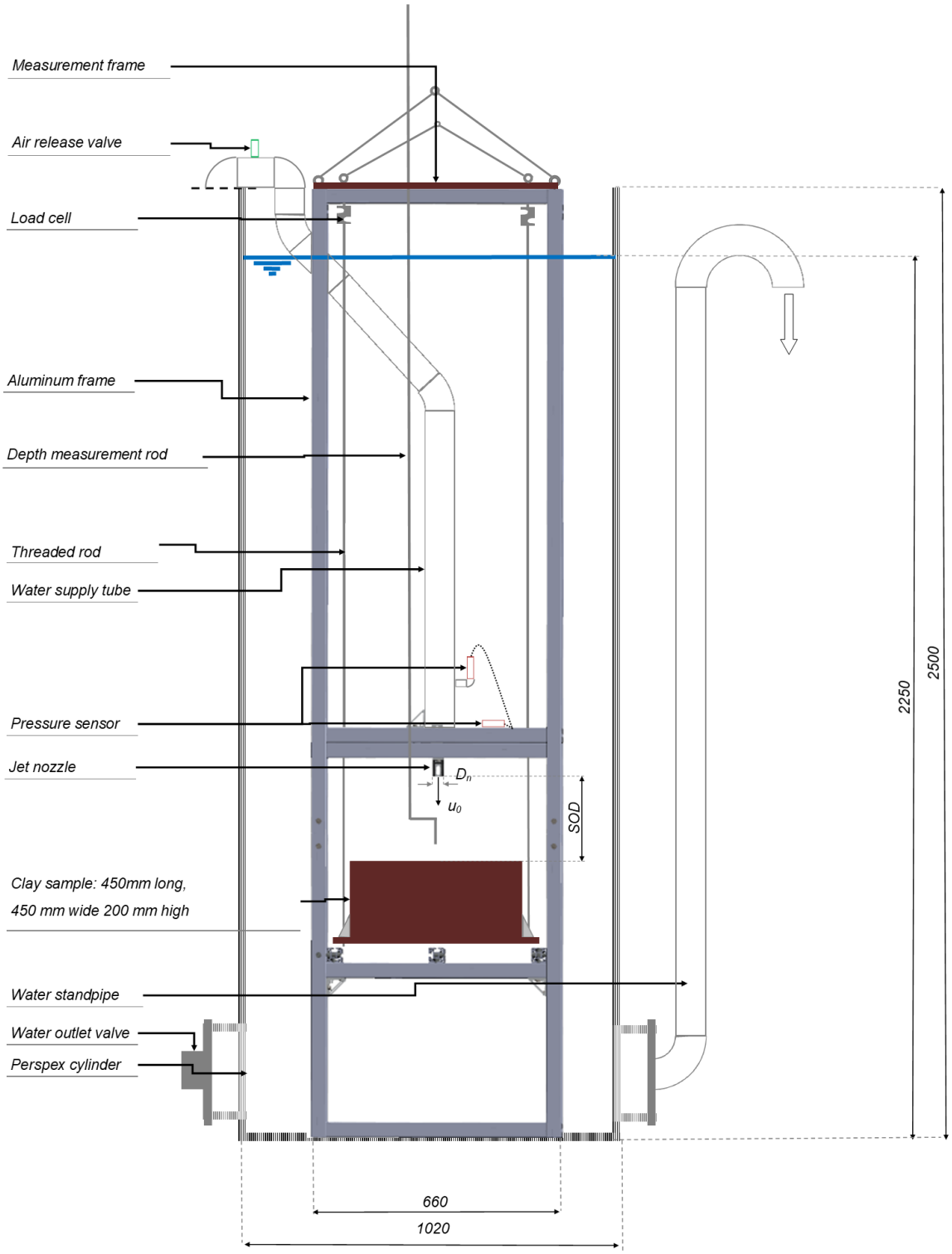

Figure 3.1: Experimental test setup

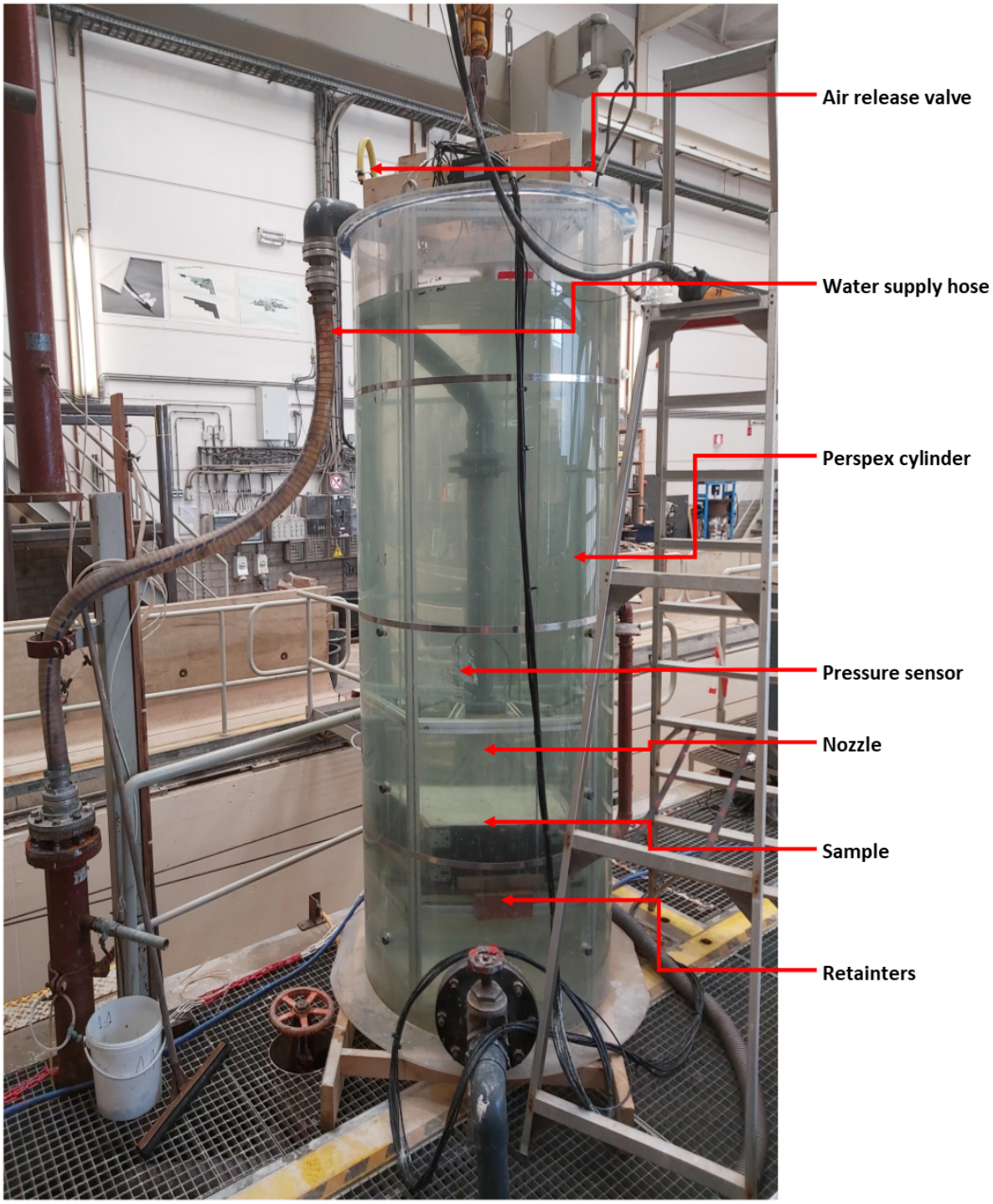

Figure 3.2: Picture of experimental test setup

Key features of the sensors are listed in table 3.1. The three S-type load cells give a combined maximum error of 15 gram over the full measurement range. All the sensors are connected to an Opto 22 which is connected to an laptop for data acquisition.

Table 3.1: Test setup sensor summary

Sensor	Type	Manufacturer	Measuring range	Accuracy [%]
S-type load sensor	AH-H3	AE-Sensors	0-25 [kg]	0.02
Pressure sensor (in line)	0-4 Bar PTM/N	AE-Sensors	0-4 [Bar]	0.25
Pressure sensor (water level)	0-10MWK PTM/N	AE-Sensors	0-1[Bar]	0.25
Flow sensor	IFC 090	Krohne	0-100 [m3/h]	0.30

3.3. Clay sample preparation

Different values of the consolidation coefficient are obtained by creating different clay mixtures. The clay samples for this study are made by mixing kaolin powder, bentonite powder sand and water together. The preparation of the clay mixture is discussed in chapter 3.3.1, the consolidation process is discussed in chapter 3.3.2.

3.3.1. Mixing

The clay mixtures are prepared manually according to the mix compositions as shown in table 3.2. A total of six different sample mixtures is taken to create different soil properties.

Table 3.2: Clay mixture composition

Clay Mix		Material	Weight percentage	Density
		[-]	[%]	[kg/m3]
Kaolin		Kaolin	67.2	2600
		Water	32.8	1000
Kaolin-Bentonite	5	Kaolin	64.6	2600
		Bentonite	5	2600
		Water	29.8	1000
	10	Kaolin	59.6	2600
		Bentonite	10.6	2600
		Water	29.8	1000
	15	Kaolin	55.2	2600
		Bentonite	15	2600
		Water	29.8	1000
	25	Kaolin	45.2	2600
		Bentonite	25	2600
		Water	29.8	1000
Kaonlin-Sand		Kaolin	35.1	2600
		Sand	35.1	1600
		Water	29.8	1000

The mixture is prepared using a mortar mixer according to the following steps:

1. First, 75% of the required amount of water is put in a container.
2. Add the kaolin by the water in parts and mix the contents.
3. The last 25% of the water is added at the end and mixed with the kaolin.
4. Mix the mixture until a homogeneous mixture is obtained.
5. Transfer the prepared clay to the clay containment frame for consolidation.

The kaolin-bentonite mixtures are prepared according to the same steps, with the only difference being that the total required amount of bentonite is added directly after the first 75% of the water is added to the container. Lastly, the kaolin sand mixture was prepared by adding both the kaolin and sand in parts to the water and mixing until a homogeneous mixture is obtained. The mortar mixer is rotated at a low RPM to reduce the entrainment of air bubbles in the clay mixture.

3.3.2. Consolidation

Just after the clay is mixed, the mixture has an undrained shear strength of approximately 5.5 kPa. To increase this strength to approximately 10 kPa the clay mix is consolidated. The consolidation is done inside the clay containment frame.

The clay containment frame with the relevant descriptions can be seen in figure 3.3. The mixed clay is being consolidated underwater level to ensure full saturation of the clay. The clay containment frame consists of the main compartment and an add on edge. The add on edge is put on the main compartment during the consolidation. Before the start of the test, the add on edge is removed, and the clay sample is cut flush with the top of the main compartment.

A load of approximately 11 kPa is applied on the top of the containment frame. In a small scale test, it is found that this pressure is sufficient to consolidate the soil mixture to the desired strength. The containment frame is drained on the top and the bottom of the frame by means of drainage holes. A filter layer is applied to the top and the bottom of the sample, to make sure that the clay does not escape the containment frame and stays fully drained. In appendix E.1 pictures of the sample preparation and consolidation can be found.

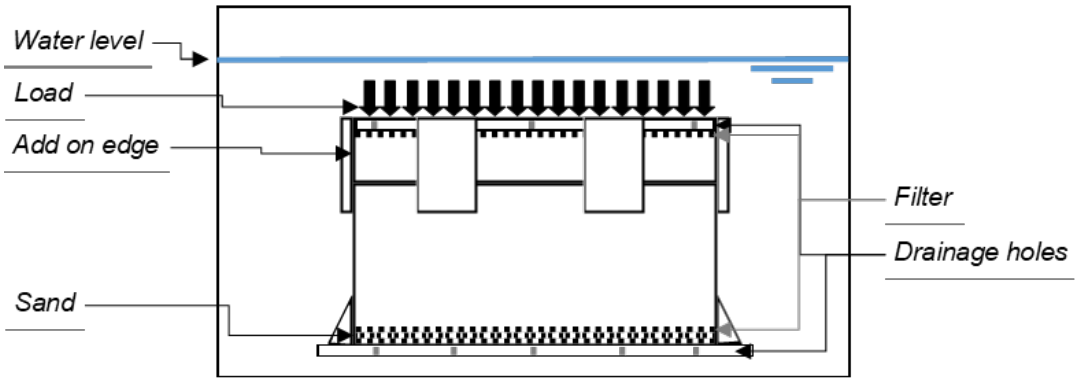

Figure 3.3: Consolidation containment frame setup and definitions

The undrained shear strength obtained after compaction can be normalised by dividing it by the vertical effective consolidation pressure σ'_{v0}. Jamiolkowki [17] (1985) found for the ratio su/σ'_{v0} of normally consolidated soils a value of approximately 0.24, whereas Ladd [20] (1991) found a value of 0.33. The undrained shear strength obtained after consolidation can be approximated using the following equation:

$$\frac{su}{\sigma'_{v0}} = 0.3 \tag{3.1}$$

The applied pressure of 11 kPa on the containment frame to consolidate to the desired strength of 10 kPa. The ratio of the obtained undrained shear strength over the applied pressure of the containment frame is approximately 0.9, which is significantly higher than the values suggested by Jamiolkowki [17] (1985) and Ladd [20] (1991). Using a normalized undrained shear strength value of 0.3 would result in an undrained shear strength of 6 kPa after consolidation. Using the clay characteristics from table 3.4 and equation 2.7 also an undrained shear strength of approximately 6 kPa is obtained. A possible explanation for the higher undrained shear strength obtained after consolidation could be due to an under-pressure present in the soil, which results in additional strength.

Consolidation measuring

The c_v value needs to be determined accurately to investigate the effect of the coefficient of consolidation on the erosion process of cohesive soils by low-pressure jets. The calculation methods are described in chapter 2.2.5.

The consolidation process is monitored, and measurements are taken to determine the consolidation coefficient (c_v). The results of the direct consolidation are validated in an oedometer test. Figures of the oedometer test setup can be found in appendix E.2. The test protocol used for the oedometer tests can be found in appendix E.5.

The direct consolidation measurements are performed by measuring the average consolidation of the four corners of the sample over time using a calliper. The average consolidation of the four

corners is taken because it is possible that the sample is not equally consolidating over the surface of the sample. A typical measurement consolidation graph is presented in figure 3.4. This graph the measured consolidation is plotted against the logarithm of time. The consolidation measurements are approximated by a Weibull fit. This Weibull fit is used to calculate the c_v values for the different methods as elaborated in chapter 2.2.5. In appendix E.4 the test protocol is given for the direct consolidation measurements.

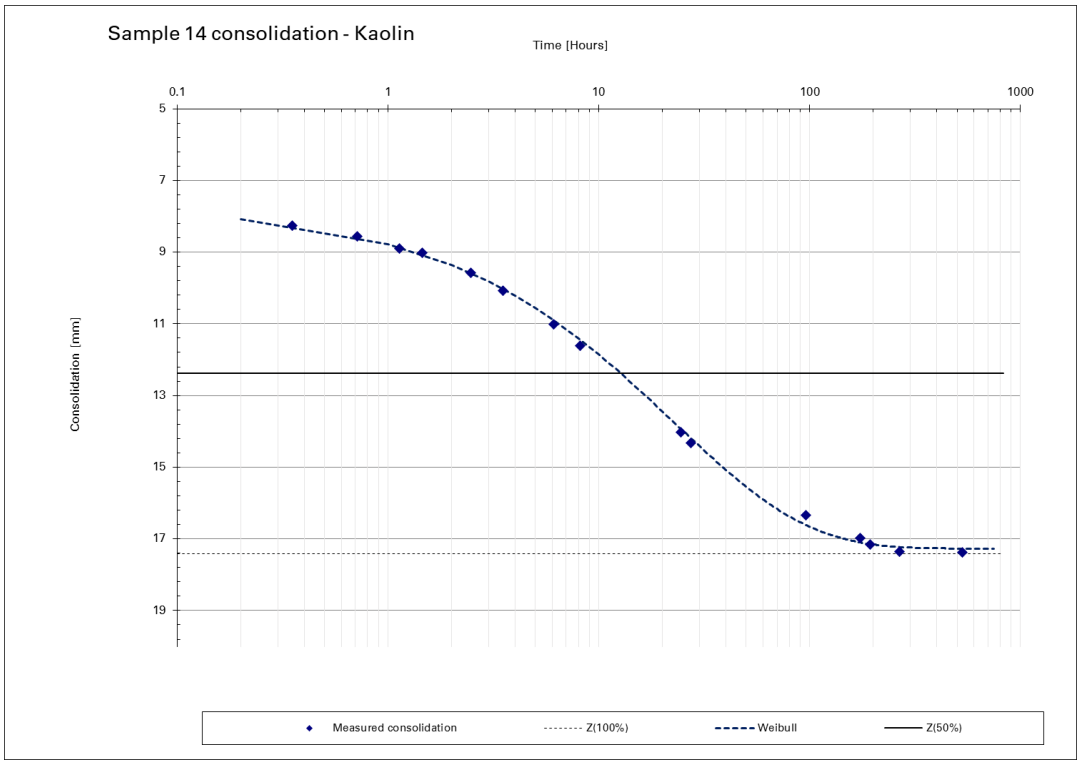

Figure 3.4: Typical consolidation graph - Sample 14 measured consolidation plotted against logarithm of time

The compressibility m_v of the sample can be calculated according to formula 2.11 by dividing the total strain ϵ by the applied stress σ'. Using the calculated consolidation coefficient c_v and the compressibility m_v and using equation 2.14, the hydraulic conductivity is determined.
In table 3.3 the calculated average c_v, m_v and k values are presented calculated from the direct consolidation and oedometer tests. For sample 1-4, no consolidation measurements are available. Also, not for every sample, an oedometer test is performed. For the samples that no consolidation test are performed the average value of c_v, m_v and k of similar soil mixtures is taken as a good approximation. In appendix A the complete table and data of all the consolidation measurements are given.

Table 3.3: Summary table consolidation of calculated consolidation coefficient, hydraulic conductivity and compressibility

		Direct consolidation			Oedometer (Consolidation)		
Sample NO	Mixture	c_v [m^2/s]	m_v [m^2/kN]	k [m/s]	c_v [m^2/s]	m_v [m^2/kN]	k [m/s]
5	Kaolin (s)	3.42E-07	5.83E-03	1.97E-06			
6	5% Bentonite	4.49E-08	2.52E-03	1.11E-07	8.31E-08	1.45E-03	1.19E-07
7	10% Bentonite	4.09E-08	3.68E-03	1.48E-07	6.57E-08	1.70E-03	1.10E-07
8	5% Bentonite	2.25E-08	2.10E-03	4.60E-08	5.29E-08	1.22E-03	6.36E-08
9	Kaolin (s)	1.27E-07	2.63E-03	3.29E-07			
10	Kaolin (s)	1.78E-07	3.39E-03	5.92E-07	4.90E-07	7.39E-03	3.55E-06
11	15% Bentonite	5.68E-08	3.62E-03	2.04E-07	1.10E-07	1.63E-03	1.78E-07
12	15% Bentonite	5.12E-08	2.95E-03	1.49E-07			
13	25% Bentonite	8.57E-08	3.56E-03	3.00E-07	6.99E-08	2.19E-03	1.79E-07
14	Kaolin	4.79E-08	3.40E-03	1.59E-07	6.77E-08	1.80E-03	1.20E-07
15	Kaolin	2.95E-08	3.87E-03	1.12E-07			
16	Kaolin	3.80E-08	3.22E-03	1.20E-07			
17	Kaolin-Sand	1.75E-07	2.52E-03	4.31E-07	1.674E-07	1.76E-03	2.89E-07
18	Kaolin	3.27E-08	2.94E-03	9.12E-08			
19	Kaolin	1.56E-08	2.95E-03	4.49E-08	7.92E-08	2.53E-03	1.97E-07

Two different manufacurers of the kaolin mineral where used for the sample preparation. During consolidation difference in the consolidation coefficient was observed. The samples in which the kaolin was used which resulted in a higher c_v value are labeled with an ”s”. A further analysis of these values is done in chapter 5.2.

3.4. Clay sample characteristics

As mentioned in chapter 3.3.1 six different clay mixtures are prepared and tested for this study. The average undrained shear strength su after consolidation 10 kPa. Table 3.4 summarizes the characteristics of the prepared clay mixtures. These samples are approximately homogeneous and do not contain planes of weaknesses. The complete test results can be found in appendix D.1.

Table 3.4: Characteristics of the clay samples obtained by Boskalis Environmental.

		Kaolin_s	Kaolin	5%Bent	10%Bent	15%Bent	25%Bent	Kaolin-Sand
clay	[%]	-	-	-	-	-	-	-
silt	[%]	-	-	-	-	-	-	-
sand	[%]	-	-	-	-	-	-	-
Water content	[%]	44.9	47	42.6	39.5	38.7	35.9	23.2
Vane-shear	[kPa]	10	10	10	10	10	10	10
LL	[%]	43	48	45	42	39	35	23
PL	[%]	28	27	25	23	23	20	15
PI	[%]	14	21	20	18	17	16	9
A	[-]	-	-	-	-	-	-	-
ρ_{dry}	[kg/m3]	1180	1134	1248	1242	1304	1279	1598
cv (average)	[m2/s]	2.32E-07	5.04E-08	4.49E-08	4.09E-08	5.4E-08	8.57E-08	1.75E-07

A sieve size test is executed only for the kaolin_s sample. The kaolin_s sample has a D_{50} of 6 μm and a D_{90} of 17 μm.

3.4.1. Clay sample characteristics other studies

In this study data from other studies are included in the analysis of the results to verify the obtained results from this experimental setup. Agreement with presented and reported experimental data of other studies is sought. A wider range of variables can be tested in the model using other studies.
The studies that are included in the analysis are selected on the basis that they used a more or less similar test setup. These studies are discussed in chapter 2.5. The sample characteristics of the different researches are given in table 3.5.

Table 3.5: Sample characteristics other studies used in analysis

		Mazurek	Hedges	Kerssens Deltares	Kerssens Kaolin	Dong
Clay	[%]	40	-	64	3	12.5
Silt	[%]	53	-	11	97	73.5
Sand	[%]	7	-	25	0	14
Water content	[%]	26	26	22.6	47.4	30-50
Vane-shear	[kPa]	20	17.8	67	7	3-26
LL	[%]	36	37	49	45	53.5
PL	[%]	18	18.2	18	33	22.5
PI	[%]	18	18.8	31	12	31
A	[-]	0.4	-	0.484375	4	2.48
ρ_{dry}	[kg/m3]	1540	-	1621	1142	1250
cv	[m2/s]	1.60E-08[1]	2.50E-07[1]	1.00E-08	2.00E-07	4.00E-08[1]

1: consolidation coefficient is unknown and is therefore derived from other parameters explained in appendix D.4.

4 Experiments

4.1. Introduction

In total, 20 tests were conducted. In these tests, both soil parameters and jet parameters were varied. A test procedure is developed to ensure that every test is executed according to the same steps and that tests are repeatable.
In this chapter first, the text matrix with the range of variables used in this study is elaborated. Secondly, the different measurements before, during and after the test are discussed. Furthermore, measurement definitions are explained. Lastly, the resulting test report is discussed.

4.2. Test matrix

The main parameters varied in this study where the stagnation pressure at the start of the test $p_{stag,0}$ relative to the undrained shear strength su, the consolidation coefficient c_v, and the standoff distance SOD.
By varying the standoff distance, while leaving the nozzle diameter the same size, the effect of the SOD on the erosion behaviour can be investigated. Together with the previous study of Kerssens [19] (2017), who altered the nozzle diameter, while leaving the ratio between standoff distance and nozzle diameter the same, the individual effects of the nozzle diameter and standoff distance on the penetration depth and volume can be investigated.
As mentioned in chapter 3.4.1, in the analysis of the results also tests of other studies will be included. In table 4.1 the range of the test variables used in this study is presented. In the same table, the range of the individual variables of the total gathered dataset is annotated with an asterisk.

Table 4.1: Range of test variables used in this study and range of variables of the total data set annotated with asterisk.
**) considered data from other studies*

Variable		Range
Undrianed shear strength su	[kPa]	7.96-12.29 2.81-61.50*
Diameter nozzle D_n	[mm]	20 3.18-40*
Standoff distance SOD	[mm]	147-298 40.00-280*
Stagnation pressure $p_{stag,0}$	[kPa]	4.00-17.50 1.57-144*
Flowspeed at nozzle u_0	[m/s]	3.46-8.44 1.06-25.9*
Consolidation coefficient c_v	[m^2/s]	2.25E-08-3.42E-07 1.00E-08-2.00E-07*
$p_{stag,0}/su$	[-]	0.42-1.46 0.26-7.57*
SOD/D_n	[-]	7.35-14.9 7-30*

The full test matrix with the data of all the executed tests is given in table 5.1. The tests are executed at ratio's of: 0.4, 0.6, 1.0, 1.4 $p_{stag,0}$ over su. All of the soil mixtures are at least once tested at a $p_{stag,0}/su$ ratio of 0.6. Most of the test of Kerssens [19] (2017) were executed with 10 mm and 40 mm nozzles. In this study, all the tests are executed with a nozzle diameter of 20 mm, giving a wider spread of the data points. Most of the tests are executed at a standoff distance of approximately 150 mm. The standoff distance is altered to 225 mm and 298 mm for only one clay mixture. The tests with the varied standoff distance are executed at 0.6 $p_{stag,0}/su$.
Some of the tests are executed in duplex to test the repeatability of the tests. The complete table with the test variables as executed is given in table 5.1.

4.3. Test procedure

The tests performed consists of different steps. Different measurements are performed at different stages of the test. In this paragraph, these measurements are elaborated. The full test protocol is given in appendix E.6.

4.3.1. Before test

Before the test, the clay sample is weighed, including the containment frame on a scale. After the test, the sample will be weighed on the same scale as an extra verification of the eroded weight of the clay. The undrained shear strength is measured on two different locations on top of the sample using a pocket vane (Appendix figure E.7a). The sample is hanged off in the aluminium measurement frame. The standoff distance between the nozzle and the flat sample bad is measured using a laser measurement tool. The aluminium frame, including the clay sample, is then lowered into the perspex tube. Before the test starts the submerged weight of the sample is noted using the S-load sensors. All the sensors are checked before the test starts as to make sure that the sample is hanged off properly and the sensors are working correctly.

4.3.2. During test

During the test, the weight of the sample is measured and logged continuously. Also, the jetting pressure, relative pressure and the flow rate are measured continuously.

In the first 12 minutes of the test, the jet is stopped every three minutes. At these 3 minute intervals, the depth of the penetration depth of the jet in the sample is measured. This interval is also used to measure the weight of the jet due to the jet momentum on the clay sample. By subtracting the sample weight when the jet is paused, from the sample weight before pausing, the momentum weight of the

jet is found.

The sample is hoisted out of the water after 12 minutes and pictures are taken of the created hole and the eroded material. Subsequently, the jetted (eroded) material is removed from the sample, this is done to have a more accurate weight measurement, and therefore a more accurate measurement of the jetted volume.

The sample is hoisted into the water, and the test is resumed, and the above-described process is repeated. However, the depth measurement intervals are altered based on the erosion speed (lower erosion speed = larger intervals between measurements).

The tests are continued until a stable erosion speed is reached or the bottom of the sample is nearly reached. When the test is stopped, the sample is hoisted one more time out and in of the water to clean the jetted material and do one last submerged weight measurement.

4.3.3. After test

After the test, the sample is taken out of the aluminium frame weighed on the scale. Furthermore, the profile of the scour hole is measured using a laser measurement device. The scour hole dimensions are measured perpendicular and cross the jet centre line as illustrated in figure 4.1; these are called section 1 and 2. An additional section is measured if deemed necessary. Section 3 is located at the maximum depth of the scour hole ($Z_{c,max}$), at the widest point of the scour hole or aligned to pass through the most relevant diameter of the scour hole, see also figure 4.1.

Afterwards, the scour-hole volume is measured by filling up the hole with a measured amount of water to the top. This process is repeated twice to have a more accurate measurement.

Afterwards, the undrained shear strength is measured using a field vane (appendix figure E.7b and a pocket vane. The field vane measurement is executed twice on an undisturbed location of the sample at a depth of 10 cm. The pocket vane measurement is also done once in on an undisturbed location and once in the scour hole. The last measurement can be used to determine the strength reduction of the clay due to the swelling of the soil.

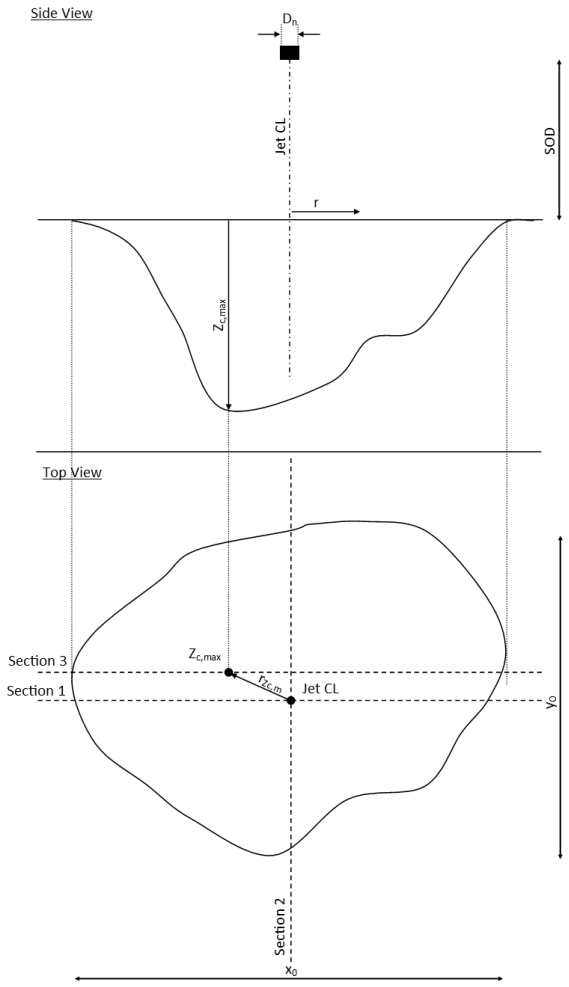

Figure 4.1: Side and top view of Jetting and scour-hole measurement definitions

4.4. Test report

A typical figure of the sample weight over the complete test is given in figure 4.2. This graph is the result of the combined logged data of the three individual loadcells. A few particularities can be seen in this figure. Every three minutes, the jet is paused to measure the penetration depth. The weight of the jet momentum on the soil sample can be seen as the difference in weight of the sample during jetting and during the pause of the jetting. A downward trend can be observed in the data, and later in the test a more or less constant weight in the loadcells. The complete sample is lifted out of the water at 11:30, 12:00, 13:15, 13:45, 14:38. At these timestamps, spikes in the weight are observed, due to the sample going from submerged to un-submerged.

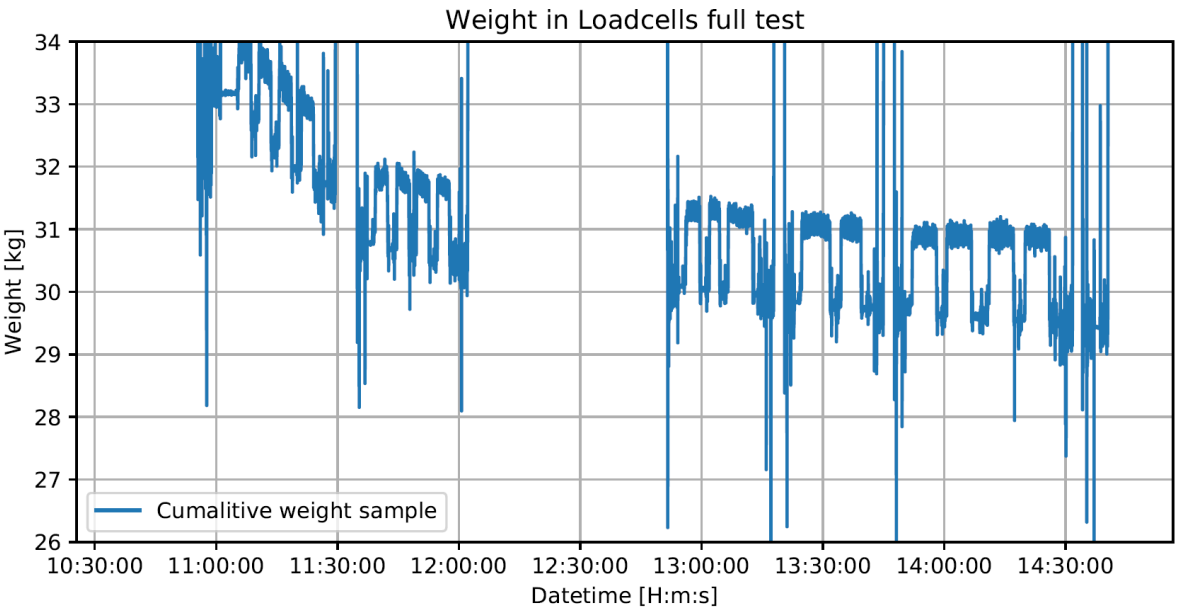

Figure 4.2: Test 10% bent. 1.4 $p_{stag,0}/su$ Weights in loadcells for complete test versus time [hh:mm:ss

The data of figure 4.2 is filtered by taking the time the jet was actually on. The result can be seen in figure 4.3. Due to the jetting, the raw data is noisy; a filter is applied to have a more fluid line of the sample weight. At 12, 24, 36, and 48 minutes of testing a jump in the weight of the sample can be observed. This jump is due to the cleaning of the sample.

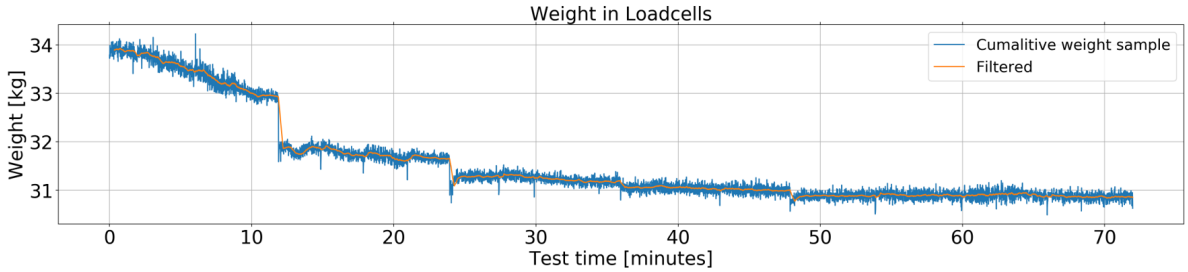

Figure 4.3: Test 10% bent. 1.4 $p_{stag,0}/su$ filtered weight versus test time in minutes

In figure 4.4 the filtered data is rewritten as the accumulated jetted volume against the test time in minutes by taking the submerged jetted weight and the density of the material. A ln fit is applied over the data. Also, in this figure, the average force due to jet momentum is given in the orange line. This is calculated by taking the weight in the loadcells during jetting and subtracting that with the weight in the loadcells when the jet is turned off. A relatively constant force due to jet momentum can be observed over the total test time.

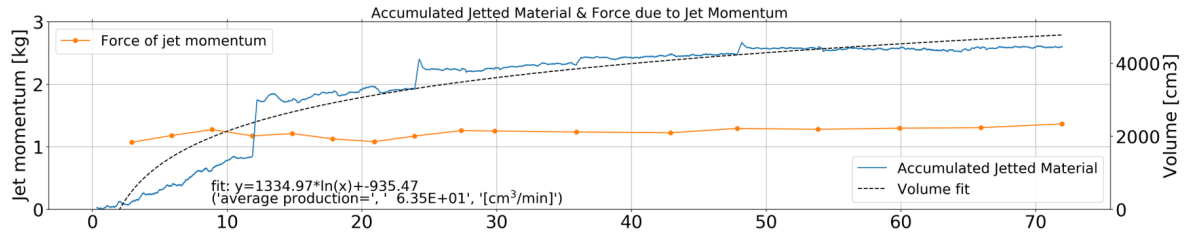

Figure 4.4: Test 10% bent. 1.4 $p_{stag,0}/su$ accumulated jetted material including fit line and force due to jet momentum versus test time in minutes

Next, the depth measurement data over the test time in minutes is given in figure 4.5. Also over this

curve, a ln fit is plotted. The depth measurements are discrete and executed when the jet is paused.

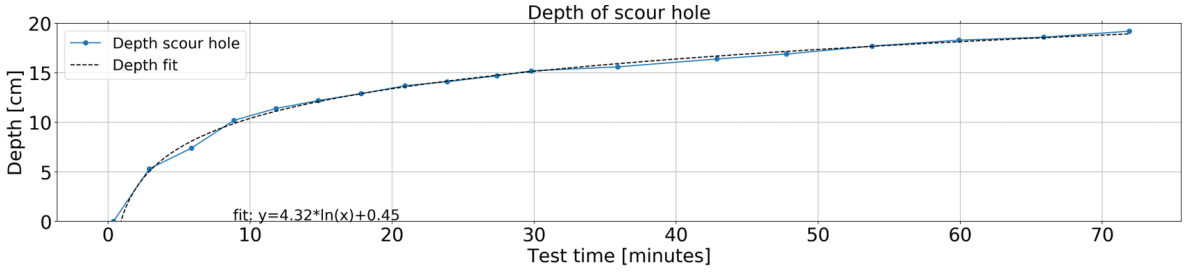

Figure 4.5: Test 10% bent. 1.4 $p_{stag,0}/su$ penetration depth versus test time in minutes

The post test data obtained from the laser measurements are plotted in figure 4.6. In this figure the jet center-line and the zone of impingement are given by the dotted lines. The data is plotted as a function of the radial distance from the jet center-line in millimeter.

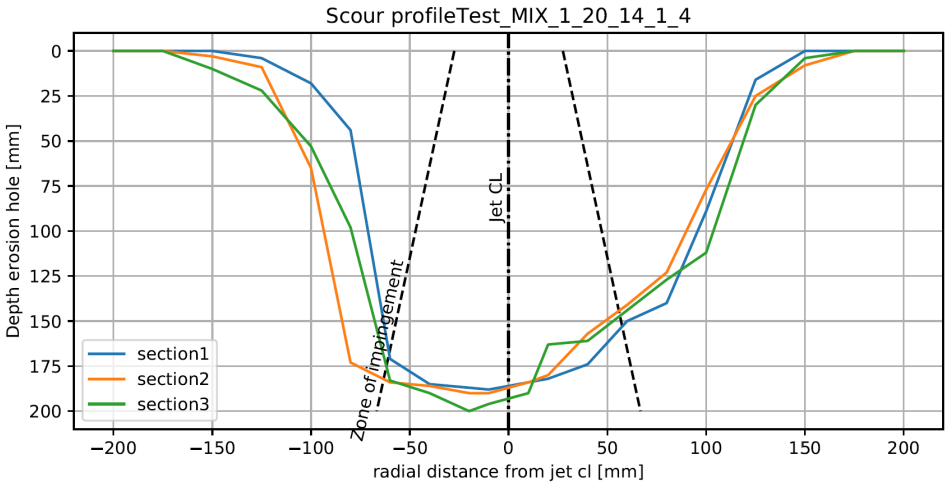

Figure 4.6: Test 10% bent. 1.4 $p_{stag,0}/su$ scour profile. Depth of erosion hole as function of the radial distance from the jet center-line

Lastly in table 4.2 data regarding the pre-and post-test data is given.

Table 4.2: Test table 10% Bent. 1.4

10% Bent_20_14_1_4			post-test				
					section 1	section 2	section 3
Date	dd/mm/yy	10/09/19	x_0	mm	250	-	-
u_0	m/s	6.19	y_0	mm	-	300	300
Q	m³/s	1.65E-03	$Z_{c,cl}$	mm	190	-	-
SOD	mm	150	$Z_{c,m}$	mm	200	-	-
D_n	mm	20	$r_{Zc,m}$	mm	20	-	-
SOD/D_n	-	7.5					
$p_{stag,0}$	kPa	13.30	V_t	cm3	5340	cm3/min	74.17
$p_{stag,0}/su$	-	1.46	V_{scale}	cm3	5206	cm3/min	72.30
t_{tot}	min	72	V_{water1}	cm3	4950	cm3/min	68.75
m_{sub}	gram	33169	V_{water2}	cm3	5150	cm3/min	71.53
pre-test			post-test				
		su			su		
pocket vane 1	kPa	9.29	pocket vane 3	kPa	8.31		
pocket vane 2	kPa	9.73	pocket vane 4	kPa	9.29		
			field vane 1	kPa	8.5		
			field vane 2	kPa	9		
			CPT	kPa	17		
Notes:	sample 7						

4.5. Repeatability of the jet tests

Some of the tests are executed in the same configuration to test the repeatability of the tests.
The repetition test of the kaolin sample at 0.6 $p_{stag,0}/su$ and 150 mm SOD, in figure 4.7, shows a deviation between the two tests at the start of the test which continues to grow throughout the test. The main contribution to the difference in the scour hole depth likely is the difference in the consolidation coefficient of the individual mixes. The c_v value of test K_15_0.6_2 is 1.27E-7 whereas the c_v value of test K_15_0.6_4 is smaller (3.27E-8). This difference in c_v value can be attributed to the mixing of different kaolin mineral batches. Furthermore, the deviation could be due to the shape of the scour hole, which would result in a difference between the shear force of the jet on the soil surface. Also, the irregularities in the soil samples could account for the deviation between the two tests. At the start of the test (after ≈ 3 min) the error between the two tests is approximately 1.45 cm which grows to 5.35 cm, however, the relative error between the two tests remains approximately 30% throughout the tests.

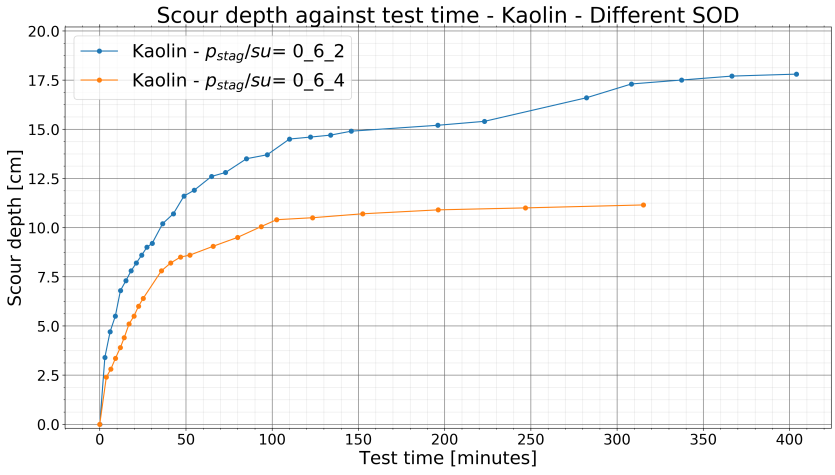

Figure 4.7: Repetition test of kaolin sample at 0.6 $p_{stag,0}/su$ and 150 mm SOD

In figure 4.8 test K_15_0.6_4 is scaled to test K_15_0.6_2 by adjusting for the difference in the consolidation coefficient c_v according to the principle explained in chapter 5.4.4. When the difference

in the consolidation coefficient is taken into account, scour depth lines over time overlap each-other.

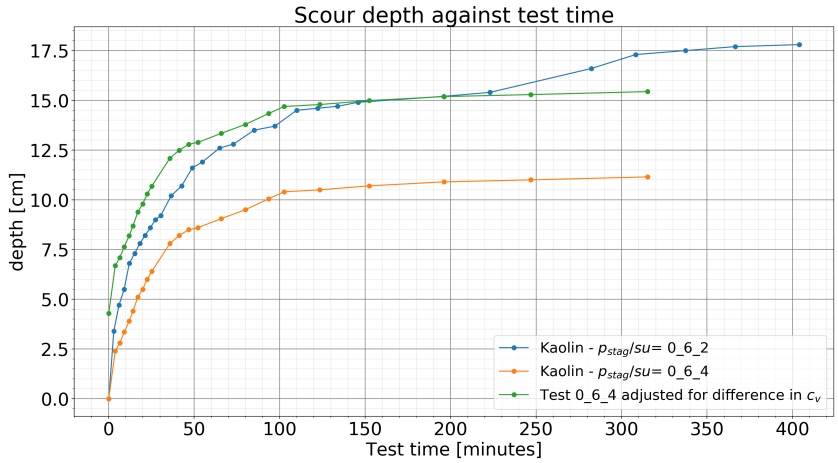

Figure 4.8: Repetition test of kaolin sample at 0.6 $p_{stag,0}/su$ and 150 mm SOD including the adjusted line

For the repetition test of the 15% bentonite sample at 0.6 $p_{stag,0}/su$ at 150 mm SOD, figure 4.9 the scour depth increase over the test time is very similar for the first 15 minutes of the test. After that time the two tests deviate from each other, the relative error between the test grows from approximately 4% after 15 minutest to 25% after 350 minutes. During the second test of the 15% bentonite sample at 0.6 $p_{stag,0}/su$ the scour hole developed eccentric, as can be seen in figure 4.10. The resulting change in the flow pattern of the jet in the scouring hole can be a explanation for the difference in in the maximum scour depth.

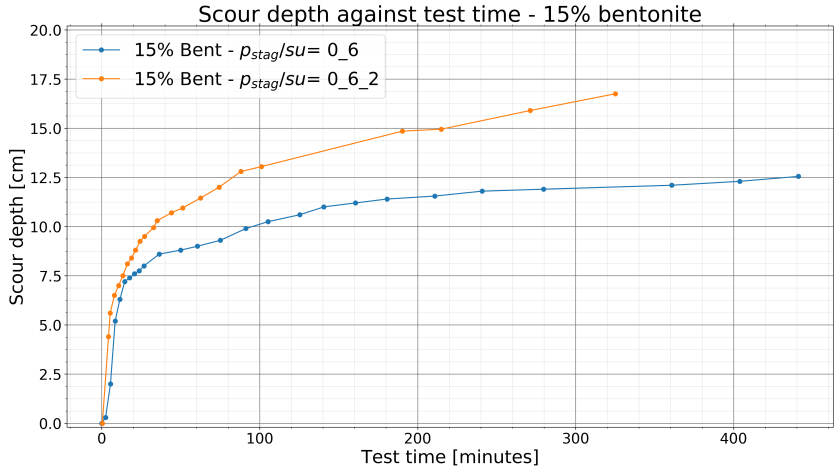

Figure 4.9: Repetition test of 15% bentonite sample at 0.6 $p_{stag,0}/su$ and 150 mm SOD

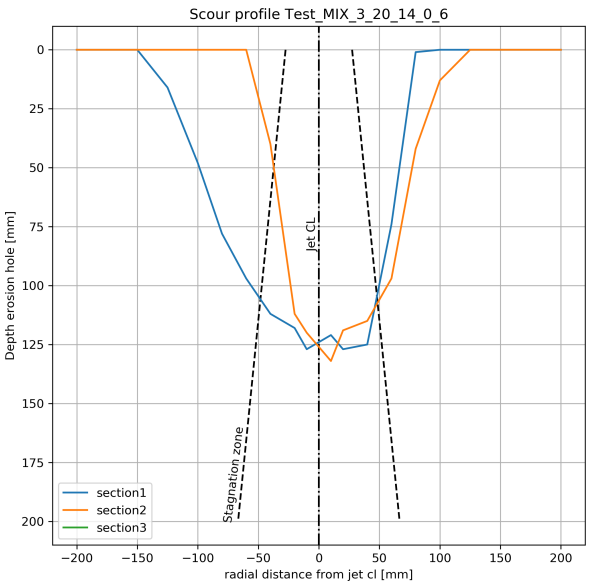

(a) Contour line of 15% betnonite test at 0.6 $p_{stag,0}/su$ and 150 mm SOD

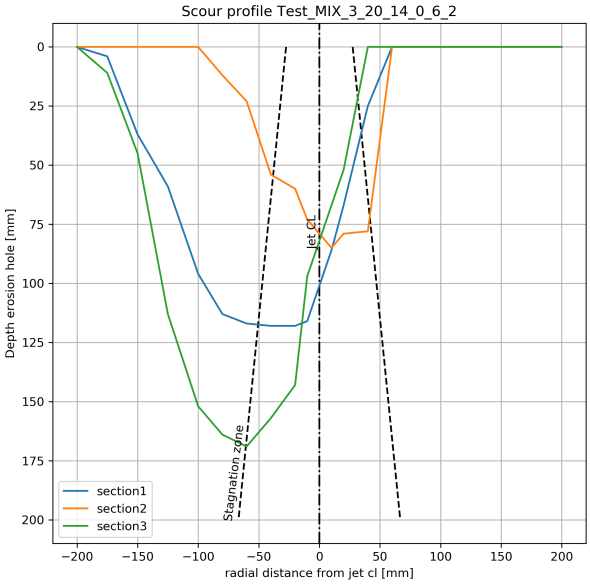

(b) Contour line of 15% betnonite second test at 0.6 $p_{stag,0}/su$ and 150 mm SOD

Figure 4.10: Contour lines of 15% bentonite tests

The last test that is repeated is the kaolin sample test at 0.6 $p_{stag,0}/su$ and 30 cm SOD. This test is repeated because, in the first test (K_30_0.6_1), a sudden increase in the scour depth is observed after 35 minutes of testing. This sudden increase leads to believe that the sample has a weak spot. The sudden increase could be due to air being trapped in the sample, or the sample is not equally consolidated, which could result in a lower undrained shear strength locally. The repetition test (K_30_0.6_2) confirms this hypothesis because the scour depth development is similar until 35 minutes of testing, however in this test the sudden increase in scour depth is not observed.

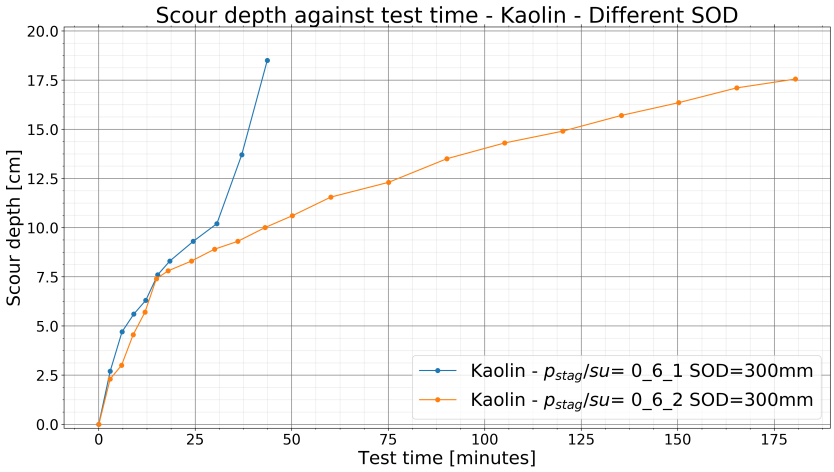

Figure 4.11: Repetition test of kaolin sample at 0.6 $p_{stag,0}/su$ and 30 cm SOD

From these repetition tests, it is concluded that the tests are reproducible. Although an exact reproduction of an individual test is hard to obtain due to variables that are hard to control, such as weak spots inside a soil sample, the obtained results are similar. Furthermore, the differences between repetition tests can be logically explained.

5

Results

5.1. Introduction

In this chapter, the results of the different tests are presented. In the first paragraph, the results of the consolidation tests are presented. In paragraph 5.3, a summary table is given of the results of the executed tests. In paragraph 5.4 the obtained scour depth results are visualised in different graphs and observations are noted. This paragraph also presents the effects of the individual jet and soil parameters on the erosion velocity. Furthermore, in paragraph 5.5, the scoured volume is coupled to the scour depth in several graphs.

5.2. Consolidation tests

As discussed in chapter 3.3, the clay samples are prepared by hand and with different mixtures to obtain different values of the consolidation coefficient. In chapter 3.3.2 the consolidation process and measurements are elaborated. In this chapter, the consolidation results are further analysed.

As can be seen in table 2.2, the typical values for the consolidation coefficient differ for different clay minerals. Bentonite consists of 2/3 montmorillonite. By mixing bentonite with kaolinite, it is expected that, when more bentonite is added to the mixture, the consolidation coefficient will become lower.
In figure 5.1a the results of the direct consolidation measurements, and the oedometer measurements are plotted against the percentage bentonite present in the mixture. At 0% the mixtures are plotted that do not contain bentonite, and only consist of kaolin. It is expected that the more bentonite is added to the mixture, the lower the consolidation coefficient will become. However, a slight increase can be observed from 5% to 25% bentonite in the consolidation coefficient. Also, for the mixtures containing bentonite, no significant lower consolidation coefficient is observed when comparing to mixtures without bentonite added. Since also a test with a sand-clay mixture is executed there is still a good spread obtained between the consolidation coefficient points of more than 1 order of magnitude.

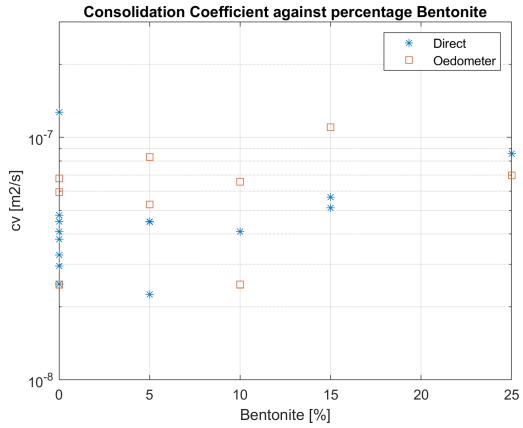

(a) Consolidation coefficient for different percentages of bentonite from direct measurements and from oedometer tests

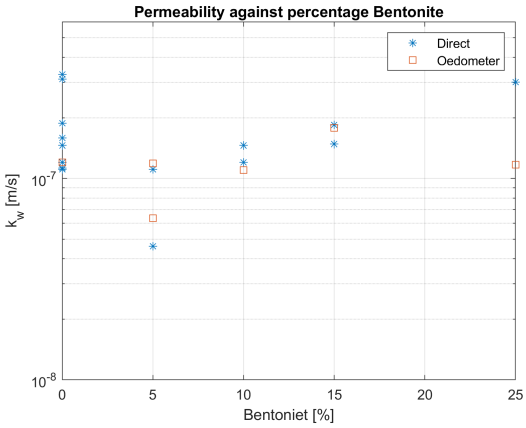

(b) Permeability for different percentages of bentonite from direct measurements and from oedometer tests

Figure 5.1: Consolidation coefficient and permeability for different percentages bentonite in the mixture

The same increasing trend between the bentonite percentage and the permeability can seen in figure 5.1b. In this figure no serious decrease in the permeability is observed. As explained, it was expected that by changing the bentonite percentage in the soil mixture, the consolidation coefficient would change, and therefore also the permeability. However, this is not the case. A possible explanation could be that the activity of the bentonite (equation 2.5) is lower than expected, resulting in a lower capability to bind water. An indication for the low activity bentonite is the decrease in the plasticity index PI as the percentage bentonite increases, as can be seen in table 3.4.
A clear trend between the consolidation coefficient and the permeability is observed, as is expected from equation 2.14. This is also visualized in figure 5.2.

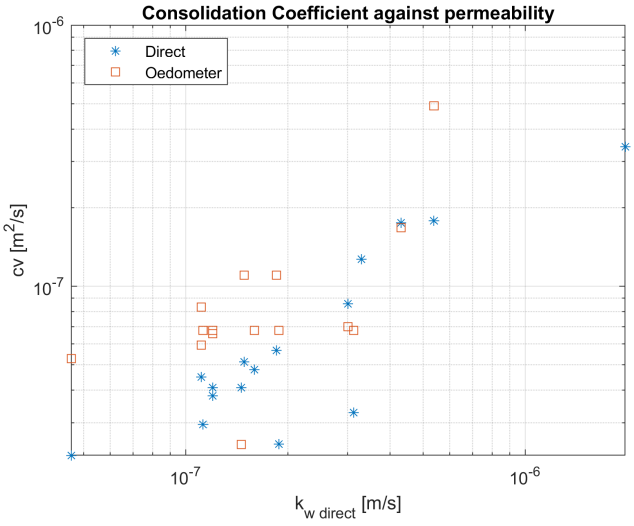

Figure 5.2: Consolidation coefficient plotted against the permeability

To verify that the measurements obtained directly from the clay samples during consolidation are within the margin of error from the values obtained from the oedometer tests the data is plotted against the data from the direct measurements in figure 5.3.

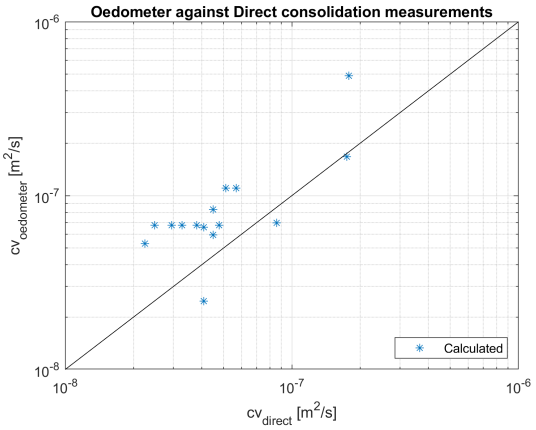

(a) Consolidation coefficient from direct measurements plotted against the oedometer measurements

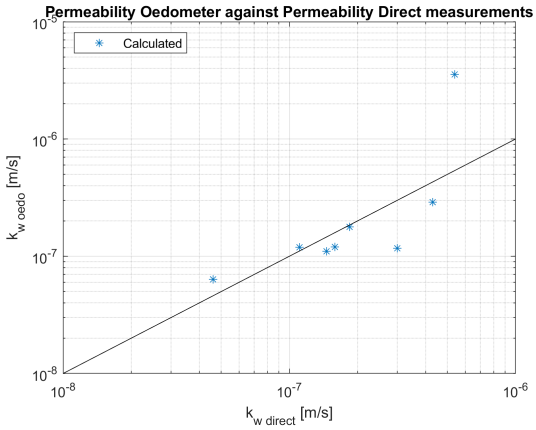

(b) Permeability from direct measurements plotted against the oedometer measurements

Figure 5.3: Consolidation coefficient and Permeability direct measurements plotted against oedometer test measurements

The average deviation between the consolidation coefficient from the oedometer and direct measurements (figure 5.3a) is $\pm$46%. The average deviation between the permeability from the direct measurements and the oedometer measurements in figure 5.3b is $\pm$50%. Excluding the outlier at $5 \cdot 10^{-7}$ for $k_{w,direct}$, the average deviation drops to $\pm$34%.
As discussed in chapter 3.3.2 obtaining a correct value of the consolidation coefficient is hard, because the measurements are sensitive to errors. The results between the different methods are within the same order of magnitude. Therefore from these results, it is concluded that the results obtained from the direct consolidation measurements are sufficiently accurate. These values will be used further in the analysis of the study. However, in the following results, a bandwidth should be kept in mind regarding the calculated values, as the c_v values are not exactly determined.

5.3. Jet test results table

In table 5.1 a summary is given of the results of the executed tests.

Table 5.1: Summary of test information and measurements

Clay_SOD_$p_{stag,0}/su$_ sequence rep	$p_{stag,0}$ [kPa]	su [kPa]	$p_{stag,0}/su$ [-]	SOD [mm]	D_n [mm]	SOD/D_n [-]	$u0$ [m/s]	Q [m^3/s]	cv_{direct} [m^2/s]	k_{direct} [m/s]	t_{tot} [min]	$Z_{c,max}$ [mm]	V_{tot} [cm3]	$r_{Zc,max}$ [mm]	x_0 [mm]	y_0 [mm]
K_15_0.4_1	4.00	9.47	0.42	147	20	7.35	3.46	8.87E-04	4.79E-08	1.59E-07	487	101	781	101	230	160
5% Bent_15_0.4_1	4.71	10.68	0.44	150	20	7.50	3.73	9.73E-04	2.25E-08	4.60E-08	855	143	1768	20	300	165
K_(s)_15_0.6_1	7.50	11.68	0.64	152	20	7.60	4.80	1.26E-03	1.78E-07	5.38E-07	12.6	197	1871	0	185	260
K_15_0.6_2	6.00	9.37	0.64	151	20	7.55	4.25	1.11E-03	1.27E-07	3.29E-07	400	183	2904	25	205	230
K_(s)_15_0.6_3	6.30	10.00	0.63	151	20	7.55	4.30	1.13E-03	1.78E-07	5.38E-07	24	187	5154	0	250	235
K_15_0.6_4	5.60	9.44	0.59	149	20	7.45	3.99	1.05E-03	3.27E-08	3.12E-07	408	115	1201	20	250	160
K_22_0.6_1	6.00	9.47	0.63	225	20	11.25	6.30	1.67E-03	2.95E-08	1.12E-07	300	162	4523	50	275	280
K_30_0.6_1	6.20	10.50	0.59	298	20	14.90	8.44	2.25E-03	3.80E-08	1.20E-07	43	184	6790	40	325	300
K_30_0.6_2	5.60	8.82	0.63	298	20	14.90	7.99	2.12E-03	2.48E-08	1.88E-07	180	181	5778	65	235	350
5% Bent_15_0.6_1	6.30	11.25	0.56	149	20	7.45	4.37	1.14E-03	4.49E-08	1.11E-07	96	122	1791	0	180	180
10% Bent_15_0.6_1	7.50	10.34	0.73	153	20	7.65	4.75	1.25E-03	4.09E-08	1.20E-07	21	151	1561	0	255	225
15% Bent_15_0.6_1	5.50	9.04	0.61	148	20	7.40	4.09	1.07E-03	5.68E-08	1.85E-07	440	132	1493	10	205	140
15% Bent_15_06_2	5.50	8.98	0.61	148	20	7.40	4.02	1.05E-03	5.12E-08	1.49E-07	422	169	2507	65	205	120
25%Bent_15_0.6_1	5.02	7.96	0.63	148	20	7.40	3.86	1.01E-03	8.57E-08	3.00E-07	423	131	270	0	200	200
K_sand_15_0.6_1	5.70	9.57	0.60	147	20	7.35	4.06	1.07E-03	1.75E-07	4.30E-07	105	168	2297	0	140	160
K_(s)_15_1.0_1	10.20	9.83	1.04	154	20	7.70	5.47	1.43E-03	3.42E-07	1.97E-06	12	200	3396	40	120	180
5% Bent_15_1.0_1	11.50	11.56	0.99	152	20	7.60	5.85	1.54E-03	4.49E-08	1.11E-07	72	200	3304	0	255	250
10% Bent_15_1.0_1	10.40	10.84	0.96	151	20	7.55	5.44	1.43E-03	4.09E-08	1.46E-07	120	200	4454	0	250	250
5% Bent_15_1.4_1	17.50	12.29	1.42	150	20	7.50	7.01	1.88E-03	4.49E-08	1.11E-07	30	192	7919	0	350	275
10% Bent_15_1.4_1	13.30	9.13	1.46	150	20	7.50	6.19	1.65E-03	4.09E-08	1.46E-07	72	200	5340	20	250	300

5.4. Scour depth results

In figure 5.4 the depth of the erosion holes, for tests with a standoff distance of 150 mm, against the test time is given. The lines are coloured according to the ratio of $p_{stag,0}/su$ at the beginning of the test.

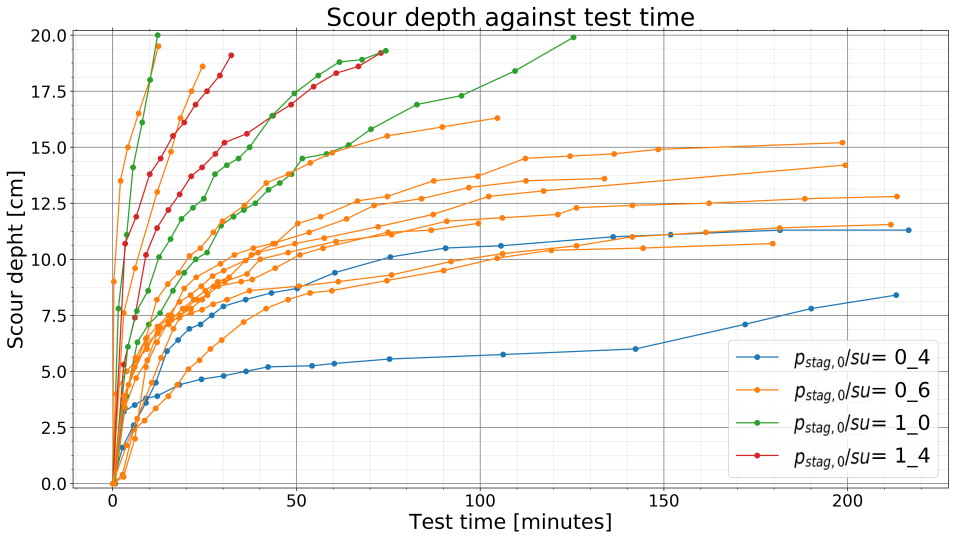

Figure 5.4: Depth of erosion hole against test time all tests, coloured by $p_{stag,0}/su$

At first glance, the results seem scattered; however, from this figure, some conclusions can be drawn. Based on figure 5.4, some zones of the scour depth can be identified. In figure 5.5 these zones are drawn. The scattering of the lines at the different stagnation pressures has several causes. Firstly different soil samples are used, which have different properties that affect the erosion. Secondly, the shape of the erosion hole at the start of the erosion affects how the rest of the hole develops, and therefore how fast the scour depth increases. Another effect influencing the depth development is the local weak spot in the soil samples.

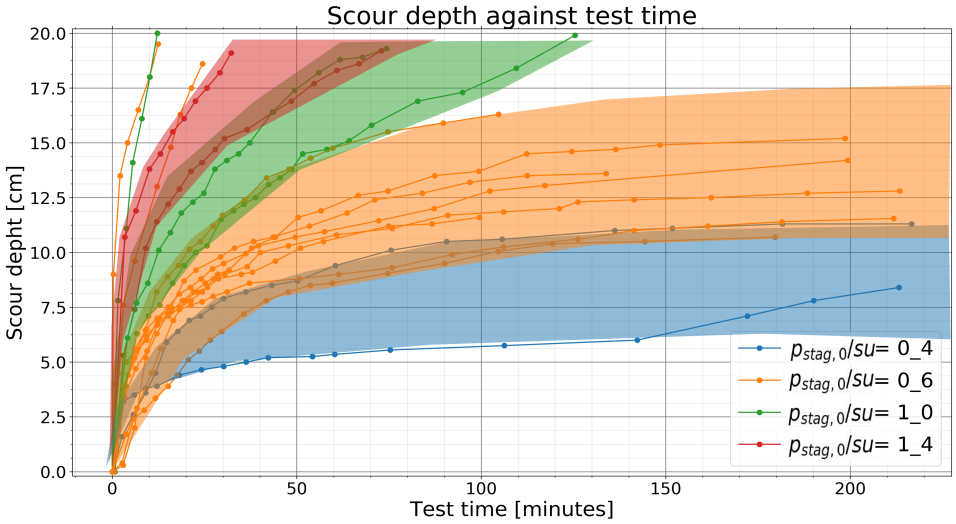

Figure 5.5: Depth of erosion hole against test time all tests with $p_{stag,0}/su$ zones

Two experiments with 0.6 $p_{stag,0}/su$ show a large deviation with respect to six other experiments. This might be attributed to the difference in the kaolin mineral batch. In table 3.4, it can be seen that the liquid limit of the two different kaolin samples is different for the two samples. Secondly, the difference between the consolidation coefficient was observed. Lastly, for test K_15_0.6_1, a hole was created in

the middle of the sample by a hand-vane to test if the undrained shear strength was uniform over the whole sample. The hole could have influenced the scour depth development and is therefore excluded from further analysis.

5.4.1. Scour depth as a function of the stagnation pressure for different soils

The lines of different soil mixtures are plotted in individual sub-figures in figure 5.6 to visualise the effect of the stagnation pressure on the scour depth over the jetted time. All the tests in figure 5.6 are executed at the same standoff distance and have the same nozzle diameter. Also, the soil mixtures had approximately the same undrained shear strength of 10 kPa, and the figures are sorted to have the same soil mixture.
In all the sub-figures, an increase in the scour depth over time can be observed for higher ratios of $p_{stag,0}/su$. This is expected as the exerted pressure on the soil increases; also, the erosion velocity will increase.

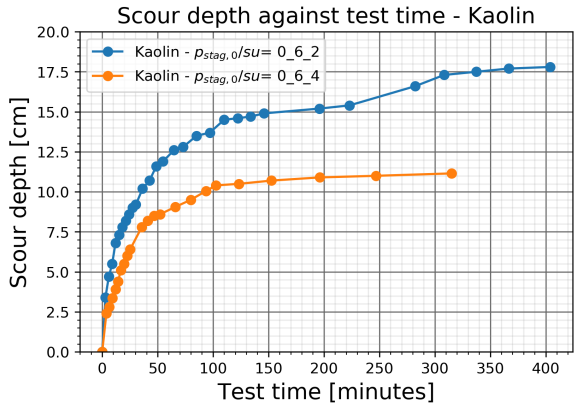

(a) Scour depth of kaolin samples against time for different stagnation pressures

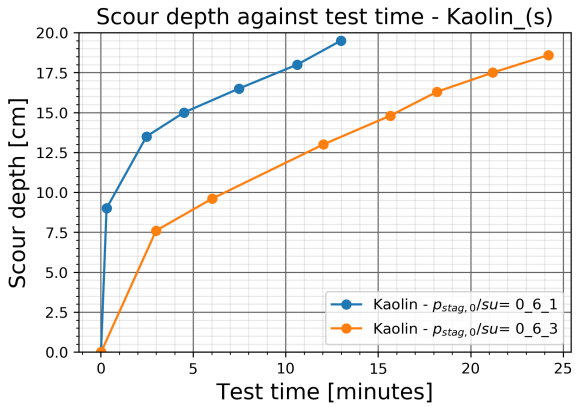

(b) Scour depth of kaolin_(s) samples against time for different stagnation pressures

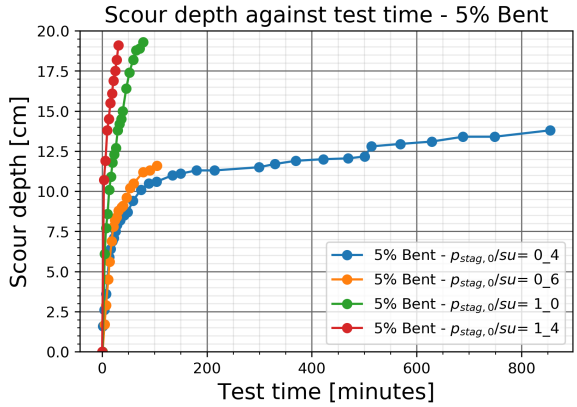

(c) Scour depth of 5% Bentonite samples against time for different stagnation pressures

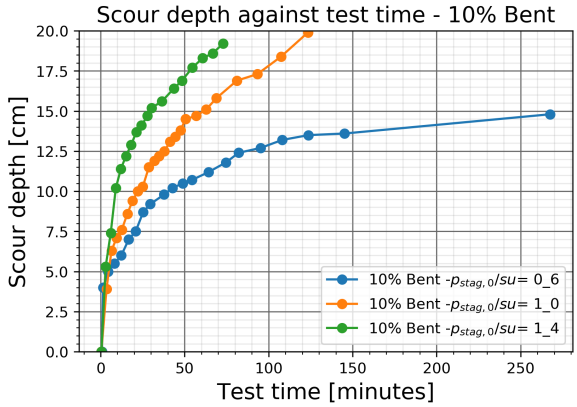

(d) Scour depth of 10% Bentonite samples against time for different stagnation pressures

Figure 5.6: Depth of the scour holes over time with equal standoff distance and nozzle for the different soil mixtures

In figure 5.7 the erosion velocity dZ_c/dt for the different soil mixtures are plotted against the stagnation pressure at the soil surface for a developing scour hole. The erosion velocity is calculated using the derivative of the ln fit of the depth of the scour hole against the test time. The ln fits for the individual tests are given in the plots in appendix B. The stagnation pressure at the surface of the soil is calculated using equation 2.55.

In figure 5.7, it can be observed that the lines for the individual tests with a different ratio of $p_{stag,0}/su$ at the start of the tests follow the same path of erosion velocity for a given stagnation pressure, within the margin of error.

In figure 5.7 the figures are plotted from a test time of 5 minutes to 400 minutes. The first five minutes are not plotted as the first depth measurement is taken after 3 minutes of testing. Secondly, the ln fit does not provide an accurate representation of the measured depth for the first few minutes. In figure 5.7a, 5.7c and 5.7d it is observed that for the the test with a lower p_{stag}/su ratio at $t = 0$ a higher value of the erosion velocity $\frac{dZ_c}{dt}$ is observed. It is assumed as explained before that this is due to the accuracy of the ln fit at the start of the test. Moreover, it could be possible that the scouring behaviour of the soil is different at the start of the test due to the fact that the jet is impinging on a flat surface. The jet impinging on a flat surface could result in another shear stress distribution on the soil, and a different pressure distribution in comparison with a partially formed scour hole.

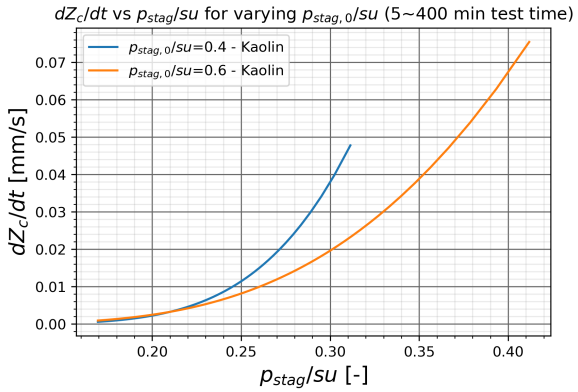

(a) Erosion velocity dZ_c/dt of kaolin samples against p_{stag}/su for different stagnation pressures

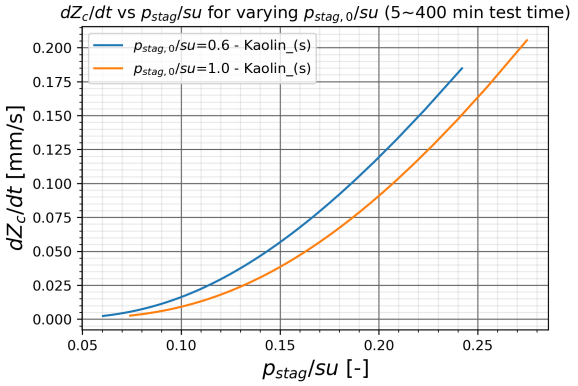

(b) Erosion velocity dZ_c/dt of kaolin_(s) samples against p_{stag}/su for different stagnation pressures

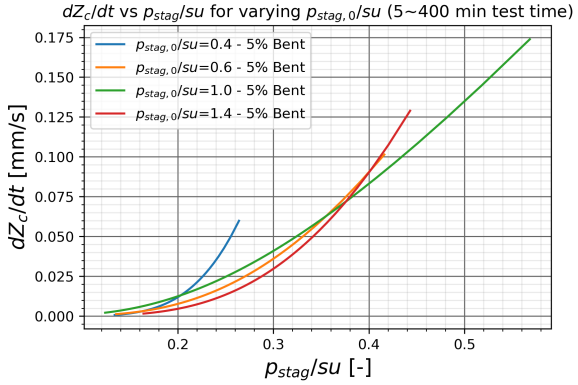

(c) Erosion velocity dZ_c/dt of 5% bentonite samples against p_{stag}/su for different stagnation pressures

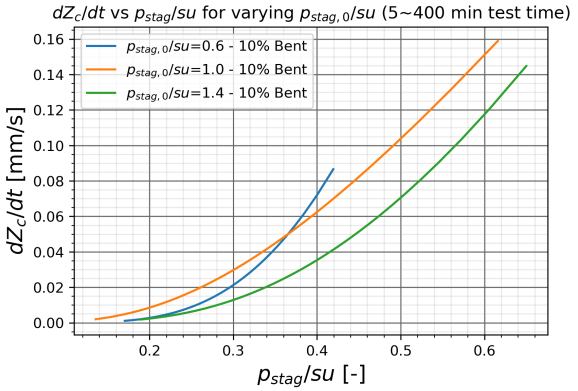

(d) Erosion velocity dZ_c/dt of 10 % bentonite samples against p_{stag}/su for different stagnation pressures

Figure 5.7: Erosion velocity dZ_c/dt of the different samples against p_{stag}/su for different stagnation pressures

5.4.2. Standoff distance

The standoff distance was varied for only for the kaolin samples. In figure 5.8a the tests with the varied standoff distance is presented.

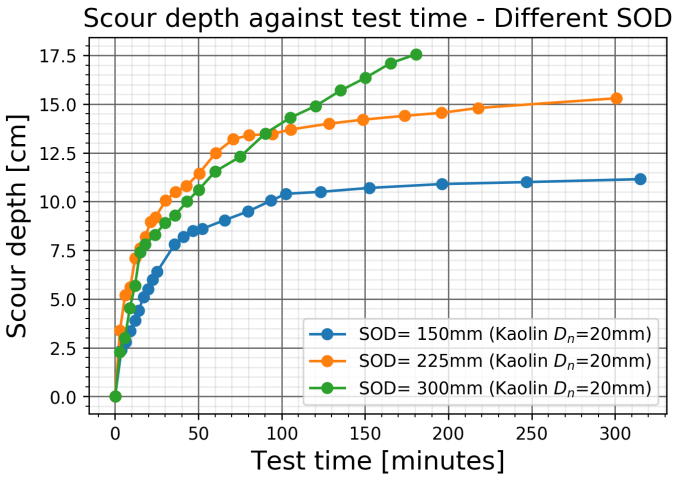

(a) Depth of erosion hole against test time for varying standoff distance

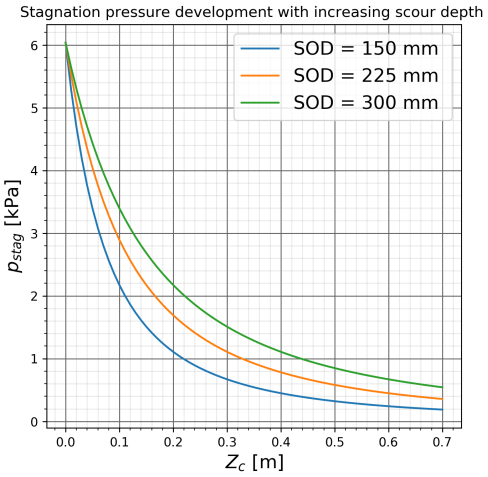

(b) Stagnation pressure development for increasing scour hole

Figure 5.8: Standoff distance

The different tests were executed at the same stagnation pressure $p_{stag,0}/su$ at the surface of the soil. With a varying standoff distance, this means that the jet pressure is different for the individual tests. Plotting the calculated stagnation pressure development for an increasing scour depth, in figure 5.8b, for different standoff distances, shows that the stagnation pressure remains higher for increasing scour hole depths for larger standoff distances.

This is related to the fact that the axial distance from the jet nozzle s is quadratically related to the stagnation pressure as can be seen in equation 2.55.

The stagnation pressure is plotted against the erosion velocity in figure 5.9 for the different standoff distances to investigate the influence of the standoff distance on the erosion velocity. The tested range of SOD/D_n increase from 7 for SOD =150 mm to approximately 15 for SOD =300 mm.

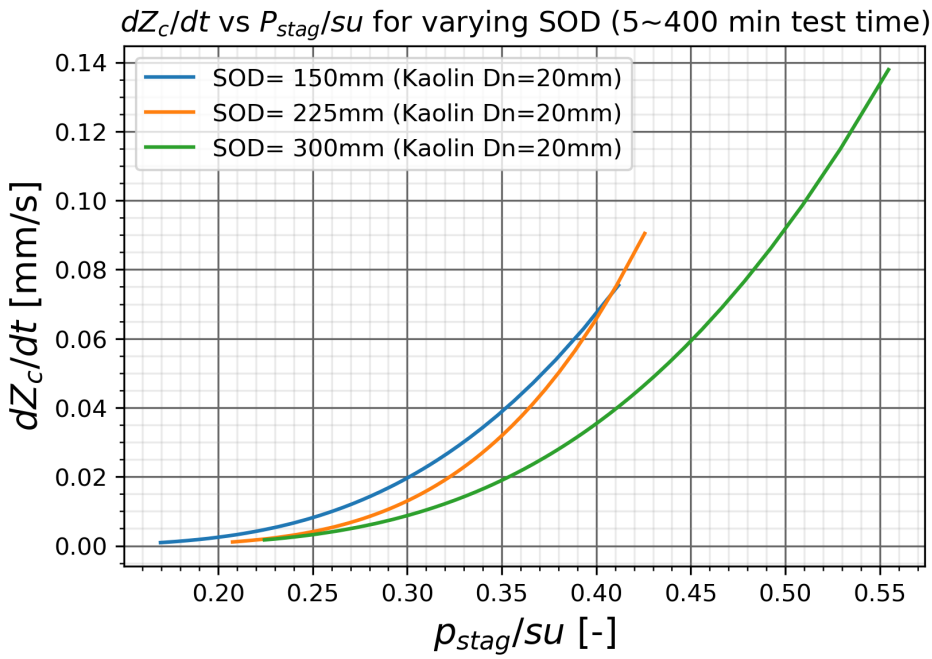

Figure 5.9: Influence of the standoff distance on the erosion velocity plotted against p_{stag}/su

As in figure 5.9 can be seen the erosion velocities dZ_c/dt are within the same range for the same

for the same ratio of p_{stag}/su. However a minimal but general trend can be observed: the larger the standoff distance, the lower the erosion velocity for the same ratio of $pstag/su$.
The decrease in erosion velocity is not merely related to the larger standoff distance, as in chapter 5.4.3 will be made clear, that tests with larger standoff distances but with the same ratio of SOD/D_n have the same erosion velocity. Therefore the decrease in erosion velocity is assumed to be related to the increase in the ratio of SOD/D_n.
The reduction in the scour depth for larger SOD/D_n ratios is in line with the findings of Moore and Masch Jr [25] (1962). Moore and Masch Jr [25] (1962) found a maximum erosion velocity for a ratio of SOD/D_n=7 which reduced as the ratio of SOD/D_n increased. The reduction in erosion velocity could be related to the uncertainty in the entrainment coefficient and the discharge coefficient of the jet.
Although a trend of lower productions for larger standoff distances at the same ratio p_{stag}/su is observed, this trend could be within the margin of error for the tests.

5.4.3. Nozzle diameter

In this study, tests are executed using only one nozzle diameter. Therefore results of some tests of Kerssens [19] (2017) are used to investigate the effect of the nozzle diameter on the erosion velocity. Although Kerssens did not report the scour depth over time, he did report the scoured volume over time and the final depth. The scour hole depth can be related to the impingement radius r_{zi}, and the observed scour volume (as will be explained in section 6.6.1). The depth of the scour hole as a function of the measured scoured volume is as follows:

$$Z_c = \frac{V}{a \cdot r_{zi}} \tag{5.1}$$

The scour depth is calculated using equation 5.1, using a value of 0.53 for a. Based on the observed final scour volume, reported by Kerssens, the final scour depth is calculated. This calculated depth is tested against the reported maximum observed depth in table 5.2. The average error is 35%, which is considerable; however, it is deemed accurate enough for calculation purposes in determining a relationship between the erosion velocity and the nozzle diameter D_n.

Table 5.2: approximated depth, measured depth, and relative error for jet tests of Kerssens [19] (2017)

Test_name (D_n.u_0.Clay)	calculated depth [cm]	measured depth [cm]	error [%]
10.15.D.2	4.39	5.50	20.1
20.15.D.1 1.5su	14.97	10.00	49.7
40.15.D.1	19.17	14.30	34.04

Using the depths at several time intervals a ln fit is used to approximate the depth of the scour hole over time. Using the derivative of the ln fit the erosion velocity can be found.

The effect of the nozzle diameter is checked against two sets of tests. The first set of tests are three tests using the 'Deltares' clay with a ratio of 1.5 $p_{stag,0}/su$ at the start of the tests. The tests are executed at a standoff distance of 70 mm, 140 mm, and 280mm, and a nozzle diameter of 10 mm, 20 mm and 40 mm respectively. Resulting in a constant ratio of SOD/D_n of approximately 7. The result of the erosion velocity against p_{stag}/su for this set of tests are given in figure 5.10a. In this figure, it can be observed that the nozzle diameter does not have a clear influence on the erosion velocity dZ_c/dt.

The second set consists of two tests. It has been observed that the Kaolin samples of Kerssens are comparable to the Kaolin_(s) clay samples used in this study. Test 40.3.K.1 of Kerssens and test K_(s)_20_14_0.6_3 of this study are used. Both tests are executed at 0.6 $p_{stag,0}/su$ at the start of the test an have a SOD/D_n ratio of approximately 7. Since the test time of these tests where lower, the ln fit was taken from 1 to 20 minutes. In figure 5.10b it can be seen that the tests with different nozzle diameter have comparable erosion velocities at the same ratio of p_{stag}/su. This is in line what is observed for the other test set.

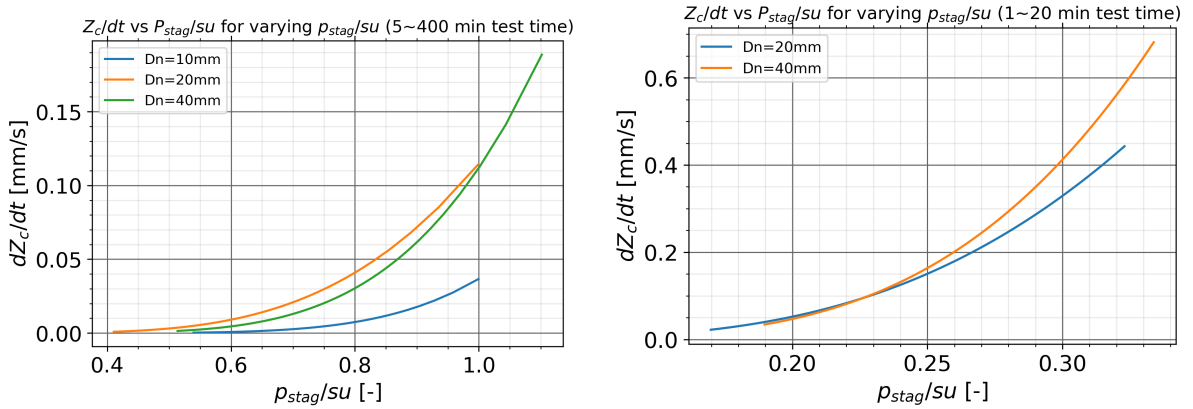

(a) Influence of the nozzle diameter on the erosion velocity plotted against p_{stag}/su for D_n=40 mm, 20 mm, and 10 mm. Using the data of Kerssens [19] (2017) of the 'Deltares Clay', with $p_{stag,0}/su$=1.5 at start of test

(b) Influence of the nozzle diameter on the erosion velocity plotted against p_{stag}/su for D_n=40 mm and 20 mm. Using the data of Kerssens [19] (2017) of the 'Kaolin Clay', with $p_{stag,0}/su$=0.6 at start of test. As well as using test K_(s)_20_14_0.6_3 of this study.

Figure 5.10: Effect of the nozzle diameter on the erosion velocity for changing $p_{stag,0}/su$

For both of the test sets in figure 5.10, the erosion velocities for the different nozzle diameters, remain more or less the same. Except for the 10 mm nozzle, for which a particular low scour volume (and therefore erosion rate) at the start of the test was observed, this could be a test anomaly. No clear relation is found between the nozzle diameter and the scour depth. Therefore it is concluded that the nozzle diameter does not have a direct effect on the erosion velocity if the ratio of SOD/D_n is kept constant at the soil surface, especially for larger nozzle diameters.

5.4.4. Influence of the consolidation coefficient on the scour depth

The data is analysed at several discrete time points to investigate the effect of the consolidation coefficient on the scour depth development. At: 5, 15, 25, 35, 55, 75, 100, 200, 300, 400 min the dimensionless depth is plotted against the consolidation coefficient. In the beginning, a higher resolution is chosen because the depth changes at a higher rate over time, whereas further in the test, the erosion velocity is lower. The results of the Kerssens [19] (2017) is included in this analysis, as the consolidation coefficient for the two soil types used in this research is directly determined from a CRS (constant rate of strain) test. The results of these tests are included in Appendix D.3 and in table 3.5 the cv values used are given.

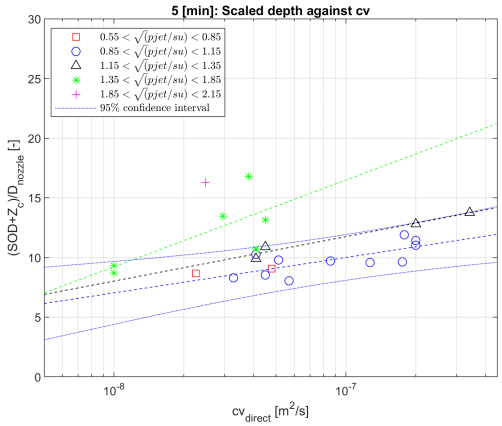

(a) Dimensionless depth of erosion hole at 5 min. against consolidation coefficient plotted for different ranges of p_{jet}/su. Including trend-lines and a 95% confidence interval

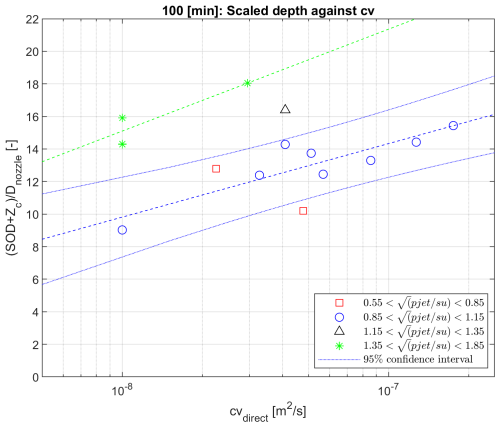

(b) Dimensionless depth of erosion hole at 100 min. against consolidation coefficient plotted for different ranges of p_{jet}/su. Including trend-lines and a 95% confidence interval

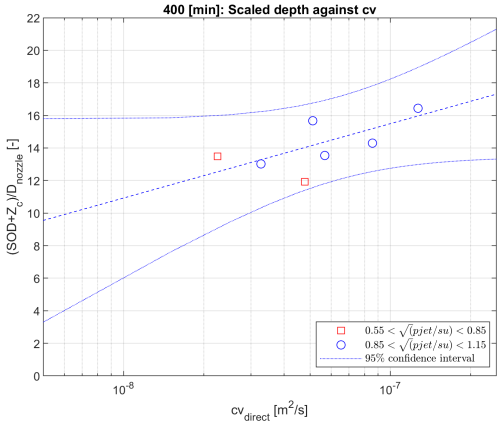

(c) Dimensionless depth of erosion hole at 400 min. against consolidation coefficient plotted for different ranges of p_{jet}/su. Including trend-lines and a 95% confidence interval

Figure 5.11: Effect of the consolidation coefficient on the dimensionless depth of the erosion hole at different time points

In figure 5.11 the plots of the dimensionless depth of the scour hole at three different discrete time points are given. A trend line is plotted for the data ranges that have three or more data points within the given p_{jet}/su range. For the range of $0.85 < \sqrt{p_{jet}/su} < 1.15$ (which corresponds to most of the points of 0.6 $p_{stag,0}/su$, a 95% confidence line is plotted. Most of the tests are executed at in this range of p_{jet} and therefore has the most data points and tends to give the most accurate depiction of the overall trend between the dimensionless scour depth and the consolidation coefficient. All the plots of the individual time points are given in appendix C.1, here also the plots for the complete data sets are given. The complete data set includes the studies of Kerssens, Mazurek, Hedges, and Dong.

Generally, a log-linear upward trend for all the time steps can be observed between the dimensionless scour depth and the consolidation coefficient. The trend lines seem to have a slightly increasing upward angle as time progresses; though, this has also to do with the availability of data points. The amount of data points per time point is not equal, which means that the 95% confidence interval increases over the range that no data points are available.

Since the trend lines at the different time points have approximately the same upward angle, it is concluded that the influence of the coefficient of consolidation remains more or less constant throughout the test.

Table 5.3: Direction coefficient of the log-linear fit ($\alpha \ln$) for 0.85<$\sqrt{p_{jet}/su}$<1.15 at discrete time points for the data of this study and of Kerssens [19] (2017)

Minute	5	15	25	35	55	75	100	200	300	400	Average
Direction coefficient	1.29	1.61	0.72	1.48	1.93	1.27	1.96	0.95	1.77	1.98	1.58

The data set $0.55 < \sqrt{p_{jet}/su} < 0.85$ shows a deviating trend. However, for this range, only 2 data points are available for most of the timestamps. The deviation for this data could also be accounted to the error for the determined coefficient of consolidation. Furthermore, the deviation could be accounted to the deviation between similarly configured jet tests, as will be discussed in chapter 4.5.
Finally, the relation that can be established is as follows:

$$\frac{SOD + Z_c}{D_n} \propto 1.58 \ln c_v \tag{5.2}$$

5.4.5. Other soil parameters influencing the erosion process

Next to the influence of the undrained shear strength and the consolidation coefficient, other relevant soil parameters and their influence on the erosion process are investigated. The parameters that are selected are the liquid limit, plasticity index and the dimensionless water-content. These parameters are selected on the basis of the found relations in other researches, as explained in chapter 2.5. In Appendix C figures are given with the plots at individual time steps for the data of this study and the study of Kerssens [19], and in separate figures, the plots for the complete data-set, which includes the data of Kerssens [19] (2017), Hedges [13] (1990), Mazurek [22] (2001) and Dong et al. [7] (2019).

Plasticity index

A general downward trend can be observed in the dimensionless scour depth for increasing values of the plasticity index. The plasticity index can indirectly be related to the consolidation coefficient c_v. As a soil becomes more plastic, the soil becomes less permeable and more compressible.

Liquid limit

The same downward trend of dimensionless scour depth for increasing values of the liquid limit, as observed for the plasticity index, is also observed for the liquid limit. This downward trend was expected as the liquid limit is negatively correlated with the consolidation coefficient.

Dimensionless water content

Because Dong et al. [7] (2019) found a relation between the dimensionless water content and the scour depth, the influence of this parameter is tested for the data obtained in this study. No clear correlation is found between the dimensionless water content and the scour depth.

5.5. Volume results

In figure 5.12 the volume of the scour hole eroded by the jet, the scour volume, is plotted against the measured scour depth for the individual samples. It can be observed in figures 5.12a and 5.12b that the stagnation pressure at the start of the test, does not influence the scour volume.

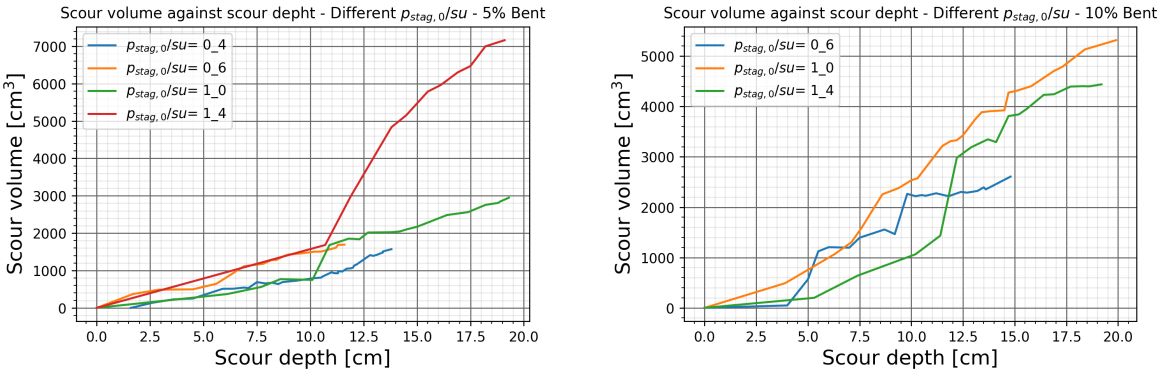

(a) Volume of scour hole plotted against the scour depth for the 5% bentonite samples

(b) Volume of scour hole plotted against the scour depth for the 10% bentonite samples

Figure 5.12: Volume of the scour hole plotted as a function of the scour depth for individual samples with different stagnation pressures at the start of the test

The scour volume and scour depth are linearly related. This means that the scour area remains more or less constant during the jetting, and that most of the volume increase is directly correlated to the depth increase. This can be visualised as a cylinder penetrating the soil over time, as is visualised in figure 5.13.

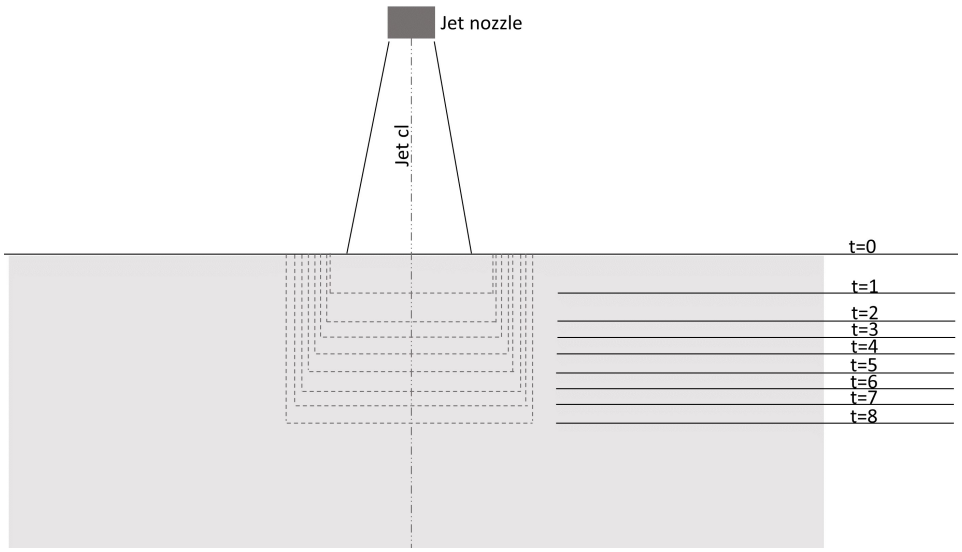

Figure 5.13: Scour depth development over time

In figure 5.14 scoured volume is plotted as a function of the depth for the tests with the varying standoff distance. It can be observed that an increased standoff distance results in a higher scour volume. This is due to the fact that by increasing the standoff distance of the jet to the soil surface, also the impact area on the soil surface is increased. The jet area increases quadratically for linear increasing standoff distance; however, a linear increase in the scour volume is observed instead of a quadratic increase. On average, when the standoff distance is increased from 150 mm to 225 mm, so a factor 1.5, the scour volume increases with a factor 1.85. Based on the fit-line trough the data. When the standoff distance is increased from 150 mm to 300 mm, a factor of 2, the scour volume increases with a factor 2.15.

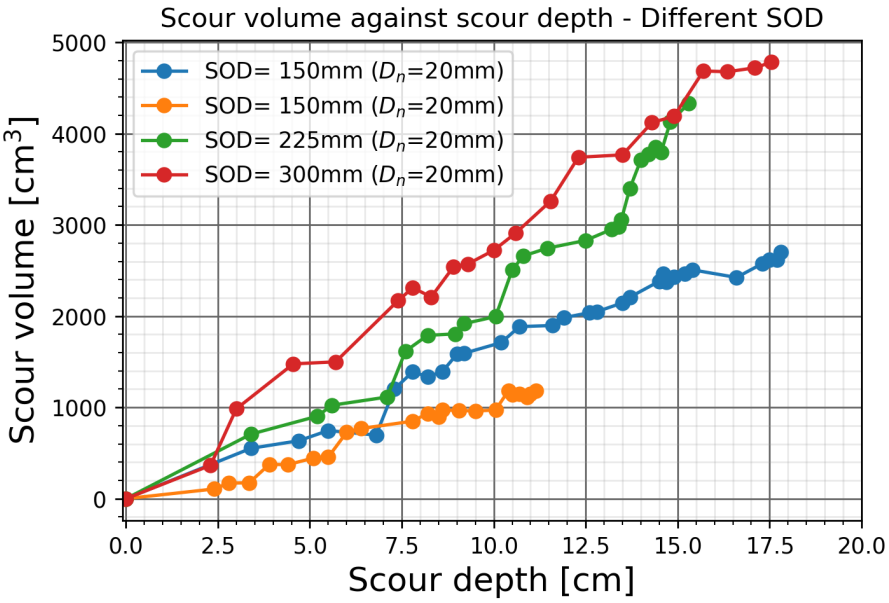

Figure 5.14: Volume of the scour hole plotted as a function of the scour depth for varying standoff distances at $p_{stag,0}/su$ =0.6

In figure 5.15 the relation between the Volume and standoff distance is visualised. A more or less linear relation exists between the scour volume and the standoff distance for different values of the scour depth Z_c. The radius of the impingement zone r_{zi} is directly linearly related to the standoff distance SOD so $r_{zi} \sim SOD$. Following up it can be concluded that the scour volume is related to the radius of the zone of impingement $V \sim r_{zi}$.

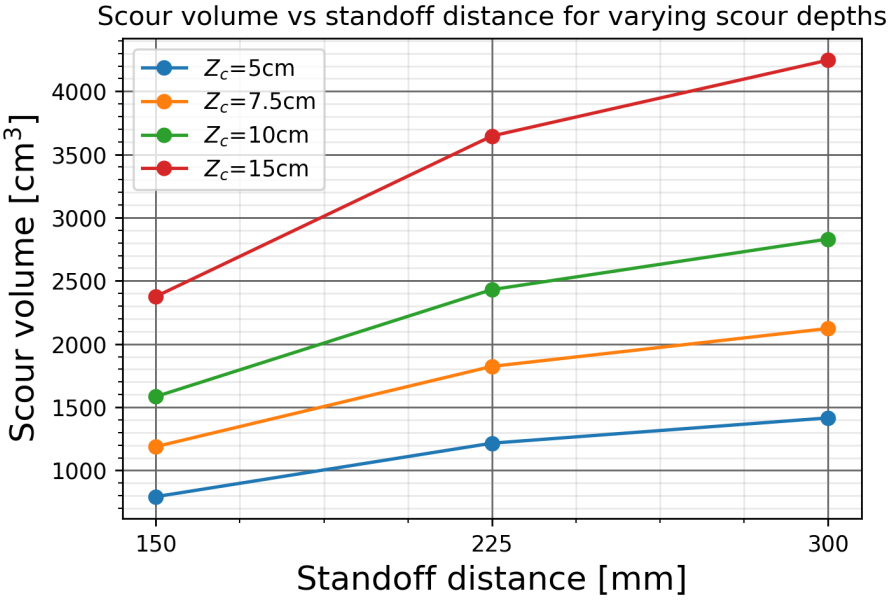

Figure 5.15: Volume of the scour hole plotted as a function of the standoff distance for varying scour depths Z_c at $p_{stag,0}/su$ =0.6

6 Analysis

6.1. Introduction

In this chapter, the obtained results are (further) analysed. Firstly in section 6.2, an attempt is made to determine whether the erosion process is drained or undrained and whether fracturing and mass erosion occurs. Subsequently, in section 6.3 the existing jet scour relations of Mazurek [22] (2001) and Dong et al. [7] (2019) are tested against the dataset. Furthermore, in section 6.4 the erosion velocities are coupled to the bed shear stress and the swelling theory.
Following up, in section 6.5, the stagnation pressure calculations are verified. In section 6.6 the erosion velocity is related to the stagnation pressure, an empirical relation is given to calculate the erosion velocity, and scoured volume. This relation is also used to scale the scour depth to full-scale sizes.

6.2. Erosion process

6.2.1. Drained versus undrained

To test whether the erosion process is a drained or undrained process, equations 2.76 and 2.77 can be used. As explained in chapter 2.4.2 the process can be considered fully drained if the Pèclet value of pore water dissipation Pe_w is smaller than 1, and fully undrained if the value is larger than 10.

The length scale is assumed to be the depth of the swelling front h_{sw}. Assuming h_{sw}=h_e the length scale can be approximated by equation 2.67, which also corrects for the pore water present in the top layer. The average value for the median diameter of the particles in the soil D_{50} is assumed to be 6μm, which is the median diameter of the kaolin sample of Kerssens [19] (2017). This sample is assumed to be a good representation for the median diameter of the particles of this study. The average volume of pore water in percentage is approximately 51%, and the air percentage is approximately 2%, which gives n_0= 0.53.

The erosion velocity is approximated using the derivatives of the 'ln' fit found for the depth of the scour hole over the test time, given in the plots in appendix B.

Lastly, the consolidation coefficient found from the direct consolidation measurements are used, given in appendix A.

In figure 6.1 the Pèclet number for pore water dissipation is plotted on a log-scale against the test time. The individual lines represent the individual test performed in this study. As in this figure can be seen, the Pèclet number remains smaller than 10 for all the tests and is smaller than 1 for all the tests after approximately 4 minutes.

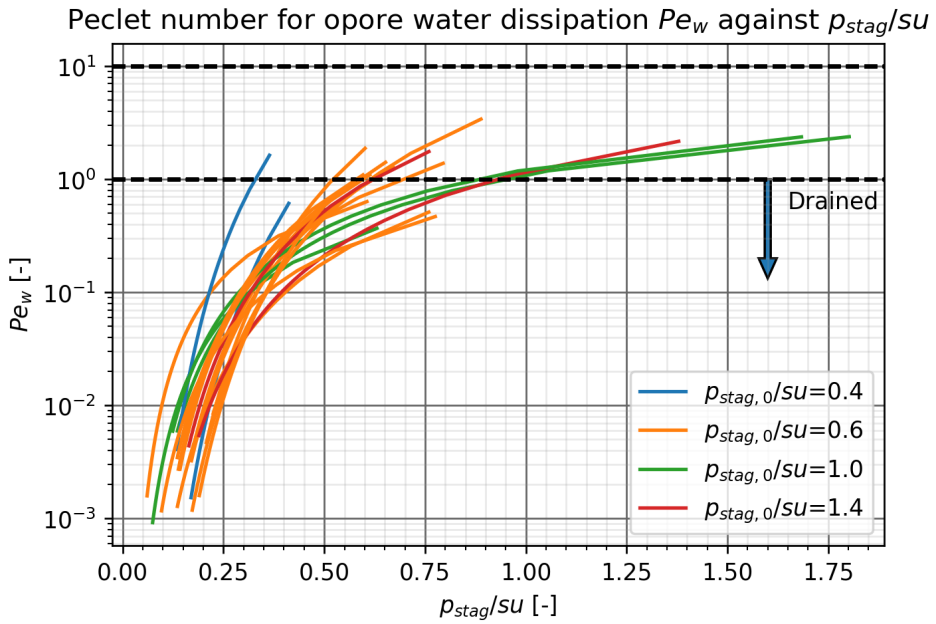

Figure 6.1: Peclet number for pore water dissipation

From figure 6.1 it can be concluded that the erosion process observed during these tests, could be a drained process.
Also, equation 2.76 van be used to test if the erosion speed v_e does not exceed the theoretical maximum surface erosion velocity. The lowest value for the maximum erosion speed is found for the smallest value of the consolidation coefficient. Taking $1.0 \cdot 10^{-8}$ as the lower bound for the consolidation coefficient with a porosity of n_0=0.53, and D_{50}=6 μm (appendix D.2), the maximum erosion velocity is about 0.5 mm/s.

If a linear increase of the scour depth in the first 5 minutes of the test is assumed, the observed maximum erosion velocity is approximately 0.5 mm/s.
Taking the observed maximum erosion velocity and dividing it by the theoretical maximum erosion velocity per individual test, therefore taking the consolidation coefficient per soil sample, results in a maximum ratio of $v_e/v_{e,max}$=0.18. This ratio of $v_e/v_{e,max}$ means that the theoretical maximum surface erosion velocity is not exceeded during the tests.
The observed erosion can be classified as a drained surface and floc erosion process taking into account the two test equations.

6.2.2. Fracturing

The timescale needed to generate stress concentrations around the cracks needs to be calculated to test whether the fracturing process can occur, as explained in section 2.4.4. Because the drainage length h_{rad} and the radius of the cracks R_{mc} are unknown, several cases are considered. Since the critical time of loading only is dependent on the drainage length, and the ratio of the drainage length and the crack radius, only the drainage length is varied. Winterwerp and Van Kesteren [44] (2004) assumed a crack radius of 0.1 mm, based on the size of discontinuities in the soil skeleton observed under a microscope.

The grain size of the kaolin clay is approximately 6μm with a maximum of 63μm (based on the grain size analysis performed in the study of Kerssens [19] (2017) on similar kaolin soil), which is smaller than the assumed crack radius. The drainage length is equal to half the distance between the adjacent micro cracks. The eroded flocs visually observed had an average size of 0.5 mm, the assumed drainage length of 0.4 mm is therefore sufficient considering that the drainage length is maximum half the floc size. For the consolidation coefficient the extreme values are considered.

Table 6.1: Critical loading time for when the stress concentrations are larger then negligible (t_{20}), also for 40 and 60% water pressure dissipation (t_{40} and t_{60} respectively), assuming a crack radius of 0.1 mm, and a consolidation coefficient of $1 \cdot 10^{-8}$ and $2 \cdot 10^{-7}$ with a varying drainage length between 0.15 mm and 0.4 mm

c_v [m^2/s]	h_{rad} [mm]	n_{mc} [-]	t_{20} [s]	t_{40} [s]	t_{60} [s]	$v_{e,20}$ [mm/s]	$v_{e,40}$ [mm/s]	$v_{e,60}$ [mm/s]
1.00E-08	0.15	1.5	3.65E-02	9.38E-02	2.36E-01	8.22	3.20	1.27
	0.2	2	1.69E-01	4.34E-01	1.09E+00	2.37	0.92	0.37
	0.4	4	2.12E+00	5.46E+00	1.37E+01	0.38	0.15	0.06
2.00E-07	0.15	1.5	1.82E-03	4.69E-03	1.18E-02	164.41	64.00	25.47
	0.2	2	8.44E-03	2.17E-02	5.45E-02	47.38	18.44	7.34
	0.4	4	1.06E-01	2.73E-01	6.86E-01	7.53	2.93	1.17

In table 6.1 the loading time for when the stress concentrations are assumed to be non negligible (t_{30}) is given. The maximum time 2.12 seconds, occurs with the greatest drainage length of 0.4 mm. This time scale suggests that fracturing could possibly occur during the jetting. However, it is hard to determine the actual size of the fracture that is needed to remove a floc. Also, the amount of stress concentrations needed for a fracture to occur is unknown.
If 40% of the water pressure needs to be dissipated, the maximum time needed for a fracture to occur increases to 5.5 seconds. The maximum observed erosion speed is around 0.2 mm per second; this could be considered in the order of the fracturing speed, assuming that the erosion rate due to fracturing can be approximated by $v_e \approx 2h_{rad}/t$, which results in an erosion rate $v_e = 0.8/5.46 \approx 0.145$mm/s assuming 40% of the water pressure needs to be dissipated with a consolidation coefficient of $1 \cdot 10^{-8}$ and a drainage length of 0.4 mm.
However, with a consolidation coefficient of $2 \cdot 10^{-7}$, the calculated erosion speeds are approximately an order higher than the observed erosion speeds. Therefore this method does not scale well with the consolidation coefficient c_v.
It is possible that for the soils with the higher consolidation coefficient, the drainage length is higher, and therefore the erosion rates are lower. The internal crack radius and drainage length are quantities that are not easily obtained and also not measured in this study. However, there is no indication of why these parameters should significantly differ between the soils.

Therefore it seems likely that internal fracturing is therefore not the main erosion mechanism governing this erosion process. However, plastic instability and fracturing due to shear failure could be influencing the erosion process. Further research into plastic instability in this failure mechanism could help in assessing whether this failure mechanism influences the erosion due to mass flow jets on cohesive soils.

6.2.3. Mass erosion

As explained in section 2.4.3 to cause mass erosion a stagnation pressure of at least two times the undrained shear strength is needed, this is a lower bound. All the tests are executed at stagnation pressures of lower than 2 times the undrained shear strength; however, due to turbulence fluctuations, it could be possible that for brief moments the stagnation pressure exceeds the lower bound for mass erosion. In section 2.3.4 a graph of the measured bed shear stress normalised by the mean bed shear stress is given. Assuming the probability density function for the stagnation pressure is similarly distributed, the probability of a n times exceedance of the mean stagnation pressure can be calculated using equation 2.53.

It is most probable that the mass erosion occurs at the beginning of the jetting process, as the stagnation pressure is the greatest. In table 6.2 the probability of the stagnation pressure exceeding two times the undrained shear strength is given for the test executed at 1.4 $p_{stag,0}/su$ with the 10% bentonite soil. At the start of the test, the peak stagnation pressure only needs to be 1.4 times larger than the mean stagnation pressure. The probability of the peak stagnation pressure being 1.4 times larger than the mean stagnation pressure is approximately 15%.
After five minutes, the scour hole is 6.4 cm deep. The ratio of p_{stag}/su is then 0.645. The peak pressure needs to be 3.1 times larger than the mean stagnation pressure to reach a ratio of p_{stag}/su of 2 after 5

minutes. The probability of a 3.1 times larger p_{stag}/su ratio is 0.01%; this can be considered unlikely to happen. If we look at the decrease in erosion speed dZ_c/dt, it can be concluded that the erosion speed and the probability of mass erosion occurring are not related. However, from table 6.2, it can be concluded that it is probable for some tests that mass erosion occurs at the beginning of the tests.

Table 6.2: Probability of mass erosion occurring based on the probability density distribution for the bed shear stress. Based on the data for the test 10% Bent SOD=150 mm with $p_{stag,0}/su$=1.4

t [minutes]	p_{stag}/su[-]	dZ_c/dt [mm/s]	Probability p_{stag}/su>2 [%]
0	1.4	0.215	15.44
5	0.645	0.145	0.01
factor	0.46	0.67	$6.48 \cdot 10^{-4}$

6.3. Comparison with existing relations

In this section the data obtained by testing in this study and the data from other similar studies (Hedges [13] (1990), Mazurek [22] (2001), Kerssens [19] (2017), and Dong et al. [7] (2019)) are tested against the existing methods to calculate the scour depth due to an impinging jet.

6.3.1. Method of Mazurek [22] (2001)

In figure 6.2 the method of Mazurek [22] (2001) to predict the maximum scour depth, as explained in chapter 2.5.2, is presented with the data of the different studies. The critical shear stress of the clay samples used in this study and that of Kerssens is estimated based on the shear stress on the soil surface at the maximum depth during a test since this parameter was not available. Secondly using equation 2.79 resulted in deviating data points with relation to the model of Mazurek. The critical shear stress for the samples used in this study and the kaolin samples of the study by Kerssens is estimated to be approximately 13 Pa, and the critical shear stress of the 'Deltares' clay samples used by Kerssens are estimated to be approximately 300 Pa.

In figure 6.2a, the dimensionless observed scour depth after 5 (blue) and 15 minutes (red) are plotted as a function of the excess shear stress term. As in this figure can be seen the data of the different studies fit the model reasonably well, especially for the data of Dong and Hedges. The data of Mazurek is a bit over predicted; however, this is expected since the formula given by Mazurek is fitted on the final maximum scour depth. In figure 6.2b the dimensionless depth after 300 (blue) and 400 (red) minutes of testing is given. Here the data of Mazurek is predicted reasonably well. On the other hand, the dimensionless maximum scour depth of this study, and the study of Kerssens is under predicted.

The underprediction is most likely due to the determination of the critical shear stress. The critical shear stress is not a typically obtained soil parameter. The empirical relations that exist to determine the critical shear stress often have a significant deviation. Secondly, the critical shear stress is dependent on a lot of different soil parameters, as explained in section 2.5.6. Therefore it is usually needed to perform a jet test to determine the critical shear stress of a particular soil.

The method of Mazurek can not be used to determine the scour depth development over time. To give an estimation of the expected production of a mass flow jet, this is however needed.

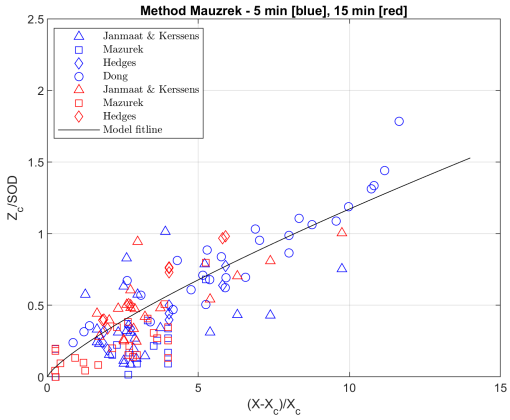

(a) Mazurek method - Dimensionless depth after 5 (red) and 15 (blue) minutes. Data of different studies and the fit-line of the method of Mazurek.

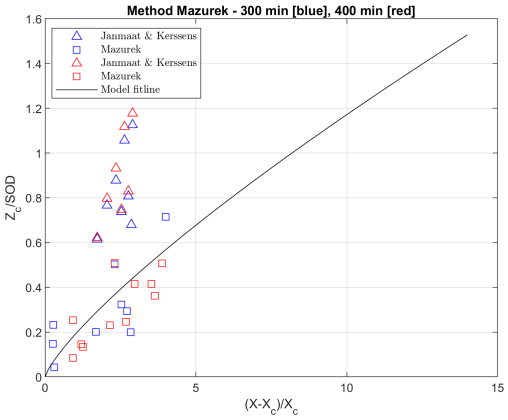

(b) Mazurek method - Dimensionless depth after 300 (blue) and 400 (red) minutes. Data of different studies and the fit-line of the method of Mazurek.

Figure 6.2: Fit of the measurement of the different studies on the calculated fit line of the method presented by Mazurek [22], 2001.

6.3.2. Method of Dong et al. [7] (2019)

In figure 6.3a, the observed dimensionless scour depth Z_c/SOD is plotted against the calculated dimensionless scour depth using the relation setup by Dong (equation 2.88). As explained in section 2.5.5, this method does give a prediction of the scour depth development over time. The scour depth of this study using this method is calculated mostly within an error margin of $\pm$35%. However, the data of Mazurek is over predicted, and almost all the data points have a larger deviation than 35% of the predicted value.

In this method, like the method of Mazurek, there is a term in the formula that divides by the critical shear strength. For the calculations of the method of Dong, the same critical shear strength is assumed as for the method of Mazurek. Dividing by the critical shear strength makes the critical shear strength a parameter that has a significant influence on the final solution as discussed in section 2.5.6 and 6.3.1 the critical shear strength is hard to determine.

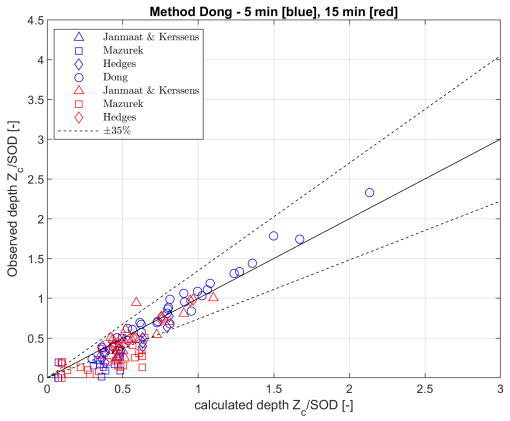

(a) Dong method - Comparison between measured and predicted dimensionless depths of the scour hole after 5 minutes (blue) and 15 minutes (red).

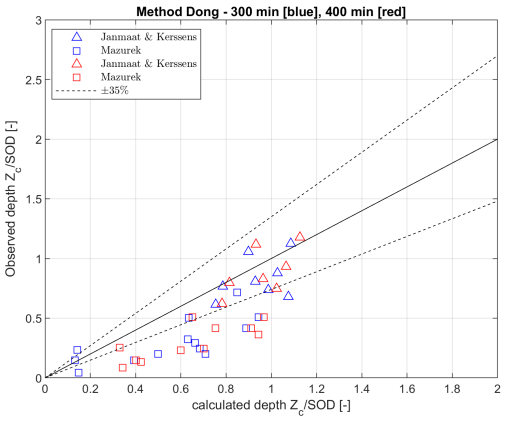

(b) Dong method - Comparison between measured and predicted dimensionless depths of the scour hole after 300 minutes (blue) and 400 minutes (red).

Figure 6.3: Fit of the measurement of the different studies on the predicted and the measured dimensionless scour hole depth using the method presented by Dong et al. [7], 2019.

6.4. Scour depth calculation based on bed shear stress and the swelling theory

To investigate whether the erosion velocity and scour-depth development over time can be approximated based on the bed shear stress exerted by the jet on the soil, as explained in the theory of Winterwerp et al. [43] (2012), an extreme case is investigated which should result in the highest erosion rate. This extreme case means the largest value for the consolidation coefficient c_v, the velocity at the jet nozzle u_0, and a high value of the equivalent roughness height k_s. The chosen parameters to calculate the friction coefficient, bed shear stress, and the resulting erosion rate are given in table 6.3.

As mentioned chapter 2.3.4 the equivalent roughness height of a soil is in the order of $5D_{50} - 1D_{90}$. Based on the sheave size analysis of the kaolin soil performed in the study of Kerssens [19], this would result in an equivalent roughness height of 13 μm (with D_{50} and D_{90} being 6 and 13 μm respectively as can be found in appendix D.2). In the theory of Rajaratnam [32] (1976) is stated that the rough bed approximation for the shear stress is only valid in a range of 0.005<k_s/h_{r0}<0.13, using a roughness height of 13 μm would result in in a too low ratio; therefore a value of 110μm is chosen, which results in a ratio which is in the middle of the validity range. Furthermore, this roughness height fits more in the range of the bed-forming flocs. For the jet distance r a minimum value of 0.01m, which results in a minimum value of the normalised jet distance $r/h_{r,0} \approx 1$. The integration constant near the bottom is assumed as $h_0 = k_s/30$, as assumed by Nobel [27] (2013). The erosion velocity parameter is given as follows, based on equation 2.72.

$$v_{e,par} = \frac{c_v \phi_s}{\alpha_e D_{50} su} \tag{6.1}$$

Table 6.3: Soil characteristics input and parameters for bed shear stress calculations

Bed shear parameters	u_0	[m/s]	8
	h_0	[m]	$3.67 \cdot 10^{-6}$
	r	[m]	0.01
	δ	[m]	$2.6 \cdot 10^{-4}$
Erosion speed parameters	c_v	[m^2/s]	$2 \cdot 10^{-7}$
	ϕ_s	[-]	0.49
	D_{50}	[μm]	$6 \cdot 10^{-6}$
	su	[kPa]	10
	k_s	[μm]	110
	n	[-]	0.51
	PI	[%]	18
	α_e	[-]	15.7

In the rough bed approximation, the friction coefficient is dependent on the distance from the jet. Using equations 2.48-2.52 the friction coefficient as a function of the normalised radial jet distance can be calculated, as presented in figure 6.4. In figure 6.4, the friction coefficient development for the rough bed approximation as a function of the normalised jet distance is given. In this figure, it can be observed that the friction coefficient reduces as the distance from the beginning of the jet increases; this is due to the boundary layer development.

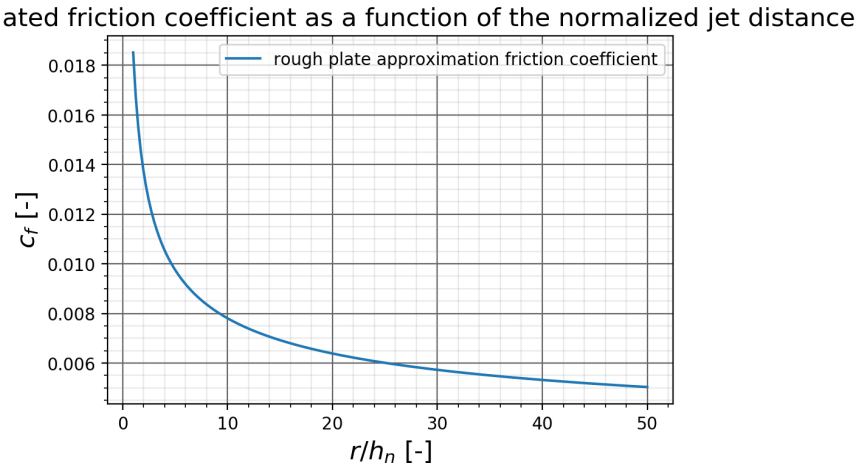

Figure 6.4: Friction coefficient development as a function of the normalized jet distance (k_s=110μm, h_{r_0} ≈0.011m)

For the calculation case the maximum value of the friction coefficient is taken at a distance of $r/h_{r0} \approx 1$ which is 0.0185. Using the same equations the bed shear stress for the rough bed approximation can be calculated.
The erosion speed can be calculated, using the critical bed shear stress calculated using equation 2.79 (≈ 1.25 Pa) and using the parameterised equation 2.75.

In table 6.4 the calculated friction coefficient, bed shear stress and the corresponding erosion speed is given for the rough bed approximation.

Table 6.4: Calculated friction coefficient, bed shear stress and erosion speed for the rough bed approximation method, calculated for the example case

	cf [-]	τ_b [N/m2]	v_e [mm/s]
Rough bed	0.0185	130	0.013

The calculated erosion rate in this extreme case is in the order of 0.01 mm/s, at a p_{stag}/su ratio of approximately 2. As figure 5.7 can be seen, this is at least a factor 10 too low even in this extreme case with a consolidation coefficient of $2 \cdot 10^{-7}$.

In figure 6.6, the calculated friction coefficient is multiplied by a factor of 40. For different tests, the calculated depth based on the bed shear stress method is plotted against the observed depth. The 35% error bar is plotted as the black dotted line, and the exact match is plotted as the continuous black line.

For the tests executed with the 10% bentonite, in figure 6.6a, the method first underestimates the depth of the scour hole and as time progresses, and the scour depth increases the calculation method tends to overestimate the scour hole depth. This is also visualised in figure 6.5, where the observed and the calculated depth are plotted against the test time.

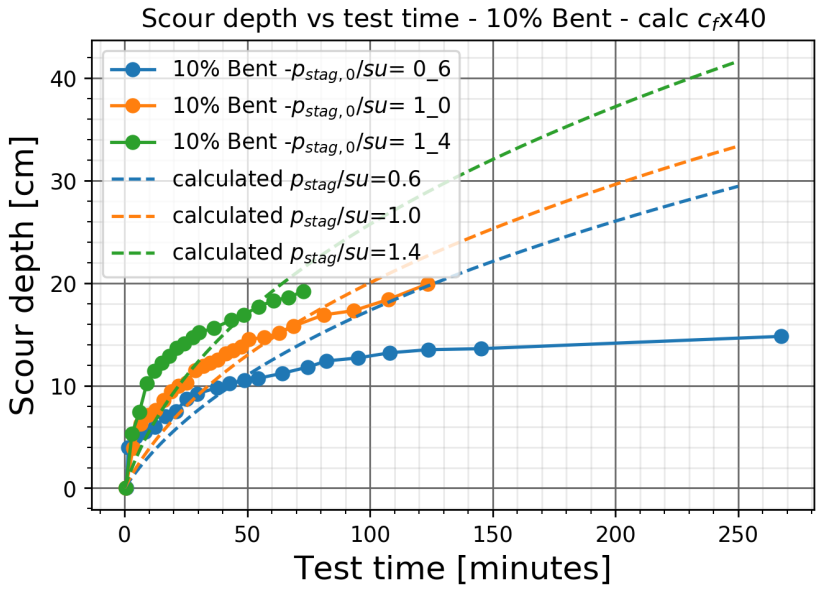

Figure 6.5: Observed and calculated scour depth over time-based on the bed shear stress calculations using 40x the friction coefficient for the 10% bentonite mixture with different $p_{stag,0}/su$

This under and overestimation means that the calculated erosion velocity at the start of the test is too low, and later on, in the test, the erosion velocity does not decrease enough to reach a 'final' depth. If the friction coefficient is further increased, the calculation method gives a better approximation of the scour depth at the start of the test; however, it tends to deviate later on in the test.
The tests executed with different types of soil with a $p_{stag,0}/su$ ratio of 0.6 at the start of the test are plotted in figure 6.6b. The same deviation as in figure 6.6a can be observed. At the start of the test, the observed scour depth is greater than the calculated, and further on in the test, the calculated scour depth becomes bigger.

Varying the scour depth results in a somewhat better fit; still, no perfect fit can be obtained to calculate the scour depth.

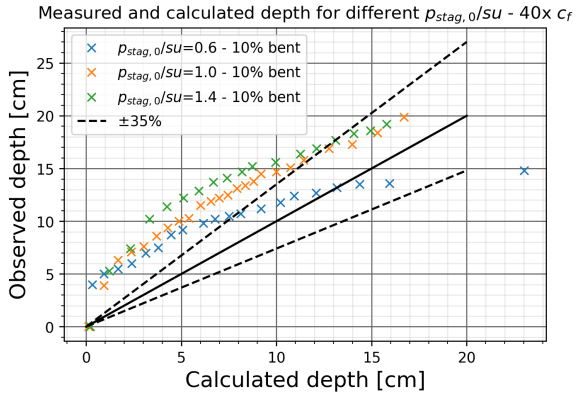

(a) Calculated versus observed scour depth for the 10% bentonite soils with different $p_{stag,0}/su$ ratios, using the smooth bed approximation and 40x the friction coefficient

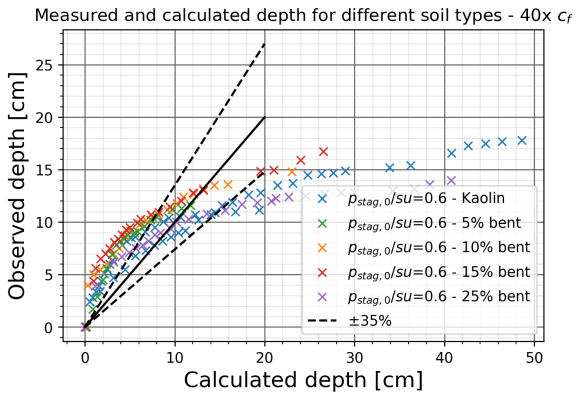

(b) Calculated versus observed scour depth for different soil types using the smooth bed approximation at a $p_{stag,0}/su$ ratio of 0.6, and 40x the friction coefficient

Figure 6.6: Observed versus calculated scour hole depth using the smooth bed approximation and the parameterised equation 2.75. The friction coefficient is multiplied by 50 to give a better fit.

As has become clear in this section, it is hard to predict the scour depth only based on the exerted shear stresses on the soil. This is partly because it is hard to correctly determine the friction coefficient, as it is dependent on a lot of different variables. Therefore to determine the friction coefficient, several

assumptions need to be made. Furthermore, even with these made assumptions and adjusted fits, the erosion velocity, and erosion velocity development does not agree with the observed erosion velocities during the tests.

6.5. Jet development and stagnation pressure approximation

6.5.1. Force due to jet momentum calculation

A special jet test was performed to test if the stagnation pressure and jet development calculations are correct. The clay containment frame was fitted with a flat wooden plate (smooth plywood) on top of it. The flow velocity was increased from 2 m/s to 18 m/s. The measured weight increase of the test sample is then attributed to the force of the jet momentum on the flat plate. The expected force on the flat wooden plate can also be calculated the calculated uniform stagnation pressure (equation 2.41) multiplied by the area of impingement ($A_{zi} = \pi r_{zi}^2$) (which can also be approximated by $force = Q \cdot \rho_w \cdot u_0/g$).
The calculated force based on the uniform stagnation pressure and the measured force is plotted in figure 6.7 as a function of the flow velocity at the nozzle. At a flow velocity of 2 m/s, the measured is 25% lower than the calculated force. This difference reduces to 10% at a flow velocity of 9 m/s. The difference between the measured and calculated force can be attributed to the loss of momentum, as in the calculation method momentum preservation is assumed.
From this measurement, it can be concluded that the calculated stagnation pressures exerted by the jet on the soil are accurate and that the calculation method is correct.

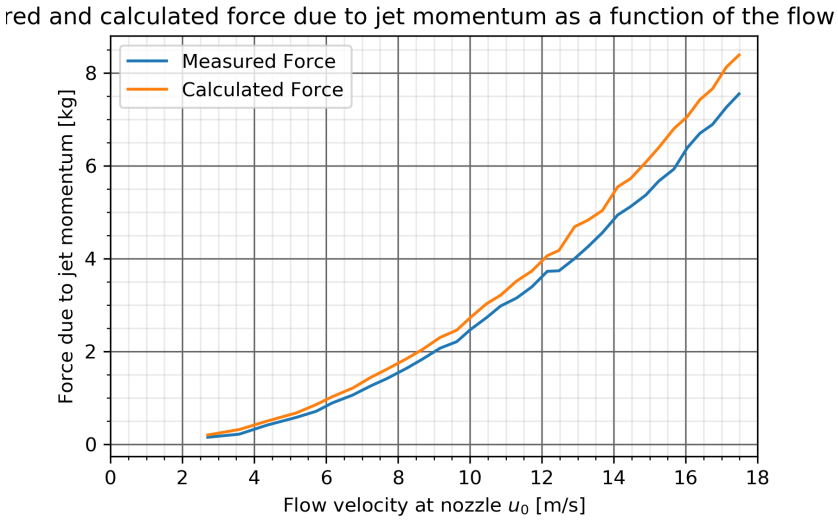

Figure 6.7: Measured and calculated force due to jet momentum as a function of the flow velocity

6.5.2. CFD model

For the calculations the assumption is made that the stagnation pressure p_{stag} inside a scour hole, can be approximated by the calculated stagnation pressure of an impinging jet on a flat plate on the same standoff distance as the standoff distance SOD plus the scour depth Z_c of the jetted hole. To test whether this assumption holds a continuum fluid dynamics (CFD) model of the test setup is created. For this model, the standard k-omega viscous model is chosen as this model performs better near walls (Mercier [23] (2013)).

In figure 6.8, the layout of the model can be seen, in which three cases are tested. The first case is a jet impinging on a flat bed with a standoff distance of 298 mm. In the second case, the standoff distance is 150 mm, and the depth of the scour hole Z_c is 148 mm, which results in a total standoff distance at the jet centre line of 298 mm. The third case, the standoff distance of the jet is 150 mm from the bed, and the scour depth is 0 mm; therefore, the jet impinges again on a flat bed.

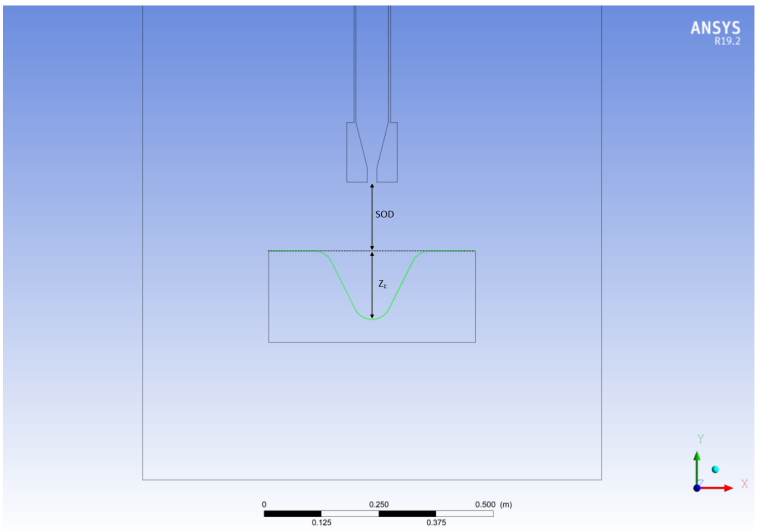

Figure 6.8: Ansys model including definitions

In figure 6.9 jet velocity as a function of the axial distance from the nozzle is plotted. The initial jet velocity, in this case, taken as approximately 3.7m/s, at the nozzle, is taken the same for the three different cases. As the axial distance from the jet increases the jet velocity decreases. As the jet approaches the bed, the jet velocity reduces as the jet begins to 'feel' the bottom. The jet velocity reduces to zero just above the bed. It can be observed that the jet velocity development follows more or less a similar path comparing the cases SOD=298 mm Z_c=0 mm and SOD=150 mm and Z_c=148 mm (the blue and orange line respectively), all be it that the jet velocity in the hole starts to reduce somewhat earlier.

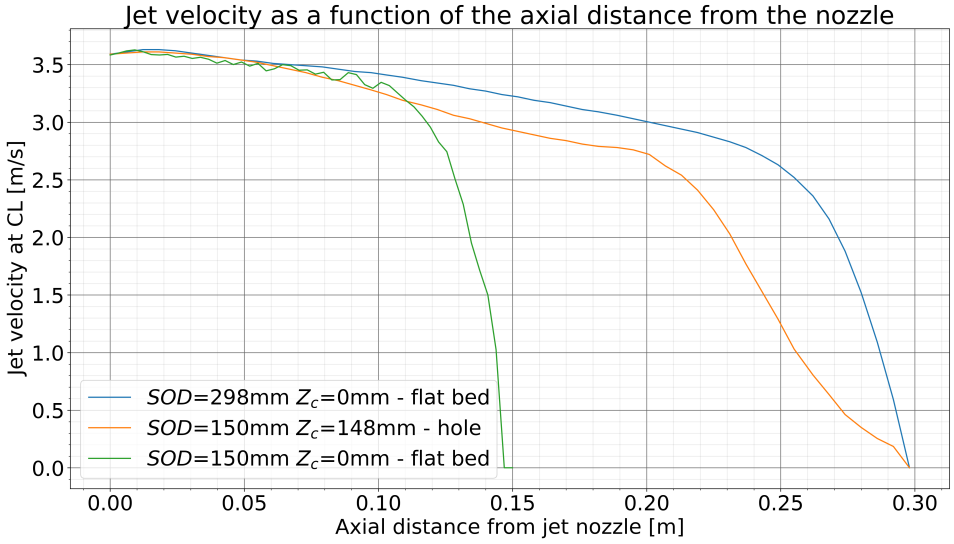

Figure 6.9: Jet velocity development at the jet centerline calculated for a standoff distance of 150 and 298 mm and for a standoff distance of 150 mm with a jet scour depth till 298 mm (Z_c=148 mm).

Following up for the three same cases, also the pressure distribution along the soil surface can be extracted from this model. In figure 6.10 the pressure distribution along the soil surface for the same three cases is plotted. The stagnation pressure is maximum along the jet centerline and reduces as the radial distance from the centerline increases. It is observed that as the standoff distance increases, the

pressure on the soil surface decreases comparing the two cases of a jet impinging on a flat surface with a varying standoff distance (the blue and the green line), as is logical since the jet velocity decreases at larger standoff distances. It can be observed that the stagnation pressure on the soil surface near the jet centerline is similar comparing the cases SOD=298 mm Z_c=0 mm and SOD=150 mm and Z_c=148 mm (the blue and orange line respectively).

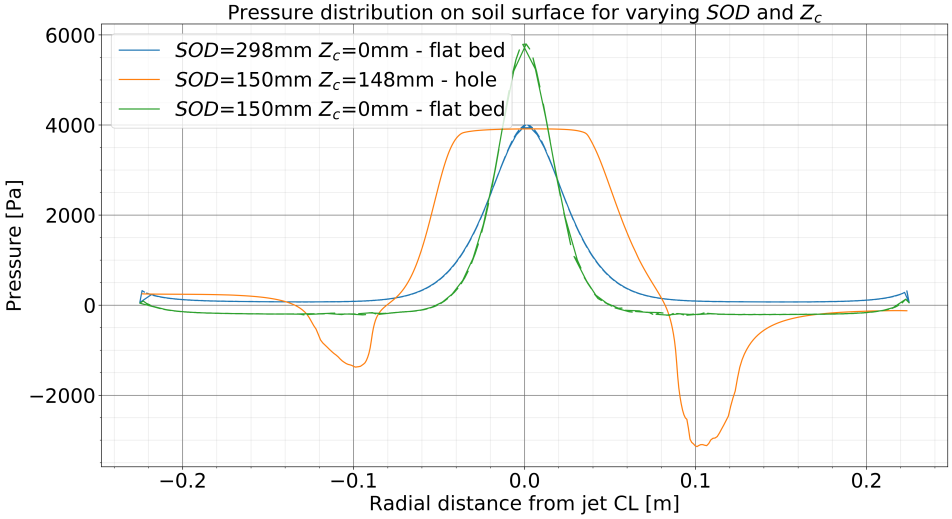

Figure 6.10: The stagnation pressure development calculated for a standoff distance of 150 and 298 mm and for a standoff distance of 150mm with a jet scour depth till 298 mm (Z_c=148 mm).

From the two figures, it can be concluded that there is an influence of the confinement of the jet inside the scour hole; however, this influence is minimal. Both figures confirm that a jet impinging on a flat plate is a good approximation of a jet inside a scour hole.

6.6. Scour depth calculation based on p_{stag}/su

Since the scour, rate and depth development calculations based on the bed shear stress did not lead to satisfactory results; another calculation method is developed partially based on the bed shear stress method.
As in figure 6.1 can be seen, all the lines follow more or less the same path for the Pèclet number for pore water dissipation as a function of p_{stag}/su. The lines being on the same path can be used to calculate the erosion velocity, as a fit line can be drawn through the lines. Taking equation 2.77 to calculate the pore water dissipation. As explained in section 2.4.2 the velocity scale is taken as the erosion velocity. For the length scale h_{sw} from equation 2.62 is taken, however instead of taking 10 times D_{50} or the floc size D_f, the same erosion factor α_e as defined in equation 2.74 is taken.
Assuming that the erosion velocity can be described as a function of a times p_{stag}/su to the power b results in the following equation:

$$a \cdot (p_{stag}/su)^b \propto \frac{v_e \alpha_e D_{50}}{(1-n_0)c_v} \tag{6.2}$$

A best fit is found for a value of 1.5 for a and a value of 2 for b. The fitline is plotted in figure 6.11 over the erosion velocity data found during the testing.
However, by adding the data of the different studies, it was found that the data gives a better fit for a static value of D_{50} of $6 \cdot 10^{-6}$m for all the studies. The same holds for the porosity value of n. Since the grain size and porosity were not explicitly varied in this study, it is hard to accurately test the effect of these parameters on the erosion behaviour. Therefore it remains unknown what the exact effect of the median particle diameter D_{50} and the porosity are in the scouring process by impinging jets.

This means that equation 6.2 reduces to the following form:

$$a \cdot (p_{stag}/su)^b \propto \frac{v_e}{c_v} \tag{6.3}$$

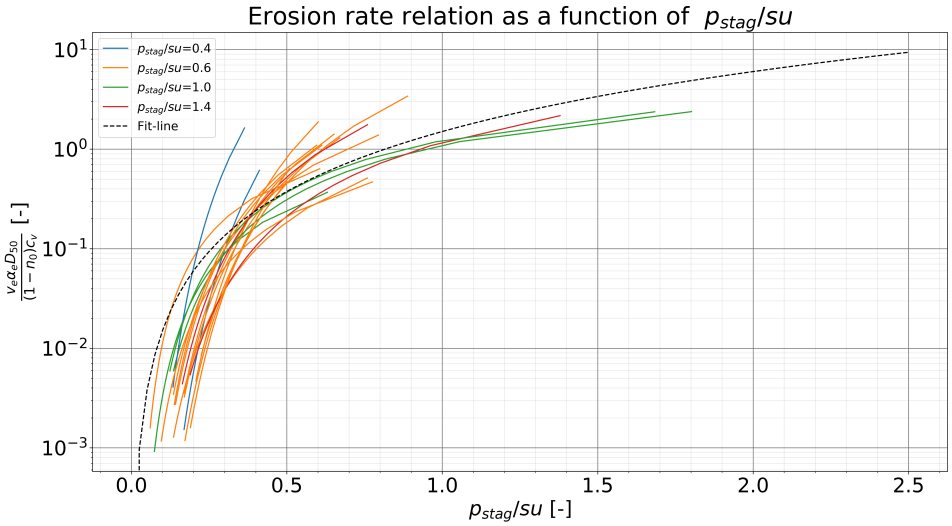

Figure 6.11: Fitline for p_{stag}/su plotted over the measured erosion rate data.

With a then being 7800. The value of 2 for the factor b could be related to the soil response due to instantaneous loading, as explained in the approximation of the degree of consolidation for small values of time (equation 2.16), knowing that $v_e = h/t$. It could be possible that the dilation of the soil does not occur due to unprompted swelling of the soil, but rather be induced by shear stresses.

Subsequently, the stagnation pressure can be calculated using equation 2.56. Using the scouring rate, the scour depth at a point in time can be calculated as follows:

$$Z_c(t) = \sum_{t=0}^{t} v_e * \Delta t \tag{6.4}$$

In which Δt is the time step for calculating the depth, taken in this study as 1 second.

A shortcoming of this fit is that it becomes less representative for p_{stag}/su ratios of lower than 0.2. From the test data, it follows that the scouring rate below a p_{stag}/su ratio of 0.2 is low. Therefore it is assumed that for $p_{stag}/su < 0.2$ the erosion velocity becomes zero.

This calculation method is applied to the test data. In the sub-figures of figure 6.12, the observed scour depth over time (solid line) is plotted against the calculated scour depth over time (dotted line). For the different soils, the calculation method gives a good approximation of the scour depth development over time. The 'bend' in the calculated scour depth is at the point the p_{stag}/su ratio reaches a value of 0.2.

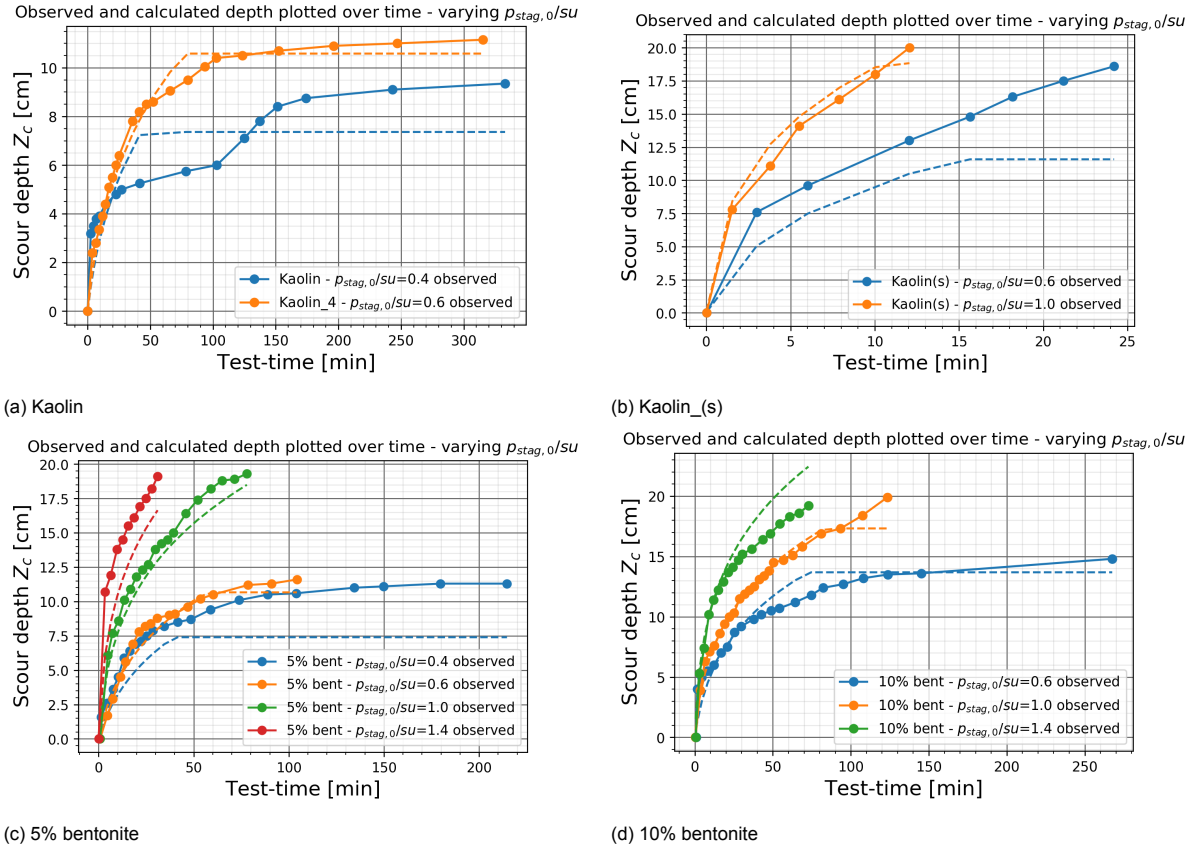

(a) Kaolin

(b) Kaolin_(s)

(c) 5% bentonite

(d) 10% bentonite

Figure 6.12: Observed (solid line) and calculated (dotted line) scouring depth Z_c sorted by per sample mixture against time for different $p_{stag,0}/su$.

To see if this method gives a good prediction of the scour depth over time. The calculated scour depth is plotted against the observed scour depth at a point in time. This is also done for other relevant studies. In figure 6.13 the observed and calculated depth is plotted for the different studies, with a 35% error line plotted as the dotted line.

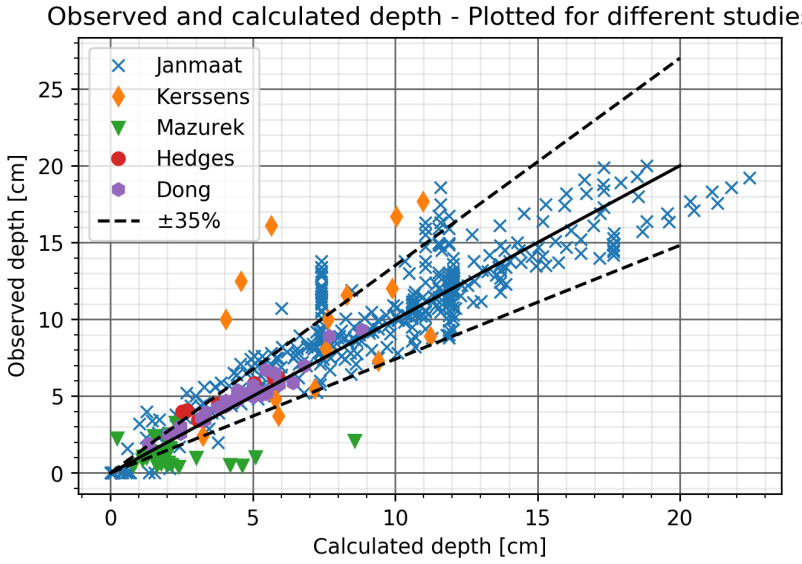

Figure 6.13: Calculated versus observed scour depth for the data of the present study, and for other relevant studies.

A relatively good fit is found using this method for the data of different studies, especially the data of Hedges and Dong, are well predicted. The data of Kerssens has a bit more scatter between the observed and the calculated scour depth. The scatter in the data could be due to the fabrication method of a part of the clay, which had some weaker planes in it; this could explain the under-prediction of the scour depth. Mazurek reported relatively low scour depths. The over prediction of some of the data points can be because the used clay has a higher resistance to erosion and that a larger value of the p_{stag}/su ratio needs to be chosen at which the erosion velocity becomes zero.
Almost all the data points are within the 35% margin of error, looking at the data obtained in this study. Some points appear to be on a straight vertical line. The straight line is because the erosion rate is set to zero at a p_{stag}/su ratio of<0.2, wherein during the tests, an increase of the scour depth is observed at a low scouring rate.

6.6.1. Empirical scour volume relation

The scour depth can linearly be related to the scour volume, as explained in chapter 5.5. It was described that the impingement radius r_{zi} and the scour volume are linearly correlated. An empirical formula can be set up to approximate the scour volume based on the impingement radius, defined in equation 2.39. The standoff distance and nozzle diameter, and the ratio between these values are accounted for by using the impingement radius, which makes scaling of the formula possible. It is assumed that the scour volume can be calculated using equation 6.5.

$$V \propto a \cdot Z_c \cdot r_{zi} \tag{6.5}$$

In which V is the scoured volume in [m^3], Z_c is the scour depth in [m] and r_{zi} is the impingement radius in [m]. From fitting, it is found that a has a value of 0.53. In figure 6.14 the measured scour volume is plotted against the measured scour depth, for different standoff distances, and therefore different values of r_{zi}. In the same figure, the calculated scour volume as a function of the scour depth is plotted as the dotted lines. A relatively good fit is found between the observed and the calculated scour volume.

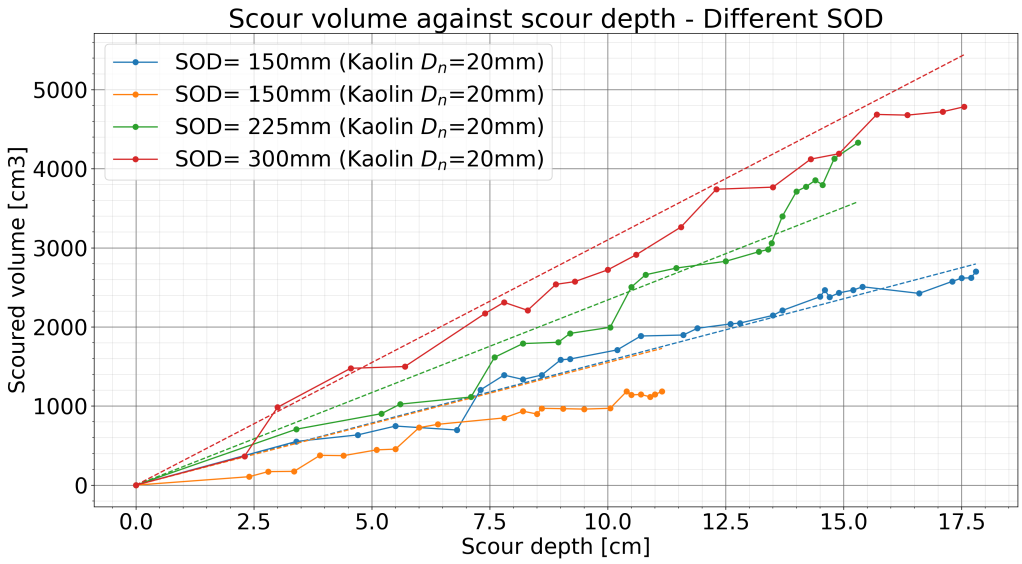

Figure 6.14: Scour volume plotted against the scour depth for different standoff distances. The solid lines are the observed values, and the dotted lines are the calculated values. Please note that the calculated results for SOD = 150 mm are on one line since it has the same standoff distance and nozzle diameter.

In this study, the nozzle diameter is kept constant. The scour volume based on the measured scour depth is calculated for the data of Kerssens [19] (2017), to test whether the proposed equation holds up. In figure 6.15, the observed scour volume is plotted against the calculated scour volume, with a 35% error margin is given. The predicted scour volume is almost all within the 35% margin of error,

except one outlier in the right top, looking at the data of this test, a sudden increase is observed in the scoured volume after 3 minutes, an anomaly in the test could explain this deviation.

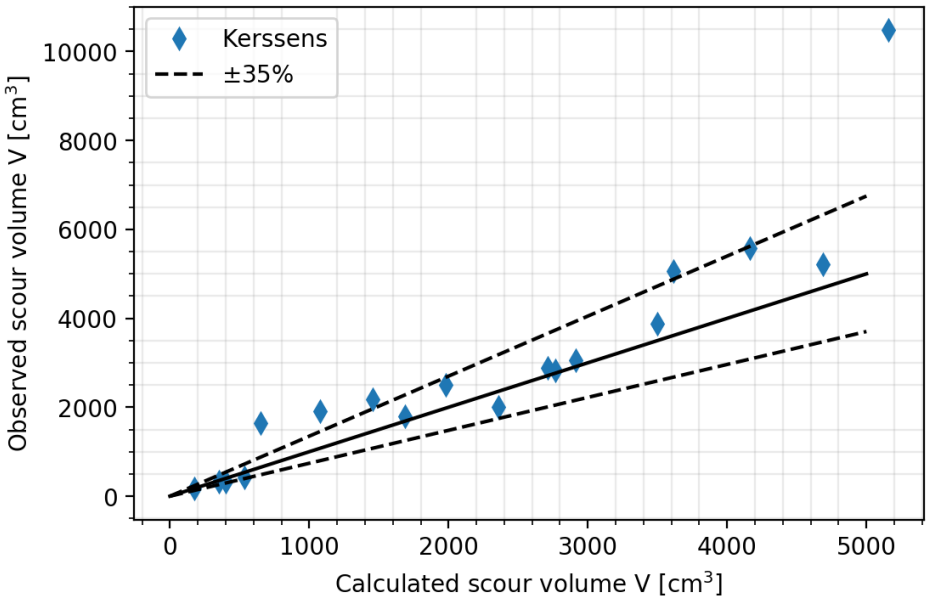

Figure 6.15: Observed scour volume plotted against the calculated scour volume based on the data of Kerssens [19] (2017), using equation 6.5.

6.6.2. Scaling based on p_{stag}/su method

The found empirical relation can be used to scale up the tests to actual sizes used offshore with mass flow jets. As the stagnation pressure is dependent on the standoff distance SOD, nozzle diameter D_n, flow velocity u_0. Using 6.3 the erosion velocity, and scour depth can be calculated. In figure 6.16 and 6.17 two calculation examples are given.

In figure 6.16 all the parameters are kept constant except the flow velocity at the nozzle. At a flow velocity of 2 meters per second, no penetration of the soil occurs as the stagnation pressure is too low. The upper bound of 10 m/s for u is chosen as the mass flow jet maximum velocity is usually in that range.

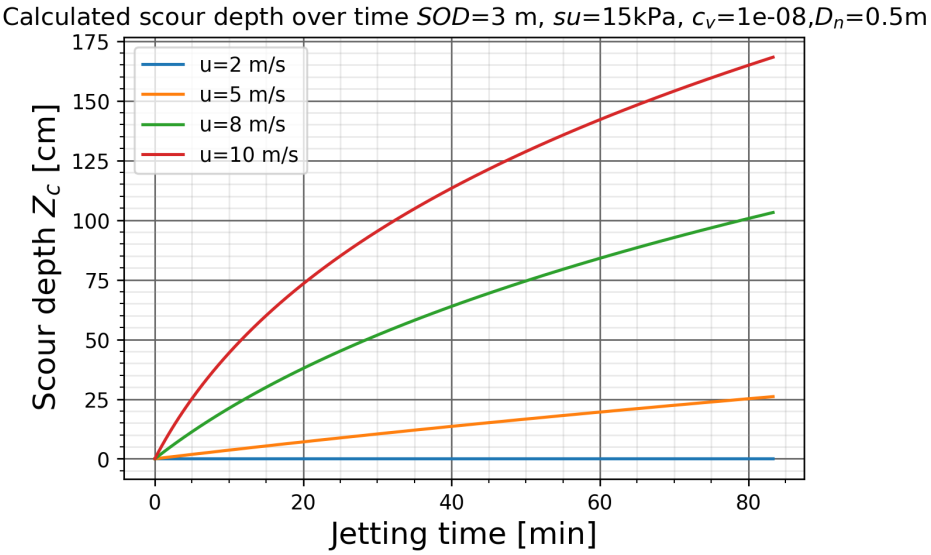

Figure 6.16: Scaled scour depth development over time for varying flow velocity at the nozzle u_0

In figure 6.17 the effect of the consolidation coefficient on the erosion velocity can be observed. The plotted range for the consolidation coefficients is partially outside the tested range. A larger consolidation coefficient leads to a larger erosion rate, however in this model; eventually the lines will go to the same scour depth Z_c, as the p_{stag}/su ratio's are the same. The depth increase will stop when a p_{stag}/su ratio of 0.2 is reached.

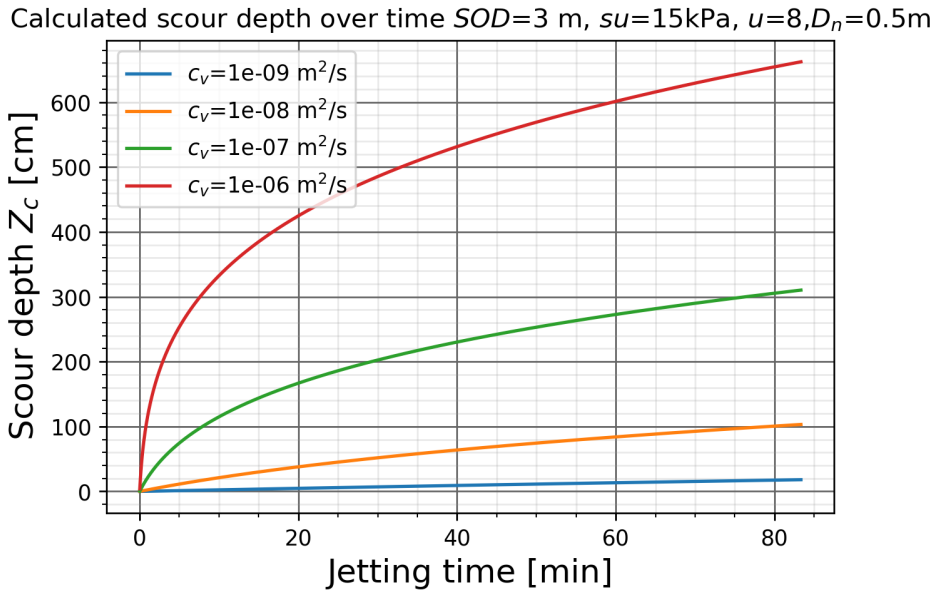

Figure 6.17: Scaled scour depth development over time for varying consolidation coefficients c_v

For the same range of consolidation coefficients as in figure 6.17 the production over time is calculated and plotted against the jetting time in figure 6.18.

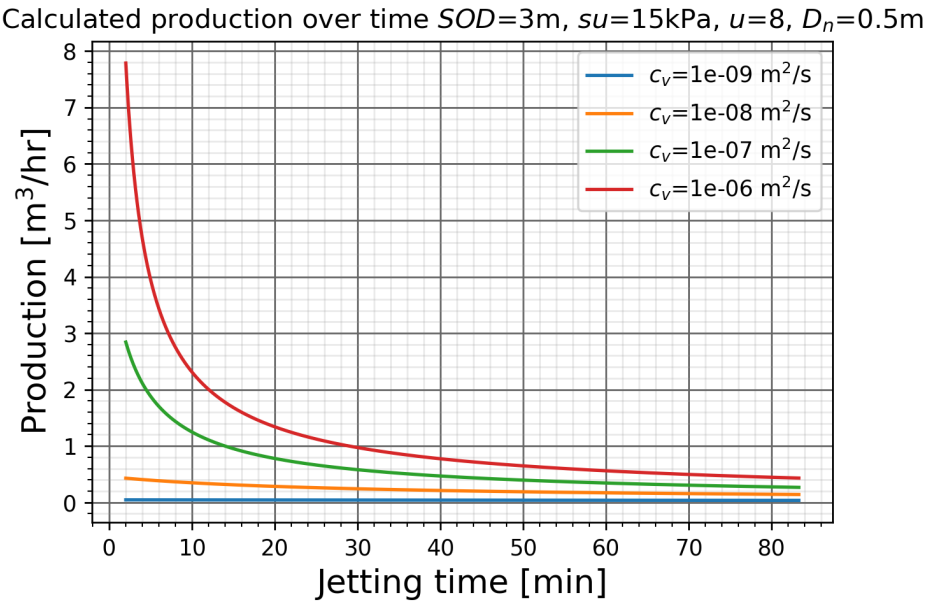

Figure 6.18: Scaled production ranges developing over time for varying consolidation coefficients c_v

In this model there are still uncertainties, since the model is optimised on data with a certain accuracy. A big uncertainty within this model comes from the determination of the consolidation coefficient c_v, as mentioned before this value is hard to determine with high accuracy. The average uncertainty in the determination of that value was approximately 30%. As also in figure 6.13, most of the data points are within the $\pm$35% error margin. Therefore an error margin of at least 35% should be taken into account for the production estimations.
The model is only tested on relatively homogeneous and uniform clay samples. As discussed before, natural variation and disturbances in the clay structure such as gravel and sand can have a significant influence on the erosion behaviour, such that fracturing of the soil occurs more rapidly. These effects are excluded from the tests. Therefore the expected production rates are assumed to be on the conservative side.

7

Conclusions and Recommendations

In this chapter, the main conclusions and recommendations of this study are presented. The main goal of this research was to quantify and be able to predict the production of a mass flow jet on cohesive soils. The main research question will be answered using the supporting sub-questions.

7.1. Conclusions

Erosion mechanism

The exact erosion process is still unknown; however some conclusions can be drawn regarding the erosion process.

- The erosion process is likely a drained process for a large part of the tests. This can be concluded based on the calculated Pèclet number of pore water dissipation being smaller than 1 for a large part of the tests. This conclusion is also supported by the visual observations of the tests; at the start, larger chunks of material were eroded from the sample, which indicates mass erosion. As as the tests progressed the typical size of the eroded material becomes in the order of millimeters, corresponding to floc erosion.
- Based on the assumption that the pressure variation due to turbulence of the jet is comparable to the bed shear stress distribution for a wall jet as given in 2.9, it is possible for mass erosion to occur at mean jet stagnation pressures smaller than 2. However, as the test progresses, the reduction in the probability of pressure peak in the stagnation pressure of $p_{stag}/su > 2$ is not proportional to the reduction in the erosion rate. Therefore it is concluded that mass erosion is not the governing process during the full length of the test.
- Erosion is observed for stagnation pressures smaller than two times the undrained shear strength. Which also corresponds with the conclusion of a drained process taking place.
- It is possible for fracturing to occur, and fracturing could possibly explain the erosion velocity development. However, in the fracturing theory, a lot of assumptions need to be made regarding the number of micro-cracks and the radius of the micro-cracks present in the soil structure. These are not typically obtained soil parameters; this makes it harder to quantify the fracturing theory. Furthermore, the internal fracturing theory does not scale well with the consolidation coefficient c_v.
- The erosion velocity over time of these tests can not directly be related to the exerted bed shear stress and the bed swelling theory as developed for uniform channel flow. The calculated bed shear stresses are too low to account for the erosion rates.

Influence of the soil and jet parameters on the erosion process

- A quadratic relationship is found between the erosion velocity and the p_{stag}/su ratio. An explanation for this relation could be the soil response due to loading for small values of time.

- It has been found that the erosion speed is mainly influenced by the ratio of p_{stag}/su, independent of the standoff distance and nozzle diameter.
- The the ratio of SOD/D_n does have an influence on the erosion velocity. Larger SOD/D_n ratio's (in the region of fully developed flow) result in lower erosion velocity for the same p_{stag}/su ratio's. Since the erosion process is still not fully understood, it is difficult to assess what influences this reduction in erosion rate. However, it is assumed that it is related to the uncertainty in the entrainment coefficient and the discharge coefficient of the jet.

Influence of the consolidation coefficient c_v on the erosion process at $p_{stag}/su < 2$

- The erosion velocity and the consolidation coefficient are positively correlated. It is found that the consolidation coefficient does affect the erosion velocity. A higher value of the consolidation coefficient results in a higher erosion velocity. A high consolidation coefficient means that a soil is more permeable and/or less compressible than for lower values of the consolidation coefficient. In a swelling soil, the higher consolidation coefficient means that the soil strength drops more quickly from the undrained shear strength towards the drained shear strength.

Production estimation of mass flow jets in cohesive soils

Based on the findings of the sub-questions an empirical model to estimate the erosion velocity and production rates is set up.
The erosion velocity and depth can be approximated based on the ratio p_{stag}/su and the consolidation coefficient c_v as follows:

$$a \cdot (p_{stag}/su)^b \propto \frac{v_e}{c_v} \tag{7.1}$$

With a being 7800 and b being 2 for the clay samples in this study. This model has been tested against data of other studies.
It has been found that the scour volume can be linearly related to the radius of the impinging jet and the scour depth. Based on the scoured volume over time, an estimation of the production can be made. This model can then be used to estimate the production rates of large scale mass flow jets.

Often in engineering practices, only the undrained shear strength is reported in the soil investigation. It is recommended when a mass flow jet is going to be deployed for excavation in cohesive soils an estimation is made of the consolidation coefficient c_v, either ideally by performing an oedometer test, or otherwise using empirical estimations from Atterberg limits.

7.2. Recommendations

The tests in this study are all executed with uniform soils, which is considered to be a conservative approach, it is recommended to test the effect of disturbances/natural variations in the soil since it has been reported that variations in the soil structure can have a large impact on the erosion velocity.

Furthermore, an extra test using a large scale mass flow jet is recommended as validation for the model.

It is still unknown how the shear stress develops under an impinging jet in a scour hole. In the model based on the bed shear stress, several assumptions needed to be made to predict the shear stress exerted on the soil, these assumptions could be the source of the error between the calculated and observed depth.

A possible explanation for the erosion occurring at stagnation pressures lower than the undrained shear strength is that it could be due to the turbulence. In this study, the pressure distribution profile of a vertically impinging jet is assumed to be similar to the bed shear stress profile distribution for a plane wall jet. A better understanding of the jet pressure distribution and the turbulence in the jet and in a developing hole could give more certainty on whether mass erosion can occur.

Tests with a moving nozzle are recommended to test the effect of the movement on the bed, as the nozzle moves the flow pattern changes. With changing flow patterns, the erosion process could

change and also the erosion rates for moving low-pressure jets is still unknown.

For the tests executed in this study mainly the permeability of the clay, samples have been varied. Only a small range of compressibility m_v has been tested. A wider variety of compressibility should be tested to test whether the compressibility has a large influence on the erosion process.

Since it is still unknown whether soil fracturing occurs during the low-pressure excavation process, and on what scale it occurs. Parameter determination for the fracturing of the soil before testing could give more insight into whether this process occurs. Fracturing mechanisms such as plastic instability and shear fracturing could play a role in this erosion process; however, this should be investigated further in a follow-up study.

Bibliography

[1] F. A. Andrade, H. A. Al-Qureshi, and D. Hotza. Measuring the plasticity of clays: A review, 1 2011. ISSN 01691317.

[2] Chita Ranjan Ariathurai. *A finite element model for sediment transport in estuaries*. University of California, Davis., 1974.

[3] Akira Asaoka. Observational procedure of settlement prediction. *Soils and Foundations*, 18(4): 87–101, 1978. doi: 10.3208/sandf1972.18.4{_}87. URL http://joi.jlc.jst.go.jp/JST.Journalarchive/sandf1972/18.4_87?from=CrossRef.

[4] Reginald A Barron. Consolidation of fine-grained soils by drain wells. *Trans Am. Soc. Civil Engineering*, 143:718–754, 1948.

[5] S. Beltaos and N. Rajaratnam. Impingement of Axisymmetric Developing Jets. *Journal of Hydraulic Research*, 15(4):311–326, 10 1977. doi: 10.1080/00221687709499637. URL http://www.tandfonline.com/doi/abs/10.1080/00221687709499637.

[6] Jean-Louis Briaud, Iman Shafii, Hamn-Ching Chen, and Zenon Medina-Cetina. *Relationship Between Erodibility and Properties of Soils*. Transportation Research Board, Washington, DC, 11 2019. ISBN 978-0-309-49354-3. doi: 10.17226/25470. URL https://www.nap.edu/catalog/25470/relationship-between-erodibility-and-properties-of-soils.

[7] Chuanming Dong, Guoliang Yu, Huaixin Zhang, and Minxi Zhang. Scouring by submerged steady water jet vertically impinging on a cohesive bed. *Ocean Engineering*, 2019. ISSN 00298018. doi: 10.1016/j.oceaneng.2019.106781.

[8] I.S. Dunn. Tractive Resistance of Cohesive Channels. *Journal of the Soil Mechanics and Foundations Division*, 85(3):1–24, 1959. URL https://cedb.asce.org/CEDBsearch/record.jsp?dockey=0011793.

[9] C.J. Dykstra and A.J. Joling. Praktijkwaarde consolidatiecoefficient bepaald met asaoka-methode, 2001. URL https://issuu.com/uitgeverijeducom/docs/geo_jrg_0502_2001_def_april.

[10] Robin Fell, Gregory Hanson, Gontran Herrier, Didier Marot, and Tony Wahl. Relationship between the erosion properties of soils and other parameters, 2013.

[11] Hugo B. Fischer, E. John List, Robert C.Y. Koh, Jörg Imberger, and Norman H. Brooks. *Mixing in inland and coastal waters*. Academic Press, 1979. ISBN 9780080511771. doi: https://doi.org/10.1016/C2009-0-22051-4. URL https://www.sciencedirect.com/book/9780080511771/mixing-in-inland-and-coastal-waters#book-description.

[12] G J Hanson and K R Cook. Apparatus, test procedures, and analytical methods to measure soil erodibility in situ. *Applied engineering in agriculture*, 20(4):455, 2004.

[13] Joseph Delbert Hedges. The Scour of Cohesive Soils By An Inclined Submerged Water Jet. Technical report, Texas A&M University, 1990. URL https://apps.dtic.mil/docs/citations/ADA223971.

[14] Bas Hofland and Jurjen A Battjes. Probability density function of instantaneous drag forces and shear stresses on a bed. *Journal of Hydraulic Engineering*, 132(11):1169–1175, 2006. ISSN 0733-9429.

[15] M. Hollick. Towards a Routine Test for the Assessment of the Critical Tractive Forces of Cohesive Soils. *Transactions of the ASAE*, 19(6):1076–1081, 1976. doi: 10.13031/2013.36179. URL http://elibrary.asabe.org/abstract.asp??JID=3&AID=36179&CID=t1976&v=19&i=6&T=1.

[16] Walter Jacobs. *Sand-mud erosion from a soil mechanical perspective*. PhD thesis, Delft University of Technology, 2011.

[17] M Jamiolkowki. New developments in field and laboratory testing of soils. In *International conference on soil mechanics and foundation engineering. 11*, pages 57–153, San Francisco, 1985.

[18] J. W. Kamphuis. Influence du sable ou du gravier dans l'érosion de sediments cohésifs. *Journal of Hydraulic Research*, 28(1):43–53, 1990. ISSN 00221686. doi: 10.1080/00221689009499146.

[19] Bob Kerssens. Mass Flow Excavation Of A Cohesive Soil. Technical report, Delft University of Technology, Delft, 2017.

[20] Charles C Ladd. Stability evaluation during staged construction. *Journal of geotechnical engineering*, 117(4):540–615, 1991. ISSN 0733-9410.

[21] M Marchi, G Gottardi, and K Soga. Fracturing pressure in clay. *Journal of Geotechnical and Geoenvironmental Engineering*, 140(2):04013008, 2013. ISSN 1090-0241.

[22] Kerry Anne Mazurek. *Scour of Clay by Jets*. PhD thesis, University of ALberta, 2001.

[23] Florian Mercier. Numerical Modelling Of Erosion Of A Cohesive Soil By A Turbulent Flow. Technical report, Aix-Marseille Université, Marseille, 2013. URL https://tel.archives-ouvertes.fr/tel-00978589.

[24] JK Mitchell and K Soga. *Fundamentals of soil behavior*. John Wiley & Sons Inc., New Jersey, third edition edition, 2005. URL http://sutlib2.sut.ac.th/sut_contents/H93569.pdf.

[25] Walter L Moore and Frank D Masch Jr. Experiments on the scour resistance of cohesive sediments. *Journal of Geophysical Research*, 67(4):1437–1446, 1962. ISSN 0148-0227.

[26] NAVFAC. 7.1: Soil Mechanics Design Manual. *Department of the Navy, Naval Facilities Engineering Command, Alexandria, VA, USA*, 1982.

[27] Arnold Johannes Nobel. *On the excavation process of a moving vertical jet in cohesive soil*. PhD thesis, Delft University of Technology, Delft, 2013.

[28] Shinnosuke Obi, Keita Inoue, Takayuki Furukawa, and Shigeaki Masuda. Experimental study on the statistics of wall shear stress in turbulent channel flows. *International journal of heat and fluid flow*, 17(3):187–192, 1996. ISSN 0142-727X.

[29] Emmanuel Partheniades. Erosion and deposition of cohesive soils. *Journal of the Hydraulics Division*, 91(1):105–139, 1965.

[30] PIANC. Classification of Soils and Rocks to be dredged. Technical report, PIANC, Brussels, 1984.

[31] Michael Poreh, Y G Tsuei, and Jack E Cermak. Investigation of a turbulent radial wall jet. *Journal of Applied Mechanics*, 34(2):457–463, 1967. ISSN 0021-8936.

[32] N. Rajaratnam. *Turbulent jets*. Elsevier Scientific Pub. Co, Amsterdam, 1976. ISBN 9780080869964. URL https://books.google.nl/books?hl=nl&lr=&id=g3R4gFObzloC&oi=fnd&pg=PP1&dq=rajatnam+1976+&ots=RsEVri6dW4&sig=WhWCrckWZt09vISbWRwCPhOGZWc#v=onepage&q=rajatnam%201976&f=false.

[33] Ernest T Smerdon and Robert Patrick Beasley. *The tractive force theory applied to stability of open channels in cohesive soils*. University of Missouri, College of Agriculture, Agricultural Experiment Station, 1959.

[34] K Soga, M Y A Ng, and K Gafar. Soil fractures in grouting. In *11th International Conference on Computer Methods and Advances in Geomechanics; Prediction, Analysis and Design in Geomechanical Applications*, volume 4, pages 397–406. Patron Editore, 2005.

[35] K Terzaghi. *Theoretical Soil Mechanics*. John Wiley & Sons Inc., New York, 1943. ISBN 9780470172766. doi: 10.1002/9780470172766.

[36] Cornell University. *Soil solidification research, Cornell University, 1946 to 1951; final report.* Ithaca, N. Y., 1951. URL //catalog.hathitrust.org/Record/009205959//catalog.hathitrust.org/Record/009205959//catalog.hathitrust.org/Record/009205959//catalog.hathitrust.org/Record/009205959.

[37] G.L.M. van der Schrieck. *Dredging Technology*. GLM van der Schrieck BV, Aerdenhout, 2016.

[38] B C Van Prooijen and J C Winterwerp. A stochastic formulation for erosion of cohesive sediments. *Journal of Geophysical Research: Oceans*, 115(C1), 2010. ISSN 2156-2202.

[39] C. van Rhee. Sediment Entrainment at High Flow Velocity. *Journal of Hydraulic Engineering*, 136 (9):572–582, 9 2010. ISSN 0733-9429. doi: 10.1061/(ASCE)HY.1943-7900.0000214. URL http://ascelibrary.org/doi/10.1061/%28ASCE%29HY.1943-7900.0000214.

[40] A. Verruijt. *Soil Mechanics*. Delft University of Technology, Delft, 2012. URL https://www.plaxis.com/content/uploads/import/kb/kb-publications/Verruijt%202010%20-%20SoilMechBook.pdf.

[41] George B Wallace and William C Otto. Differential settlement at selfridge air force base. *Journal of the Soil Mechanics and Foundations Division*, 90(5):197–220, 1964.

[42] R.J.S. Whitehouse, R.L. Soulsby, W. Roberts, and H.J. Mitchener. Dynamics of estuarine muds. Technical report, 2000.

[43] J C Winterwerp, W G M Kesteren, B Prooijen, and W Jacobs. A conceptual framework for shear flow–induced erosion of soft cohesive sediment beds. *Journal of Geophysical Research: Oceans*, 117(C10), 2012. ISSN 2156-2202.

[44] Johan C Winterwerp and Walther G M Van Kesteren. *Introduction to the physics of cohesive sediment dynamics in the marine environment*, volume 56. Elsevier, 2004. ISBN 0080473733.

[45] C P Wroth and D M Wood. The correlation of index properties with some basic engineering properties of soils. *Canadian Geotechnical Journal*, 15(2):137–145, 1978. ISSN 0008-3674.

List of Figures

List of Tables

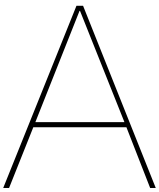

Consolidation Measurements and Coefficient of Consolidation determination for tests executed in this study

		Direct consolidation				Oedometer (Consolidation) - Stage 1				Oedometer (Consolidation) - Stage 2				Oedometer (Swell)				Oedometer (re-Consolidation) - Stage 3				Oedometer (re-Consolidation) - Stage 3			
Clay Sample #NO	**Mixture**	**Method**	**cv**	**mv [m^2/kN]**	**k [m/s]**	**Method**	**cv**	**mv [m^2/kN]**	**k [m/s]**	**Method**	**cv**	**mv [m^2/kN]**	**k [m/s]**	**Method**	**cv**	**mv [m^2/kN]**	**k [m/s]**	**Method**	**cv**	**mv [m^2/kN]**	**k [m/s]**	**Method**	**cv**	**mv [m^2/kN]**	**k [m/s]**
5	Kaolin (s)	Log(t)	3.38E-07	5.83E-03	1.97E-06																				
		Osaka	3.39E-07																						
		sqrt(t)	3.48E-07																						
		Average	**3.42E-07**																						
6	5% Bentonite	Log(t)	4.42E-08	2.52E-03	1.11E-07	Log(t)	8.18E-08	1.45E-03	1.19E-07					Log(t)	5.85E-08	1.80E-04	1.05E-08								
1.4 stag/su		Osaka	4.49E-08			Osaka	8.28E-08							Osaka	5.92E-08										
		sqrt(t)	4.57E-08			sqrt(t)	8.49E-08							sqrt(t)	6.07E-08										
		Average	**4.49E-08**			Average	**8.31E-08**							Average	**5.95E-08**										
7	10% Bentonite	Log(t)	4.01E-08	3.68E-03	1.48E-07	Log(t)	6.46E-08	1.70E-03	1.10E-07	Log(t)	1.84E-07	1.39E-03	2.56E-07	Log(t)	2.43E-08	2.00E-04	4.86E-09	Log(t)	3.10E-07	1.08E-03	3.36E-07				
1.4 stag/su		Osaka	4.09E-08			Osaka	6.55E-08			Osaka	1.86E-07			Osaka	2.46E-08			Osaka	3.14E-07						
		sqrt(t)	4.17E-08			sqrt(t)	6.72E-08			sqrt(t)	1.9E-07			sqrt(t)	2.52E-08			sqrt(t)	3.21E-07						
		Average	**4.09E-08**			Average	**6.57E-08**			Average	**1.87E-07**			Average	**2.47E-08**			Average	**3.15E-07**						
8	5% Bentonite	Log(t)	2.19E-08	2.10E-03	4.60E-08	Log(t)	5.20E-08	1.22E-03	6.36E-08	Log(t)	1.34E-07	1.01E-03	1.36E-07	Log(t)	2.16E-08	1.45E-04	3.12E-09	Log(t)	2.53E-07	0.000792	2.00332E-07				
0.4 stag/su		Osaka	2.25E-08			Osaka	5.27E-08			Osaka	1.36E-07			Osaka	1.83E-08			Osaka	2.56E-07	0	0				
		sqrt(t)	2.31E-08			sqrt(t)	5.39E-08			sqrt(t)	1.39E-07			sqrt(t)	2.24E-08			sqrt(t)	2.63E-07	0	0				
		Average	**2.25E-08**			Average	**5.29E-08**			Average	**1.36E-07**			Average	**2.07E-08**			Average	**2.57E-07**						
9	Kaolin	Log(t)	1.25E-07	2.63E-03	3.29E-07																				
*		Osaka	1.27E-07																						
		sqrt(t)	1.30E-07																						
		Average	**1.27E-07**																						
10	Kaolin (s)	Log(t)	1.75E-07	3.39E-03	5.92E-07	Log(t)	4.80E-07	7.39E-03	3.55E-06	Log(t)	4.62E-07	4.25E-03	1.97E-06	Log(t)	1.36E-07	3.68E-04	5.02E-08								
		Osaka	1.79E-07			Osaka	4.90E-07			Osaka	4.68E-07			Osaka	1.36E-07										
		sqrt(t)	1.81E-07			sqrt(t)	5.01E-07			sqrt(t)	4.80E-07			sqrt(t)	1.39E-07										
		Average	**1.78E-07**			Average	**4.90E-07**			Average	**4.70E-07**			Average	**1.37E-07**										
11	15% Bentonite	Log(t)	5.65E-08	3.62E-03	2.04E-07	Log(t)	1.09E-07	1.63E-03	1.78E-07	Log(t)	1.77E-07	1.31E-03	2.31E-07	Log(t)	2.21E-08	2.93E-04	6.47E-09	Log(t)	2.68E-07	9.88E-04	2.64E-07				
0.6		Osaka	5.69E-08			Osaka	1.10E-07			Osaka	1.79E-07			Osaka	2.24E-08			Osaka	2.72E-07						
		sqrt(t)	5.69E-08			sqrt(t)	1.12E-07			sqrt(t)	1.83E-07			sqrt(t)	2.29E-08			sqrt(t)	2.78E-07						
		Average	**5.68E-08**			Average	**1.10E-07**			Average	**1.80E-07**			Average	**2.25E-08**			Average	**2.73E-07**						
12	15% Bentonite	Log(t)	5.04E-08	2.95E-03	1.49E-07																				
0.6_2		Osaka	5.09E-08																						
		sqrt(t)	5.23E-08																						
		Average	**5.12E-08**																						
13	25% Bentonite	Log(t)	8.43E-08	3.56E-03	3.00E-07	Log(t)	8.18E-08	2.19E-03	1.79E-07					Log(t)	2.94E-08	2.27E-04	6.67E-09	Log(t)	6.48E-08	2.66E-03	1.73E-07	Log(t)	4.71E-08	1.77E-03	8.33E-08
0.6		Osaka	8.54E-08			Osaka	4.30E-08							Osaka	2.97E-08			Osaka	6.55E-08			Osaka	3.89E-08		
		sqrt(t)	8.75E-08			sqrt(t)	8.49E-08							sqrt(t)	3.04E-08			sqrt(t)	6.72E-08			sqrt(t)	4.87E-08		
		Average	**8.57E-08**			Average	**6.99E-08**							Average	**2.98E-08**			Average	**6.58E-08**			Average	**4.49E-08**		
14	Kaolin	Log(t)	4.68E-08	3.40E-03	1.59E-07	Log(t)	6.69E-08	1.80E-03	1.20E-07					Log(t)	2.12E-08	4.03E-04	8.54E-09								
0.4 stag/su		Osaka	4.78E-08			Osaka	6.67E-08							Osaka	2.15E-08										
		sqrt(t)	4.89E-08			sqrt(t)	6.95E-08							sqrt(t)	2.20E-08										
		Average	**4.79E-08**			Average	**6.77E-08**							Average	**2.15E-08**										
15	Kaolin	Log(t)	2.90E-08	3.87E-03	1.12E-07																				
		Osaka	2.94E-08																						
		sqrt(t)	3.01E-08																						
		Average	**2.95E-08**																						
16	Kaolin	Log(t)	3.74E-08	3.22E-03	1.20E-07																				
		Osaka	3.78E-08																						
		sqrt(t)	3.87E-08																						
		Average	**3.80E-08**																						
17	Kaolin_Sand	Log(t)	1.71E-07	2.52E-03	4.31E-07	Log(t)	1.64E-07	1.76E-03	2.89E-07					Log(t)	9.46E-08	1.34E-04	1.27E-08	Log(t)	1.73E-07	2.48E-03	4.30E-07	Log(t)	3.47E-07	2.74E-03	9.49E-07
		Osaka	1.74E-07			Osaka	1.67E-07							Osaka	9.59E-08			Osaka	1.76E-07			Osaka	3.57E-07		
		sqrt(t)	1.79E-07			sqrt(t)	1.71E-07							sqrt(t)	9.82E-08			sqrt(t)	1.81E-07			sqrt(t)	3.60E-07		
		Average	**1.75E-07**			Average	**1.67E-07**							Average	**9.62E-08**			Average	**1.77E-07**			Average	**3.55E-07**		
18	Kaolin	Log(t)	3.13E-08	2.94E-03	9.20E-08																				
		Osaka	3.31E-08																						
		sqrt(t)	3.38E-08																						
		Average	**3.27E-08**																						
19	Kaolin	Log(t)	1.52E-08	2.95E-03	4.49E-08	Log(t)	7.80E-08	2.53E-03	1.97E-07																
		Osaka	1.55E-08			Osaka	7.89E-08																		
		sqrt(t)	1.60E-08			sqrt(t)	8.06E-08																		
		Average	**1.56E-08**			Average	**7.92E-08**																		

A.1. Direct consolidation measurements

Table A.1: Direct consolidation sample 5

Direct consolidation [mm] sample:			5	Kaolin		
cons. loc 1	cons. loc 2	cons. loc 3	cons. loc 4	Avg. Cons.	DateTime	Hours
0	0	0	0	4.3375	9/5/2019 15:27	0.0
0.06	-0.05	0.3	0.14	4.45	9/5/2019 15:38	0.2
0.3	2.3	2.68	0.44	5.7675	9/5/2019 16:05	0.6
0.78	3.8	4.14	0.64	6.6775	9/5/2019 16:20	0.9
0.45	4.8	5.77	0.86	7.3075	9/5/2019 16:40	1.2
0.9	6.56	7.55	0.94	8.325	9/5/2019 17:01	1.6
0.97	7.41	8.18	1.16	8.7675	9/5/2019 17:18	1.8
0.9	7.95	9	1.19	9.0975	9/5/2019 17:34	2.1
1.59	16.03	26.15	9.54	17.665	9/6/2019 9:14	17.8
4.37	15.5	26.25	12.09	18.89	9/6/2019 12:08	20.7
4.39	15.37	26.3	12.14	18.89	9/6/2019 13:01	21.6
4.42	15.3	26.42	12.44	18.9825	9/6/2019 14:52	23.4
4.45	15.33	26.15	12.69	18.9925	9/6/2019 16:48	25.3
5.14	15.35	26.2	13.19	19.3075	9/9/2019 9:09	89.7
5.15	15.85	26.7	13.44	19.6225	9/11/2019 14:10	142.7
5.4	15.85	26.9	13.89	19.8475	9/13/2019 9:26	186.0

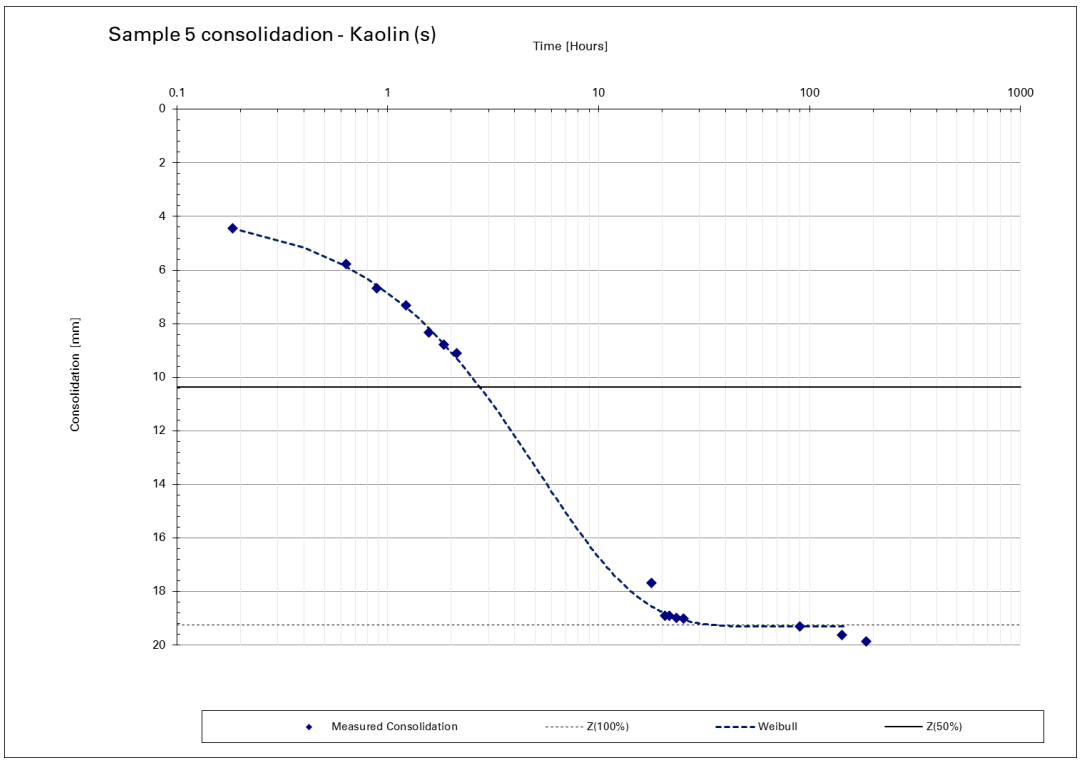

Figure A.1: Direct consolidation measurement graph sample 5

Table A.2: Direct consolidation sample 6 - 5% Bent

Direct consolidation [mm] sample:			6	5% Bent.		
cons. loc 1	cons. loc 2	cons. loc 3	cons. loc 4	Avg. Cons.	DateTime	Hours
0	0	0	0	4.71	9/11/2019 14:29	0.0
0.1	-0.04	0.03	0.2	4.79	9/11/2019 14:37	0.1
0.35	-0.12	0.3	0.3	4.92	9/11/2019 14:51	0.4
1.4	3.4	0.87	-2.4	5.53	9/11/2019 15:42	1.2
1.3	3.4	-0.02	-1.8	5.43	9/11/2019 16:29	2.0
1.3	3.5	0.55	-1.25	5.74	9/11/2019 17:38	3.1
1.4	5.12	5.35	2.43	8.29	9/12/2019 9:32	19.0
2.4	5.8	6.1	2.8	8.99	9/12/2019 13:17	22.8
1.58	6.25	6.6	3.2	9.12	9/12/2019 16:34	26.1
2.15	7.05	7.9	4.18	10.03	9/13/2019 9:20	42.8
2.2	7.07	8.03	4	10.04	9/13/2019 12:06	45.6
2.3	7.2	8.1	4.4	10.21	9/13/2019 16:40	50.2
2.8	8.25	9.05	5.07	11.01	9/16/2019 9:20	114.8
3	8.2	9.05	5.1	11.05	9/16/2019 17:17	122.8
3.3	8.55	9.4	5.35	11.36	9/18/2019 9:17	162.8
3.3	8.55	9.5	5.35	11.39	9/18/2019 16:51	170.4
3.36	8.72	9.64	5.15	11.43	9/19/2019 10:27	188.0
3.97	9	9.85	5.65	11.83	9/20/2019 11:05	212.6
4.08	9.02	9.95	5.88	11.95	9/24/2019 9:34	307.1
3.95	9.17	9.95	6	11.98	9/25/2019 10:16	331.8
4.02	9.2	10.1	5.75	11.98	9/27/2019 9:09	378.7
4.06	9.2	10.05	5.97	12.03	9/30/2019 14:19	455.8
4.1	9.25	10.25	5.83	12.07	10/1/2019 9:20	474.8

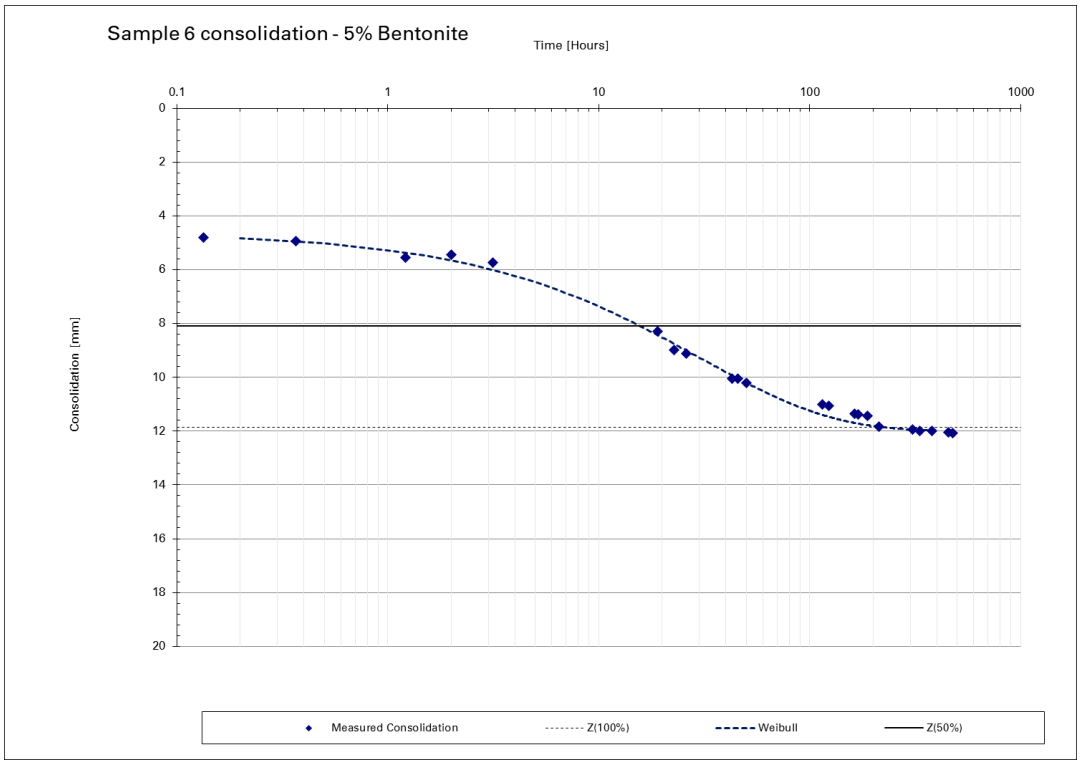

Figure A.2: Direct consolidation measurement graph sample 6 - 5% Bent.

Table A.3: Direct consolidation sample 7 - 10% Bent

Direct consolidation [mm] sample:			7	10% Bent.		
cons. loc 1	cons. loc 2	cons. loc 3	cons. loc 4	Avg. Cons.	DateTime	Hours
0	0	0	0	4.53	9/12/2019 10:11	0.00
0.28	0.4	0.87	0.45	5.03	9/12/2019 10:32	0.35
0.28	0.6	2	1	5.50	9/12/2019 11:21	1.17
0.26	1.53	3.15	1.5	6.14	9/12/2019 13:12	3.02
0.58	2.82	5.55	1.95	7.25	9/12/2019 16:38	6.45
2.75	8.85	4.9	2.45	9.26	9/13/2019 9:14	23.05
3.98	8.85	8.4	2.87	10.55	9/13/2019 12:00	25.82
5.15	8.95	9.04	3.9	11.29	9/13/2019 16:34	30.38
9.66	10.69	9.35	7.2	13.75	9/16/2019 9:17	95.10
10.03	11.08	9.65	7.95	14.20	9/16/2019 17:20	103.15
10.5	11.35	10.06	7.7	14.43	9/18/2019 9:12	143.02
10.55	11.39	9.92	8.05	14.50	9/18/2019 15:41	149.50
11.29	11.8	10.2	8.45	14.96	9/19/2019 16:35	174.40
11.48	11.95	10.6	8.75	15.22	9/20/2019 10:49	192.63
11.68	12.03	10.4	8.84	15.26	9/24/2019 9:30	287.32
11.83	12.1	10.42	8.81	15.32	9/25/2019 11:46	313.58
11.78	12.25	10.3	8.79	15.31	9/27/2019 8:59	358.80
12.3	12.3	10.85	8.9	15.61	9/30/2019 14:17	436.10
11.93	12.3	10.83	9.28	15.61	10/1/2019 9:31	455.33
11.93	12.34	10.87	9.15	15.60	10/3/2019 17:12	511.02

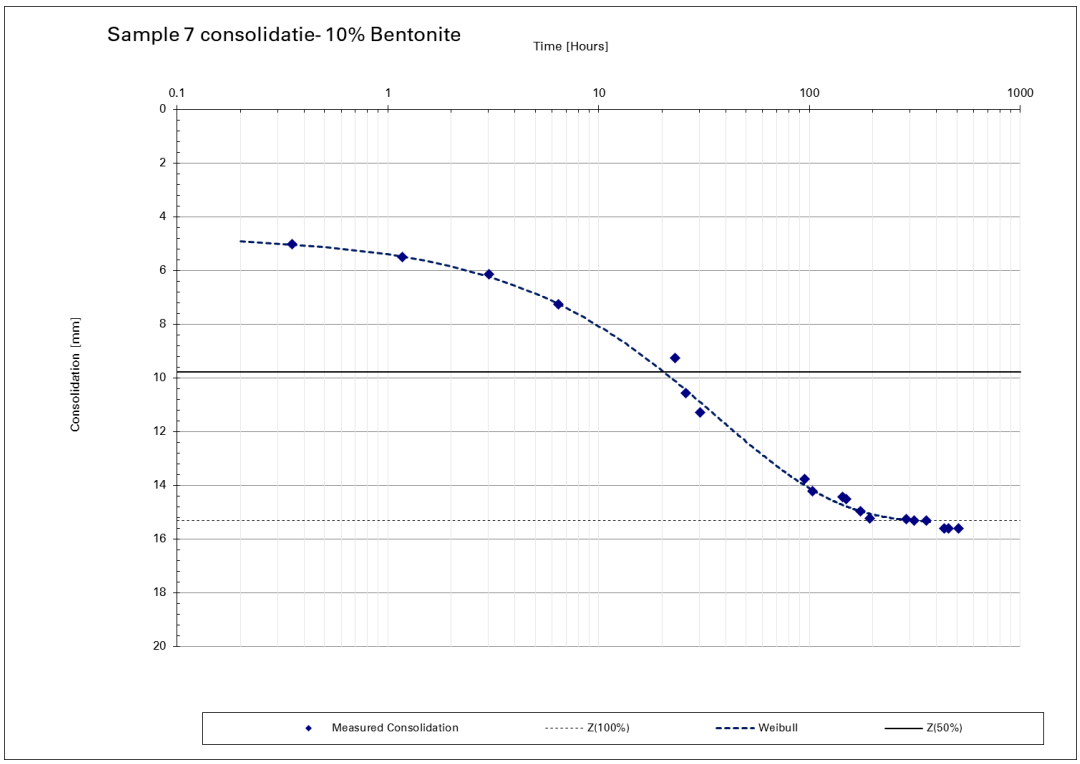

Figure A.3: Direct consolidation measurement graph sample 7 - 10% Bent.

Table A.4: Direct consolidation sample 8 - 5% Bent

Direct consolidation [mm] sample:			8	5% Bent.		
cons. loc 1	cons. loc 2	cons. loc 3	cons. loc 4	Avg. Cons.	DateTime	Hours
0	0	0	0	16.55	9/20/2019 10:46	0.00
-0.17	0	0.13	-0.2	16.49	9/20/2019 10:55	0.15
-0.17	0.01	0.58	-0.45	16.54	9/20/2019 11:10	0.40
-0.15	0.1	1.53	0.25	16.98	9/20/2019 12:54	2.13
-0.15	0.13	2.58	1.2	17.49	9/20/2019 15:34	4.80
0.05	0.13	3.4	1.55	17.83	9/20/2019 17:02	6.27
2.15	0.36	7.08	6.8	20.65	9/24/2019 9:23	94.62
2.35	0.36	7.63	7.3	20.96	9/25/2019 11:41	120.92
2.3	-0.02	8.13	7.75	21.09	9/27/2019 8:54	166.13
3	0.38	8.78	8.4	21.69	9/30/2019 14:12	243.43
2.93	0.26	8.66	8.95	21.75	10/1/2019 9:27	262.68
3.03	0.36	8.61	8.85	21.76	10/2/2019 17:09	294.38
3.05	0.13	8.66	8.95	21.75	10/3/2019 17:09	318.38
3.05	0.53	8.93	9	21.93	10/4/2019 17:26	342.67
3.35	0.33	9.08	9.3	22.07	10/7/2019 15:23	412.62
3.25	0.43	9.03	9.45	22.09	10/9/2019 13:54	459.13
3.15	0.25	9.25	9.55	22.10	10/11/2019 17:14	510.47
3.1	0.28	9.25	9.3	22.03	10/14/2019 10:33	575.78
3.25	0.11	9	9.28	21.96	10/18/2019 9:28	670.70
3.35	0.18	9.5	9.5	22.18	10/21/2019 9:37	742.85

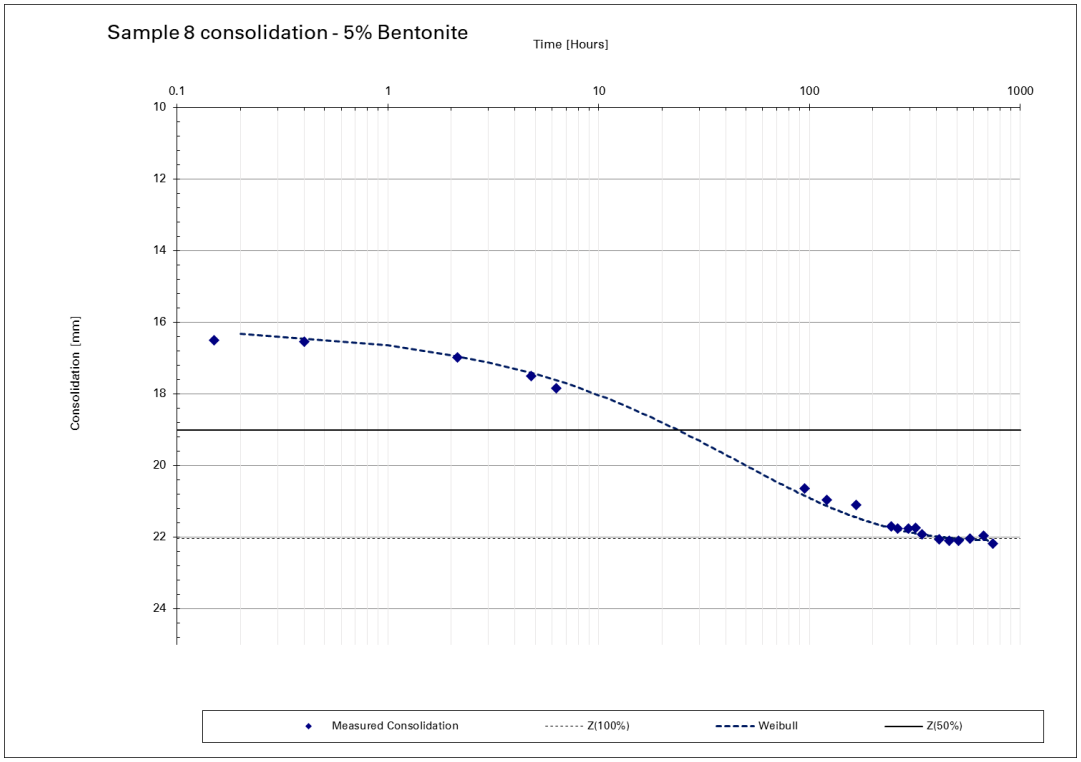

Figure A.4: Direct consolidation measurement graph sample 8 - 5% Bent.

Table A.5: Direct consolidation sample 9 - Kaolin

Direct consolidation [mm] sample:			9	Kaolin		
cons. loc 1	cons. loc 2	cons. loc 3	cons. loc 4	Avg. Cons.	DateTime	Hours
0	0	0	0	12.81	9/20/2019 9:55	0.00
0.05	0.1	1.2	0.65	13.31	9/20/2019 10:02	0.12
0.15	0.07	1	0.7	13.29	9/20/2019 10:14	0.32
0.35	-0.1	2.18	1.4	13.77	9/20/2019 10:34	0.65
0.15	0.14	2.22	1.8	13.89	9/20/2019 10:58	1.05
0.35	-0.08	2.69	2.35	14.14	9/20/2019 11:25	1.50
0.16	0.1	4.21	3.71	14.86	9/20/2019 12:51	2.93
0.6	0.12	5.78	5.75	15.88	9/20/2019 15:31	5.60
0.35	0.1	6.68	6.35	16.18	9/20/2019 17:05	7.17
3.9	0.52	11.18	14.15	20.25	9/24/2019 9:13	95.30
3.91	0.55	11.21	14.17	20.27	9/25/2019 9:27	119.53

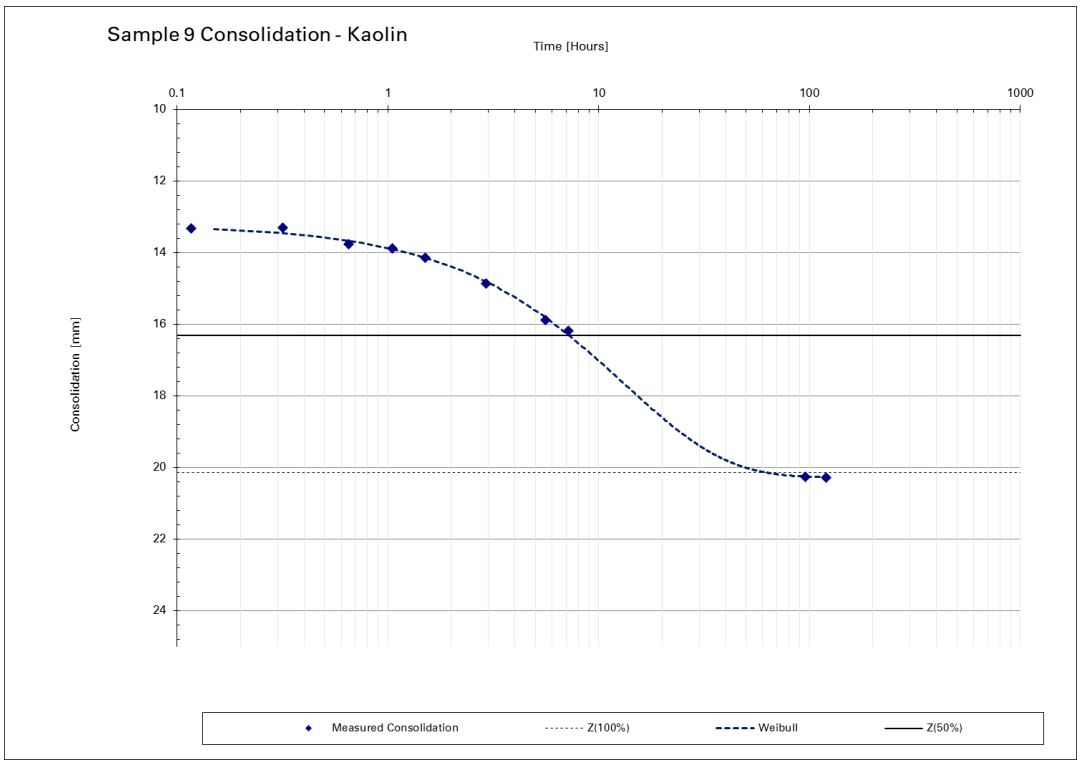

Figure A.5: Direct consolidation measurement graph sample 9 - Kaolin

Table A.6: Direct consolidation sample 10 - Kaolin (soft)

Direct consolidation [mm] sample:			10	Kaolin		
cons. loc 1	cons. loc 2	cons. loc 3	cons. loc 4	Avg. Cons.	DateTime	Hours
0	0	0	0	27.38	9/27/2019 8:51	0.00
0.08	0.72	-0.23	-0.05	27.51	9/27/2019 9:02	0.18
0.18	2	1.17	0.12	28.25	9/27/2019 9:25	0.57
0.25	3.1	1.87	0.22	28.74	9/27/2019 9:50	0.98
0.6	3.95	2.92	0.2	29.30	9/27/2019 10:19	1.47
0.47	5.2	4.02	0.3	29.88	9/27/2019 10:56	2.08
1.3	6.7	6.07	0.4	31.00	9/27/2019 12:04	3.22
1.18	8.1	7.17	0.95	31.73	9/27/2019 13:19	4.47
1.17	9	8.09	1.15	32.23	9/27/2019 14:23	5.53
0.98	9.7	9.42	1.1	32.68	9/27/2019 15:42	6.85
1.05	10.15	9.37	1.25	32.84	9/27/2019 16:48	7.95
2	14	13.27	1.85	35.16	9/30/2019 14:06	77.25
2.04	14.4	13.92	1.7	35.40	10/1/2019 9:24	96.55
2.03	14.72	15.47	0.98	35.68	10/2/2019 17:12	128.35
2.03	14.72	15.57	3.1	36.24	10/3/2019 17:05	152.23
1.82	14.95	15.63	3.15	36.27	10/4/2019 17:29	176.63
2.08	14.58	16.02	3.05	36.31	10/7/2019 9:24	240.55

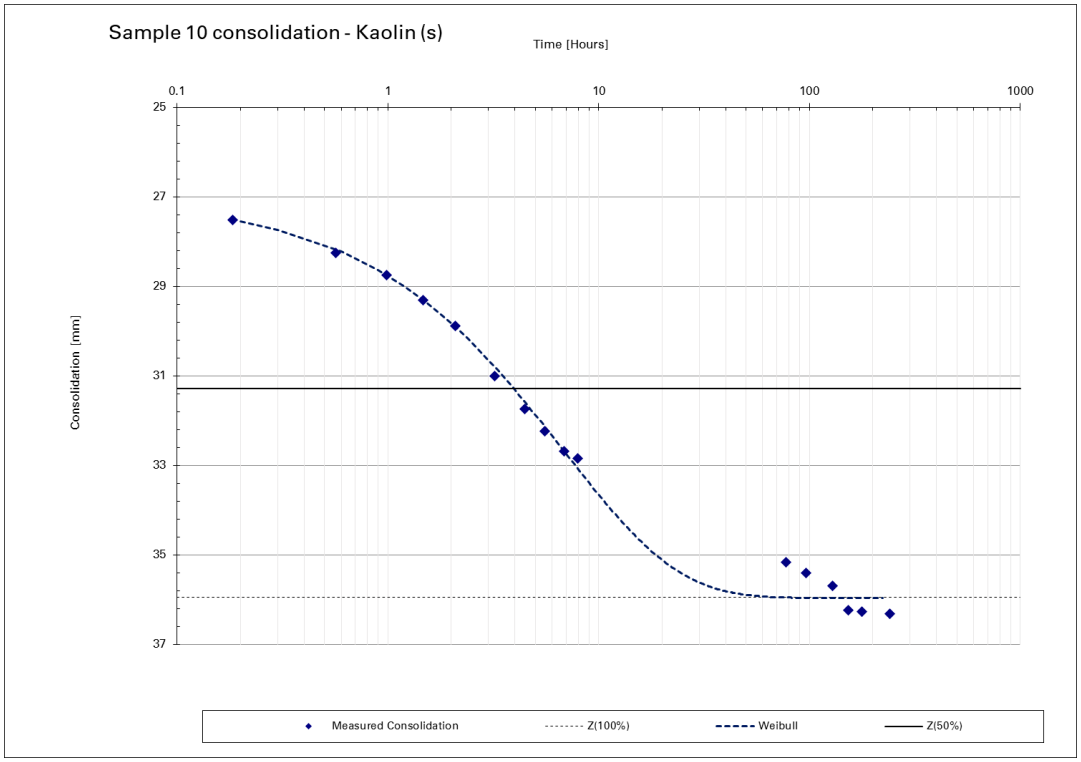

Figure A.6: Direct consolidation measurement graph sample 10 - Kaolin

Table A.7: Direct consolidation sample 11 - 15% Bent

Direct consolidation [mm] sample:			11	15% Bent.		
cons. loc 1	cons. loc 2	cons. loc 3	cons. loc 4	Avg. Cons.	DateTime	Hours
0	0	0	0	24.79	10/3/2019 14:51	0.00
26.96	0.65	0.25	0.35	31.85	10/3/2019 14:59	0.13
27.86	0.5	0.35	0.75	32.16	10/3/2019 15:13	0.37
28.93	1.05	0.15	1.25	32.64	10/3/2019 15:43	0.87
29.21	1.45	0.2	1.55	32.90	10/3/2019 16:19	1.47
29.96	2.05	0.2	1.85	33.31	10/3/2019 16:59	2.13
30.59	2.55	0.18	2.05	33.64	10/3/2019 17:41	2.83
36.93	7.05	0.92	5.02	37.27	10/4/2019 9:25	18.57
38.26	8.3	1.69	5.8	38.31	10/4/2019 17:23	26.53
40.26	10.9	5.42	7.67	40.86	10/7/2019 16:39	97.80
40.21	10.77	5.3	7.85	40.83	10/9/2019 13:26	142.58
40.23	10.85	5.42	8.12	40.95	10/11/2019 17:21	194.50
40.26	11.1	5.4	8.15	41.02	10/14/2019 12:01	261.17
40.21	10.8	5.68	7.93	40.95	10/18/2019 10:00	355.15
40.27	10.95	5.62	7.98	41.00	10/21/2019 16:06	433.25
40.31	11.08	5.64	7.86	41.02	10/22/2019 13:05	454.23
40.46	11	5.62	8.4	41.16	10/24/2019 9:22	498.52

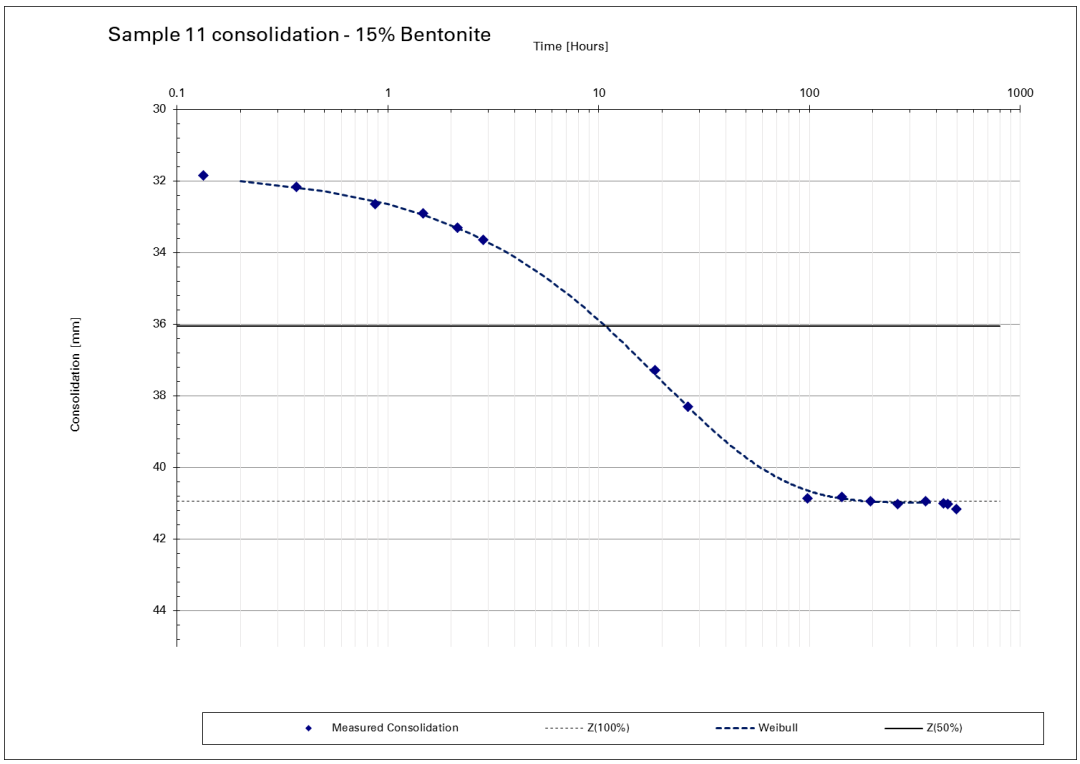

Figure A.7: Direct consolidation measurement graph sample 11 - 15% Bent.

Table A.8: Direct consolidation sample 12 - 15% Bent

Direct consolidation [mm] sample:			12	15% Bent.		
cons. loc 1	cons. loc 2	cons. loc 3	cons. loc 4	Avg. Cons.	DateTime	Hours
0	0	0	0	18.33	10/3/2019 16:16	0.00
0.2	0.03	1.1	0.25	18.72	10/3/2019 16:25	0.15
0.2	-0.1	1.35	1.05	18.95	10/3/2019 17:02	0.77
0	-0.35	2.3	1.45	19.18	10/3/2019 17:38	1.37
0.07	-0.35	9.4	8.43	22.71	10/4/2019 9:34	17.30
0.15	-0.15	11.2	10.05	23.64	10/4/2019 17:20	25.07
0.25	-0.35	16	14.25	25.86	10/7/2019 16:47	96.52
0.13	-0.23	16.4	14.8	26.10	10/9/2019 13:29	141.22
0.05	-0.25	17.25	15.05	26.35	10/11/2019 17:24	193.13
0.25	-0.14	17.2	15.45	26.52	10/14/2019 10:41	258.42
0.1	-0.25	17.05	15.25	26.36	10/18/2019 10:02	353.77
0.6	-0.32	17.22	15.33	26.53	10/21/2019 15:53	431.62
0.05	-0.37	17.12	15.47	26.39	10/22/2019 13:07	452.85
0.22	-0.49	17.3	15.36	26.42	10/25/2019 11:44	523.47

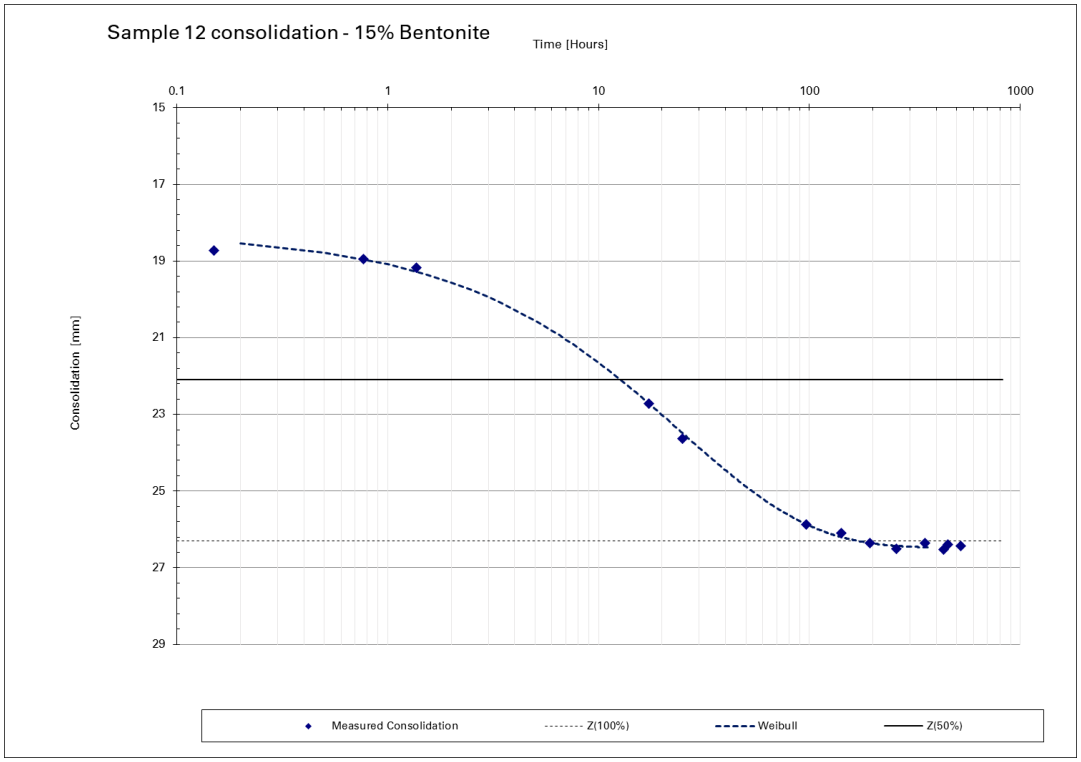

Figure A.8: Direct consolidation measurement graph sample 12 - 15% Bent.

Table A.9: Direct consolidation sample 13 - 25% Bent

Direct consolidation [mm] sample:			13	25% Bent.		
cons. loc 1	cons. loc 2	cons. loc 3	cons. loc 4	Avg. Cons.	DateTime	Hours
0	0	0	0	12.38	10/4/2019 9:18	0.00
0.2	0.17	0.25	-0.3	12.46	10/4/2019 9:29	0.18
-0.15	0.05	0.7	-0.05	12.51	10/4/2019 9:37	0.32
0	0.3	1.1	0.2	12.78	10/4/2019 9:43	0.42
0.05	0.4	1.45	-0.35	12.76	10/4/2019 9:56	0.63
0.05	1.25	1.9	-0.2	13.13	10/4/2019 10:21	1.05
0.07	1.3	2.3	-0.2	13.24	10/4/2019 10:43	1.42
0.1	3.82	4.45	-0.2	14.42	10/4/2019 13:30	4.20
0.05	6.4	6.9	0.1	15.74	10/4/2019 17:16	7.97
0	17.65	19.6	1.45	22.05	10/7/2019 16:51	79.55
0.1	18	18.85	1.7	22.04	10/9/2019 13:36	124.30
0.3	17.8	19.3	1.75	22.16	10/11/2019 17:18	176.00
0.45	17.68	19.15	1.58	22.09	10/14/2019 10:39	241.35
1.3	17.85	18.75	1.7	22.28	10/18/2019 9:56	336.63
1.58	17.95	19.75	1.62	22.60	10/21/2019 15:56	414.63
1.15	18.02	19.6	2.1	22.59	10/22/2019 13:10	435.87
0.35	18.19	19.23	2.05	22.33	10/25/2019 11:47	506.48
0.35	18.19	18.85	1.82	22.18	10/29/2019 9:07	599.82

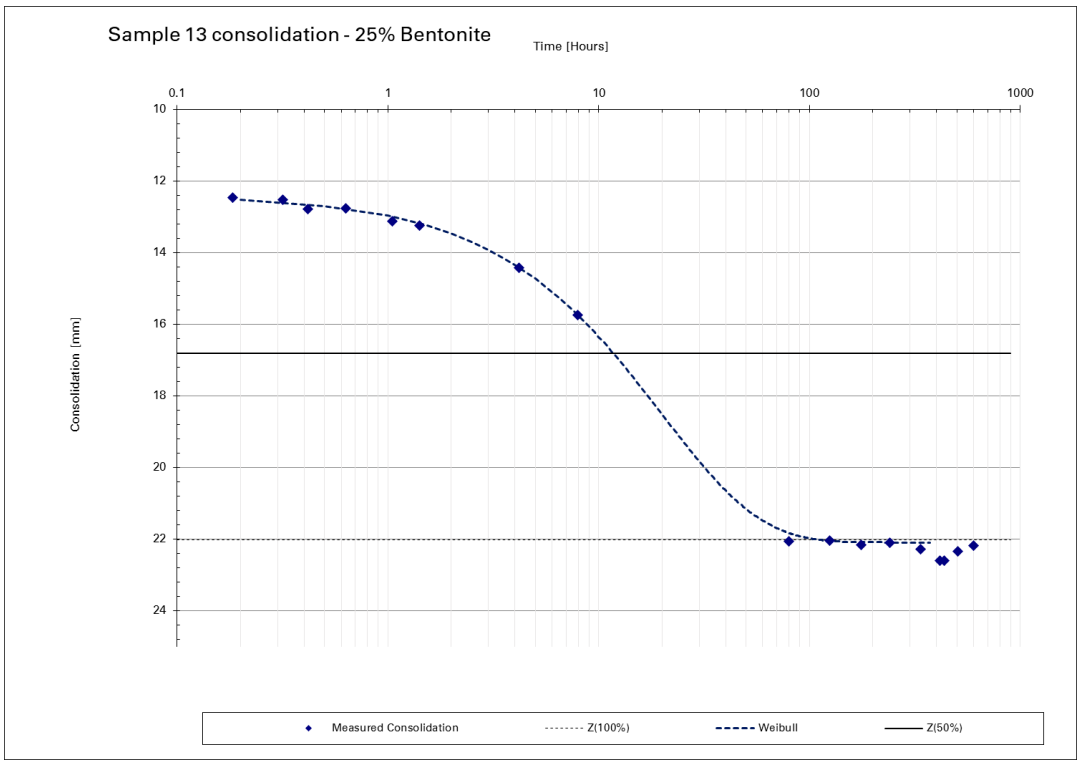

Figure A.9: Direct consolidation measurement graph sample 13 - 25% Bent.

Table A.10: Direct consolidation sample 14 - Kaolin

Direct consolidation [mm] sample:			14	Kaolin		
cons. loc 1	cons. loc 2	cons. loc 3	cons. loc 4	Avg. Cons.	DateTime	Hours
0	0	0	0	7.83	10/14/2019 9:23	0.00
0.1	0.3	0	0.4	8.03	10/14/2019 9:28	0.08
0	0.8	0.5	0.45	8.27	10/14/2019 9:44	0.35
0.2	1.4	0.82	0.5	8.56	10/14/2019 10:06	0.72
0.3	1.85	1.65	0.45	8.89	10/14/2019 10:31	1.13
0.22	2.18	1.75	0.6	9.02	10/14/2019 10:50	1.45
0.3	3.13	2.6	0.95	9.57	10/14/2019 11:51	2.47
0.42	3.85	3.95	0.8	10.08	10/14/2019 12:53	3.50
0.75	5.35	5.68	1	11.02	10/14/2019 15:29	6.10
0.72	6.9	6	1.5	11.61	10/14/2019 17:34	8.18
1.28	10.65	10.4	2.45	14.02	10/15/2019 9:48	24.42
1.45	10.45	11.35	2.7	14.32	10/15/2019 12:48	27.42
2.2	13.12	13.97	4.75	16.34	10/18/2019 9:25	96.03
2.533	13.38	15.1	5.55	16.97	10/21/2019 15:06	173.72
2.75	13.4	15.65	5.53	17.16	10/22/2019 11:23	194.00
2.92	13.6	16	5.62	17.36	10/25/2019 11:55	266.53
2.8	14.05	15.6	5.75	17.38	11/5/2019 9:09	527.77

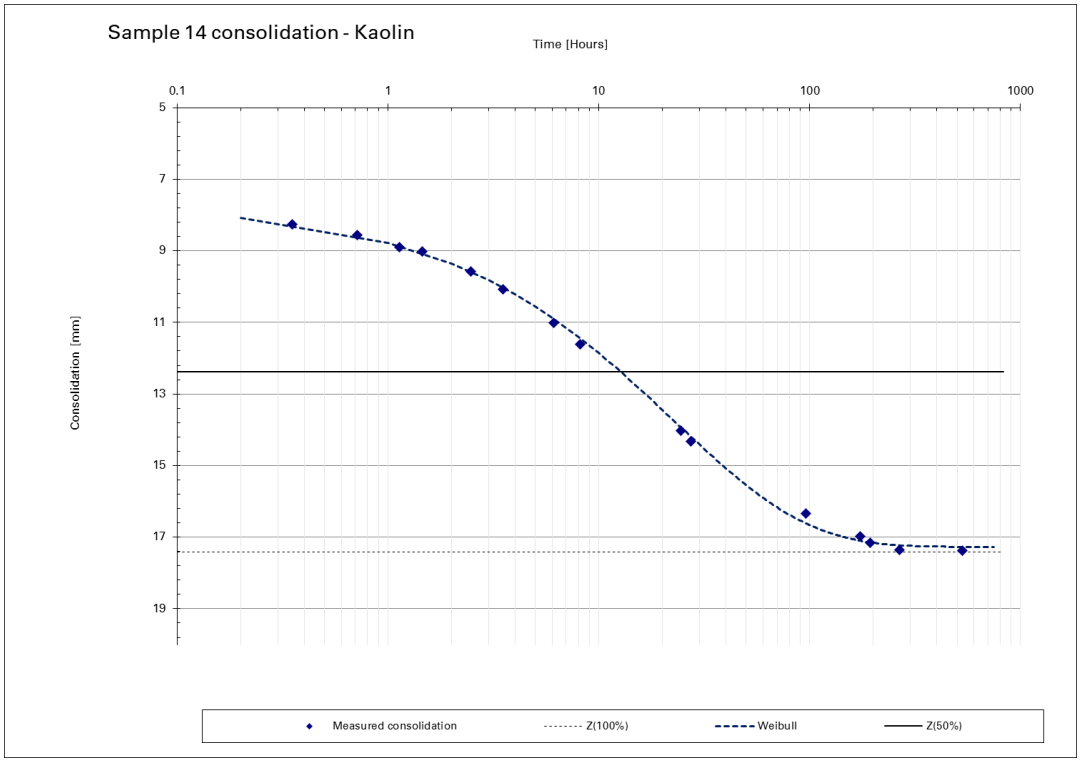

Figure A.10: Direct consolidation measurement graph sample 14 - Kaolin

Table A.11: Direct consolidation sample 15 - Kaolin

Direct consolidation [mm] sample:			15	Kaolin		
cons. loc 1	cons. loc 2	cons. loc 3	cons. loc 4	Avg. Cons.	DateTime	Hours
0	0	0	0	8.70	10/14/2019 9:41	0.00
0.75	0.85	0.2	-1.2	8.85	10/14/2019 9:50	0.15
1.25	2	0.55	-0.85	9.44	10/14/2019 10:04	0.38
1.8	2.9	1	-1.05	9.86	10/14/2019 10:28	0.78
2.07	3.5	1.3	-1.1	10.14	10/14/2019 10:54	1.22
2.85	4.95	2	-0.6	11.00	10/14/2019 11:53	2.20
3.2	6	2.3	-0.95	11.34	10/14/2019 12:56	3.25
4.25	8.15	3.45	-0.73	12.48	10/14/2019 15:36	5.92
4.9	9.35	4	-0.8	13.06	10/14/2019 17:36	7.92
8.95	14.95	5.32	-0.7	15.83	10/15/2019 9:51	24.17
9.05	15.55	5.35	-0.75	16.00	10/15/2019 12:43	27.03
11.8	18.48	7.85	-0.25	18.17	10/18/2019 9:33	95.87
12.87	19.4	8.72	0.2	19.00	10/21/2019 15:15	173.57
13.04	19.67	8.45	0.95	19.23	10/22/2019 11:32	193.85
13.15	19.7	8.25	0.9	19.20	10/25/2019 11:58	266.28
14	20.35	8.88	1.15	19.80	11/13/2019 10:20	720.65

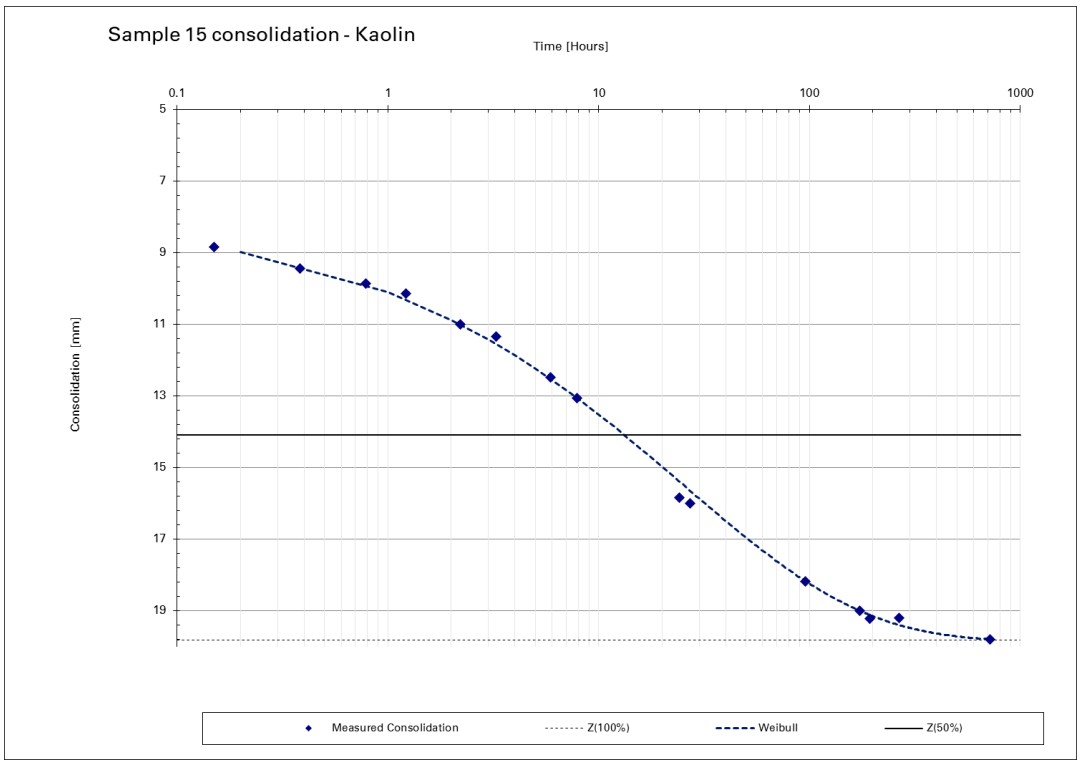

Figure A.11: Direct consolidation measurement graph sample 15 - Kaolin

Table A.12: Direct consolidation sample 16 - Kaolin

Direct consolidation [mm] sample:			16	Kaolin		
cons. loc 1	cons. loc 2	cons. loc 3	cons. loc 4	Avg. Cons.	DateTime	Hours
0	0	0	0	8.70	10/14/2019 10:01	0.00
0.05	0.9	0.52	0.1	9.09	10/14/2019 10:09	0.13
0.1	1.63	1.2	-0.15	9.40	10/14/2019 10:24	0.38
0.41	2.35	1.85	-0.2	9.80	10/14/2019 10:45	0.73
0.37	3.85	3.25	-0.13	10.54	10/14/2019 11:55	1.90
0.27	4.85	4.3	0	11.06	10/14/2019 12:59	2.97
0.45	6.68	6.35	-0.15	12.03	10/14/2019 15:33	5.53
0.42	7.6	7.45	0	12.57	10/14/2019 17:41	7.67
1.4	11.85	11.95	0.22	15.06	10/15/2019 9:33	23.53
1.45	12.25	12.4	0.38	15.32	10/15/2019 12:50	26.82
2.97	13.55	14.2	2.65	17.04	10/18/2019 9:37	95.60
3.28	14.4	15.15	3.2	17.71	10/21/2019 15:25	173.40
3.45	14.58	14.9	3.35	17.77	10/22/2019 11:21	193.33
3.9	14.8	15.37	3.4	18.07	10/25/2019 11:52	265.85
4.65	15.4	15.75	3.7	18.58	11/12/2019 10:26	696.42

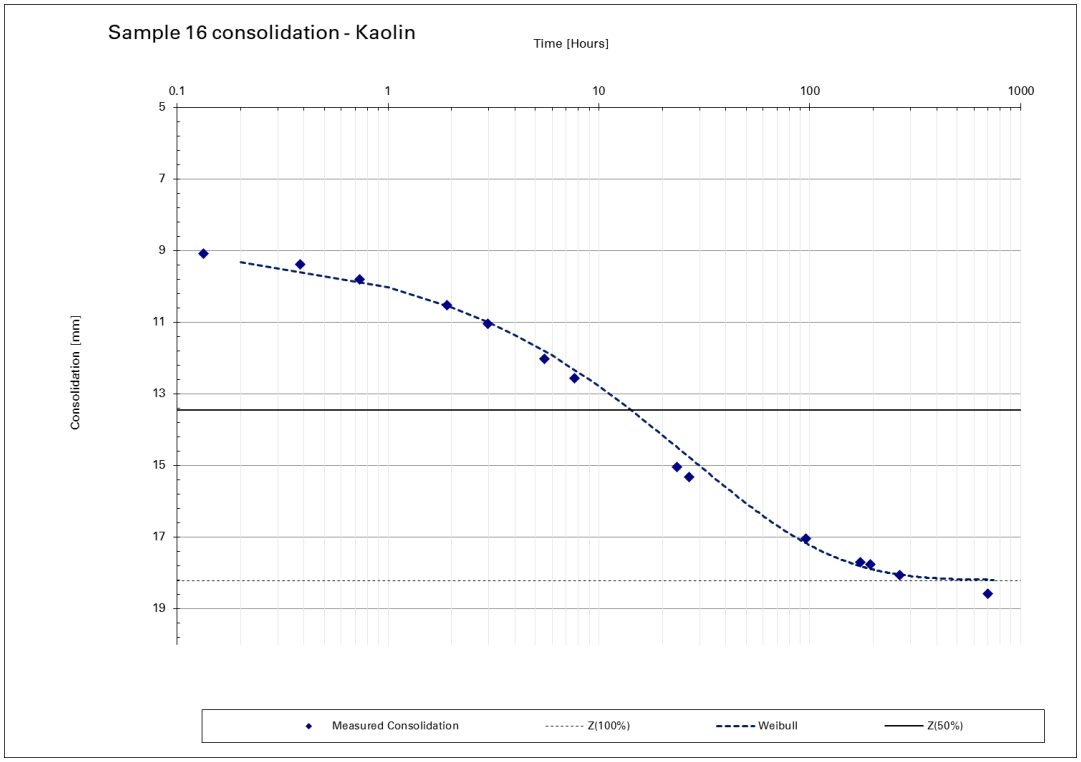

Figure A.12: Direct consolidation measurement graph sample 16 - Kaolin

Table A.13: Direct consolidation sample 17 - Kaolin-Sand

Direct consolidation [mm] sample:			17	Kaolin-Sand		
cons. loc 1	cons. loc 2	cons. loc 3	cons. loc 4	Avg. Cons.	DateTime	Hours
0	0	0	0	21.20	11/19/2019 13:08	0.00
4.8	4.2	-1.48	-2.89	22.36	11/19/2019 13:13	0.08
4.8	4.85	-1.5	-2.89	22.52	11/19/2019 13:23	0.25
4.9	3.9	-1.35	-2.85	22.35	11/19/2019 13:36	0.47
5.45	5.55	-1.22	-2.55	23.01	11/19/2019 14:01	0.88
5.15	6.96	-0.95	-2.15	23.45	11/19/2019 15:16	2.13
5.25	7.4	0.1	-1.92	23.91	11/19/2019 16:02	2.90
6.4	8.82	0.12	-1.75	24.60	11/19/2019 17:28	4.33
10.3	12.77	2.55	0.47	27.72	11/20/2019 9:01	19.88
10.45	13	2.88	1.2	28.08	11/20/2019 11:56	22.80
10.6	13.2	3	1.3	28.23	11/20/2019 16:57	27.82
11	13.45	3.42	1.45	28.53	11/21/2019 9:05	43.95
11	13.45	3.5	1.45	28.55	11/21/2019 18:25	53.28
11.4	13.7	3.5	1.65	28.76	11/25/2019 10:31	141.38

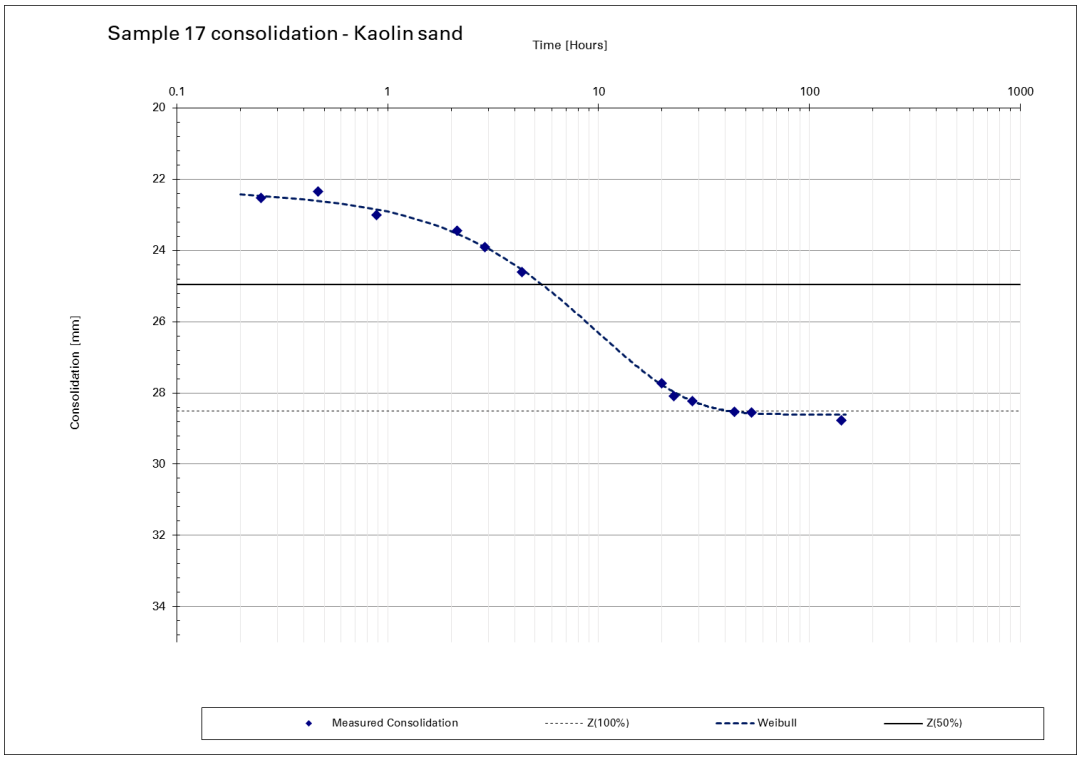

Figure A.13: Direct consolidation measurement graph sample 17 - Kaolin-Sand

Table A.14: Direct consolidation sample 18 - Kaolin

Direct consolidation [mm] sample:			18	Kaolin		
cons. loc 1	cons. loc 2	cons. loc 3	cons. loc 4	Avg. Cons.	DateTime	Hours
0	0	0	0	0.95	11/20/2019 9:20	0.00
0.08	0.05	0.03	0.22	1.05	11/20/2019 9:27	0.12
0	-0.15	-1.52	0.08	0.55	11/20/2019 9:41	0.35
0.23	0.62	0.13	0.22	1.25	11/20/2019 10:09	0.82
0.43	1.45	0.41	0.35	1.61	11/20/2019 11:15	1.92
0.88	2.33	0.73	-0.02	1.93	11/20/2019 13:01	3.68
2.03	3.6	1.08	0.6	2.78	11/20/2019 16:23	7.05
5.43	8.02	2.83	0.75	5.21	11/21/2019 10:41	25.35
5.98	8.35	3.03	1.35	5.63	11/21/2019 18:20	33.00
8.48	9.9	4.58	3.18	7.49	11/25/2019 15:11	125.85
9.53	10.05	5.63	6.15	8.79	11/26/2019 8:58	143.63
9.55	10	5.93	6.05	8.83	11/27/2019 8:50	167.50
9.88	10.45	6.08	5.82	9.01	11/29/2019 8:43	215.38
10.18	11.15	6.56	5.75	9.36	12/2/2019 10:48	289.47

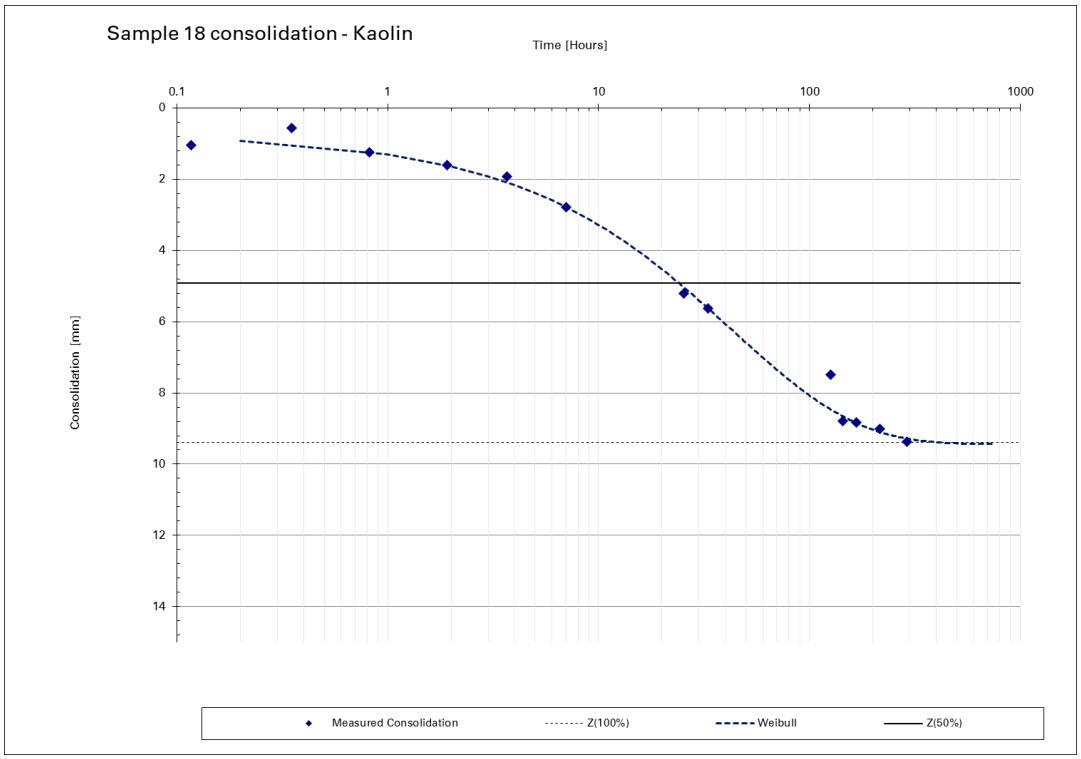

Figure A.14: Direct consolidation measurement graph sample 18 - Kaolin

Table A.15: Direct consolidation sample 19 - Kaolin

Direct consolidation [mm] sample:			19	Kaolin		
cons. loc 1	cons. loc 2	cons. loc 3	cons. loc 4	Avg. Cons.	DateTime	Hours
0	0	0	0	9.98	11/20/2019 9:37	0.00
0.5	-0.05	0.75	0.53	10.41	11/20/2019 9:45	0.13
0.7	-0.2	1.38	1.43	10.80	11/20/2019 10:07	0.50
0.53	0.05	2.4	2.7	11.40	11/20/2019 11:21	1.73
0.45	0.02	3.45	3.85	11.92	11/20/2019 12:58	3.35
0.5	-0.05	5.2	5.65	12.80	11/20/2019 16:54	7.28
1.3	-0.05	8.86	9.97	15.00	11/21/2019 9:21	23.73
2.6	0.08	8.85	10.2	15.41	11/21/2019 18:23	32.77
5.15	2.38	9.82	11.5	17.19	11/25/2019 15:03	125.43
5.95	4.45	10.02	11.33	17.91	11/26/2019 9:01	143.40
6	4.1	10.4	11.17	17.89	11/27/2019 8:45	167.13
6.6	5.58	10.55	11.2	18.46	11/29/2019 8:47	215.17
7.62	7.2	11.25	11.23	19.30	12/2/2019 10:45	289.13
7.58	7.15	11.25	11.2	19.27	12/3/2019 11:17	313.67
7.75	7.2	11.55	11.2	19.40	12/5/2019 9:08	359.52

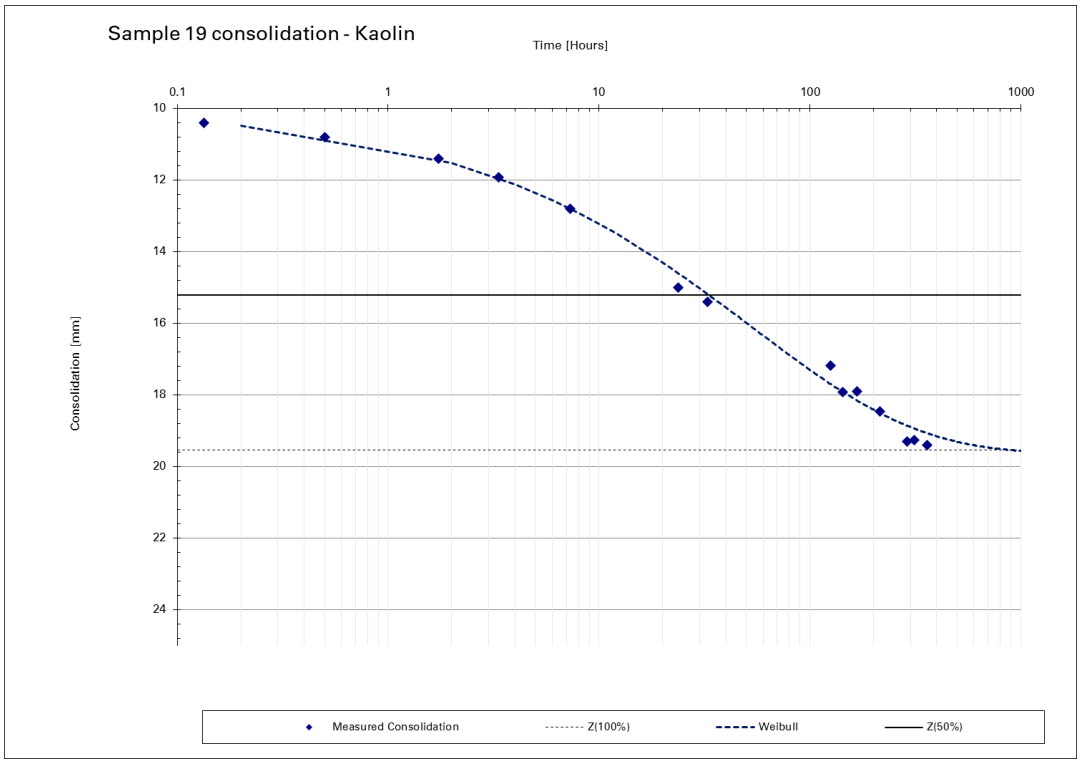

Figure A.15: Direct consolidation measurement graph sample 19 - Kaolin

A.2. Oedometer measurements

Table A.16: Oedometer test - Sample 10 - Kaolin Stage 1

Oedometer test				
Sample NO#	10 Kaolin (soft)			
Ring diameter:	65.475	Height sample (ring-0.5mm):	19.5	
Surface ring [mm2]	3367	Stress [kPa]	22.1	
Mass ring [g]:	34.55	Mass sample [g]	143.34	
Mass blocks [g]:	5010.7	Mass measure device [g]	2580	
Date [dd/mm]	Time [hh:mm:ss]	Readout [mm]		seconds
31-Oct	14:48:32	0.832	Initial readout	0
31-Oct	14:49:08	1.323	direct @ start	36
31-Oct	14:49:34	1.5		62
31-Oct	14:49:53	1.68		81
31-Oct	14:50:38	1.95		126
31-Oct	14:50:52	2		140
31-Oct	14:51:33	2.09		181
31-Oct	14:52:49	2.143		257
31-Oct	14:54:31	2.159		359
31-Oct	14:56:41	2.165		489
31-Oct	15:02:14	2.243		822
31-Oct	15:06:41	2.248		1089
31-Oct	15:11:32	2.251		1380
31-Oct	15:21:33	2.255		1981
31-Oct	15:27:14	2.256		2322
31-Oct	15:34:05	2.258		2733
31-Oct	15:47:42	2.261		3549
31-Oct	16:00:53	2.263		4341
31-Oct	16:11:44	2.264		4992
31-Oct	16:30:47	2.266		6135

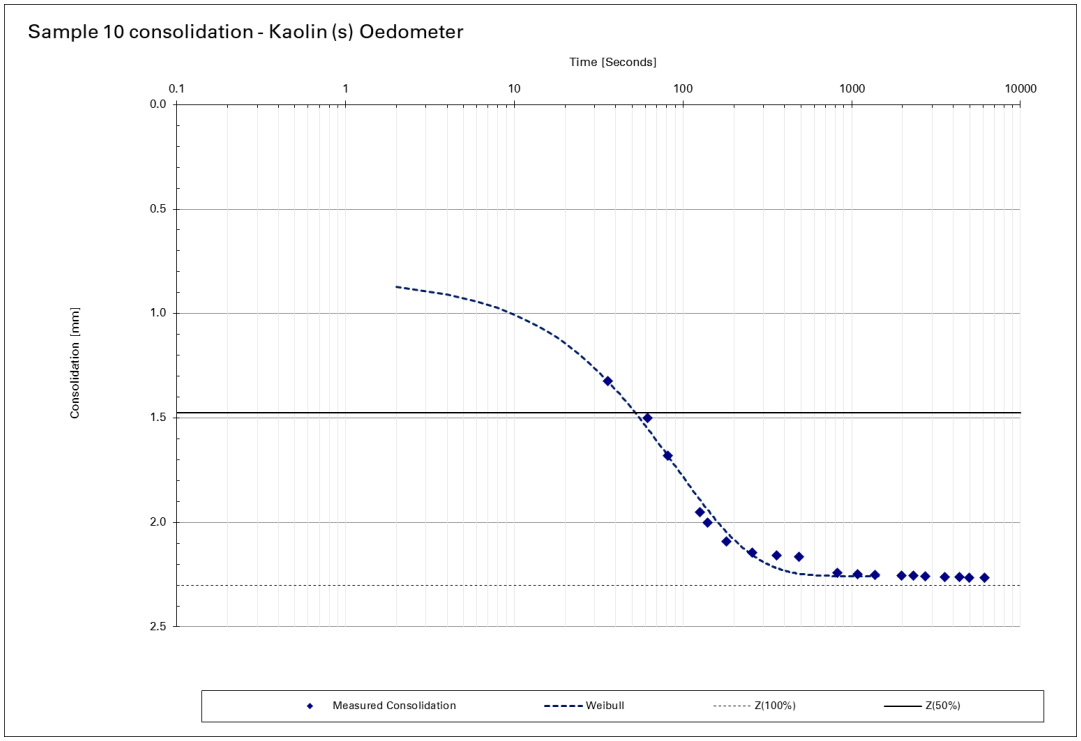

Figure A.16: Oedometer measurement graph sample 10 - Kaolin Stage 1

Table A.17: Oedometer test - Sample 10 - Kaolin Stage 2

Oedometer test				
Sample NO#	10 Kaolin (soft) - Stage 2			
Ring diameter:	65.475	Height sample (ring-0.5mm):	19.5	
Surface ring [mm2]	3367	Stress (increase) [kPa]	43.7	
Mass ring [g]:	34.55	Mass sample [g]	143.34	
Mass blocks [g]:	5010.7	Mass measure device [g]	2580	
Date [dd/mm]	Time [hh:mm:ss]	Readout [mm]		seconds
1-Nov	11:22:08	0.001	Initial readout	0
1-Nov	11:22:19	0.1	direct @ start	10
1-Nov	11:22:31	0.15		22
1-Nov	11:22:37	0.19		29
1-Nov	11:22:53	0.235		45
1-Nov	11:23:09	0.255		60
1-Nov	11:23:27	0.266		79
1-Nov	11:24:04	0.276		116
1-Nov	11:25:05	0.283		177
1-Nov	11:27:36	0.29		328
1-Nov	11:29:53	0.294		465
1-Nov	11:32:28	0.297		620
1-Nov	11:35:58	0.3		830
1-Nov	11:41:52	0.303		1184

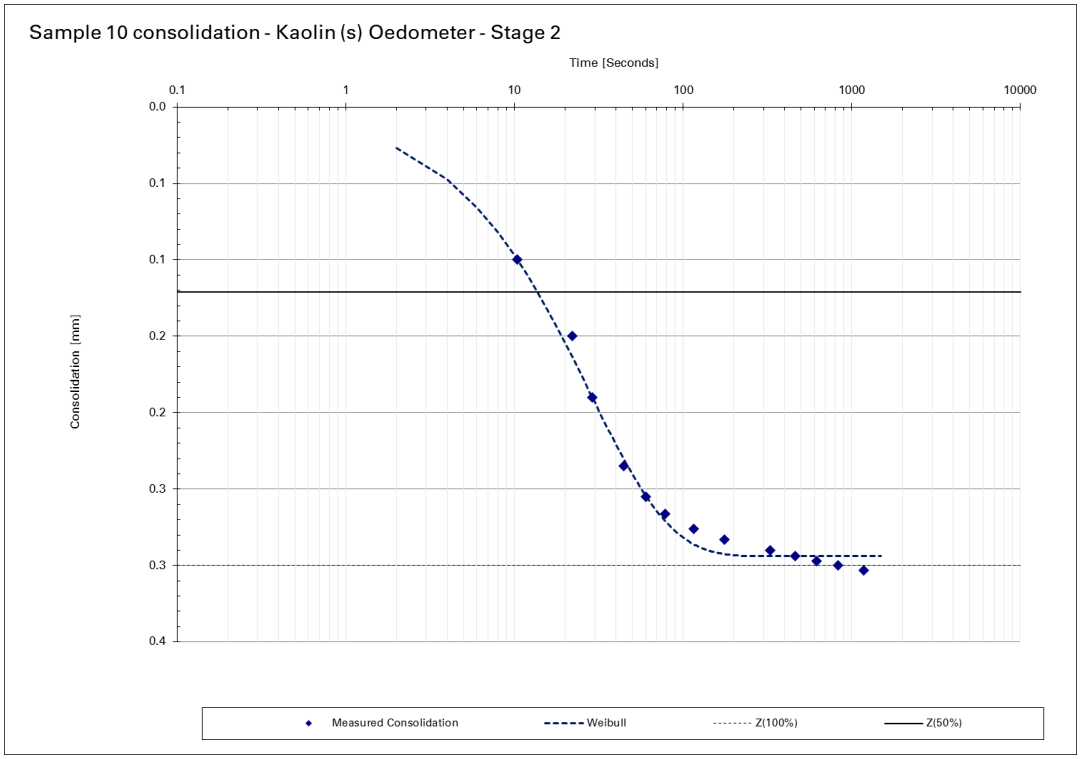

Figure A.17: Oedometer measurement graph sample 10 - Kaolin Stage 2

Table A.18: Oedometer test - Sample 10 - Kaolin Unload

Oedometer test				
Sample NO#	10 Kaolin (soft) - Unload			
Ring diameter:	65.475	Height sample (ring-0.5mm):	19.5	
Surface ring [mm2]	3367	Stress (decrease) [kPa]	43.7	
Mass ring [g]:	34.55	Mass sample [g]	143.34	
Mass blocks [g]:	5010.7	Mass measure device [g]	2580	
Date [dd/mm]	Time [hh:mm:ss]	Readout [mm]		seconds
1-Nov	11:51:12	0.336	Initial readout	0
1-Nov	11:51:14	0.334	direct @ start	2
1-Nov	11:51:20	0.33		8
1-Nov	11:51:29	0.327		17
1-Nov	11:51:40	0.325		28
1-Nov	11:52:11	0.323		59
1-Nov	11:52:20	0.322		68
1-Nov	11:53:06	0.321		114
1-Nov	11:54:16	0.32		184
1-Nov	11:58:39	0.318		447
1-Nov	12:00:36	0.317		564
1-Nov	12:06:33	0.317		921
1-Nov	12:15:15	0.316		1443
1-Nov	12:21:17	0.3158		1805
1-Nov	12:22:33	0.315		1881
1-Nov	13:40:20	0.314		6548
1-Nov	16:57:03	0.312		18351

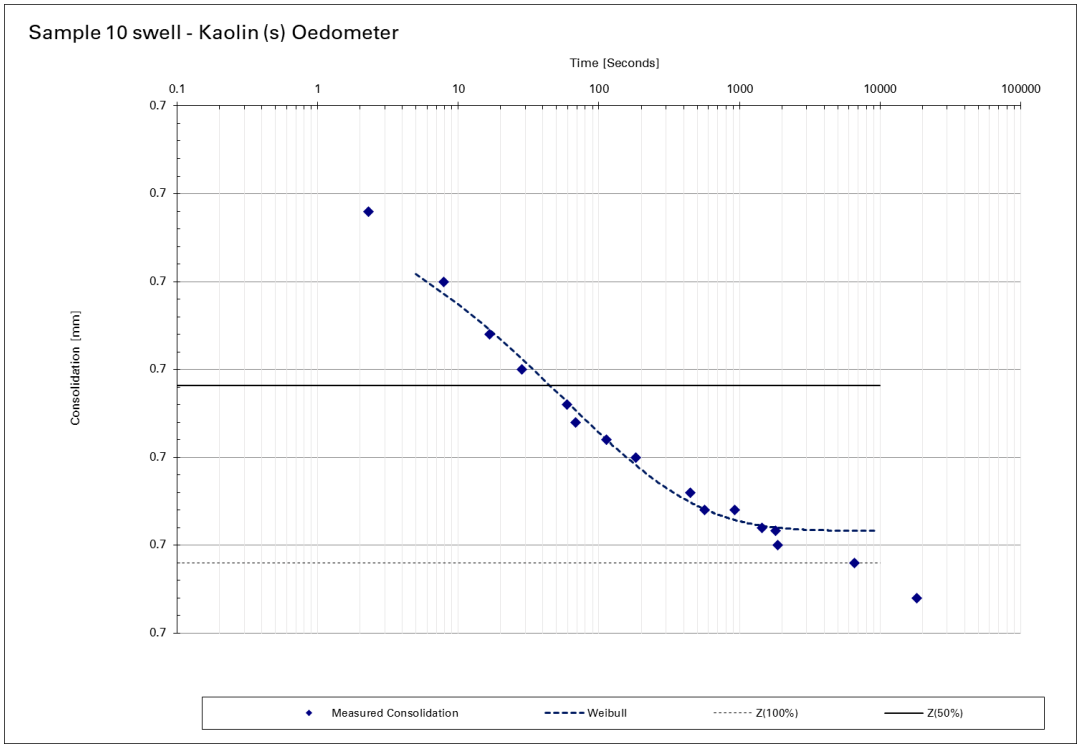

Figure A.18: Oedometer measurement graph sample 10 - Kaolin Unload

Table A.19: Oedometer test - Sample 8 - 5% Bent. Stage 1

Oedometer test				
Sample NO#	8 5% Bent.			
Ring diameter:	64.725	Height sample (ring-0.5mm):	19.5	
Surface ring [mm2]	3290	Stress [kPa]	22.6	
Mass ring [g]:	44.37	Mass sample [g]	159.68	
Mass blocks [g]:	4995.24	Mass measuredevice [g]	2580	
Date [dd/mm]	Time [hh:mm:ss]	Readout [mm]		seconds
1-Nov	14:00:57	0.3	Initial readout	0
1-Nov	14:01:01	0.388	direct @ start	4
1-Nov	14:01:09	0.445		12
1-Nov	14:01:17	0.485		20
1-Nov	14:01:29	0.53		32
1-Nov	14:01:40	0.56		43
1-Nov	14:01:49	0.58		52
1-Nov	14:01:59	0.6		62
1-Nov	14:02:26	0.64		89
1-Nov	14:02:58	0.675		122
1-Nov	14:03:16	0.69		139
1-Nov	14:03:29	0.7		152
1-Nov	14:04:22	0.732		206
1-Nov	14:05:35	0.764		279
1-Nov	14:06:36	0.788		339
1-Nov	14:08:07	0.824		430
1-Nov	14:09:53	0.863		536
1-Nov	14:11:46	0.897		649
1-Nov	14:13:25	0.921		748
1-Nov	14:14:51	0.937		834
1-Nov	14:17:06	0.958		969
1-Nov	14:21:48	0.987		1251
1-Nov	14:25:27	1.004		1471
1-Nov	14:30:52	1.023		1795
1-Nov	14:35:57	1.035		2100
1-Nov	14:43:29	1.048		2553
1-Nov	14:48:36	1.055		2859
1-Nov	15:05:43	1.072		3886
1-Nov	15:20:08	1.079		4751
1-Nov	15:38:52	1.085		5875
1-Nov	16:08:35	1.089		7658
1-Nov	16:39:38	1.091		9522
1-Nov	16:57:43	1.092		10606

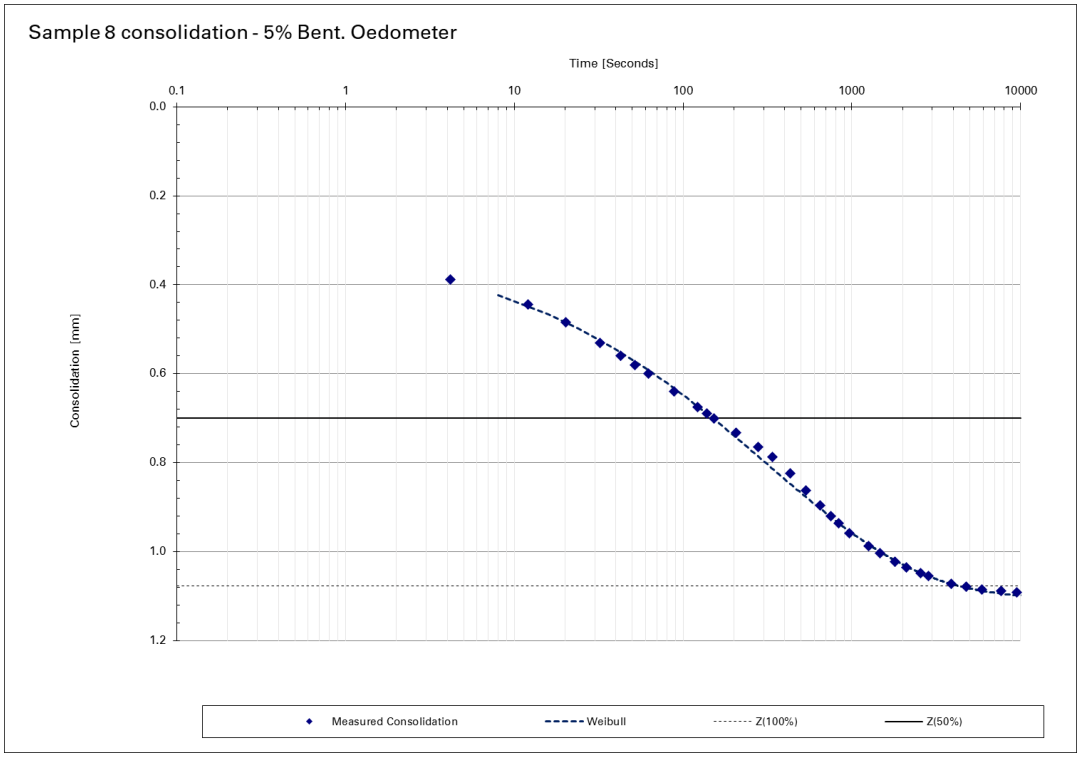

Figure A.19: Oedometer measurement graph sample 8 - 5% Bent. Stage 1

Table A.20: Oedometer test - Sample 8 - 5% Bent. Stage 2

Oedometer test				
Sample NO#	8 5% Bent. - stage 2			
Ring diameter:	64.725	Height sample (ring-0.5mm):	19.5	
Surface ring [mm2]	3290	Stress increase [kPa]	44.8	
Mass ring [g]:	44.37	Mass sample [g]	159.68	
Mass blocks [g]:	4995.24	Mass measuredevice [g]	2580	
Date [dd/mm]	Time [hh:mm:ss]	Readout [mm]		seconds
4-Nov	11:06:35	1	Initial readout	0
4-Nov	11:06:38	1.1	direct @ start	3
4-Nov	11:06:46	1.14		12
4-Nov	11:06:54	1.17		19
4-Nov	11:07:03	1.2		28
4-Nov	11:07:20	1.252		46
4-Nov	11:07:39	1.3		64
4-Nov	11:08:27	1.4		113
4-Nov	11:09:30	1.495		175
4-Nov	11:11:19	1.599		284
4-Nov	11:14:17	1.681		462
4-Nov	11:18:01	1.717		687
4-Nov	11:30:01	1.748		1407
4-Nov	11:43:22	1.759		2207
4-Nov	12:02:28	1.766		3353
4-Nov	12:44:18	1.775		5863

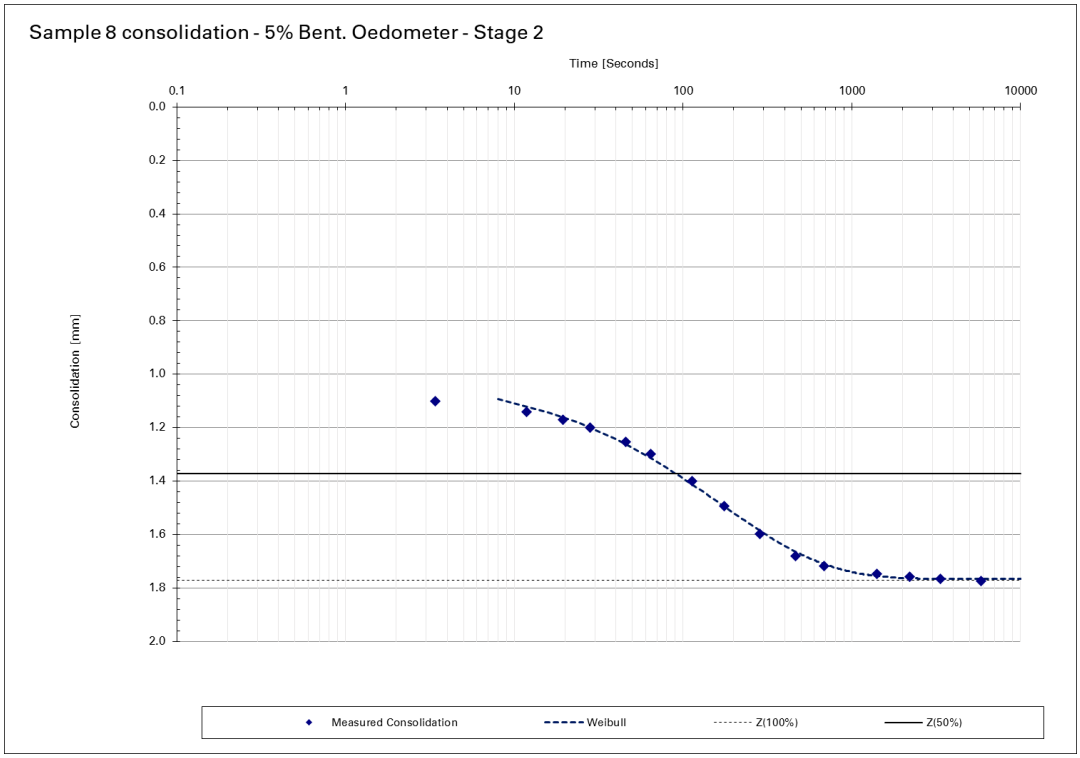

Figure A.20: Oedometer measurement graph sample 8 - 5% Bent. Stage 2

Table A.21: Oedometer test - Sample 8 - 5% Bent. Unload

Oedometer test				
Sample NO#	8 5% Bent. - Unload			
Ring diameter:	64.725	Height sample (ring-0.5mm):	19.5	
Surface ring [mm2]	3290	Stress (decrease) [kPa]	64.2	
Mass ring [g]:	34.55	Mass sample [g]	143.34	
Mass blocks [g]:	4995.24	Mass measuredevice [g]	2580	
Date [dd/mm]	Time [hh:mm:ss]	Readout [mm]		seconds
4-Nov	13:45:35	1.85	Initial readout	0
4-Nov	13:45:37	1.84	direct @ start	2
4-Nov	13:45:41	1.804		6
4-Nov	13:45:51	1.793		16
4-Nov	13:46:08	1.769		33
4-Nov	13:46:51	1.729		76
4-Nov	13:47:32	1.703		117
4-Nov	13:48:09	1.685		154
4-Nov	13:50:03	1.647		268
4-Nov	13:52:17	1.619		402
4-Nov	13:55:23	1.594		588
4-Nov	13:59:15	1.575		820
4-Nov	14:02:28	1.564		1013
4-Nov	14:06:31	1.553		1256
4-Nov	14:11:46	1.544		1571
4-Nov	14:20:01	1.535		2066
4-Nov	14:28:54	1.529		2599
4-Nov	14:44:04	1.523		3509
4-Nov	15:19:50	1.516		5655
4-Nov	15:31:38	1.515		6363
4-Nov	15:46:03	1.514		7228
4-Nov	15:58:44	1.513		7989
4-Nov	16:11:19	1.513		8744

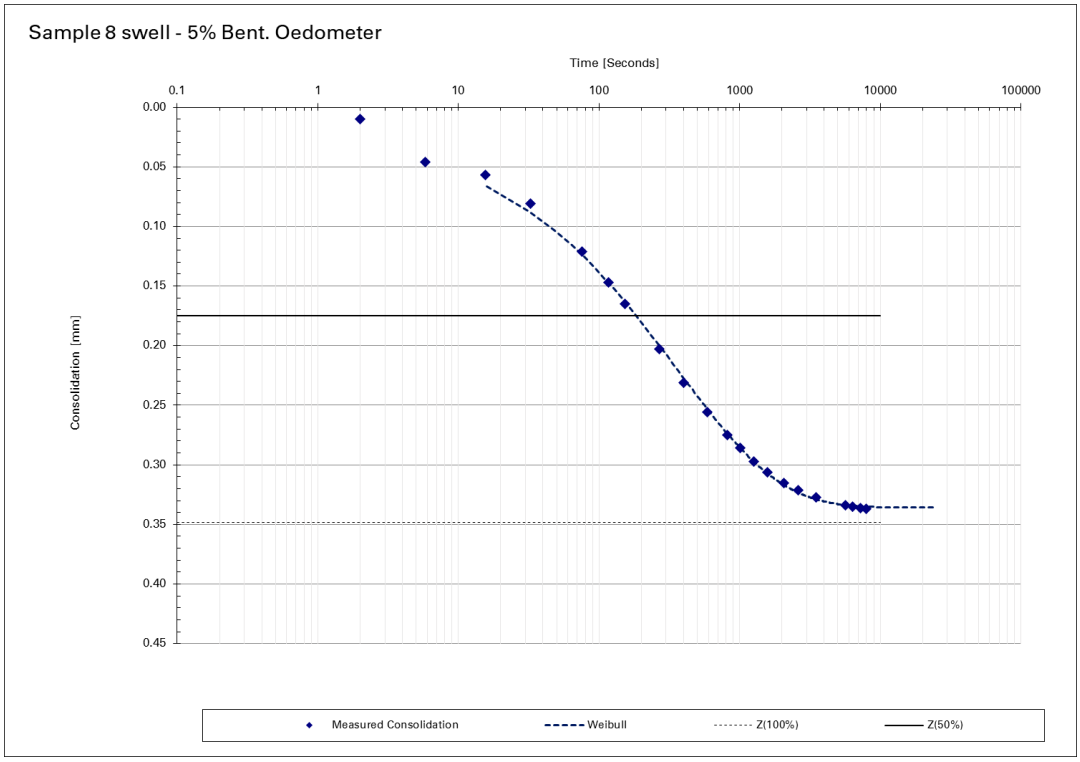

Figure A.21: Oedometer measurement graph sample 8 - 5% Bent. Unload

Table A.22: Oedometer test - Sample 8 - 5% Bent. Stage 3

Oedometer test				
Sample NO#	8 5% Bent. - stage 3			
Ring diameter:	64.725	Height sample (ring-0.5mm):	19.5	
Surface ring [mm2]	3290	Stress increase [kPa]	64.4	
Mass ring [g]:	44.37	Mass sample [g]	159.68	
Mass blocks [g]:	4995.24	Mass measuredevice [g]	2580	
Date [dd/mm]	Time [hh:mm:ss]	Readout [mm]		seconds
4-Nov	16:12:55	1.57	Initial readout	0
4-Nov	16:12:56	1.62	direct @ start	1
4-Nov	16:13:05	1.655		10
4-Nov	16:13:13	1.685		18
4-Nov	16:13:23	1.71		28
4-Nov	16:13:40	1.75		46
4-Nov	16:14:20	1.82		85
4-Nov	16:15:29	1.89		154
4-Nov	16:16:24	1.923		209
4-Nov	16:20:14	1.969		440
4-Nov	16:25:51	1.983		776
4-Nov	16:34:24	1.991		1289
4-Nov	16:41:48	1.995		1733
4-Nov	16:50:29	1.998		2254
4-Nov	17:30:35	2.005		4661
4-Nov	17:54:02	2.007		6068

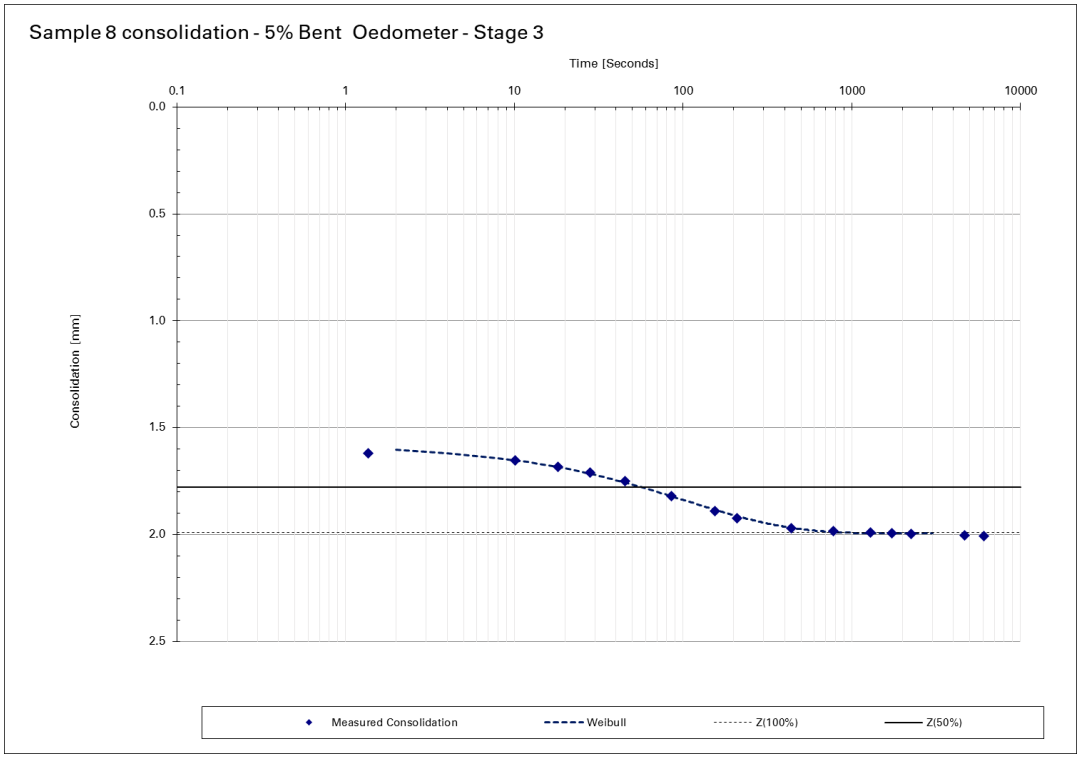

Figure A.22: Oedometer measurement graph sample 8 - 5% Bent. Stage 3

Table A.23: Oedometer test - Sample 7 - 10% Bent. Stage 1

Oedometer test				
Sample NO#	7 - 10% Bent.			
Ring diameter:	65.475	Height sample (ring-0.5mm):	19.5	
Surface ring [mm2]	3367	Stress [kPa]	22.1	
Mass ring [g]:	34.55	Mass sample [g]	151.6	
Mass blocks [g]:	4994.48	Mass measuredevice [g]	2580	
Date [dd/mm]	Time [hh:mm:ss]	Readout [mm]		seconds
4-Nov	9:58:07	0.27	Initial readout	0
4-Nov	9:58:19	0.37	direct @ start	12
4-Nov	9:58:27	0.42		20
4-Nov	9:58:37	0.47		30
4-Nov	9:58:43	0.5		37
4-Nov	9:58:52	0.53		45
4-Nov	9:58:59	0.555		53
4-Nov	9:59:07	0.58		61
4-Nov	9:59:14	0.6		68
4-Nov	9:59:34	0.65		87
4-Nov	9:59:58	0.72		111
4-Nov	10:00:15	0.76		129
4-Nov	10:00:50	0.825		164
4-Nov	10:03:12	1.01		305
4-Nov	10:08:01	1.201		594
4-Nov	10:11:00	1.252		773
4-Nov	10:17:10	1.298		1144
4-Nov	10:21:14	1.3113		1388
4-Nov	10:25:57	1.32		1670
4-Nov	10:28:41	1.323		1835
4-Nov	10:34:32	1.328		2186
4-Nov	10:40:25	1.331		2539
4-Nov	10:50:24	1.336		3137
4-Nov	11:04:01	1.339		3954
4-Nov	11:20:14	1.343		4927
4-Nov	11:44:10	1.346		6363
4-Nov	12:46:57	1.351		10131
4-Nov	14:08:18	1.354		15011

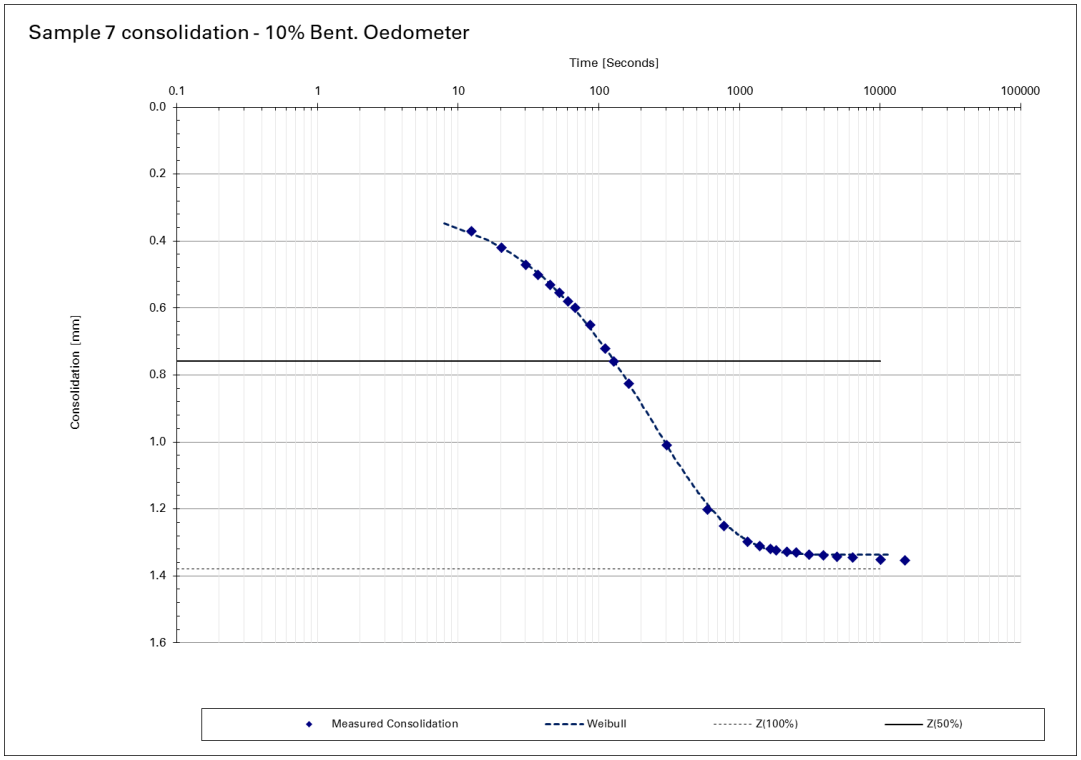

Figure A.23: Oedometer measurement graph sample 7 - 10% Bent. Stage 1

Table A.24: Oedometer test - Sample 7 - 10% Bent. Stage 2

Oedometer test				
Sample NO#	7 10% Bent. - Stage 2			
Ring diameter:	65.475	Height sample (ring-0.5mm):	19.5	
Surface ring [mm2]	3367	Stress increase [kPa]	43.8	
Mass ring [g]:	34.55	Mass sample [g]	151.6	
Mass blocks [g]:	4994.48	Mass measuredevice [g]	2580	
Date [dd/mm]	Time [hh:mm:ss]	Readout [mm]		seconds
4-Nov	14:10:06	1.745	Initial readout	0
4-Nov	14:10:11	1.875	direct @ start	5
4-Nov	14:10:23	1.945		17
4-Nov	14:10:31	1.975		25
4-Nov	14:10:41	2.01		35
4-Nov	14:10:55	2.05		49
4-Nov	14:11:17	2.1		71
4-Nov	14:12:04	2.178		119
4-Nov	14:14:16	2.282		250
4-Nov	14:19:12	2.343		546
4-Nov	14:24:35	2.36		869
4-Nov	14:29:38	2.368		1172
4-Nov	14:43:01	2.378		1975
4-Nov	14:56:39	2.384		2793
4-Nov	15:20:31	2.39		4225

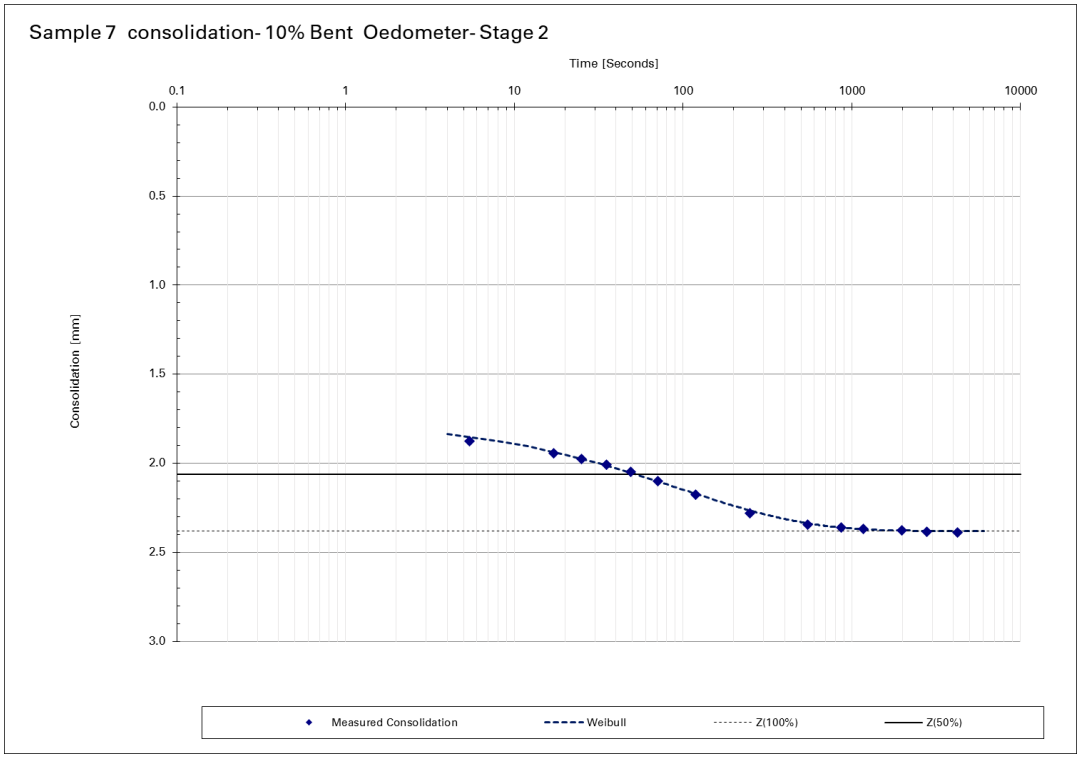

Figure A.24: Oedometer measurement graph sample 7 - 10% Bent. Stage 2

Table A.25: Oedometer test - Sample 7 - 10% Bent. Unload

Oedometer test				
Sample NO#	7 10% Bent. - Unload			
Ring diameter:	65.475	Height sample (ring-0.5mm):	19.5	
Surface ring [mm2]	3367	Stress (decrease) [kPa]	62.7	
Mass ring [g]:	34.55	Mass sample [g]	151.6	
Mass blocks [g]:	4994.48	Mass measuredevice [g]	2580	
Date [dd/mm]	Time [hh:mm:ss]	Readout [mm]		seconds
4-Nov	15:21:45	2.391	Initial readout	0
4-Nov	15:21:52	2.306	direct @ start	7
4-Nov	15:22:02	2.28		17
4-Nov	15:22:11	2.26		26
4-Nov	15:22:21	2.24		36
4-Nov	15:22:33	2.22		48
4-Nov	15:23:08	2.18		83
4-Nov	15:24:56	2.108		191
4-Nov	15:26:14	2.078		269
4-Nov	15:30:17	2.027		512
4-Nov	15:33:03	2.007		678
4-Nov	15:38:40	1.984		1015
4-Nov	15:45:38	1.969		1433
4-Nov	15:57:42	1.957		2157
4-Nov	16:10:31	1.952		2926
4-Nov	16:26:53	1.949		3908
4-Nov	16:45:37	1.947		5032
4-Nov	16:57:47	1.947		5762
4-Nov	17:13:19	1.946		6694

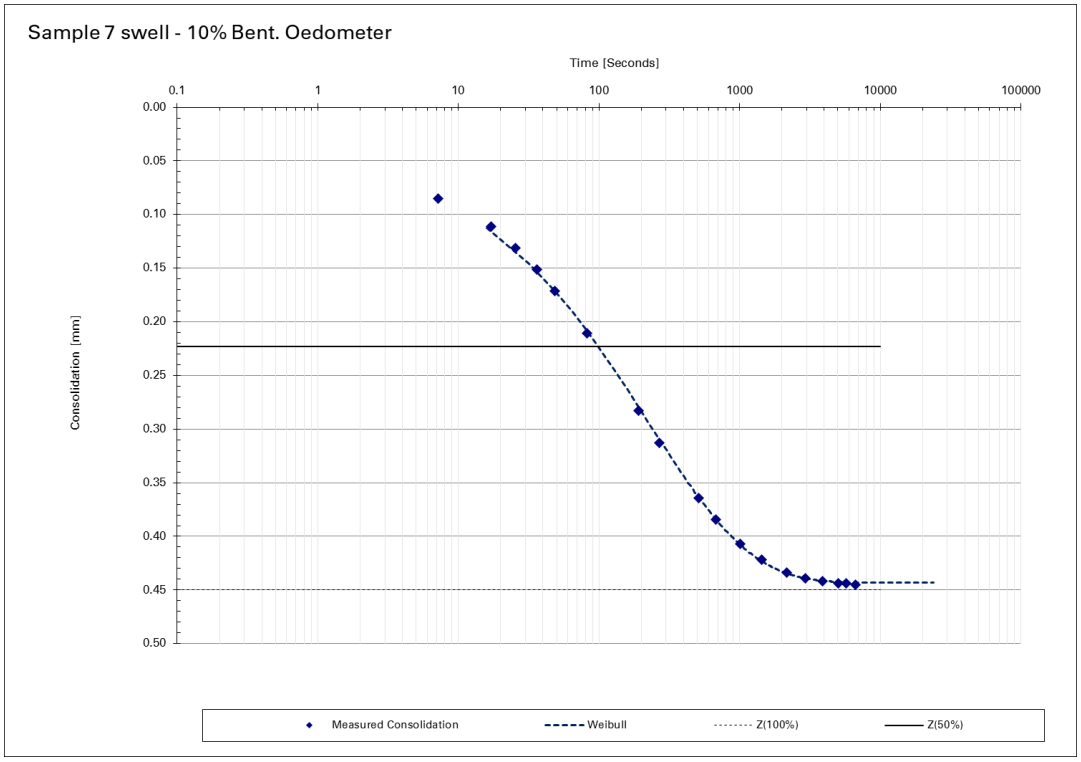

Figure A.25: Oedometer measurement graph sample 7 - 10% Bent. Unload

Table A.26: Oedometer test - Sample 7 - 10% Bent. Stage 3

Oedometer test				
Sample NO#	7 10% Bent - Stage 3			
Ring diameter:	65.475	Height sample (ring-0.5mm):	19.5	
Surface ring [mm2]	3367	Stress increase [kPa]	63.0	
Mass ring [g]:	34.55	Mass sample [g]	151.6	
Mass blocks [g]:	4994.48	Mass measuredevice [g]	2580	
Date [dd/mm]	Time [hh:mm:ss]	Readout [mm]		seconds
4-Nov	17:16:57	2.2	Initial readout	0
4-Nov	17:16:59	2.25	direct @ start	3
4-Nov	17:17:11	2.3		14
4-Nov	17:17:27	2.36		30
4-Nov	17:17:41	2.4		44
4-Nov	17:18:02	2.45		65
4-Nov	17:18:24	2.49		87
4-Nov	17:19:10	2.55		133
4-Nov	17:20:22	2.6		205
4-Nov	17:21:32	2.625		275
4-Nov	17:23:47	2.647		411
4-Nov	17:25:36	2.655		520
4-Nov	17:27:05	2.659		609
4-Nov	17:30:03	2.664		786
4-Nov	17:35:11	2.67		1095
4-Nov	17:39:48	2.673		1372
4-Nov	17:44:15	2.677		1638
4-Nov	17:55:28	2.681		2311

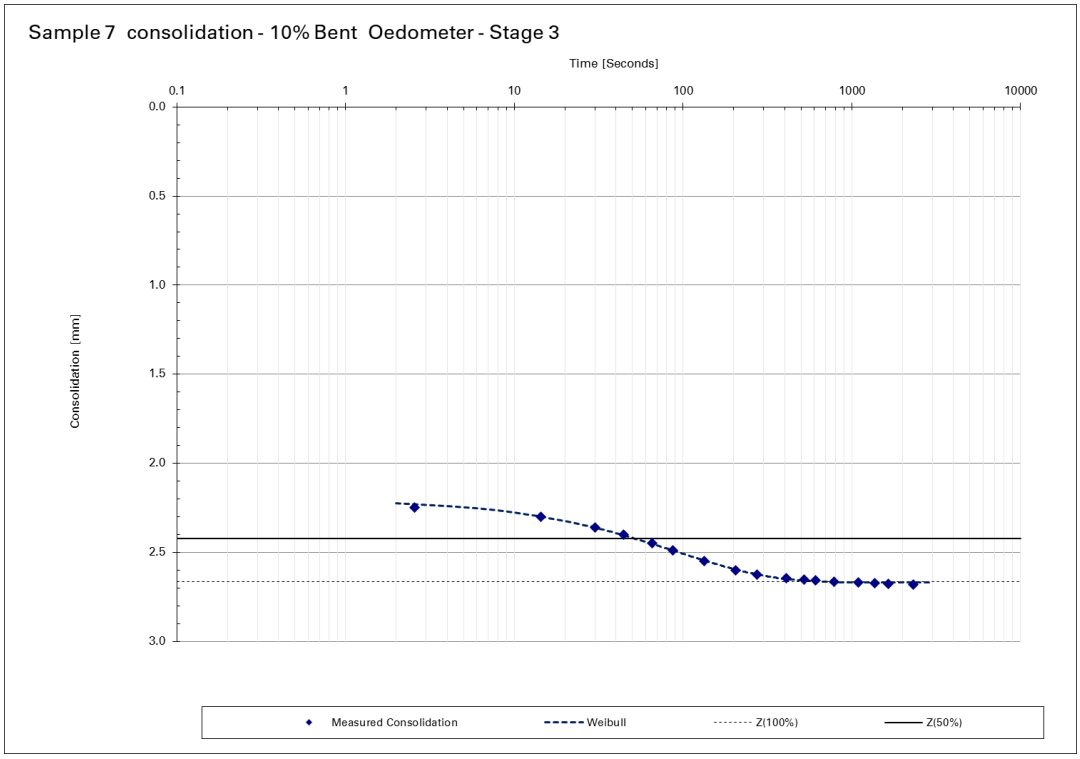

Figure A.26: Oedometer measurement graph sample 7 - 10% Bent. Stage 3

Table A.27: Oedometer test - Sample 11 - 15% Bent. Stage 1

Oedometer test				
Sample NO#	11 - 15% Bent.			
Ring diameter:	64.925	Height sample (ring-0.5mm):	19.5	
Surface ring [mm2]	3311	Stress [kPa]	22.5	
Mass ring [g]:	38.68	Mass sample [g]	150.56	
Mass blocks [g]:	5002.04	Mass measuredevice [g]	2580	
Date [dd/mm]	Time [hh:mm:ss]	Readout [mm]		seconds
4-Nov	10:24:22	0.29	Initial readout	0
4-Nov	10:24:25	0.66	direct @ start	3
4-Nov	10:24:36	0.72		15
4-Nov	10:24:43	0.77		22
4-Nov	10:24:51	0.8		29
4-Nov	10:25:05	0.85		44
4-Nov	10:25:33	0.92		71
4-Nov	10:26:16	1		115
4-Nov	10:26:57	1.06		155
4-Nov	10:28:23	1.155		242
4-Nov	10:30:24	1.245		362
4-Nov	10:33:47	1.33		566
4-Nov	10:39:46	1.384		925
4-Nov	10:50:01	1.408		1540
4-Nov	11:03:44	1.418		2362
4-Nov	11:19:25	1.425		3303
4-Nov	11:43:53	1.429		4771
4-Nov	12:11:53	1.432		6452
4-Nov	12:45:37	1.435		8476
4-Nov	13:54:39	1.439		12617

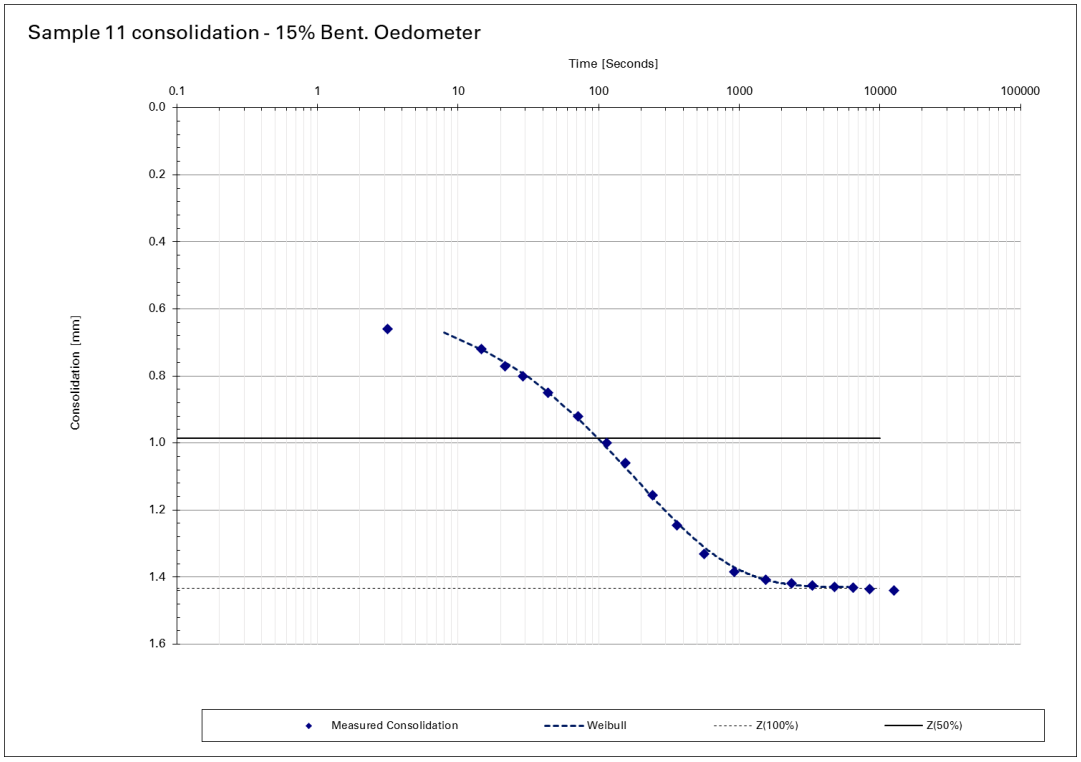

Figure A.27: Oedometer measurement graph sample 11 - 15% Bent. Stage 1

Table A.28: Oedometer test - Sample 11 - 15% Bent. Stage 2

Oedometer test				
Sample NO#	11 15% Bent - Stage 2			
Ring diameter:	64.925	Height sample (ring-0.5mm):	19.5	
Surface ring [mm2]	3311	Stress increase [kPa]	44.6	
Mass ring [g]:	38.68	Mass sample [g]	150.56	
Mass blocks [g]:	5002.04	Mass measuredevice [g]	2580	
Date [dd/mm]	Time [hh:mm:ss]	Readout [mm]		seconds
4-Nov	13:57:10	1.73	Initial readout	0
4-Nov	13:57:14	1.822	direct @ start	4
4-Nov	13:57:22	1.846		12
4-Nov	13:57:29	1.878		19
4-Nov	13:57:36	1.9		26
4-Nov	13:57:45	1.925		34
4-Nov	13:58:03	1.97		53
4-Nov	13:58:18	2		68
4-Nov	13:58:53	2.055		103
4-Nov	13:59:48	2.115		158
4-Nov	14:01:12	2.17		242
4-Nov	14:06:14	2.235		544
4-Nov	14:11:30	2.254		859
4-Nov	14:19:44	2.267		1354
4-Nov	14:24:50	2.271		1660
4-Nov	14:29:59	2.275		1969
4-Nov	14:43:18	2.281		2768
4-Nov	14:56:52	2.286		3582

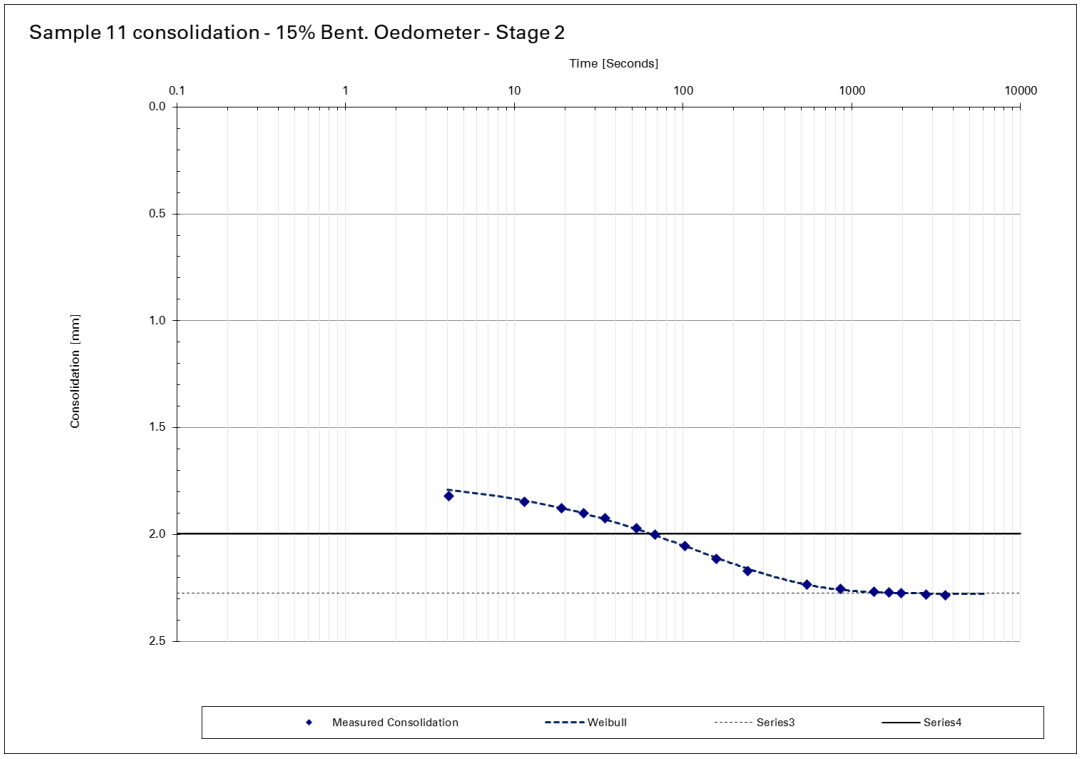

Figure A.28: Oedometer measurement graph sample 11 - 15% Bent. Stage 2

Table A.29: Oedometer test - Sample 11 - 15% Bent. Unload

Oedometer test				
Sample NO#	11 15% Bent. - Unload			
Ring diameter:	64.925	Height sample (ring-0.5mm):	19.5	
Surface ring [mm2]	3311	Stress (decrease) [kPa]	63.8	
Mass ring [g]:	38.68	Mass sample [g]	150.56	
Mass blocks [g]:	5002.04	Mass measuredevice [g]	2580	
Date [dd/mm]	Time [hh:mm:ss]	Readout [mm]		seconds
4-Nov	15:28:22	2.293	Initial readout	0
4-Nov	15:28:24	2.066	direct @ start	2
4-Nov	15:28:33	2.033		11
4-Nov	15:28:41	2.01		19
4-Nov	15:28:49	1.99		27
4-Nov	15:29:02	1.965		40
4-Nov	15:29:58	1.892		96
4-Nov	15:31:00	1.845		158
4-Nov	15:32:45	1.793		263
4-Nov	15:38:51	1.71		629
4-Nov	15:44:52	1.675		990
4-Nov	15:57:12	1.644		1730
4-Nov	16:10:47	1.631		2545
4-Nov	16:26:31	1.624		3489
4-Nov	16:45:59	1.619		4657
4-Nov	16:59:35	1.616		5473
4-Nov	17:12:16	1.614		6234
4-Nov	17:21:59	1.613		6817

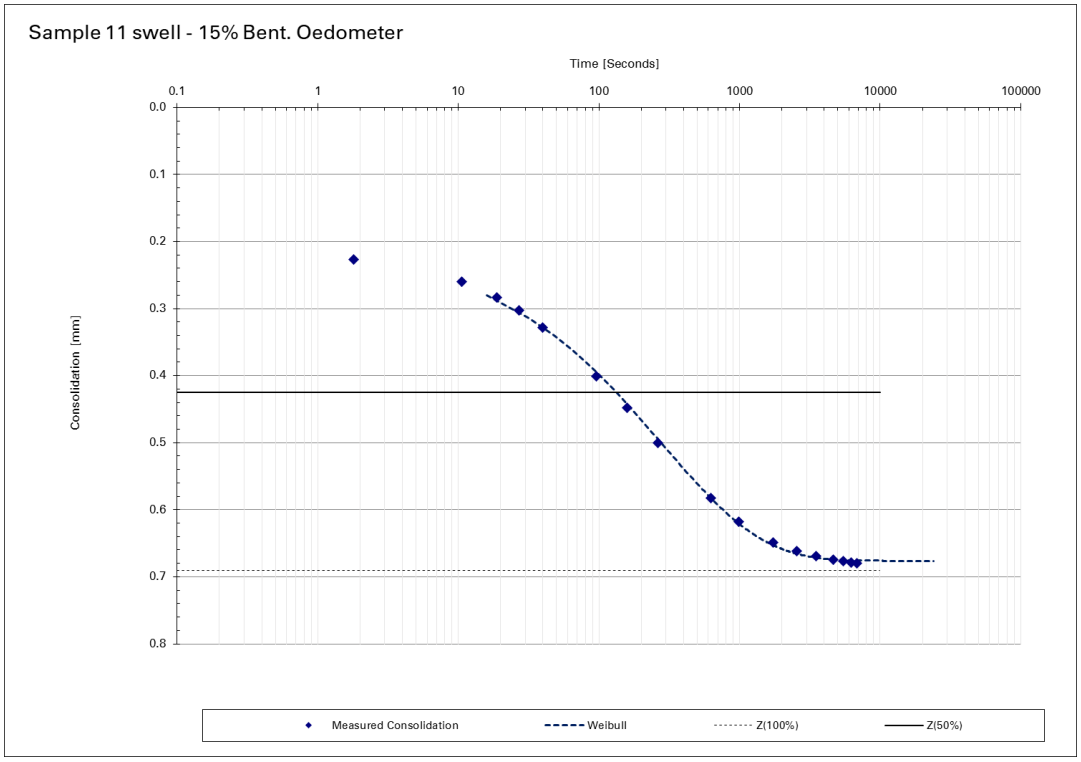

Figure A.29: Oedometer measurement graph sample 11 - 15% Bent. Unload

Table A.30: Oedometer test - Sample 11 - 15% Bent. Stage 3

Oedometer test				
Sample NO#	11 15% Bent - Stage 3			
Ring diameter:	64.925	Height sample (ring-0.5mm):	19.5	
Surface ring [mm2]	3311	Stress increase [kPa]	64.1	
Mass ring [g]:	38.68	Mass sample [g]	150.56	
Mass blocks [g]:	5002.04	Mass measuredevice [g]	2580	
Date [dd/mm]	Time [hh:mm:ss]	Readout [mm]		seconds
4-Nov	17:22:58	1.98	Initial readout	0
4-Nov	17:23:04	2.1	direct @ start	6
4-Nov	17:23:13	2.13		15
4-Nov	17:23:32	2.19		33
4-Nov	17:24:21	2.298		83
4-Nov	17:24:57	2.345		119
4-Nov	17:25:52	2.388		174
4-Nov	17:29:47	2.437		409
4-Nov	17:35:41	2.452		763
4-Nov	17:39:33	2.457		995
4-Nov	17:44:50	2.461		1312
4-Nov	17:54:51	2.466		1912

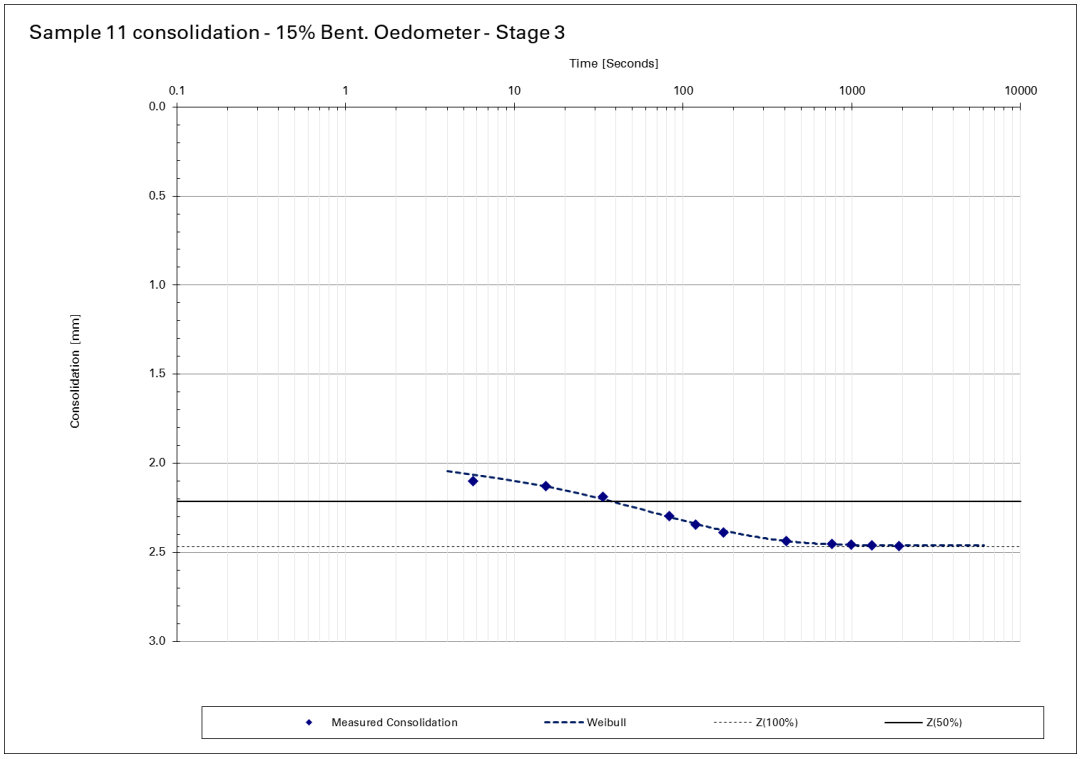

Figure A.30: Oedometer measurement graph sample 11 - 15% Bent. Stage 3

Table A.31: Oedometer test - Sample 6 - 5% Bent. Stage 1

Oedometer test				
Sample NO#	6 - 5% Bent.			
Ring diameter:	65.475	Height sample (ring-0.5mm):	19.5	
Surface ring [mm2]	3367	Stress [kPa]	11.9	
Mass ring [g]:	34.55	Mass sample [g]	148.67	
Mass blocks [g]:	1498.69	Mass measuredevice [g]	2580	
Date [dd/mm]	Time [hh:mm:ss]	Readout [mm]		seconds
7-Nov	10:25:50	0.089	Initial readout	0
7-Nov	10:26:01	0.121	direct @ start	11
7-Nov	10:26:09	0.14		19
7-Nov	10:26:18	0.155		28
7-Nov	10:26:27	0.17		37
7-Nov	10:26:52	0.205		62
7-Nov	10:27:26	0.245		96
7-Nov	10:27:55	0.275		125
7-Nov	10:28:22	0.3		152
7-Nov	10:29:31	0.355		220
7-Nov	10:30:48	0.405		298
7-Nov	10:31:55	0.441		365
7-Nov	10:34:07	0.495		497
7-Nov	10:37:00	0.54		670
7-Nov	10:46:10	0.593		1220
7-Nov	10:59:09	0.609		1999
7-Nov	11:07:55	0.613		2524
7-Nov	11:15:51	0.615		3001
7-Nov	11:30:12	0.619		3862

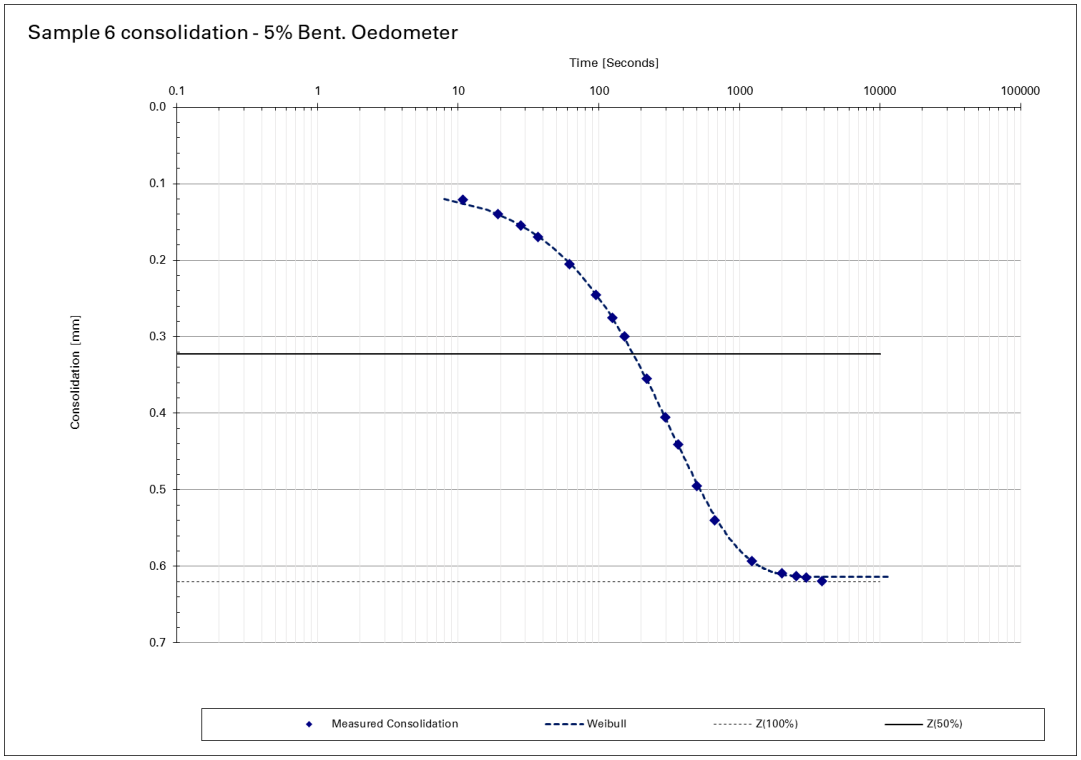

Figure A.31: Oedometer measurement graph sample 6 - 5% Bent.

Table A.32: Oedometer test - Sample 6 - 5% Bent. Unload

Oedometer test				
Sample NO#	6 - 5% Bent. - Unload			
Ring diameter:	65.475	Height sample (ring-0.5mm):	19.5	
Surface ring [mm2]	3367	Stress (decrease) [kPa]	9.6	
Mass ring [g]:	34.55	Mass sample [g]	151.6	
Mass blocks [g]:	1498.69	Mass measuredevice [g]	2580	
Date [dd/mm]	Time [hh:mm:ss]	Readout [mm]		seconds
7-Nov	11:31:03	0.619	Initial readout	0
7-Nov	11:31:21	0.617	direct @ start	18
7-Nov	11:31:31	0.61		28
7-Nov	11:31:39	0.607		36
7-Nov	11:31:56	0.602		53
7-Nov	11:32:23	0.596		80
7-Nov	11:32:59	0.59		116
7-Nov	11:34:44	0.579		221
7-Nov	11:37:33	0.571		390
7-Nov	11:41:17	0.565		614
7-Nov	11:45:53	0.563		890
7-Nov	11:51:16	0.561		1213
7-Nov	11:55:59	0.56		1496
7-Nov	12:08:00	0.559		2217
7-Nov	12:19:13	0.558		2890
7-Nov	12:27:31	0.558		3388

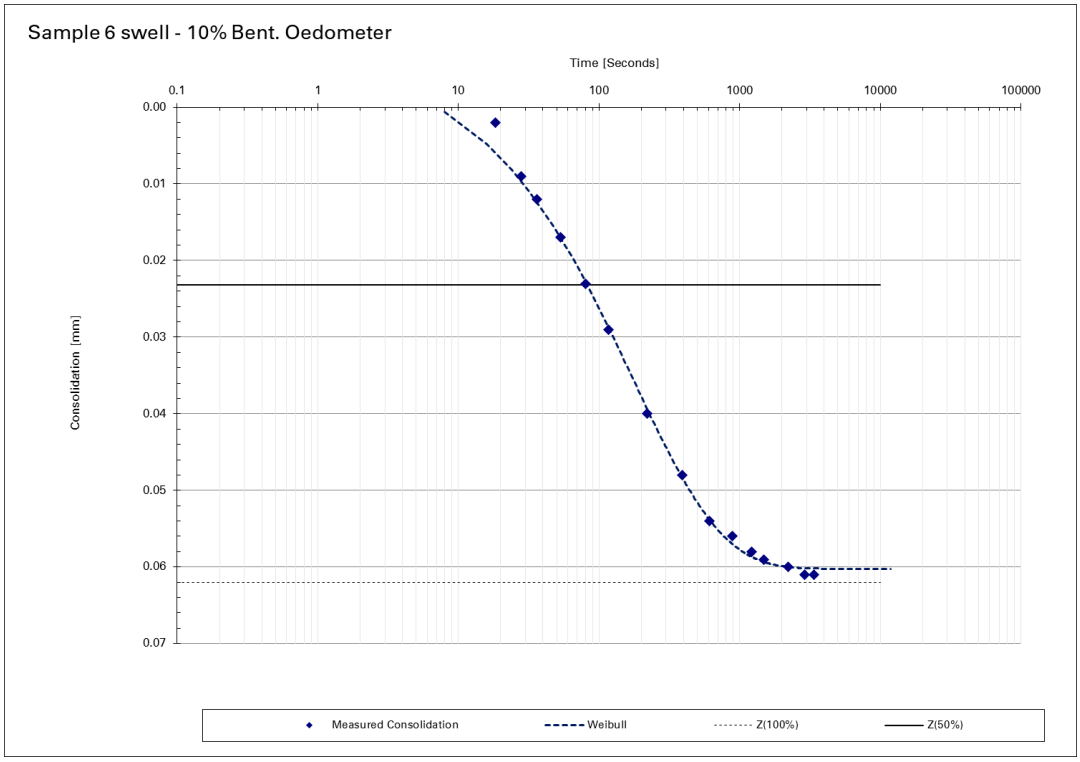

Figure A.32: Oedometer measurement graph sample 6 - 5% Bent. Unload

Table A.33: Oedometer test - Sample 14 - Kaolin Stage 1

Oedometer test				
Sample NO#	14 - Kaolin (sib)			
Ring diameter:	64.925	Height sample (ring-0.5mm):	19.5	
Surface ring [mm2]	3311	Stress [kPa]	12.1	
Mass ring [g]:	38.68	Mass sample [g]	148.7	
Mass blocks [g]:	1507.5	Mass measuredevice [g]	2580	
Date [dd/mm]	Time [hh:mm:ss]	Readout [mm]		seconds
7-Nov	10:00:21	0.24	Initial readout	0
7-Nov	10:00:25	0.247	direct @ start	5
7-Nov	10:00:32	0.27		12
7-Nov	10:00:41	0.29		20
7-Nov	10:00:52	0.31		31
7-Nov	10:01:08	0.335		47
7-Nov	10:01:32	0.365		71
7-Nov	10:02:21	0.415		120
7-Nov	10:03:02	0.45		161
7-Nov	10:04:26	0.511		246
7-Nov	10:05:16	0.541		295
7-Nov	10:06:52	0.593		391
7-Nov	10:08:41	0.643		500
7-Nov	10:10:00	0.675		579
7-Nov	10:13:54	0.746		814
7-Nov	10:18:59	0.799		1118
7-Nov	10:26:37	0.834		1576
7-Nov	10:34:18	0.847		2037
7-Nov	10:39:21	0.851		2341
7-Nov	10:45:58	0.855		2738
7-Nov	10:59:31	0.859		3550
7-Nov	11:07:10	0.861		4009
7-Nov	11:19:09	0.863		4728

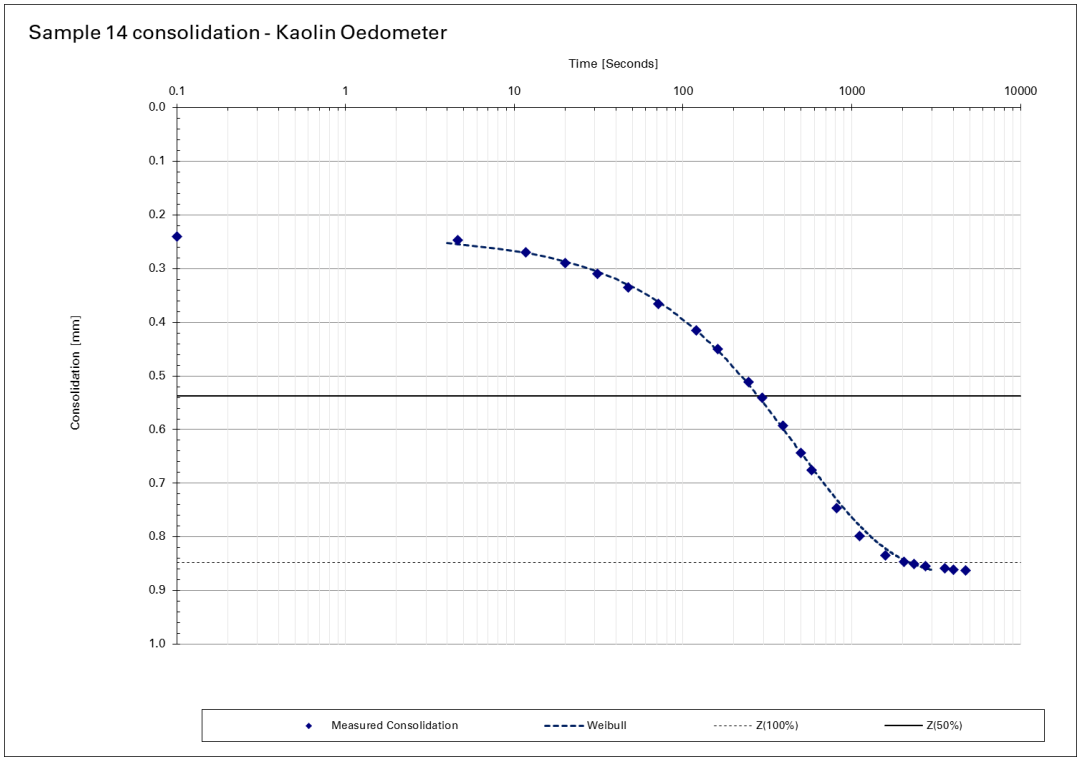

Figure A.33: Oedometer measurement graph sample 14 - Kaolin Stage 1

Table A.34: Oedometer test - Sample 14 - Kaolin Unload

Oedometer test				
Sample NO#	14 Kaolin - Unload			
Ring diameter:	64.925	Height sample (ring-0.5mm):	19.5	
Surface ring [mm2]	3311	Stress (decrease) [kPa]	9.8	
Mass ring [g]:	38.68	Mass sample [g]	150.56	
Mass blocks [g]:	1507.5	Mass measuredevice [g]	2580	
Date [dd/mm]	Time [hh:mm:ss]	Readout [mm]		seconds
7-Nov	11:20:31	0.863	Initial readout	0
7-Nov	11:20:33	0.804	direct @ start	2
7-Nov	11:20:41	0.795		9
7-Nov	11:20:54	0.79		22
7-Nov	11:21:12	0.782		41
7-Nov	11:21:50	0.771		78
7-Nov	11:22:34	0.762		123
7-Nov	11:23:40	0.753		188
7-Nov	11:25:12	0.745		280
7-Nov	11:28:20	0.736		468
7-Nov	11:33:09	0.729		757
7-Nov	11:37:24	0.726		1012
7-Nov	11:41:47	0.725		1276
7-Nov	11:46:03	0.723		1531
7-Nov	11:51:05	0.722		1833
7-Nov	11:55:41	0.721		2110
7-Nov	12:07:49	0.72		2838
7-Nov	12:19:23	0.719		3531
7-Nov	12:27:14	0.718		4003

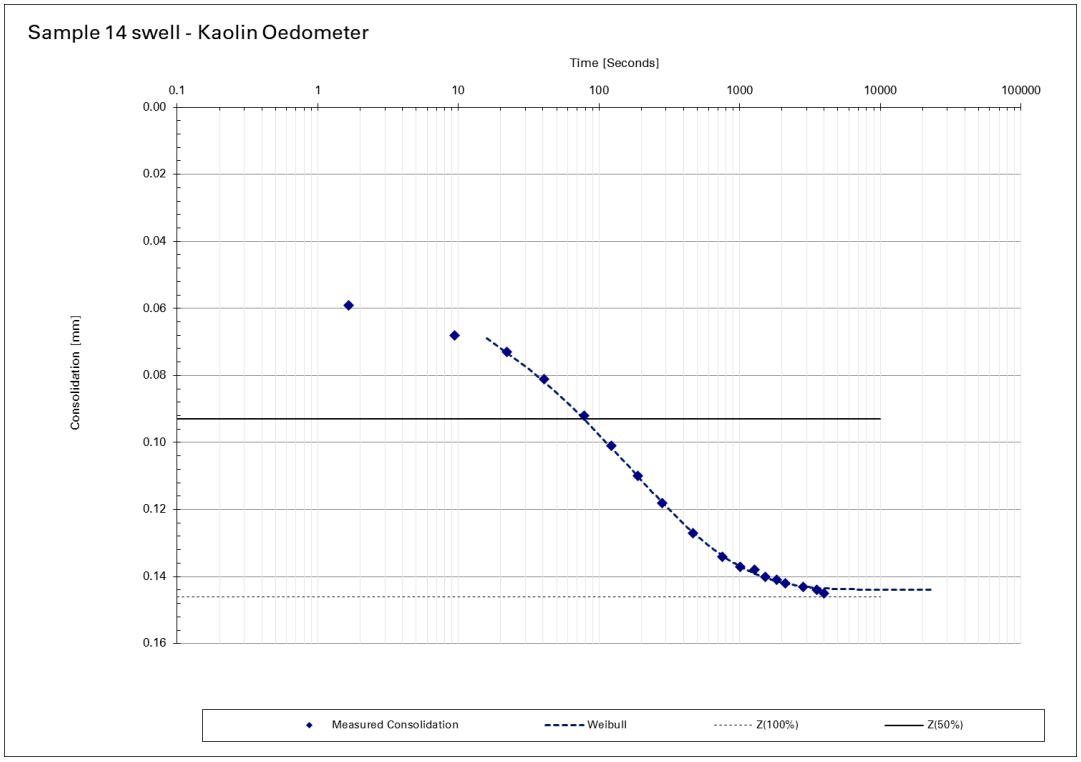

Figure A.34: Oedometer measurement graph sample 14 - Kaolin Unload

Table A.35: Oedometer test - Sample 13 - 25% Bent. Stage 1

Oedometer test				
Sample NO#	13 - 25% Bent.			
Ring diameter:	65.475	Height sample (ring-0.5mm):	19.5	
Surface ring [mm2]	3367	Stress [kPa]	11.9	
Mass ring [g]:	34.55	Mass sample [g]	153	
Mass blocks [g]:	1498.69	Mass measuredevice [g]	2580	
Date [dd/mm]	Time [hh:mm:ss]	Readout [mm]		seconds
22-Nov	11:13:41	0.024	Initial readout	0
22-Nov	11:13:44	0.197	direct @ start	2
22-Nov	11:13:51	0.226		10
22-Nov	11:14:04	0.245		23
22-Nov	11:14:10	0.27		28
22-Nov	11:14:18	0.285		36
22-Nov	11:14:36	0.315		55
22-Nov	11:15:15	0.365		94
22-Nov	11:15:51	0.404		129
22-Nov	11:17:07	0.472		206
22-Nov	11:18:26	0.53		285
22-Nov	11:20:40	0.609		419
22-Nov	11:23:13	0.679		572
22-Nov	11:31:37	0.821		1075
22-Nov	11:35:25	0.856		1304
22-Nov	11:39:24	0.879		1543
22-Nov	11:42:56	0.894		1755
22-Nov	11:50:42	0.911		2221
22-Nov	11:58:40	0.92		2698
22-Nov	12:05:04	0.925		3083
22-Nov	12:16:19	0.93		3758
22-Nov	12:24:40	0.932		4259
22-Nov	12:37:47	0.935		5046
22-Nov	12:44:28	0.936		5447

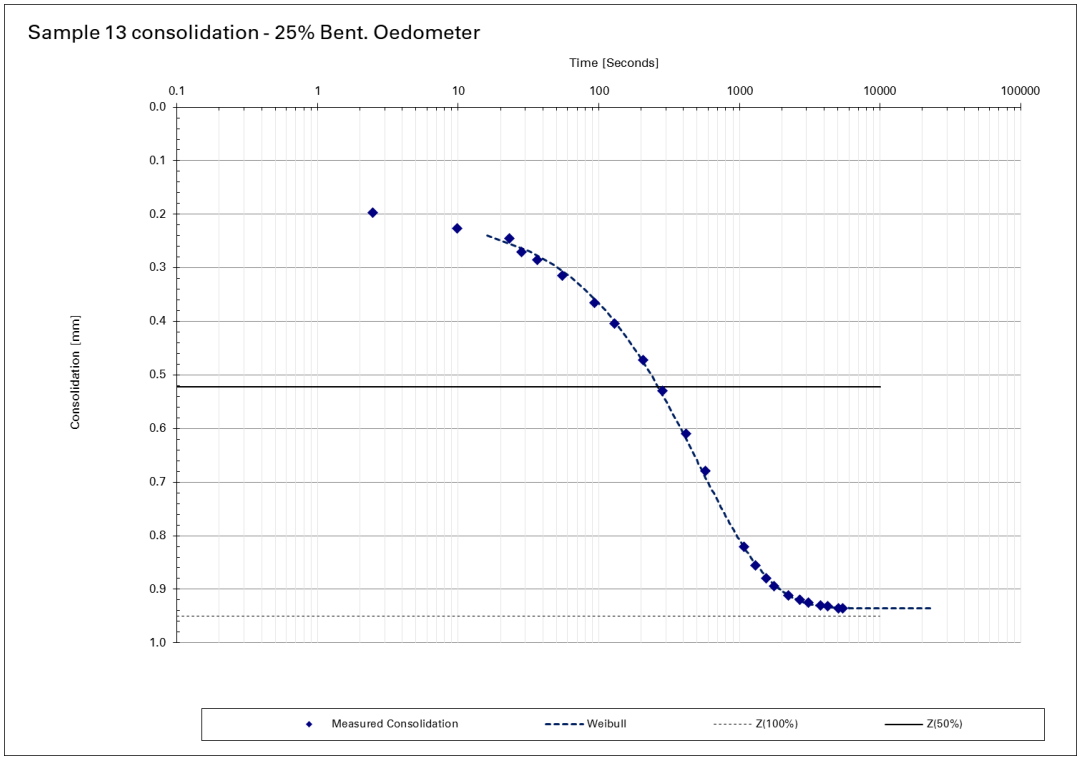

Figure A.35: Oedometer measurement graph sample 13 - 25% Bent. Stage 1

Table A.36: Oedometer test - Sample 13 - 25% Bent. Unload

Oedometer test				
Sample NO#	13 25% Bent. Unload			
Ring diameter:	65.475	Height sample (ring-0.5mm):	19.5	
Surface ring [mm2]	3367	Stress (decrease) [kPa]	9.6	
Mass ring [g]:	34.55	Mass sample [g]	153	
Mass blocks [g]:	1498.69	Mass measuredevice [g]	2580	
Date [dd/mm]	Time [hh:mm:ss]	Readout [mm]		seconds
22-Nov	12:45:11	0.936	Initial readout	0.0
22-Nov	12:45:14	0.927	direct @ start	2.1
22-Nov	12:45:24	0.921		12.3
22-Nov	12:45:35	0.917		23.6
22-Nov	12:46:01	0.909		49.6
22-Nov	12:46:15	0.906		63.7
22-Nov	12:47:06	0.898		114.7
22-Nov	12:48:14	0.89		182.5
22-Nov	12:48:51	0.887		219.7
22-Nov	12:50:22	0.881		310.9
22-Nov	12:52:16	0.876		424.6
22-Nov	12:53:45	0.873		513.4
22-Nov	12:55:50	0.87		638.6
22-Nov	13:01:43	0.866		991.7
22-Nov	13:07:56	0.863		1364.8
22-Nov	13:20:28	0.861		2116.6
22-Nov	13:30:38	0.86		2727.0
22-Nov	13:46:13	0.859		3661.5
22-Nov	14:02:16	0.859		4624.8

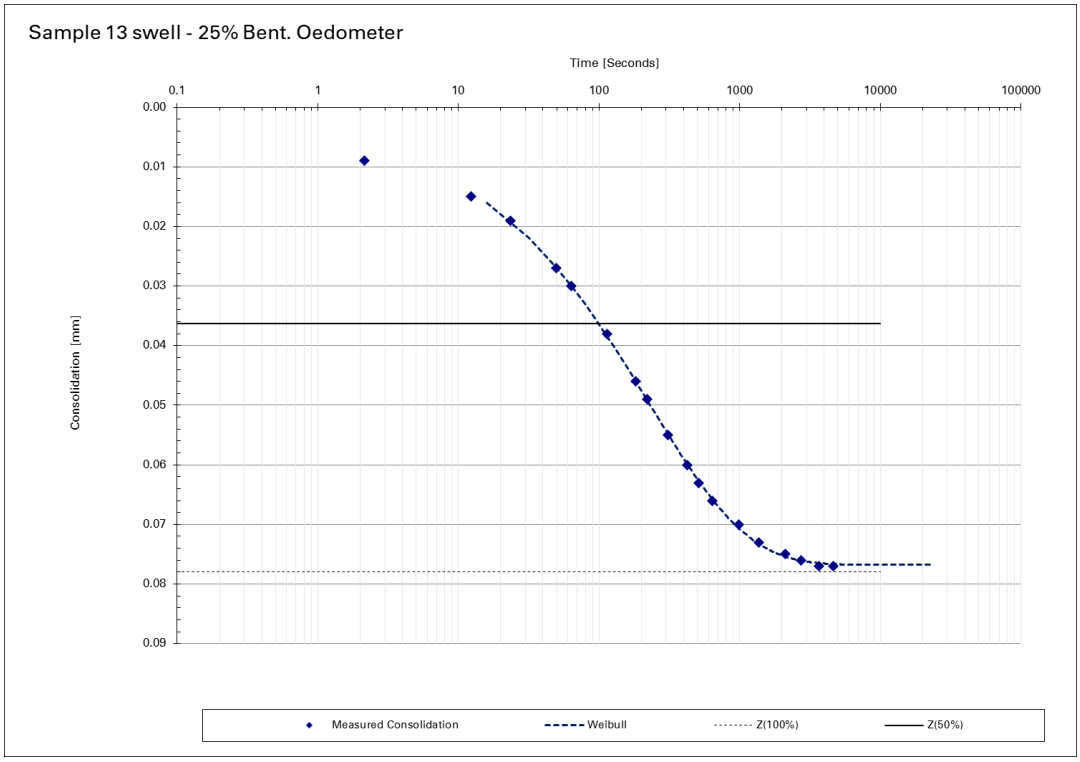

Figure A.36: Oedometer measurement graph sample 13 - 25% Bent. Unload

Table A.37: Oedometer test - Sample 13 - 25% Bent. Stage 2

Oedometer test				
Sample NO#	13 - 25% Bent. - Stage 2			
Ring diameter:	65.475	Height sample (ring-0.5mm):	19.5	
Surface ring [mm2]	3367	Stress [kPa]	9.6	
Mass ring [g]:	34.55	Mass sample [g]	153	
Mass blocks [g]:	1498.69	Mass measuredevice [g]	2580	
Date [dd/mm]	Time [hh:mm:ss]	Readout [mm]		seconds
22-Nov	14:13:10	0.907	Initial readout	0
22-Nov	14:13:13	0.914	direct @ start	2
22-Nov	14:13:19	0.915		8
22-Nov	14:13:32	0.921		22
22-Nov	14:14:05	0.932		54
22-Nov	14:14:34	0.94		83
22-Nov	14:16:04	0.957		173
22-Nov	14:18:08	0.969		297
22-Nov	14:19:10	0.972		359
22-Nov	14:21:38	0.978		508
22-Nov	14:27:42	0.984		872
22-Nov	14:31:48	0.987		1118
22-Nov	14:44:50	0.991		1900
22-Nov	14:54:49	0.992		2498
22-Nov	15:05:01	0.994		3110
22-Nov	15:16:20	0.995		3789

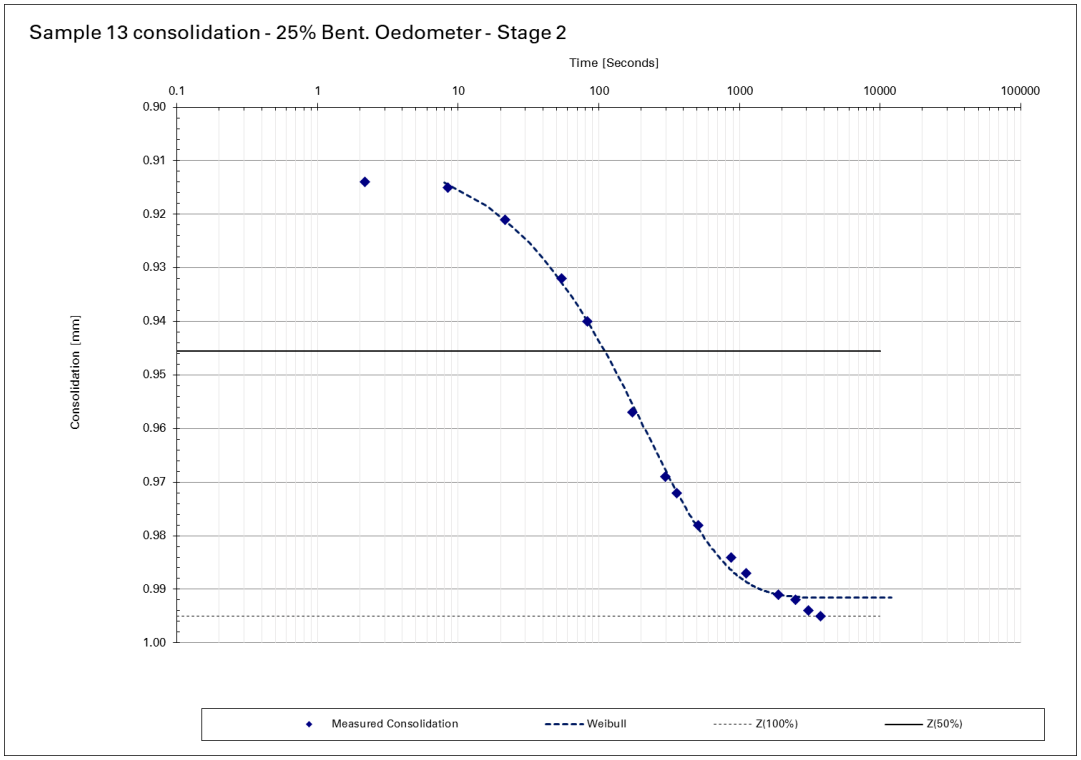

Figure A.37: Oedometer measurement graph sample 13 - 25% Bent. Stage 2

Table A.38: Oedometer test - Sample 13 - 25% Bent. Stage 3

Oedometer test				
Sample NO#	13 - 25% Bent. - Stage 3			
Ring diameter:	65.475	Height sample (ring-0.5mm):	19.5	
Surface ring [mm2]	3367	Stress [kPa]	18.9	
Mass ring [g]:	34.55	Mass sample [g]	153	
Mass blocks [g]:	1498.69	Mass measuredevice [g]	2580	
Date [dd/mm]	Time [hh:mm:ss]	Readout [mm]		seconds
22-Nov	15:29:54	0.978	Initial readout	0
22-Nov	15:29:56	1.005	direct @ start	2
22-Nov	15:30:03	1.018		9
22-Nov	15:30:18	1.037		24
22-Nov	15:30:36	1.055		42
22-Nov	15:30:52	1.068		58
22-Nov	15:31:26	1.091		92
22-Nov	15:32:01	1.111		127
22-Nov	15:32:31	1.126		157
22-Nov	15:33:07	1.141		193
22-Nov	15:33:58	1.158		244
22-Nov	15:36:35	1.195		401
22-Nov	15:38:06	1.21		491
22-Nov	15:42:46	1.238		771
22-Nov	15:45:42	1.248		948
22-Nov	15:50:10	1.258		1216
22-Nov	16:03:27	1.272		2013
22-Nov	16:09:48	1.276		2394
22-Nov	16:20:17	1.281		3023
22-Nov	16:25:30	1.282		3336
22-Nov	16:38:44	1.286		4130
22-Nov	16:45:23	1.287		4529

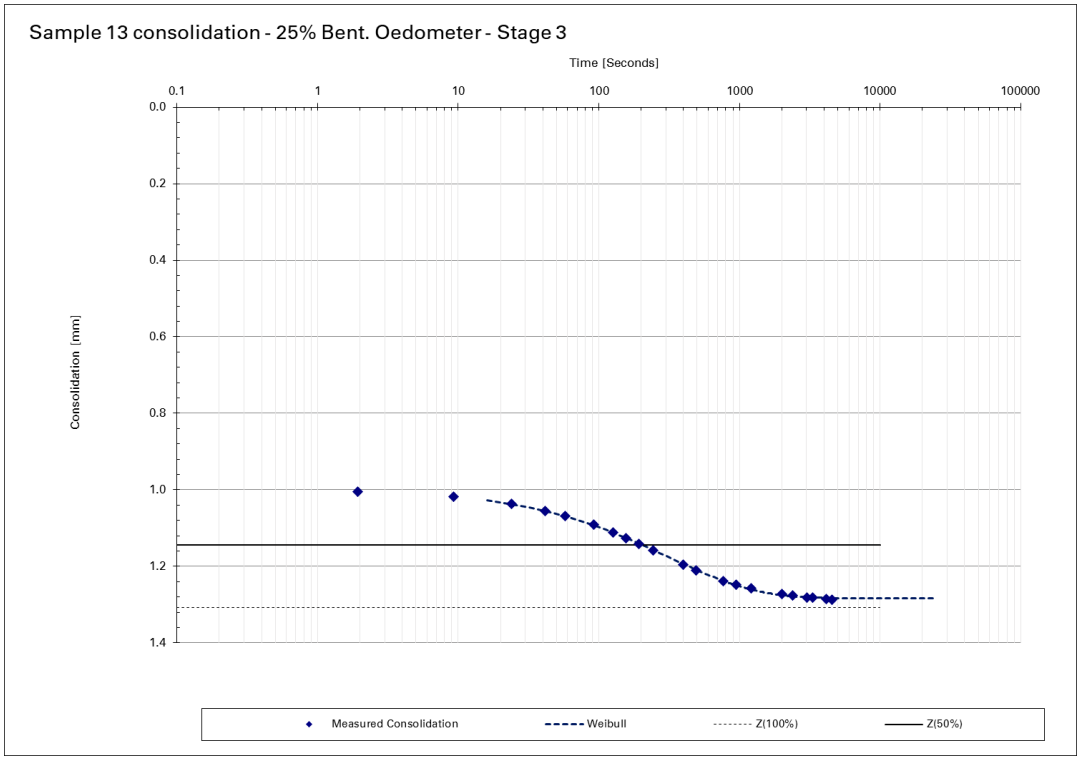

Figure A.38: Oedometer measurement graph sample 13 - 25% Bent. Stage 3

Table A.39: Oedometer test - Sample 17 - Kaolin-Sand Stage 1

Oedometer test				
Sample NO#	17 - Kaolin sand			
Ring diameter:	64.925	Height sample (ring-0.5mm):	19.5	
Surface ring [mm2]	3311	Stress [kPa]	12.1	
Mass ring [g]:	38.68	Mass sample [g]	148.7	
Mass blocks [g]:	1507.5	Mass measuredevice [g]	2580	
Date [dd/mm]	Time [hh:mm:ss]	Readout [mm]		seconds
22-Nov	11:46:09	0.011	Initial readout	0
22-Nov	11:46:10	0.197	direct @ start	1
22-Nov	11:46:16	0.233		7
22-Nov	11:46:22	0.257		12
22-Nov	11:46:30	0.286		21
22-Nov	11:46:51	0.333		42
22-Nov	11:47:02	0.365		53
22-Nov	11:47:42	0.44		93
22-Nov	11:48:24	0.51		134
22-Nov	11:49:17	0.581		188
22-Nov	11:51:22	0.692		312
22-Nov	11:54:09	0.775		480
22-Nov	11:56:09	0.802		599
22-Nov	11:58:19	0.82		730
22-Nov	12:04:49	0.835		1119
22-Nov	12:09:46	0.839		1416
22-Nov	12:16:07	0.842		1797
22-Nov	12:24:56	0.844		2326
22-Nov	12:38:01	0.846		3112
22-Nov	12:50:43	0.848		3873

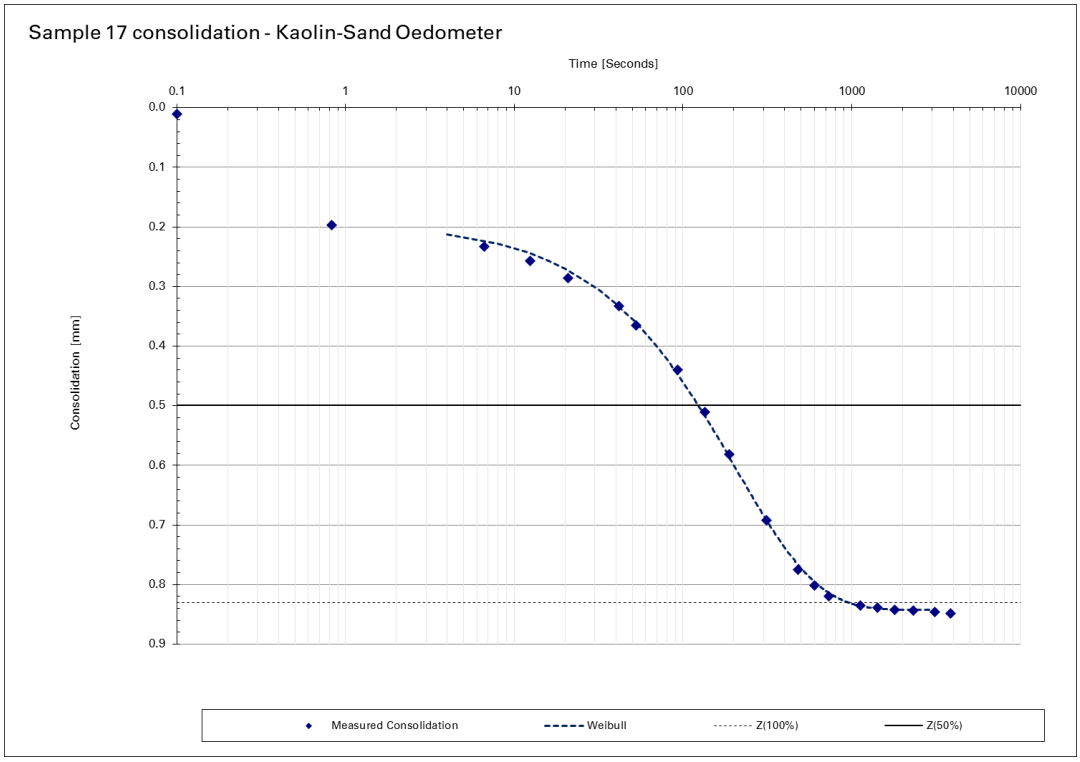

Figure A.39: Oedometer measurement graph sample 17 - Kaolin-Sand Stage 1

Table A.40: Oedometer test - Sample 17 - Kaolin-Sand Unload

Oedometer test				
Sample NO#	17 Kaolin_sand - Unload			
Ring diameter:	64.925	Height sample (ring-0.5mm):	19.5	
Surface ring [mm2]	3311	Stress (decrease) [kPa]	9.8	
Mass ring [g]:	38.68	Mass sample [g]	150.56	
Mass blocks [g]:	1507.5	Mass measuredevice [g]	2580	
Date [dd/mm]	Time [hh:mm:ss]	Readout [mm]		seconds
22-Nov	12:51:15	0.967	Initial readout	0
22-Nov	12:51:21	0.965	direct @ start	6
22-Nov	12:51:28	0.959		13
22-Nov	12:51:42	0.952		27
22-Nov	12:52:01	0.946		46
22-Nov	12:53:35	0.933		140
22-Nov	12:55:40	0.928		265
22-Nov	13:01:33	0.924		618
22-Nov	13:08:07	0.923		1012
22-Nov	13:20:19	0.922		1744
22-Nov	13:30:27	0.921		2352
22-Nov	13:46:04	0.92		3289
22-Nov	14:01:57	0.92		4242

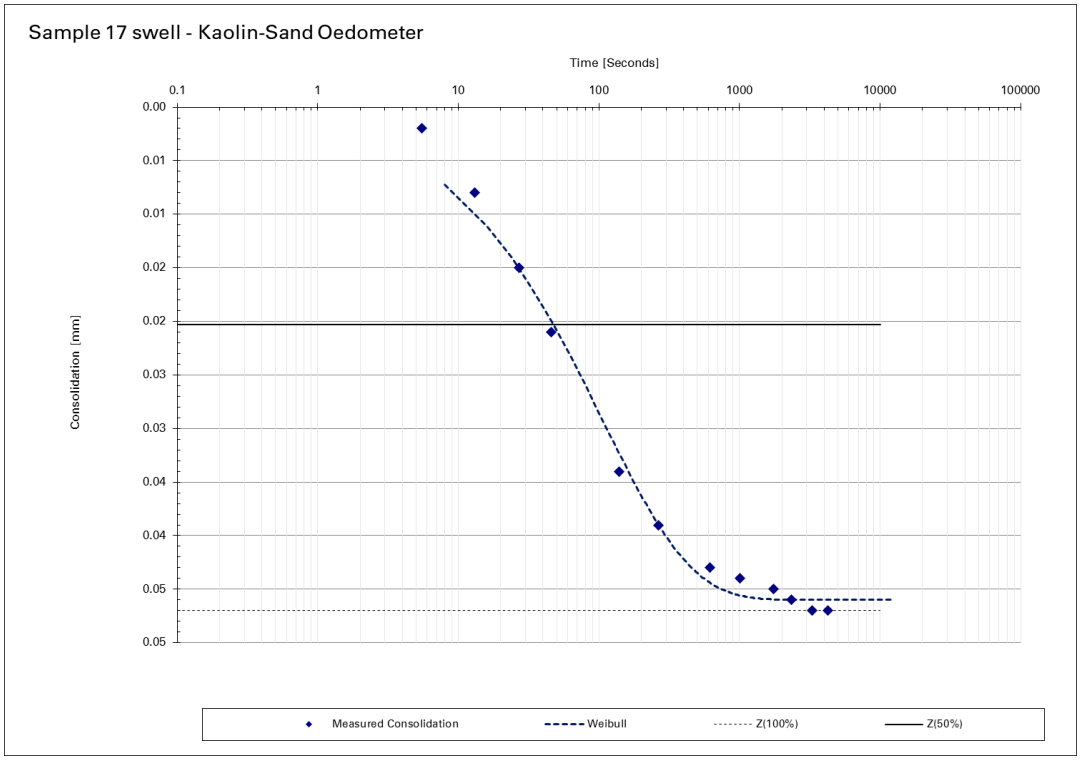

Figure A.40: Oedometer measurement graph sample 17 - Kaolin-Sand Unload

Table A.41: Oedometer test - Sample 17 - Kaolin-Sand Stage 2

Oedometer test				
Sample NO#	17 - Kaolin sand - Stage 2			
Ring diameter:	64.925	Height sample (ring-0.5mm):	19.5	
Surface ring [mm2]	3311	Stress [kPa]	9.8	
Mass ring [g]:	38.68	Mass sample [g]	148.7	
Mass blocks [g]:	1507.5	Mass measuredevice [g]	2580	
Date [dd/mm]	Time [hh:mm:ss]	Readout [mm]		seconds
22-Nov	14:17:28	0.87	Initial readout	0
22-Nov	14:17:31	0.875	direct @ start	3
22-Nov	14:17:40	0.888		12
22-Nov	14:17:53	0.899		25
22-Nov	14:18:19	0.913		51
22-Nov	14:18:57	0.922		89
22-Nov	14:19:23	0.927		115
22-Nov	14:21:21	0.935		233
22-Nov	14:27:52	0.942		624
22-Nov	14:31:38	0.944		850
22-Nov	14:44:34	0.947		1626
22-Nov	14:55:51	0.948		2303
22-Nov	15:04:45	0.949		2837
22-Nov	15:16:40	0.95		3552

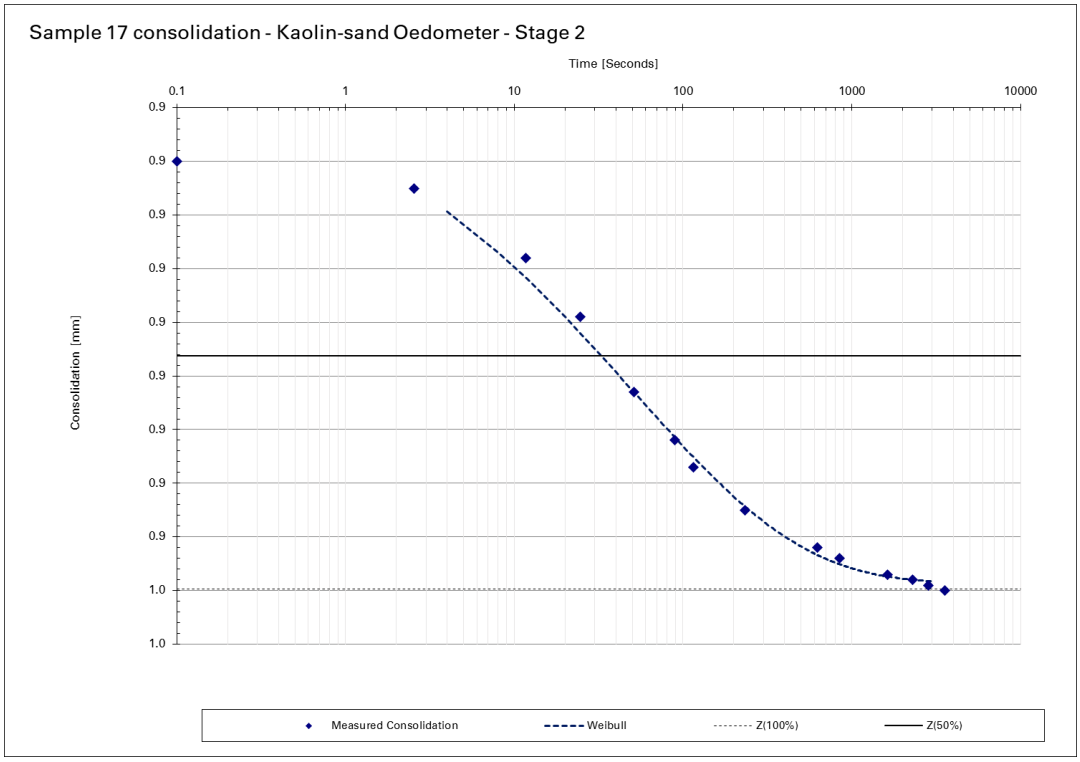

Figure A.41: Oedometer measurement graph sample 17 - Kaolin-Sand Stage 2

Table A.42: Oedometer test - Sample 17 - Kaolin-Sand Stage 3

Oedometer test				
Sample NO#	17 - Kaolin sand - Stage 3			
Ring diameter:	64.925	Height sample (ring-0.5mm):	19.5	
Surface ring [mm2]	3311	Stress [kPa]	19.3	
Mass ring [g]:	38.68	Mass sample [g]	148.7	
Mass blocks [g]:	1507.5	Mass measuredevice [g]	2580	
Date [dd/mm]	Time [hh:mm:ss]	Readout [mm]		seconds
22-Nov	15:35:51	1.74	Initial readout	0
22-Nov	15:35:54	1.777	direct @ start	2
22-Nov	15:36:02	1.82		11
22-Nov	15:36:14	1.859		23
22-Nov	15:36:26	1.888		35
22-Nov	15:36:50	1.93		58
22-Nov	15:37:52	1.988		121
22-Nov	15:39:06	2.023		195
22-Nov	15:41:40	2.04		349
22-Nov	15:46:05	2.048		614
22-Nov	15:49:56	2.05		845
22-Nov	15:57:03	2.053		1272
22-Nov	16:03:00	2.055		1629
22-Nov	16:10:19	2.056		2068
22-Nov	16:25:10	2.058		2959
22-Nov	16:36:08	2.06		3617

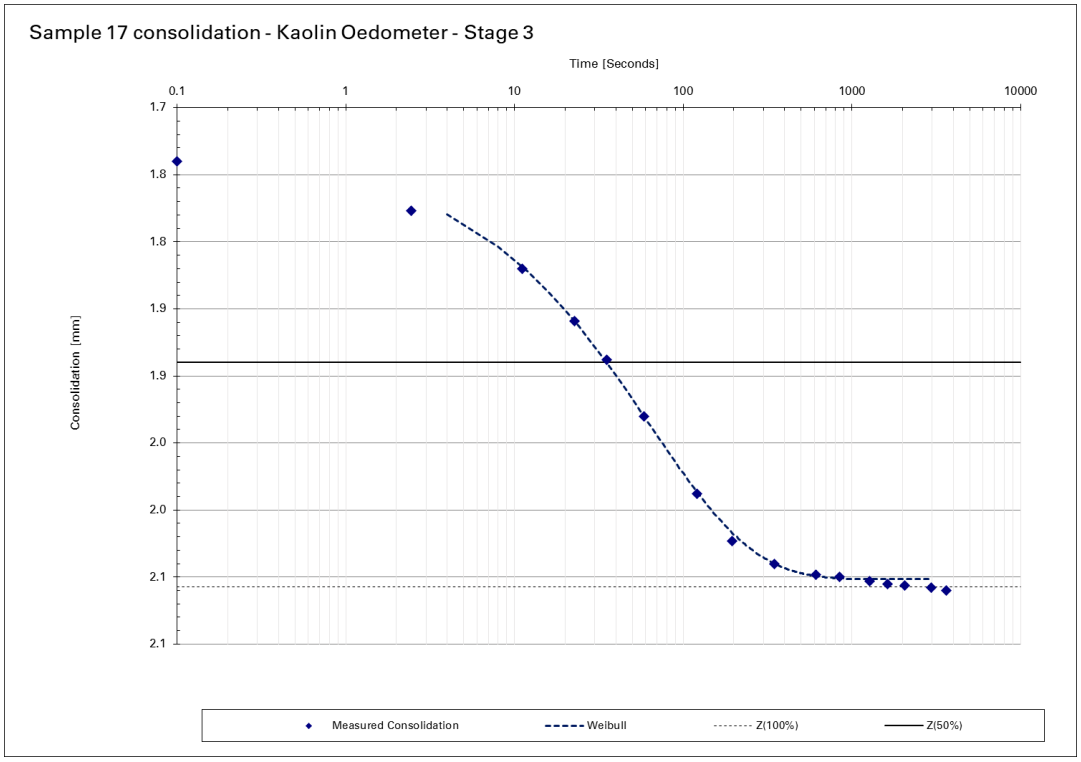

Figure A.42: Oedometer measurement graph sample 17 - Kaolin-Sand Stage 3

Table A.43: Oedometer test - Sample 19 - Kaolin Stage 1

Oedometer test				
Sample NO#	19 - Kaolin			
Ring diameter:	65.025	Height sample (ring-0.5mm):	19.5	
Surface ring [mm2]	3321	Stress [kPa]	22.4	
Mass ring [g]:	38.64	Mass sample [g]	150	
Mass blocks [g]:	5006.33	Mass measuredevice [g]	2580	
Date [dd/mm]	Time [hh:mm:ss]	Readout [mm]		seconds
.	12:03:53	0.9	Initial readout	0
19-Dec	12:03:55	1.21	direct @ start	2
19-Dec	12:04:05	1.256		12
19-Dec	12:04:29	1.309		36
19-Dec	12:04:42	1.34		49
19-Dec	12:05:13	1.403		79
19-Dec	12:05:47	1.465		114
19-Dec	12:06:25	1.527		151
19-Dec	12:06:59	1.58		186
19-Dec	12:07:48	1.65		234
19-Dec	12:08:41	1.721		287
19-Dec	12:11:13	1.885		440
19-Dec	12:15:25	2.06		691
19-Dec	12:20:51	2.155		1018
19-Dec	12:27:59	2.192		1445
19-Dec	12:30:37	2.198		1604
19-Dec	12:36:40	2.205		1966
19-Dec	12:40:51	2.209		2218
19-Dec	12:49:31	2.213		2737
19-Dec	13:10:20	2.219		3986
19-Dec	15:27:29	2.231		12216

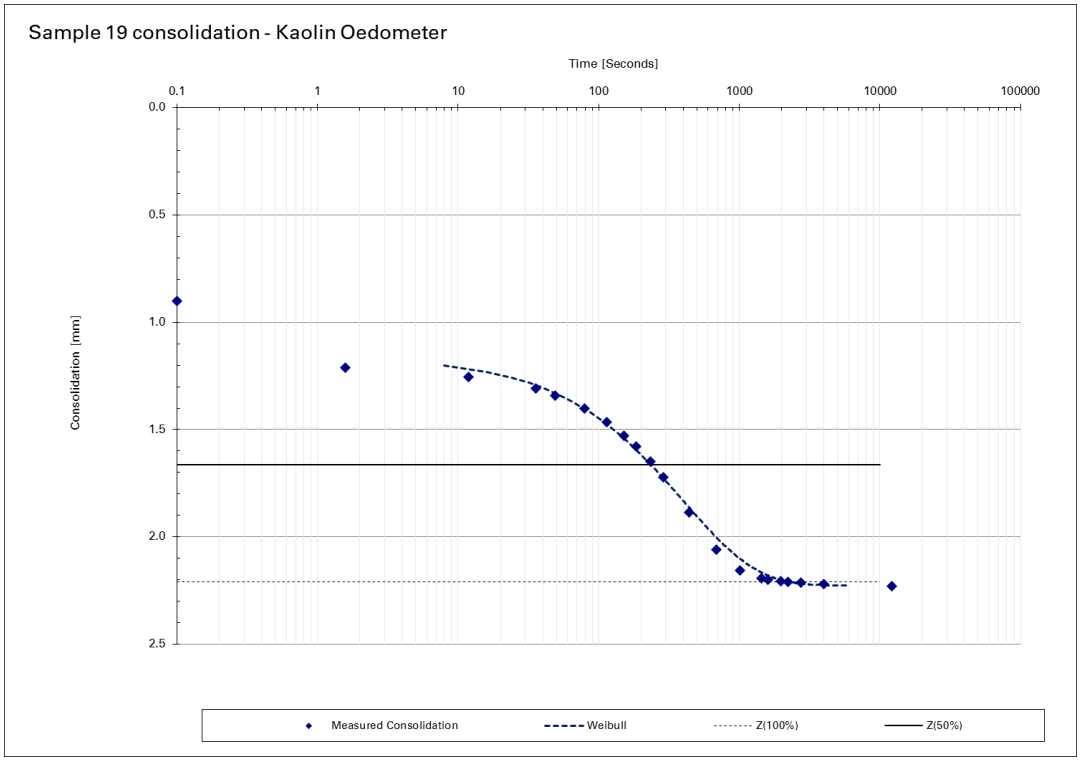

Figure A.43: Oedometer measurement graph sample 19 - Kaolin Stage 1

B

Jet testing Results

Table B.1: Test K_15_0.4_1

TEST_K_15_0.4_1			pre-test	su	post-test		section 1	section 2	section 3
Date	11/05/19	dd/mm/yy		kPa	xo	mm	230	-	-
u_0	3.46	m/s	pocket vane 1	9.84	yo	mm	-	160	-
Q	8.87E-04	m³/s	pocket vane 2	9.29	$Z_{c,cl}$	mm	99	-	-
s	147	mm	post-test	su	$Z_{c,max}$	mm	101	-	-
D_n	20	mm		kPa	$r_{Zc,max}$	mm	60	-	-
SOD/D_n	7.4	-	pocket vane 3	8.74					
$p_{stag,0}$	4.00	kPa	pocket vane 4	8.09	V_t	781	cm3	1.60	cm3/min
$p_{stag,0}/su$	0.42	-	field vane 1	9.00	V_{scale}	828	cm3	1.70	cm3/min
t_{tot}	487	min	field vane 2	9.75	V_{water1}	1000	cm3	2.05	cm3/min
m_{sub}	30595	gram	CPT	5	V_{water2}	1020	cm3	2.09	cm3/min
Notes:	Kaolin, Sample 14								

Test_K_20_15_0_4_1

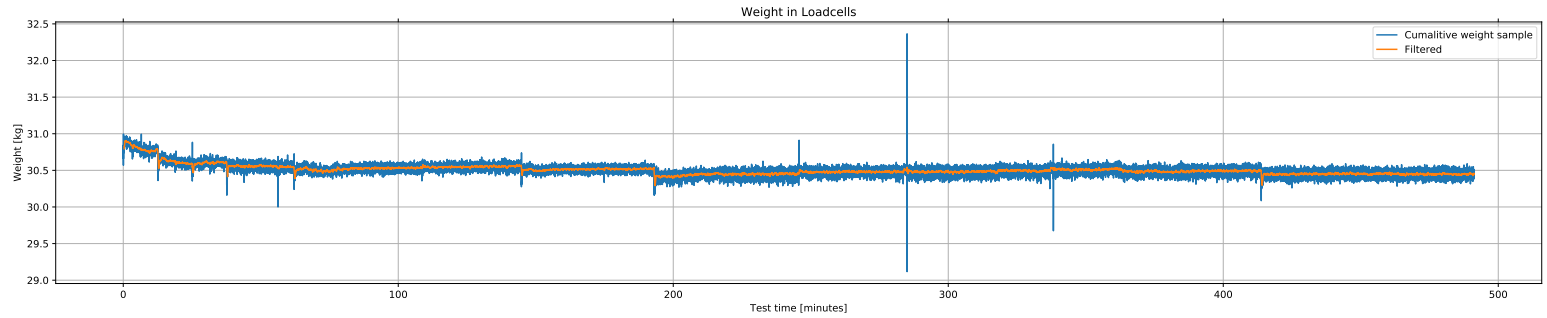

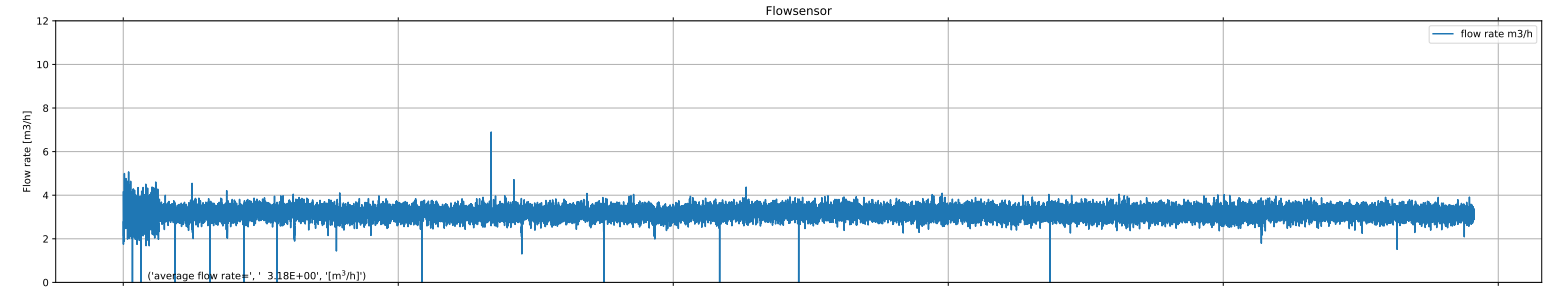

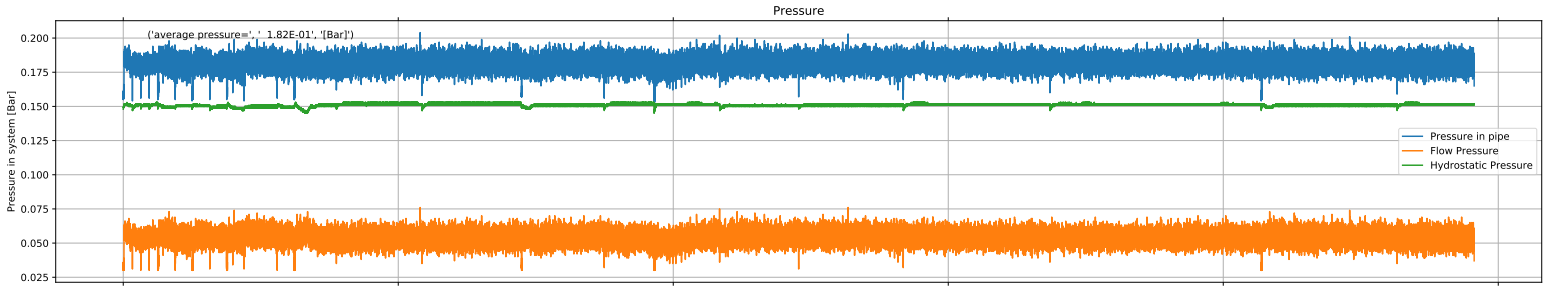

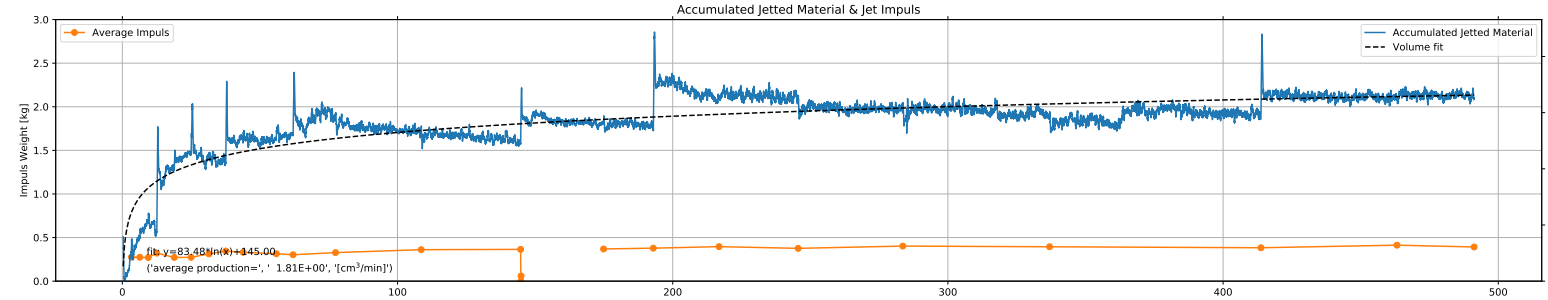

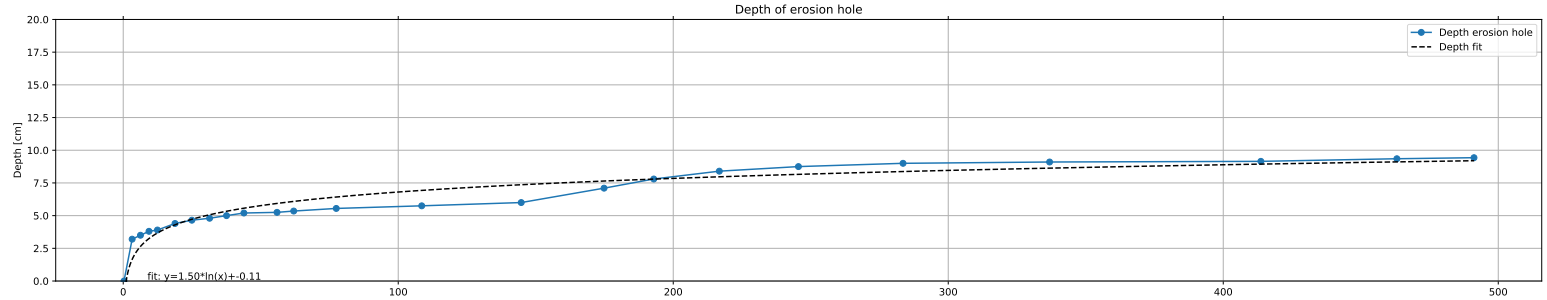

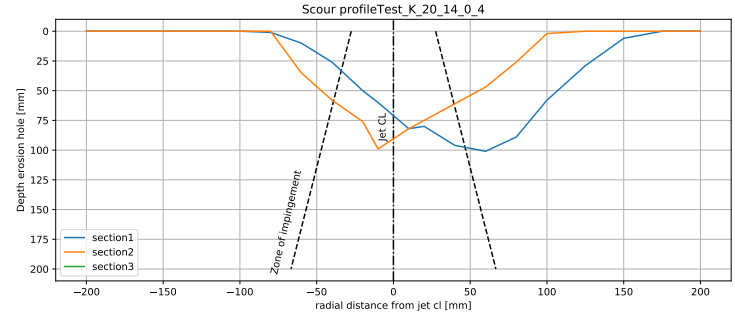

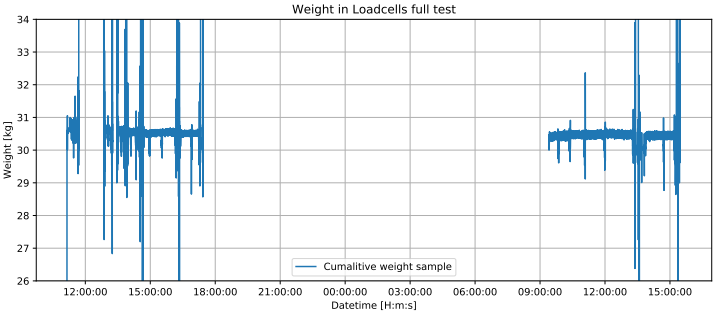

Table B.2: Test 5% Bent_15_0.4_1

TEST_5% Bent_15_0.4_1			pre-test	su	post-test		section 1	section 2	section 3
Date	10/21/19	dd/mm/yy		kPa	xo	mm	300	-	-
u_0	3.73	m/s	pocket vane 1	11.59	yo	mm	-	120	165
Q	9.73E-04	m³/s	pocket vane 2	11.15	$Z_{c,cl}$	mm	140	-	-
SOD	150	mm	post-test	su	$Z_{c,max}$	mm	143	-	-
D_n	20	mm		kPa	$r_{Zc,max}$	mm	20	-	-
SOD/D_n	7.5	-	pocket vane 3	9.18					
$p_{stag,0}$	4.71	kPa	pocket vane 4	7.65	V_t	1768	cm3	2.07	cm3/min
$p_{stag,0}/su$	0.44	-	field vane 1	10.50	V_{scale}	1787	cm3	2.09	cm3/min
t_{tot}	855	min	field vane 2	9.50	V_{water1}	1900	cm3	2.22	cm3/min
m_{sub}	31287	gram	CPT	12.00	V_{water2}	1950	cm3	2.28	cm3/min
Notes:	5% Bentonite, sample 8, jump in depth and weight around 500 min probably due to sample standing over night, 2nd stage, horizontal hole build out								

Test_5% Bent_20_15_0.4

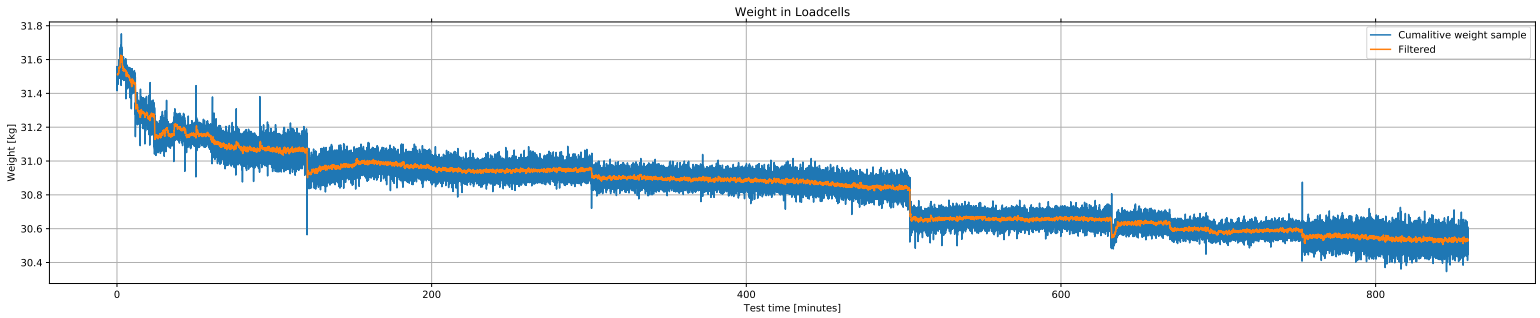

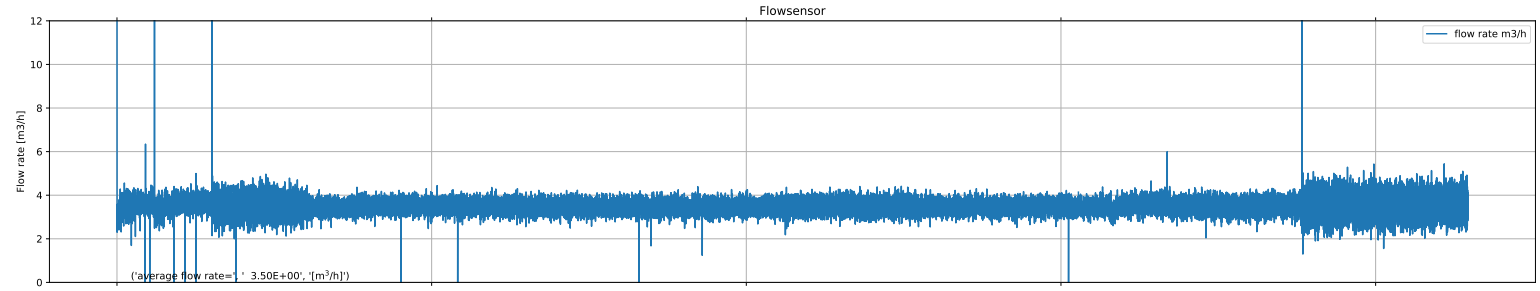

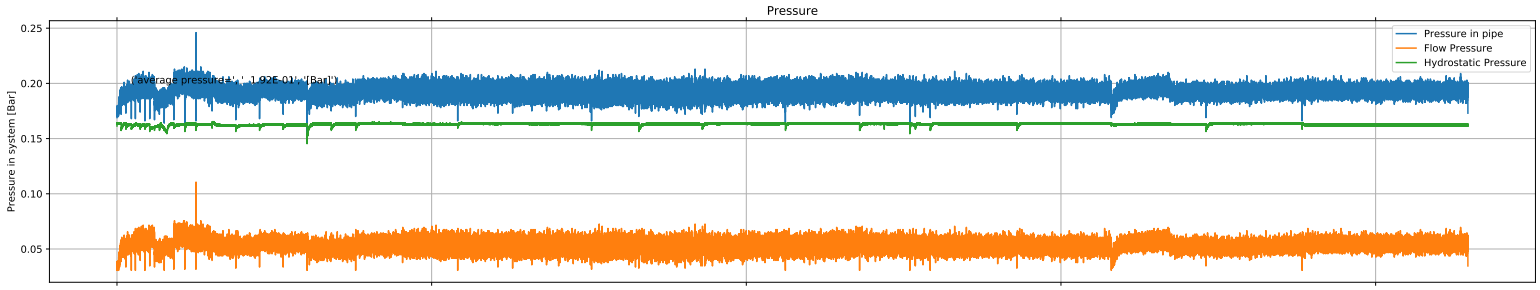

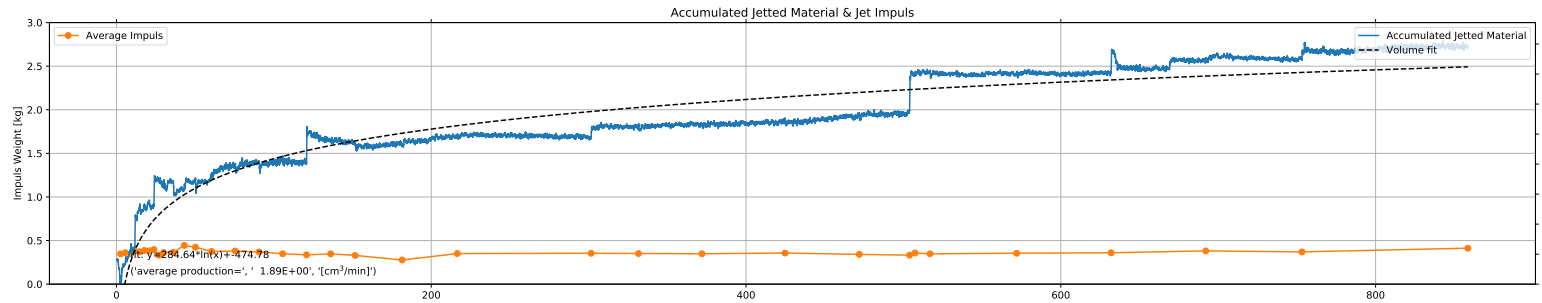

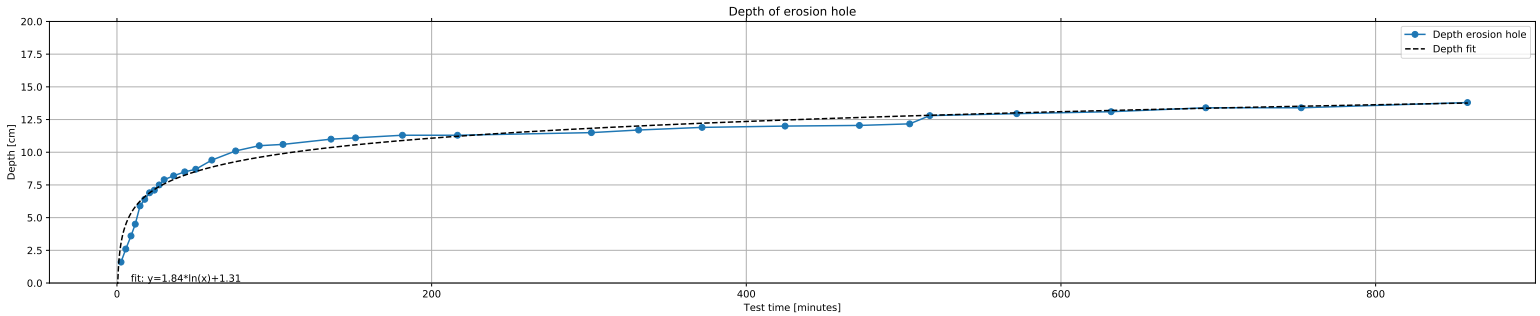

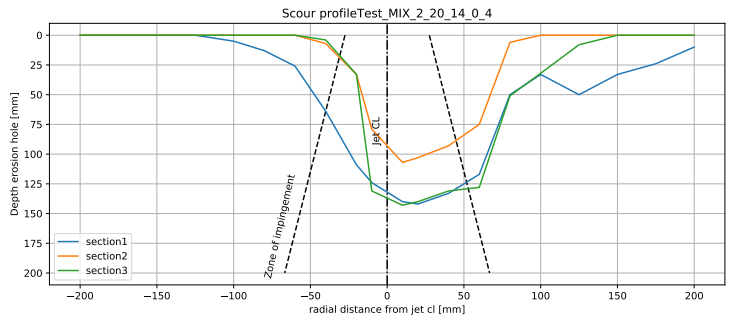

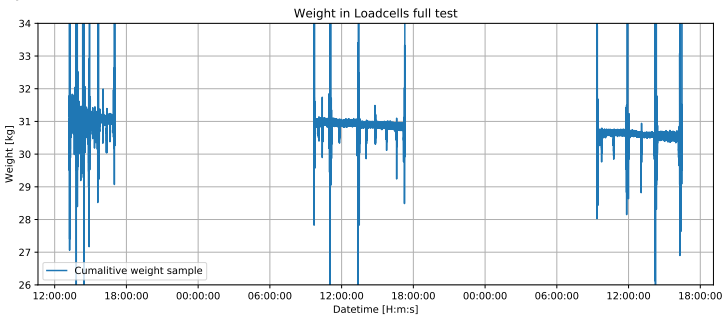

Table B.3: Test K_15_0.6_1

TEST_K_15_0.6_1			pre-test	su	post-test				
				kPa			section 1	section 2	section 3
Date	31/07/19	dd/mm/yy		kPa	xo	mm	185	-	-
u_0	4.8	m/s	pocket vane 1	9.6	yo	mm	-	260	0
Q	1.26E-03	m³/s	pocket vane 2	10.1	$Z_{c,cl}$	mm	197	-	-
SOD	152	mm	post-test	su	$Z_{c,max}$	mm	197	-	-
D_n	20	mm		kPa	$r_{Zc,max}$	mm	0	-	-
SOD/D_n	7.6	-	pocket vane 3	10.9					
$p_{stag,0}$	7.50	kPa	pocket vane 4	12	V_t	1871	cm3	148.53	cm3/min
$p_{stag,0}/su$	0.64	-	field vane 1	13.5	V_{scale}	1906	cm3	151.26	cm3/min
t_{tot}	12.60	min	field vane 2	14	V_{water1}	-	cm3	-	cm3/min
m_{sub}	29450	gram	CPT	-	V_{water2}	-	cm3	-	cm3/min
Notes:	Hole at jet cl to measure strength of soil using a handvane								

Test_K_15_0.6_1

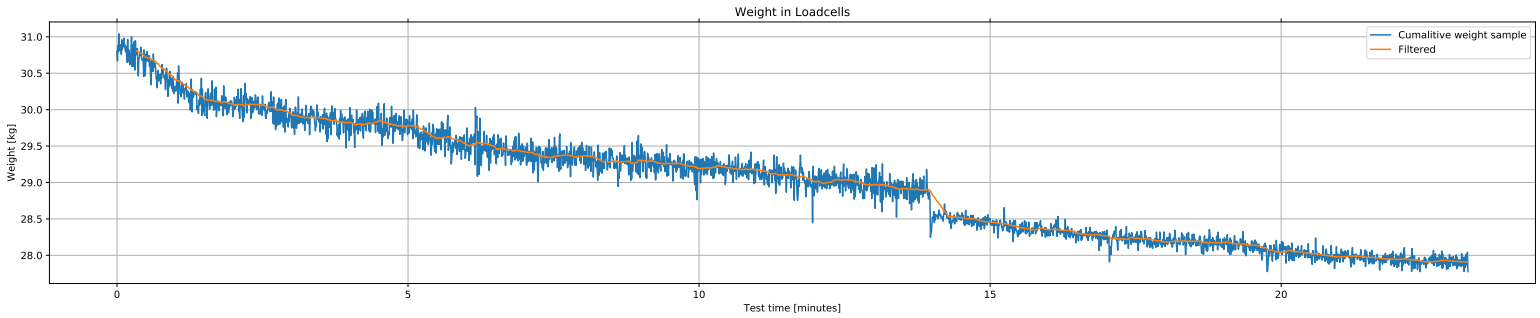
Weight in Loadcells
Cumalitive weight sample
Filtered
Weight [kg]
Test time [minutes]

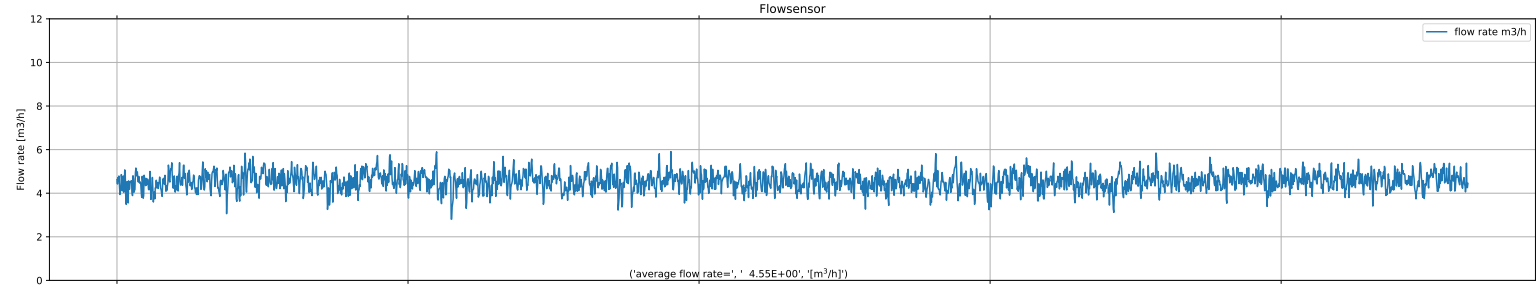
Flowsensor
flow rate m3/h
Flow rate [m3/h]
('average flow rate=', ' 4.55E+00', '[m3/h]')

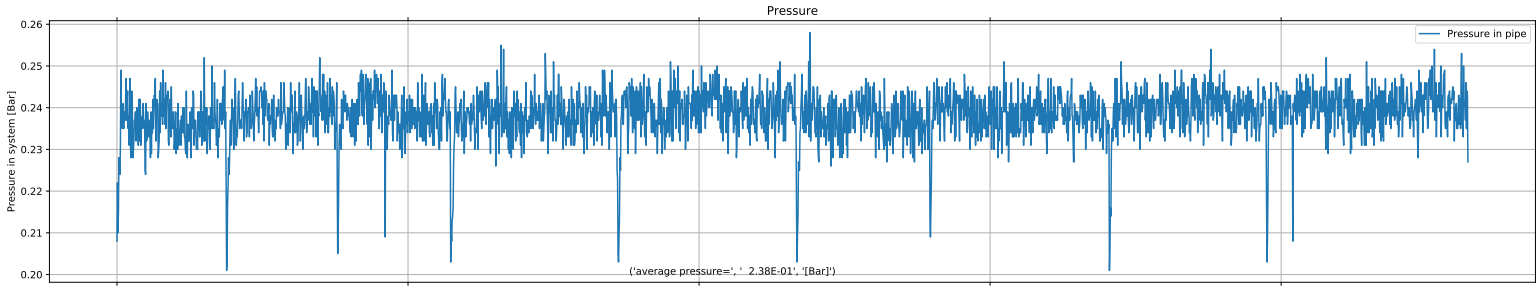
Pressure
Pressure in pipe
Pressure in system [Bar]
('average pressure=', ' 2.38E-01', '[Bar]')

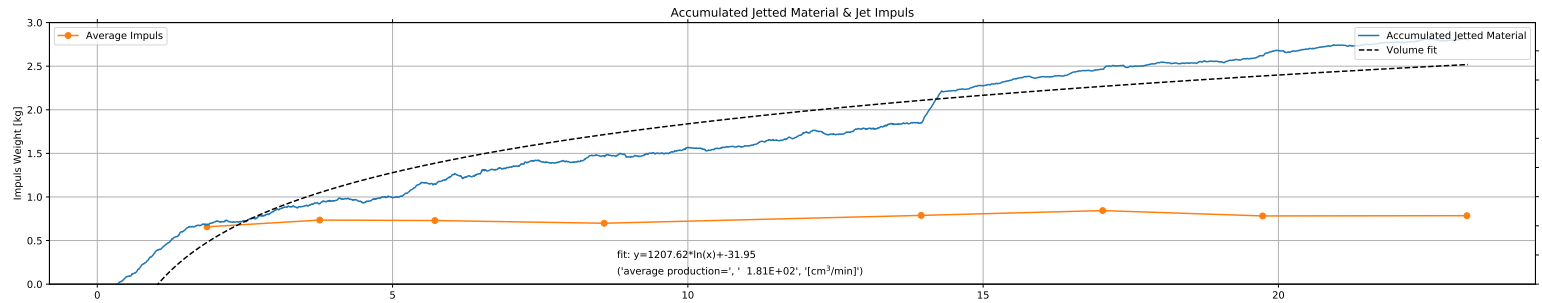
Accumulated Jetted Material & Jet Impuls
Average Impuls
Accumulated Jetted Material
Volume fit
Impuls Weight [kg]
Volume [cm3]
fit: y=1207.62*ln(x)+-31.95
('average production=', ' 1.81E+02', '[cm3/min]')

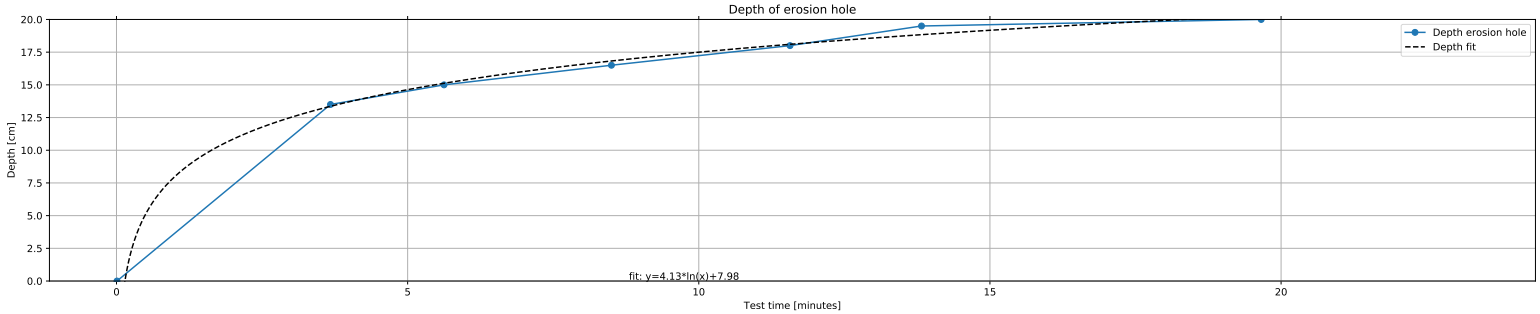
Depth of erosion hole
Depth erosion hole
Depth fit
Depth [cm]
fit: y=4.13*ln(x)+7.98
Test time [minutes]

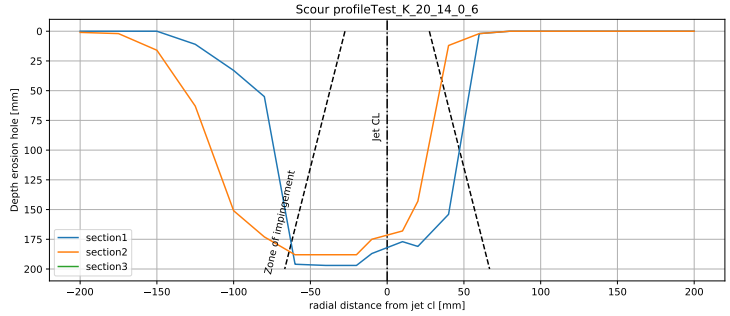
Scour profileTest_K_20_14_0_6
Depth erosion hole [mm]
Zone of impingement
Jet CL
section1
section2
section3
radial distance from jet cl [mm]

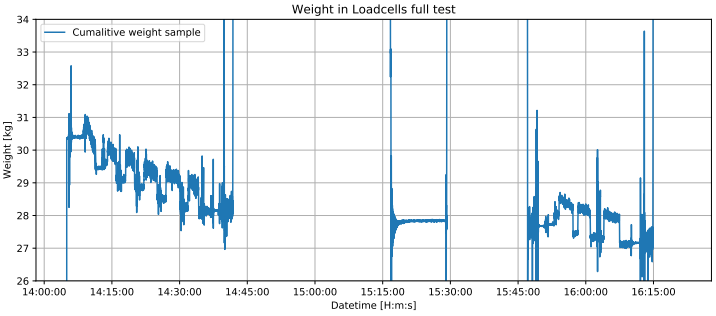
Weight in Loadcells full test
Cumalitive weight sample
Weight [kg]
Datetime [H:m:s]

Table B.4: Test K_15_0.6_2

TEST_K_15_0.6_2			pre-test	su	post-test		section 1	section 2	section 3
Date	9/24/2019	dd/mm/yy		kPa	xo	mm	205	-	-
u_0	4.25	m/s	pocket vane 1	9.84	yo	mm	-	230	205
Q	1.11E-03	m³/s	pocket vane 2	9.40	$Z_{c,cl}$	mm	171	-	-
SOD	151	mm	post-test	su	$Z_{c,max}$	mm	183	-	-
D_n	20	mm		kPa	$r_{Zc,max}$	mm	25	-	-
SOD/D_n	7.6	-	pocket vane 3	7.21					
$p_{stag,0}$	6.00	kPa	pocket vane 4	6.56	V_t	2904	cm3	7.26	cm3/min
$p_{stag,0}/su$	0.64	-	field vane 1	9.25	V_{scale}	3047	cm3	7.62	cm3/min
t_{tot}	400	min	field vane 2	9	V_{water1}	3300	cm3	8.25	cm3/min
m_{sub}	28855	gram	CPT	15	V_{water2}	3250	cm3	8.13	cm3/min

Notes: Kaolin, sample 9, weight pre test -150 gram (gemeten 83.25). Weakly deflected
Wide hole at the start, wide return flow angle (~80 degrees)

Test_K_15_0.6_2

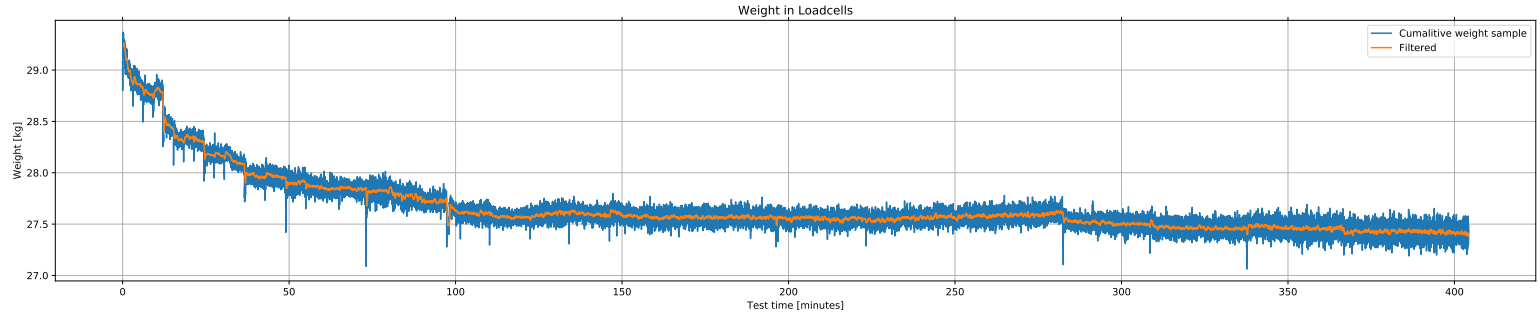
Weight in Loadcells
Cumalitive weight sample
Filtered
Weight [kg]
Test time [minutes]

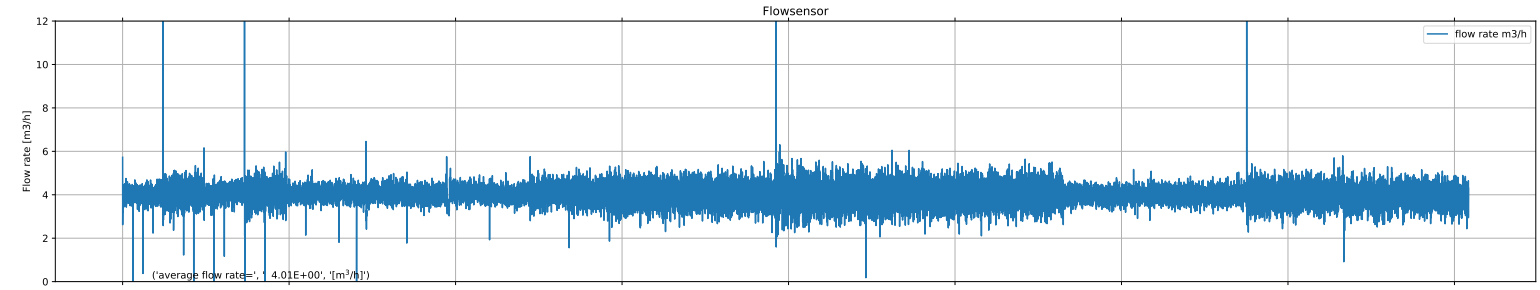
Flowsensor
flow rate m3/h
Flow rate [m3/h]
('average flow rate=', ' 4.01E+00', '[m³/h]')

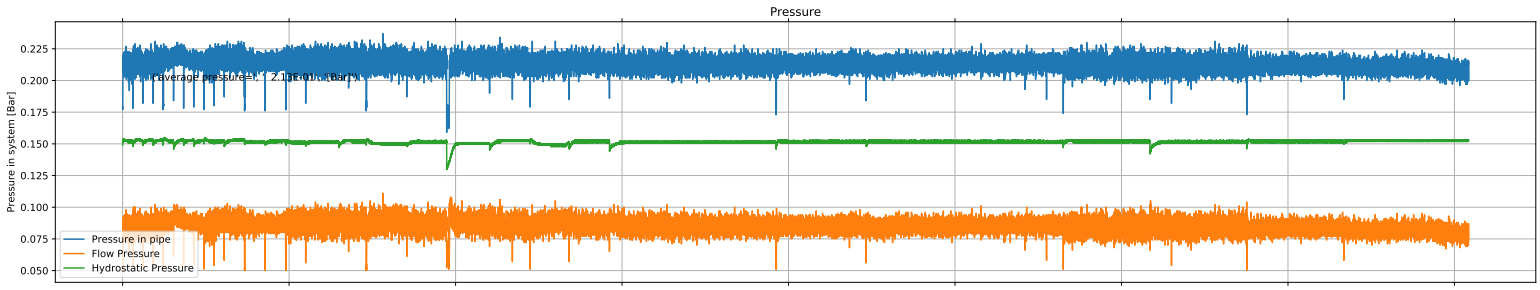
Pressure
('average pressure=', ' 2.16E+00', '[bar]')
Pressure in system [Bar]
Pressure in pipe
Flow Pressure
Hydrostatic Pressure

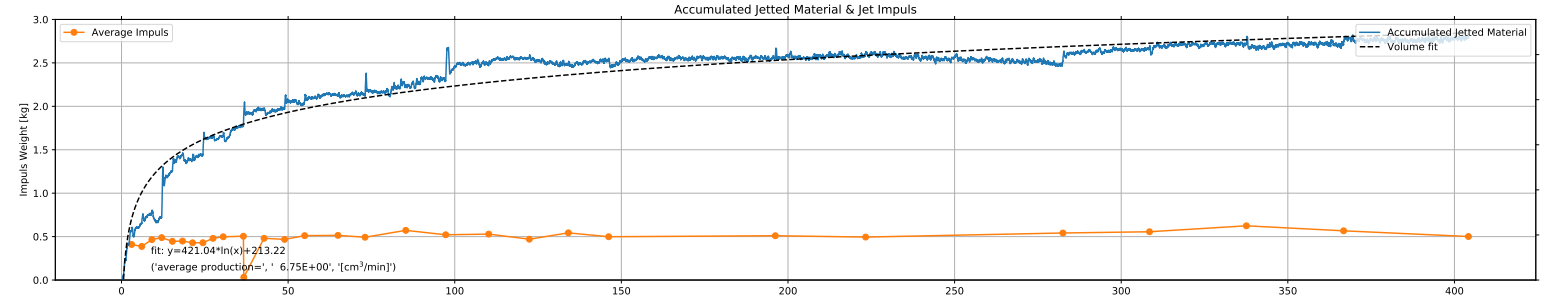
Accumulated Jetted Material & Jet Impuls
Average Impuls
Accumulated Jetted Material
Volume fit
Impuls Weight [kg]
Volume [cm3]
fit: y=421.04*ln(x)+213.22
('average production=', ' 6.75E+00', '[cm³/min]')

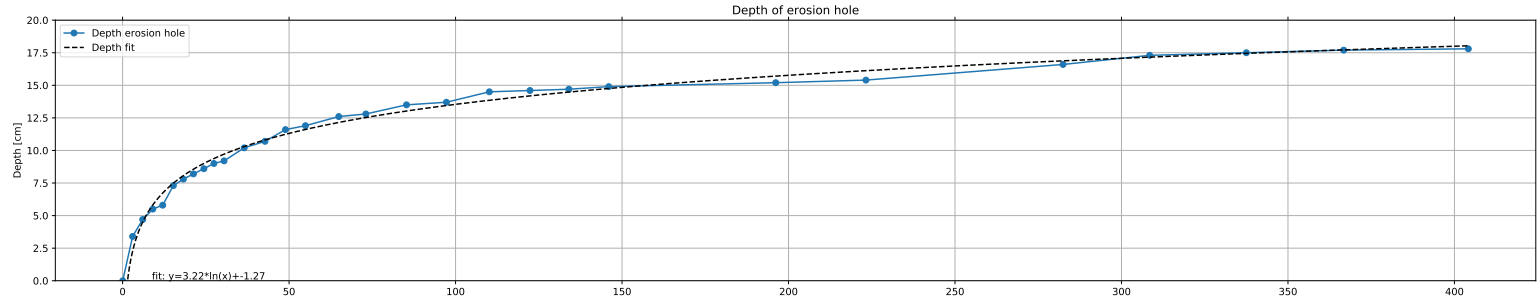
Depth of erosion hole
Depth erosion hole
Depth fit
Depth [cm]
fit: y=3.22*ln(x)+-1.27
Test time [minutes]

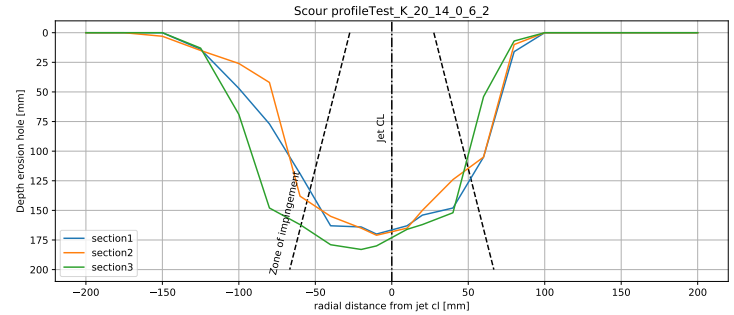
Scour profileTest_K_20_14_0_6_2
Depth erosion hole [mm]
Jet CL
Zone of impingement
section1
section2
section3
radial distance from jet cl [mm]

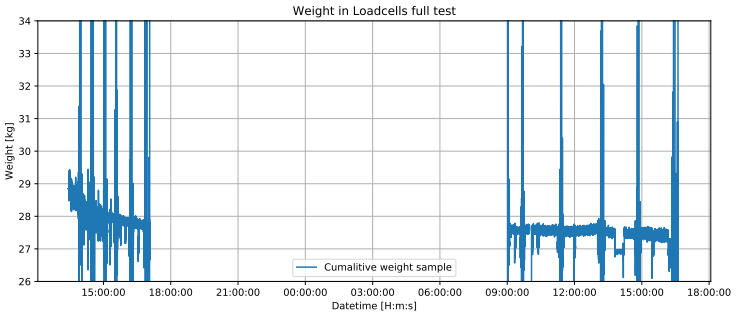
Weight in Loadcells full test
Weight [kg]
Cumalitive weight sample
Datetime [H:m:s]

Table B.5: Test K_15_0.6_3

TEST_K_15_0.6_3			pre-test	su	post-test		section 1	section 2	section 3
Date	10/7/2019	dd/mm/yy		kPa	xo	mm	250	-	-
u_0	4.3	m/s	pocket vane 1	10.16	yo	mm	-	235	0
Q	1.13E-03	m³/s	pocket vane 2	9.84	$Z_{c,cl}$	mm	187	-	-
SOD	151	mm	post-test	su	$Z_{c,max}$	mm	187	-	-
D_n	20	mm		kPa	$r_{Zc,max}$	mm	0	-	-
SOD/D_n	7.6	-	pocket vane 3	9.29					
$p_{stag,0}$	6.30	kPa	pocket vane 4	8.74	V_t	5154	cm3	214.76	cm3/min
$p_{stag,0}/su$	0.63	-	field vane 1	9.5	V_{scale}	5159	cm3	214.95	cm3/min
t_{tot}	24	min	field vane 2	10.5	V_{water1}	4950	cm3	206.25	cm3/min
m_{sub}	30622	gram	CPT	18	V_{water2}	4800	cm3	200.00	cm3/min

Notes: Kaolin, sample 10, started off with a bit higher stag/su pressure (0.64 instead of 0.6)
second time less water in hole, due to deforming of hole))

Test_K_15_0.6_3

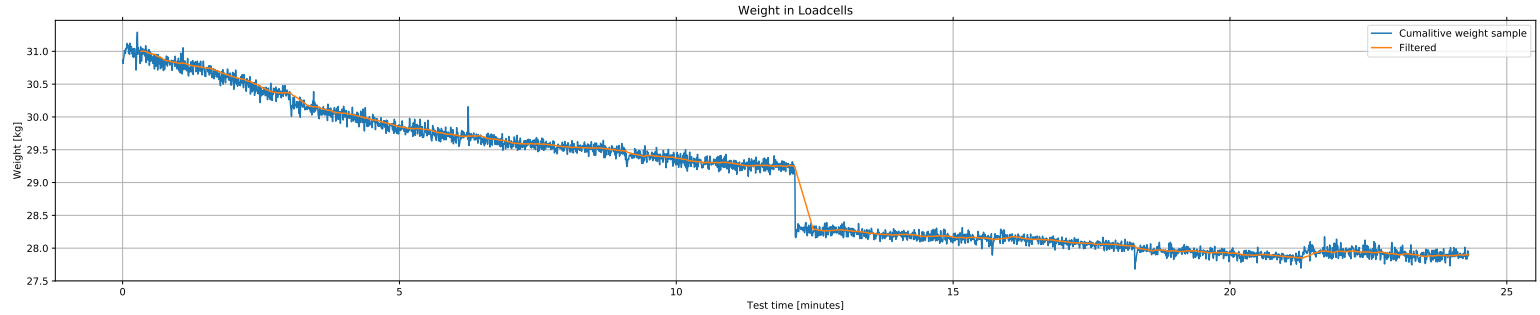
Weight in Loadcells
Cumalitive weight sample
Filtered
Weight [kg]
Test time [minutes]

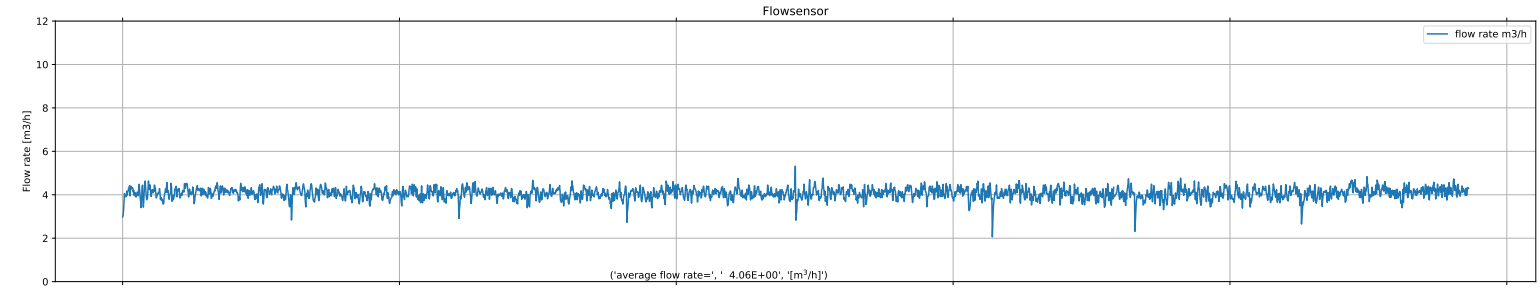
Flowsensor
flow rate m3/h
Flow rate [m3/h]
('average flow rate=', ' 4.06E+00', '[m^3/h]')

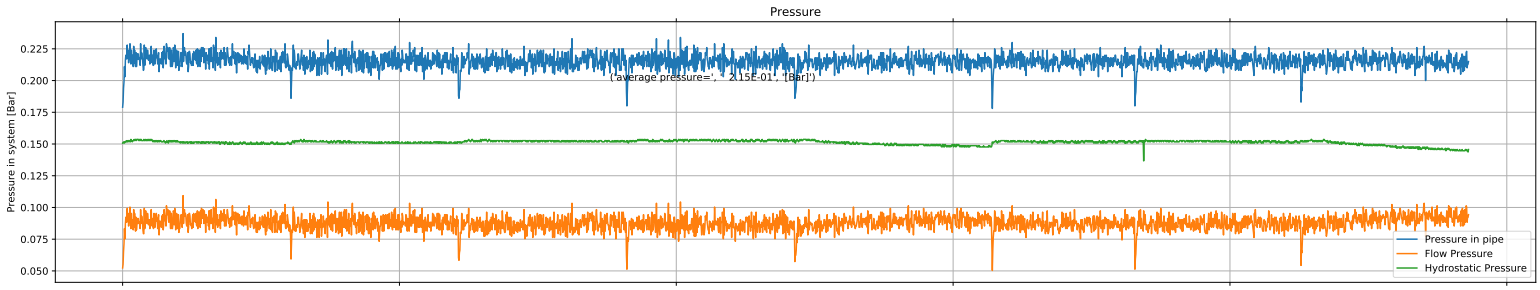
Pressure
('average pressure=', ' 2.15E-01', '[Bar]')
Pressure in system [Bar]
Pressure in pipe
Flow Pressure
Hydrostatic Pressure

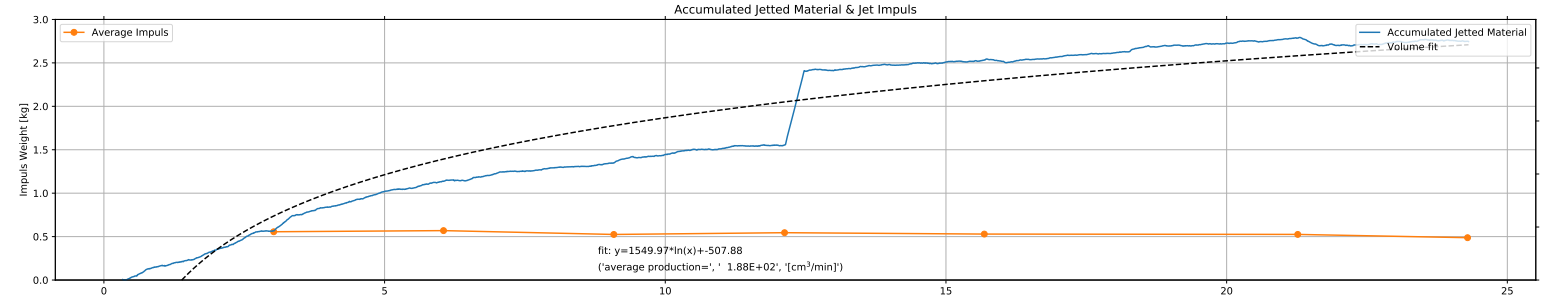
Accumulated Jetted Material & Jet Impuls
Average Impuls
Accumulated Jetted Material
Volume fit
Impuls Weight [kg]
Volume [cm3]
fit: y=1549.97*ln(x)+-507.88
('average production=', ' 1.88E+02', '[cm^3/min]')

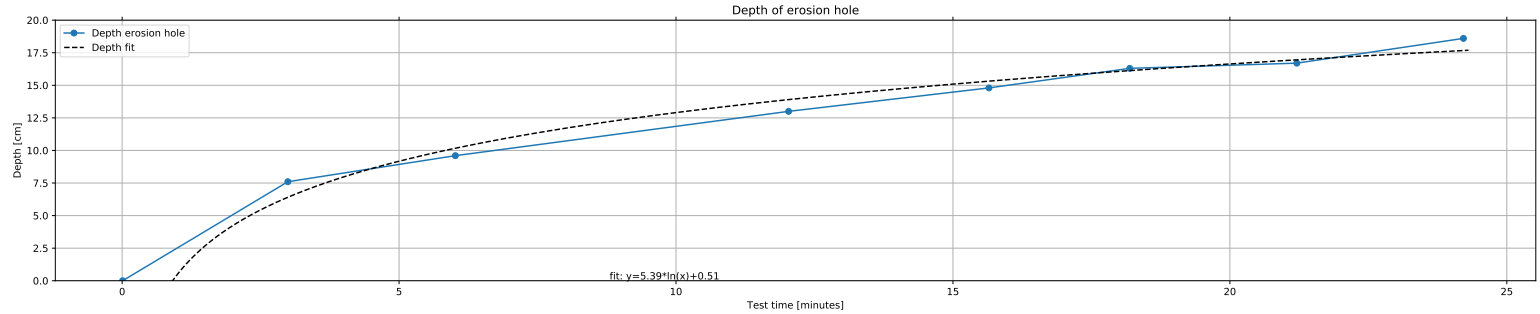
Depth of erosion hole
Depth erosion hole
Depth fit
Depth [cm]
fit: y=5.39*ln(x)+0.51
Test time [minutes]

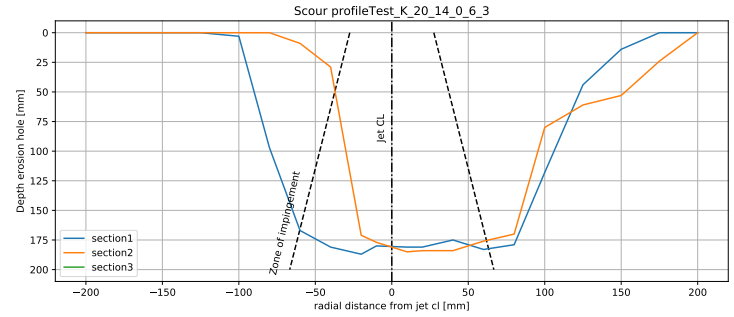
Scour profileTest_K_20_14_0_6_3
Depth erosion hole [mm]
Jet CL
Zone of impingement
section1
section2
section3
radial distance from jet cl [mm]

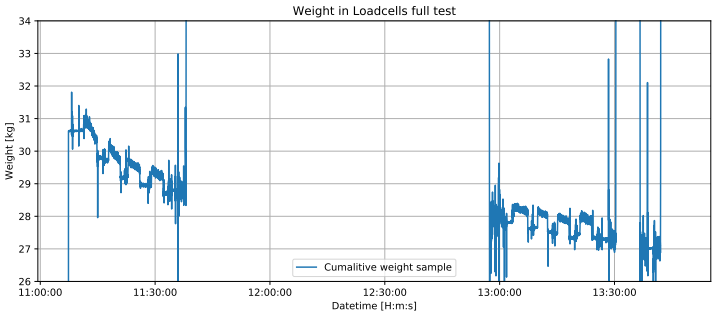
Weight in Loadcells full test
Weight [kg]
Cumalitive weight sample
Datetime [H:m:s]

Table B.6: Test K_15_0.6_4

TEST_K_15_0.6_4			pre-test	su	post-test		section 1	section 2	section 3
Date	12/02/19	dd/mm/yy		kPa	xo	mm	250	-	-
u_0	3.99	m/s	pocket vane 1	9.18	yo	mm	-	160	-
Q	1.05E-03	m³/s	pocket vane 2	8.74	$Z_{c,cl}$	mm	114	-	-
SOD	149	mm	post-test	su	$Z_{c,max}$	mm	115	-	-
D_n	20	mm		kPa	$r_{Zc,max}$	mm	20	-	-
SOD/D_n	7.5	-	pocket vane 3	8.53					
$p_{stag,0}$	5.60	kPa	pocket vane 4	7.65	V_t	1201	cm3	2.94	cm3/min
$p_{stag,0}/su$	0.59	-	field vane 1	10.50	V_{scale}	1420	cm3	3.48	cm3/min
t_{tot}	408	min	field vane 2	9.35	V_{water1}	1550	cm3	3.80	cm3/min
m_{sub}	29936	gram	CPT	-	V_{water2}	1520	cm3	3.73	cm3/min

Notes: Kaolin, Sample 18. Weakly deflected at start, wide hole.

Test_K_15_0.6_4

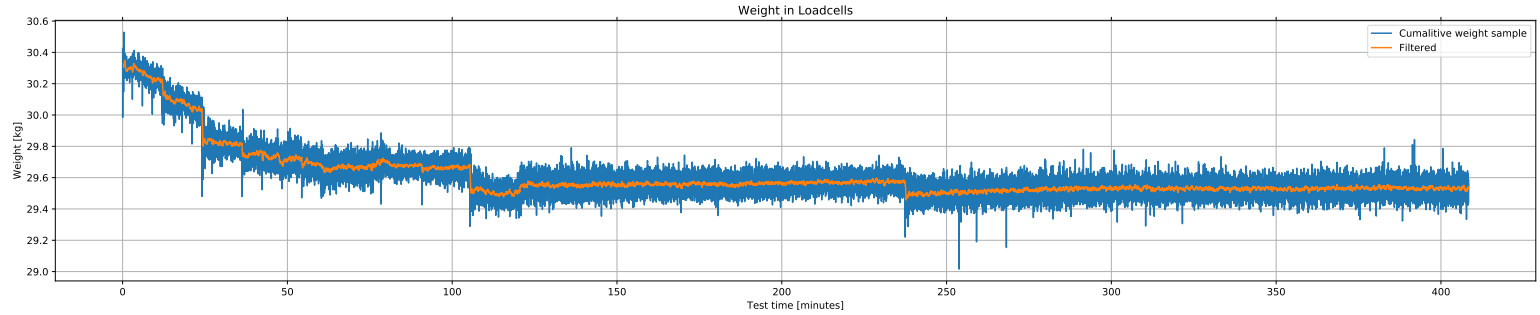
Weight in Loadcells
Cumalitive weight sample
Filtered
Weight [kg]
Test time [minutes]

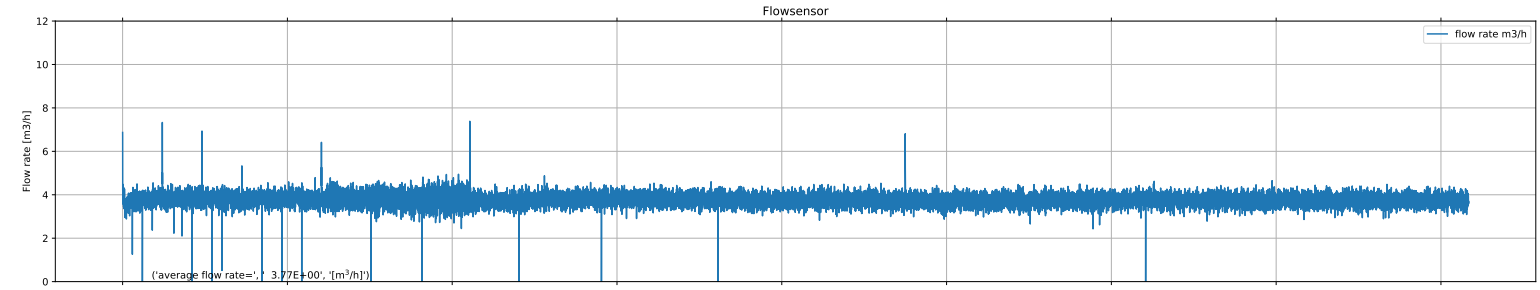
Flowsensor
flow rate m3/h
Flow rate [m3/h]
('average flow rate=', ' 3.77E+00', '[m³/h]')

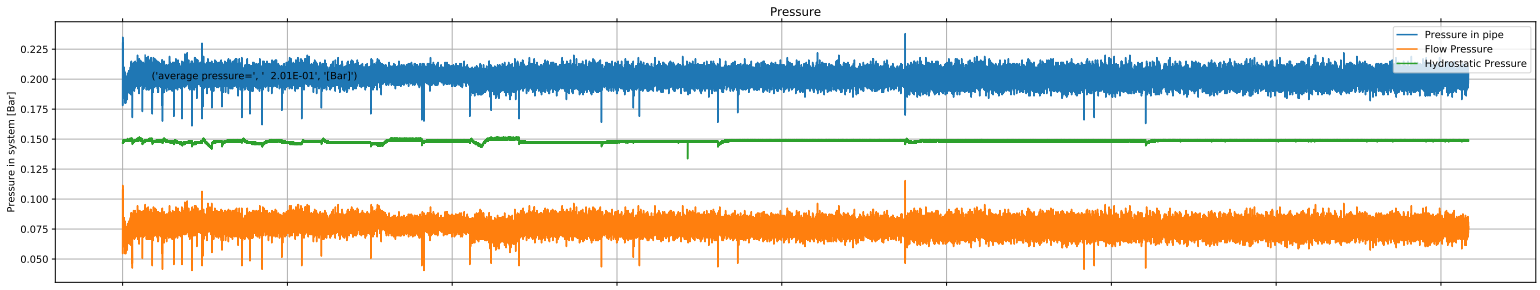
Pressure
Pressure in pipe
Flow Pressure
Hydrostatic Pressure
Pressure in system [Bar]
('average pressure=', ' 2.01E-01', '[Bar]')

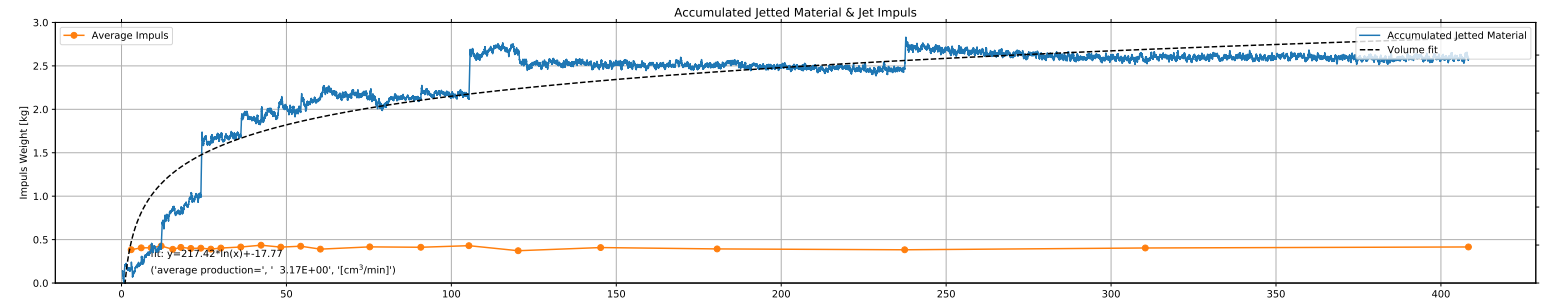
Accumulated Jetted Material & Jet Impuls
Average Impuls
Accumulated Jetted Material
Volume fit
Impuls Weight [kg]
Volume [cm3]
fit: y=217.42*ln(x)+-17.77
('average production=', ' 3.17E+00', '[cm³/min]')

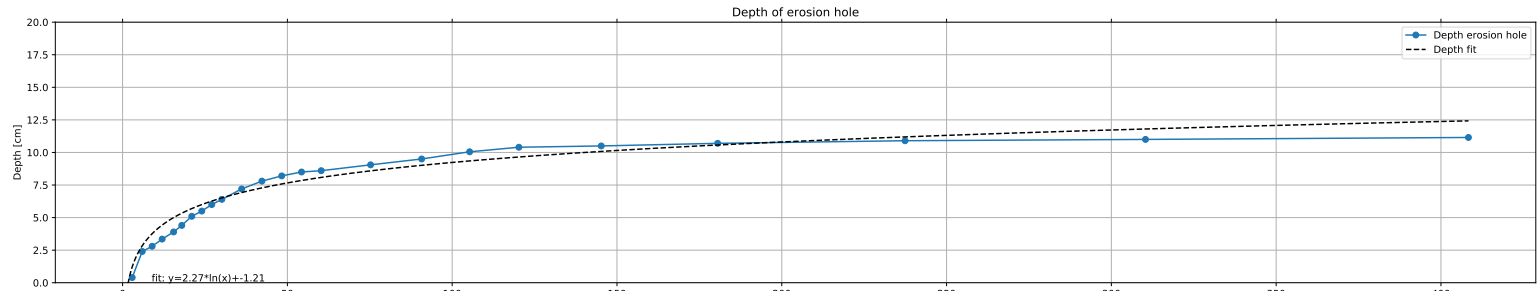
Depth of erosion hole
Depth erosion hole
Depth fit
Depth [cm]
fit: y=2.27*ln(x)+-1.21
Test time [minutes]

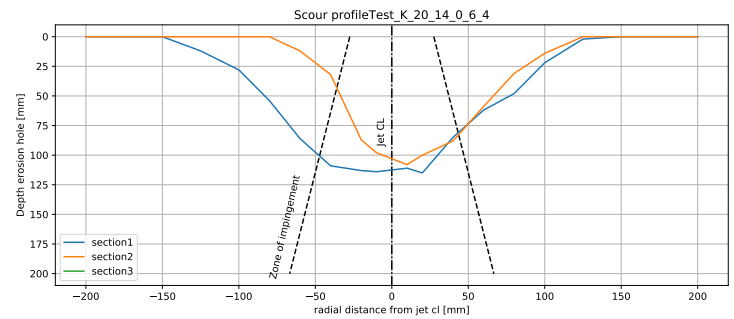
Scour profileTest_K_20_14_0_6_4
Depth erosion hole [mm]
Jet CL
Zone of impingement
section1
section2
section3
radial distance from jet cl [mm]

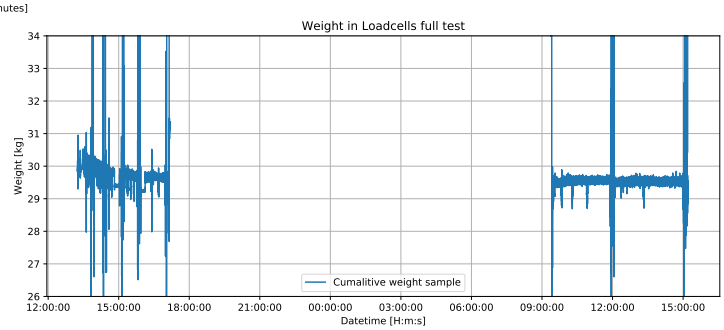
Weight in Loadcells full test
Weight [kg]
Cumalitive weight sample
Datetime [H:m:s]

Table B.7: Test K_22_0.6_1

TEST_K_22_0.6_1			pre-test	su	post-test		section 1	section 2	section 3
Date	11/13/2019	dd/mm/yy		kPa	xo	mm	275	-	-
u_0	6.3	m/s	pocket vane 1	9.84	yo	mm	-	250	280
Q	1.67E-03	m³/s	pocket vane 2	10.06	$Z_{c,cl}$	mm	154	-	-
SOD	225	mm	post-test	su	$Z_{c,max}$	mm	162	-	-
D_n	20	mm		kPa	$r_{Zc,max}$	mm	50	-	-
SOD/D_n	11.3	-	pocket vane 3	9.84					
$p_{stag,0}$	6.00	kPa	pocket vane 4	7.65	V_t	4523	cm3	15.08	cm3/min
$p_{stag,0}/su$	0.63	-	field vane 1	9.00	V_{scale}	4527	cm3	15.09	cm3/min
t_{tot}	300	min	field vane 2	9.00	V_{water1}	-	cm3	-	cm3/min
m_{sub}	30828	gram	CPT	10	V_{water2}	-	cm3	-	cm3/min

Notes: Kaolin, Sample 15, sod 322.5 cm, no water measurements possible, sample fell after Section measurements))

Test_K_22_0.6_1

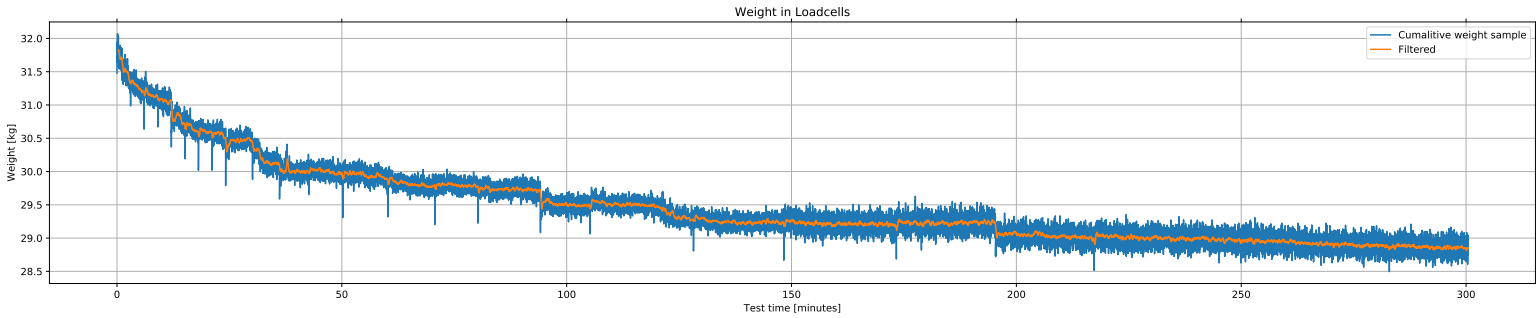
Weight in Loadcells
Cumalitive weight sample
Filtered
Weight [kg]
Test time [minutes]

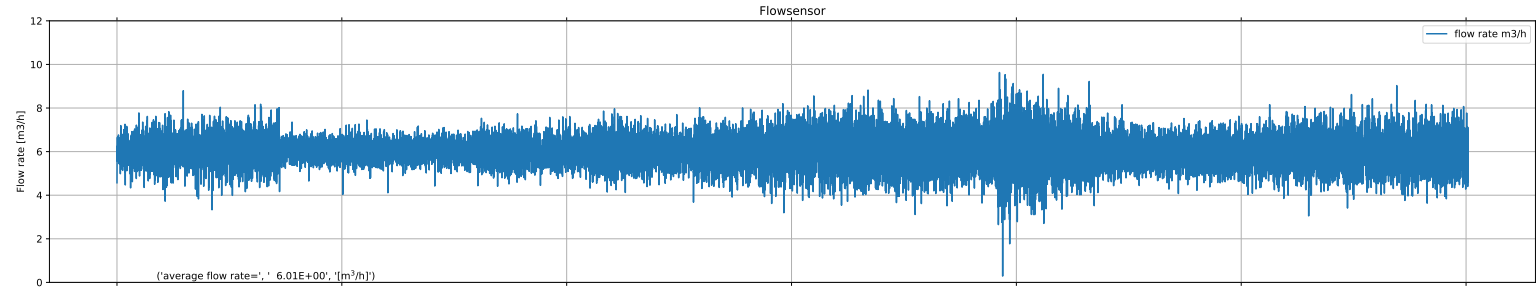
Flowsensor
flow rate m3/h
Flow rate [m3/h]
('average flow rate=', ' 6.01E+00', '[m3/h]')

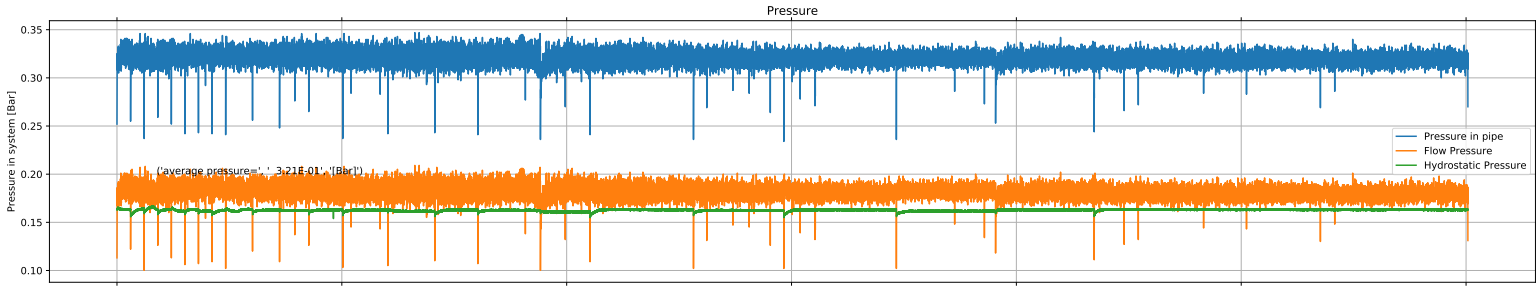
Pressure
Pressure in pipe
Flow Pressure
Hydrostatic Pressure
Pressure in system [Bar]
('average pressure=', ' 3.21E-01', '[Bar]')

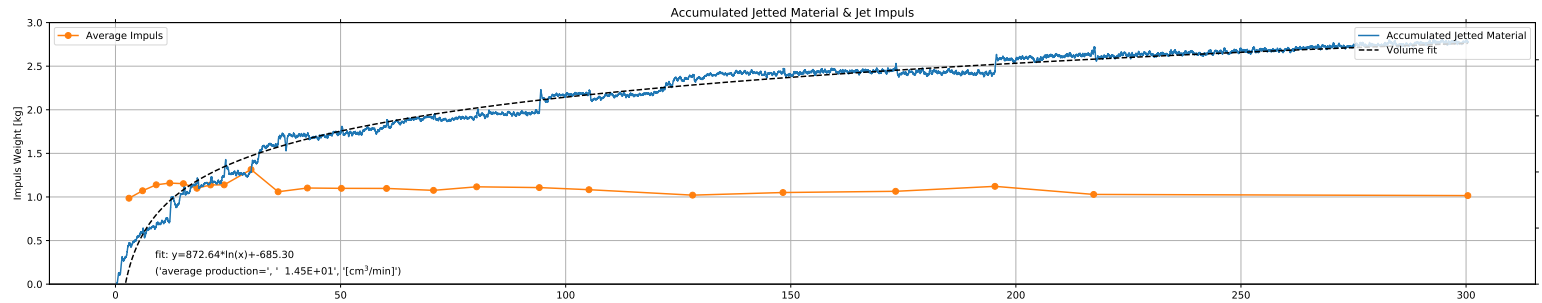
Accumulated Jetted Material & Jet Impuls
Average Impuls
Accumulated Jetted Material
Volume fit
Impuls Weight [kg]
Volume [cm3]
fit: y=872.64*ln(x)+-685.30
('average production=', ' 1.45E+01', '[cm3/min]')

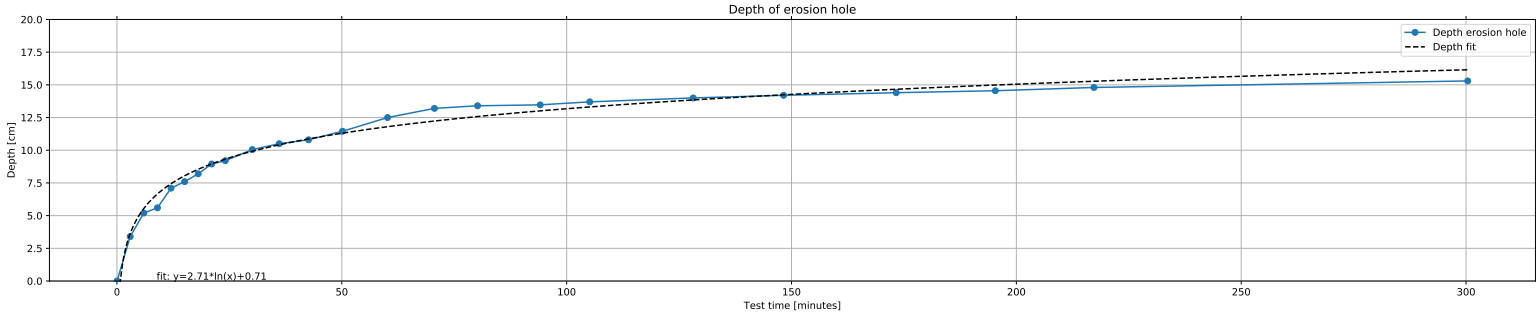
Depth of erosion hole
Depth erosion hole
Depth fit
Depth [cm]
fit: y=2.71*ln(x)+0.71
Test time [minutes]

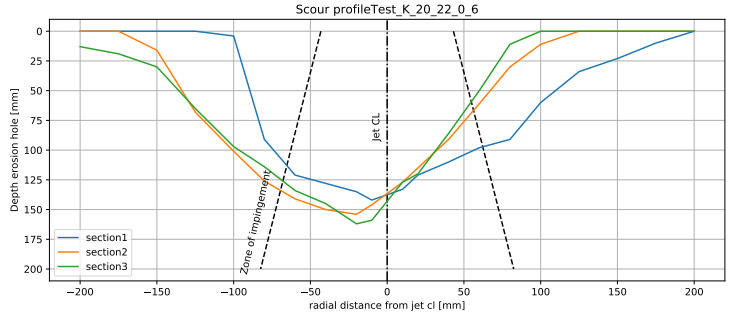
Scour profileTest_K_20_22_0_6
Depth erosion hole [mm]
Jet CL
Zone of impingement
section1
section2
section3
radial distance from jet cl [mm]

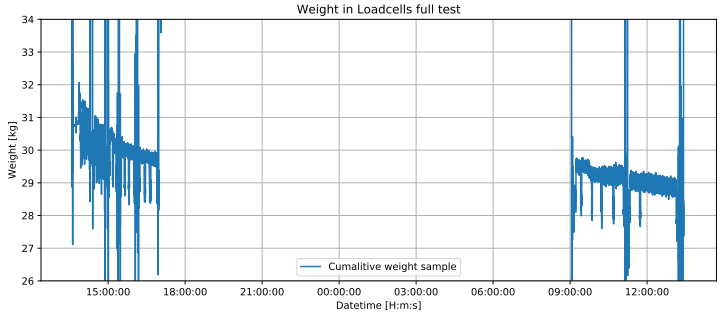
Weight in Loadcells full test
Weight [kg]
Cumalitive weight sample
Datetime [H:m:s]

Table B.8: Test K_30_0.6_1

TEST_K_30_0.6_1			pre-test	su	post-test				
							section 1	section 2	section 3
Date	11/04/19	dd/mm/yy		kPa	xo	mm	325	-	-
u_0	8.44	m/s	pocket vane 1	10.93	yo	mm	-	300	-
Q	2.25E-03	m³/s	pocket vane 2	9.84	$Z_{c,cl}$	mm	172	-	-
SOD	298	mm	post-test	su	$Z_{c,max}$	mm	184	-	-
D_n	20	mm		kPa	$r_{Zc,max}$	mm	40	-	-
SOD/D_n	14.9	-	pocket vane 3	9.84					
$p_{stag,0}$	6.20	kPa	pocket vane 4	8.53	V_t	6790	cm3	157.90	cm3/min
$p_{stag,0}/su$	0.59	-	field vane 1	11.00	V_{scale}	6953	cm3	161.69	cm3/min
t_{tot}	43	min	field vane 2	10.25	V_{water1}	7200	cm3	167.44	cm3/min
m_{sub}	30460	gram	CPT	10	V_{water2}	7300	cm3	169.77	cm3/min
Notes:	Kaolin, Sample 16, sod 30 cm, at 35 min sudden increase in production and depth.								

Test_K_30_0.6_1

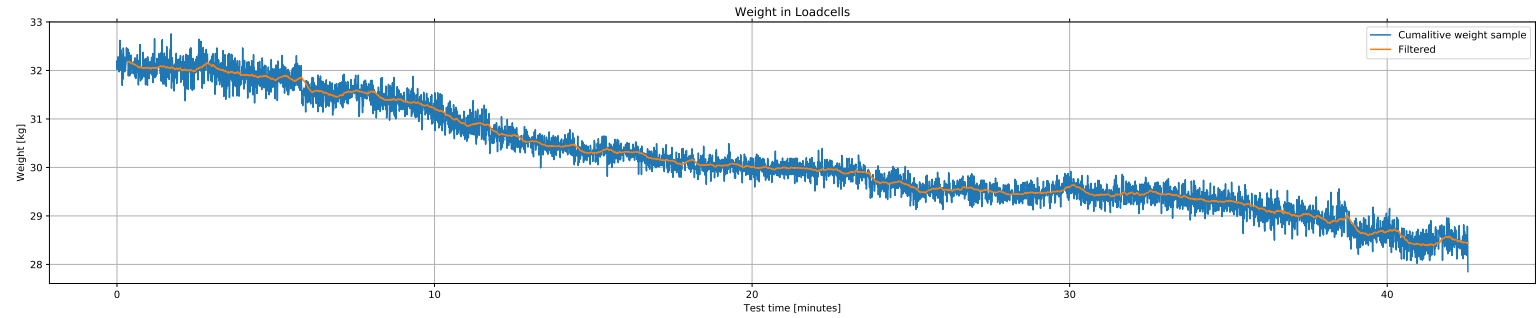
Weight in Loadcells
Weight [kg]
Test time [minutes]
Cumalitive weight sample
Filtered

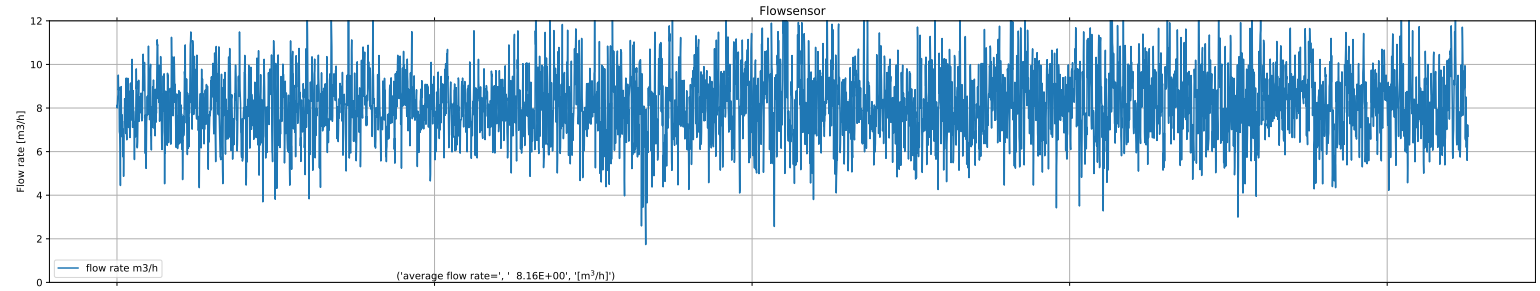
Flowsensor
Flow rate [m3/h]
flow rate m3/h
('average flow rate=', ' 8.16E+00', '[m3/h]')

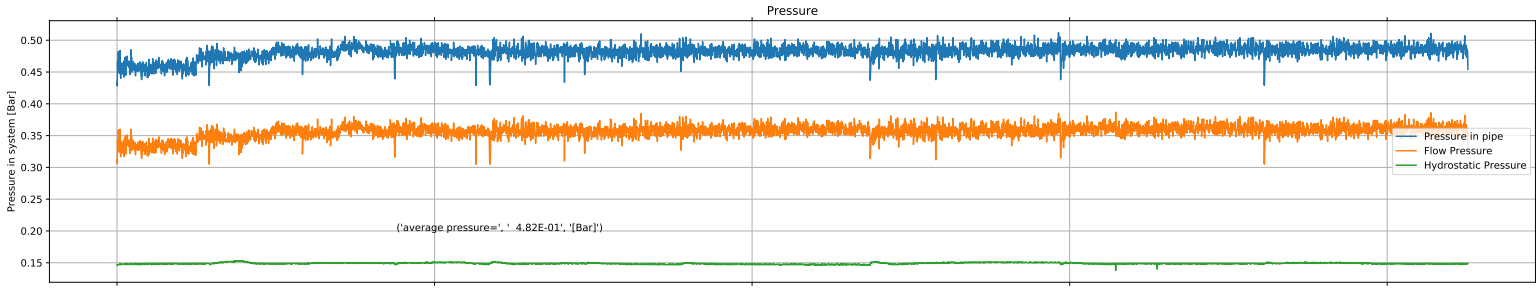
Pressure
Pressure in system [Bar]
Pressure in pipe
Flow Pressure
Hydrostatic Pressure
('average pressure=', ' 4.82E-01', '[Bar]')

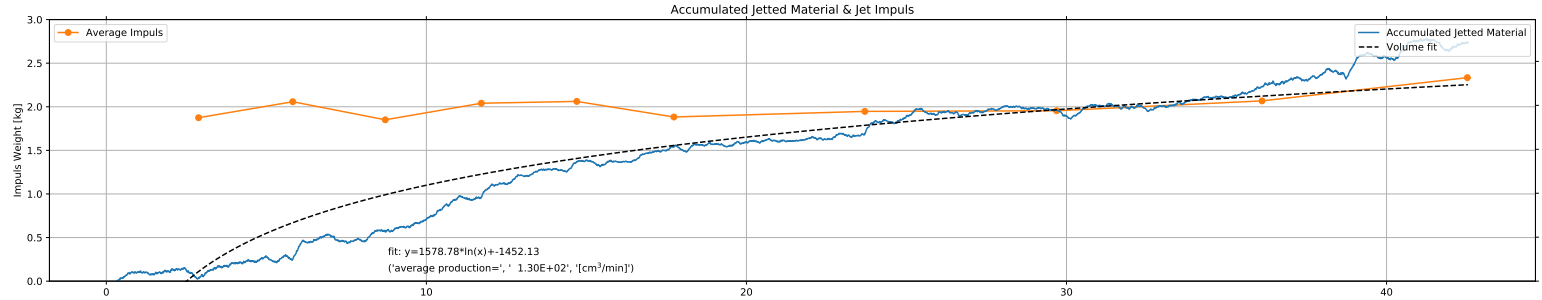
Accumulated Jetted Material & Jet Impuls
Impuls Weight [kg]
Volume [cm3]
Average Impuls
Accumulated Jetted Material
Volume fit
fit: y=1578.78*ln(x)+-1452.13
('average production=', ' 1.30E+02', '[cm3/min]')

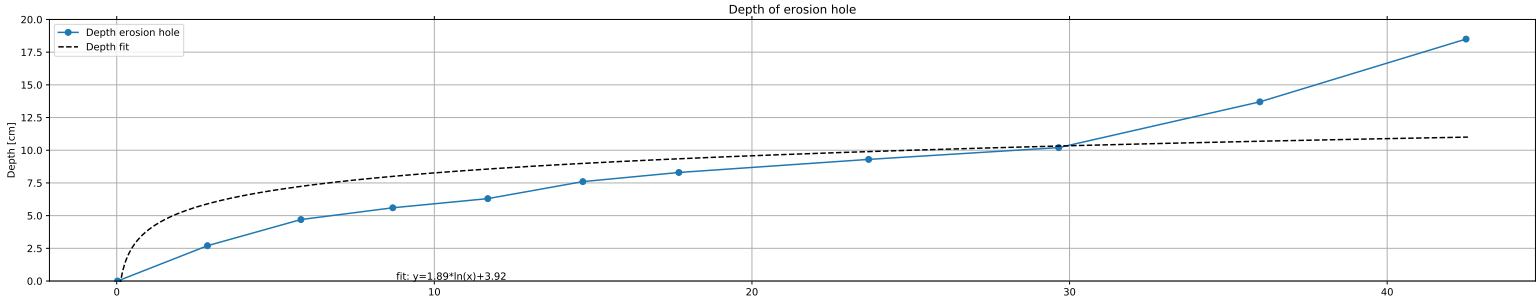
Depth of erosion hole
Depth [cm]
Depth erosion hole
Depth fit
fit: y=1.89*ln(x)+3.92
Test time [minutes]

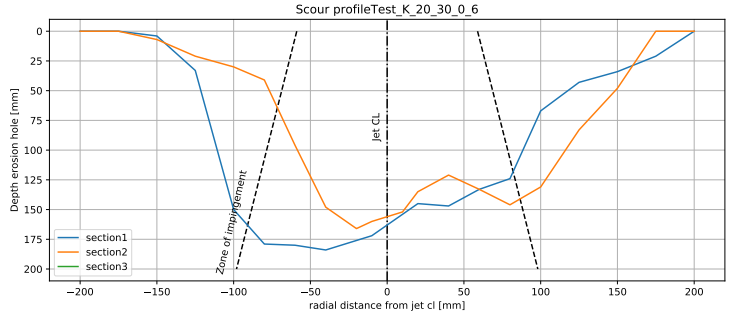
Scour profileTest_K_20_30_0_6
Depth erosion hole [mm]
radial distance from jet cl [mm]
Jet CL
Zone of impingement
section1
section2
section3

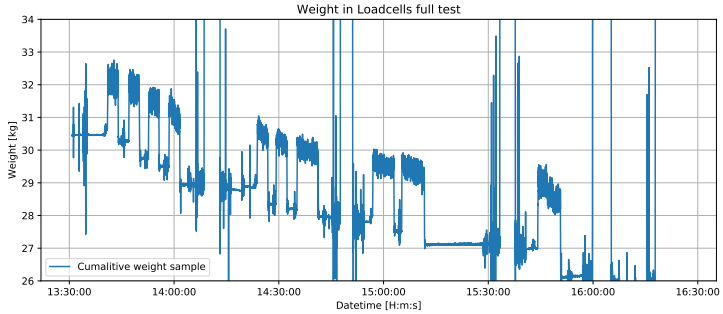
Weight in Loadcells full test
Weight [kg]
Datetime [H:m:s]
Cumalitive weight sample

Table B.9: Test K_30_0.6_2

TEST_K_30_0.6_2			pre-test	su	post-test		section 1	section 2	section 3
Date	12/05/19	dd/mm/yy		kPa	xo	mm	235	-	-
u_0	7.99	m/s	pocket vane 1	8.74	yo	mm	-	350	-
Q	2.12E-03	m³/s	pocket vane 2	9.29	$Z_{c,cl}$	mm	157	-	-
SOD	298	mm	post-test	su	$Z_{c,max}$	mm	181	-	-
D_n	20	mm		kPa	$r_{Zc,max}$	mm	65	-	-
SOD/D_n	14.9	-	pocket vane 3	5.90					
$p_{stag,0}$	5.60	kPa	pocket vane 4	7.65	V_t	5778	cm3	32.10	cm3/min
$p_{stag,0}/su$	0.63	-	field vane 1	8.75	V_{scale}	5769	cm3	32.05	cm3/min
t_{tot}	180	min	field vane 2	8.5	V_{water1}	5500	cm3	30.56	cm3/min
m_{sub}	30455	gram	CPT	-	V_{water2}	5650	cm3	31.39	cm3/min

Notes: Kaolin, Sample 19, sod 30 cm. At beginning hole to 1 half of the sample (not in middle). Steep at jet cl. Between 60 and 70 min, preferential direction changed; towards no hole side))

Test_K_30_0.6_2

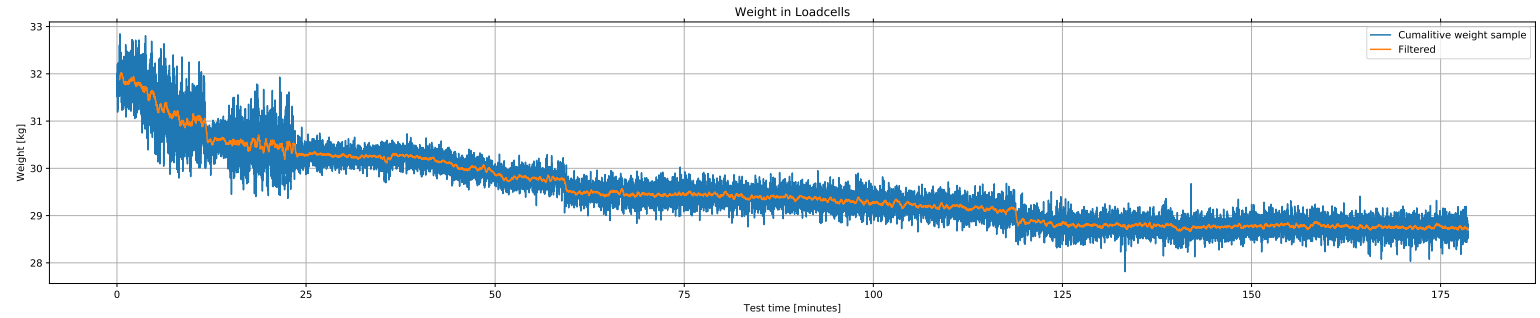
Weight in Loadcells
Cumalitive weight sample
Filtered
Weight [kg]
Test time [minutes]

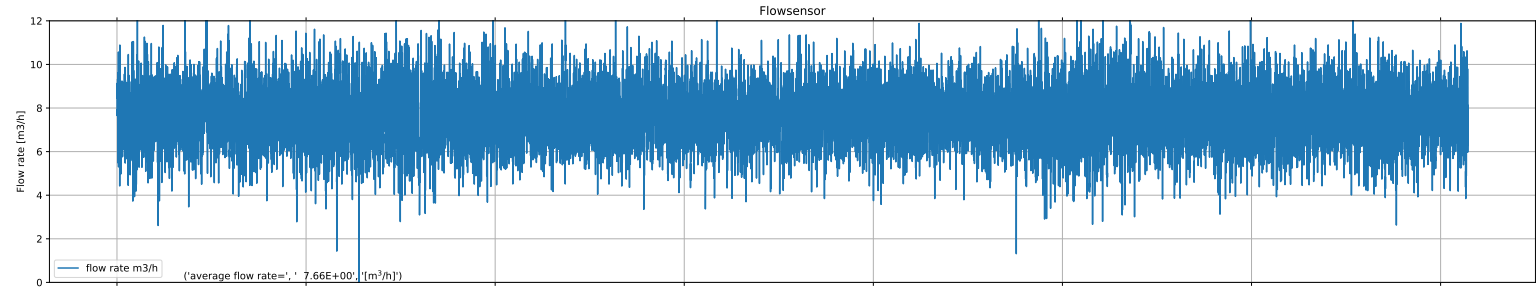
Flowsensor
flow rate m3/h
('average flow rate=', ' 7.66E+00', '[m3/h]')
Flow rate [m3/h]

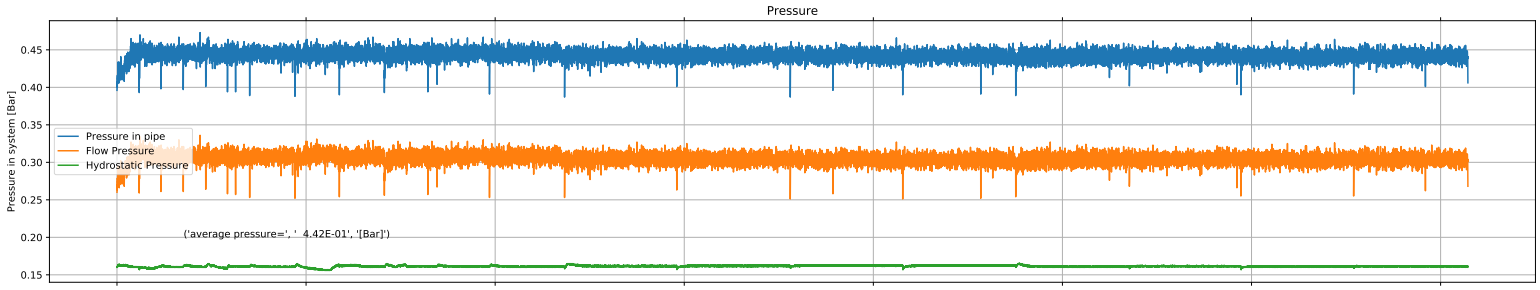
Pressure
Pressure in pipe
Flow Pressure
Hydrostatic Pressure
('average pressure=', ' 4.42E-01', '[Bar]')
Pressure in system [Bar]

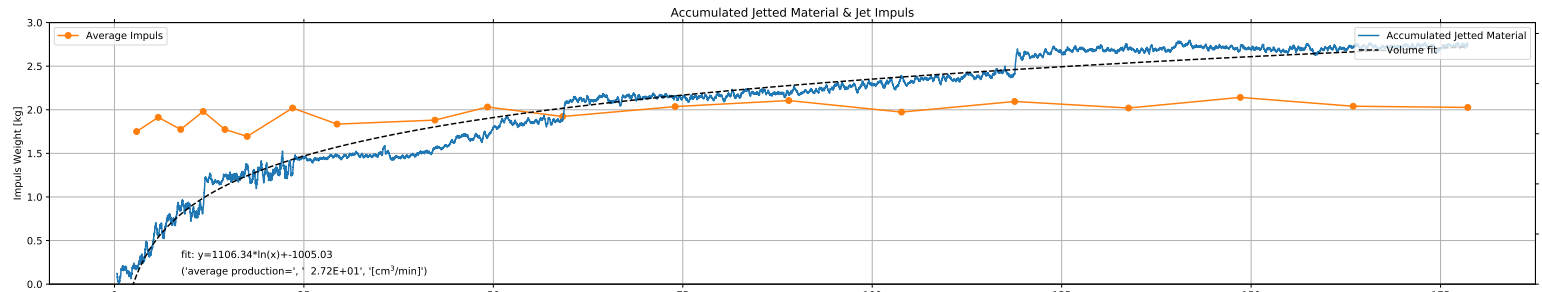
Accumulated Jetted Material & Jet Impuls
Average Impuls
Accumulated Jetted Material
Volume fit
fit: y=1106.34*ln(x)+-1005.03
('average production=', ' 2.72E+01', '[cm3/min]')
Impuls Weight [kg]
Volume [cm3]

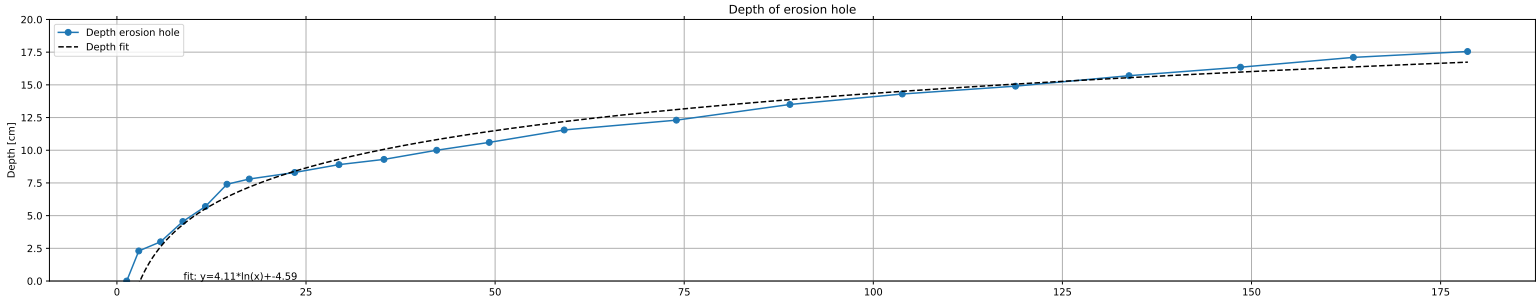
Depth of erosion hole
Depth erosion hole
Depth fit
fit: y=4.11*ln(x)+-4.59
Depth [cm]
Test time [minutes]

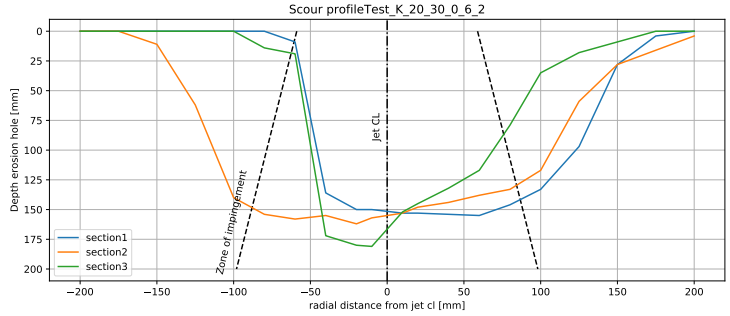
Scour profileTest_K_20_30_0_6_2
Zone of impingment
Jet CL
section1
section2
section3
Depth erosion hole [mm]
radial distance from jet cl [mm]

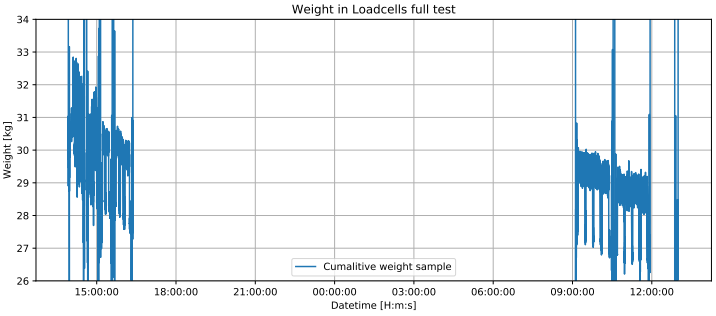
Weight in Loadcells full test
Cumalitive weight sample
Weight [kg]
Datetime [H:m:s]

Table B.10: Test 5% Bent_15_0.6_1

TEST_5% Bent_15_0.6_1			pre-test	su	post-test		section 1	section 2	section 3
Date	09/09/19	dd/mm/yy		kPa	xo	mm	180	0	-
u_0	4.37	m/s	pocket vane 1	10.06	yo	mm	-	180	180
Q	1.14E-03	m³/s	pocket vane 2	10.93	$Z_{c,cl}$	mm	122	-	-
SOD	149	mm	post-test	su	$Z_{c,max}$	mm	122	-	-
D_n	20	mm		kPa	$r_{Zc,max}$	mm	0	-	-
SOD/D_n	7.5	-	pocket vane 3	8.09					
$p_{stag,0}$	6.30	kPa	pocket vane 4	8.53	V_t	1791	cm3	18.66	cm3/min
$p_{stag,0}/su$	0.56	-	field vane 1	12.50	V_{scale}	1971	cm3	20.53	cm3/min
t_{tot}	96	min	field vane 2	11.50	V_{water1}	1800	cm3	18.75	cm3/min
m_{sub}	32090	gram	CPT	0	V_{water2}	1795	cm3	18.70	cm3/min
Notes:	5% bentonite								

Test_5%_Bent_15_0.6_1

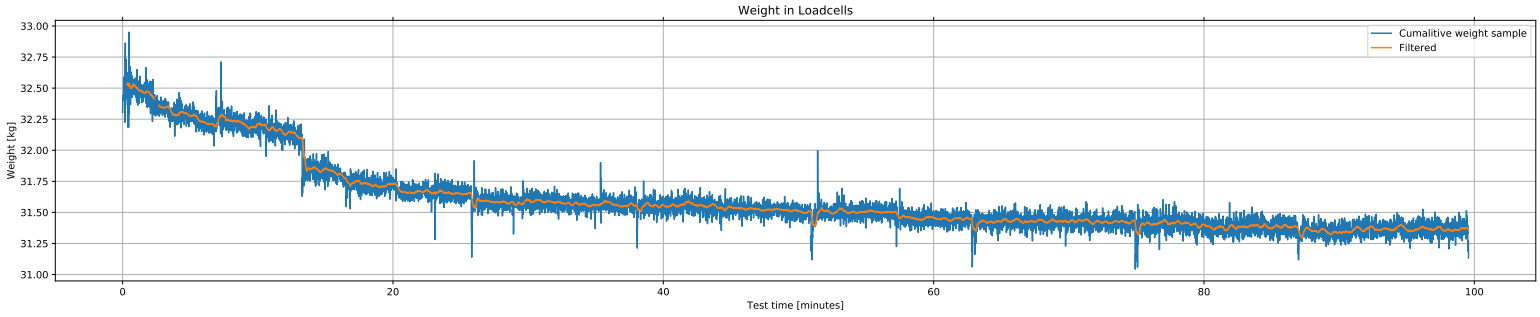

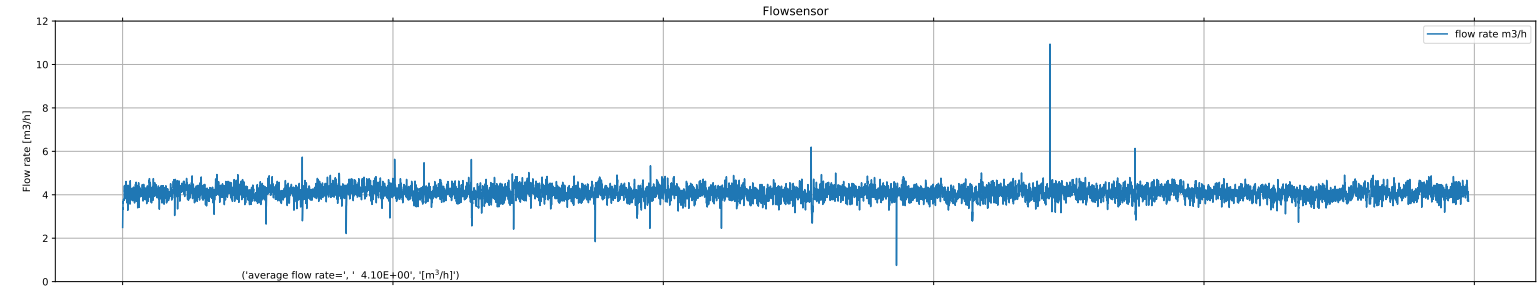

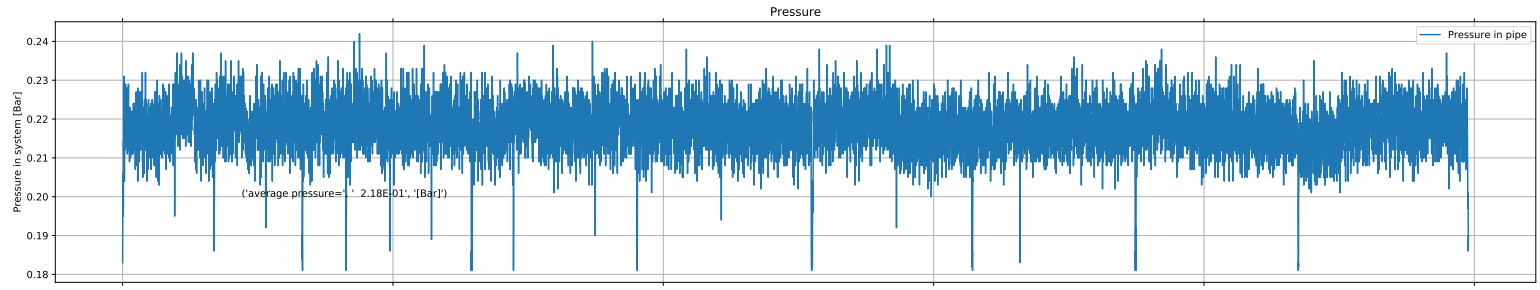

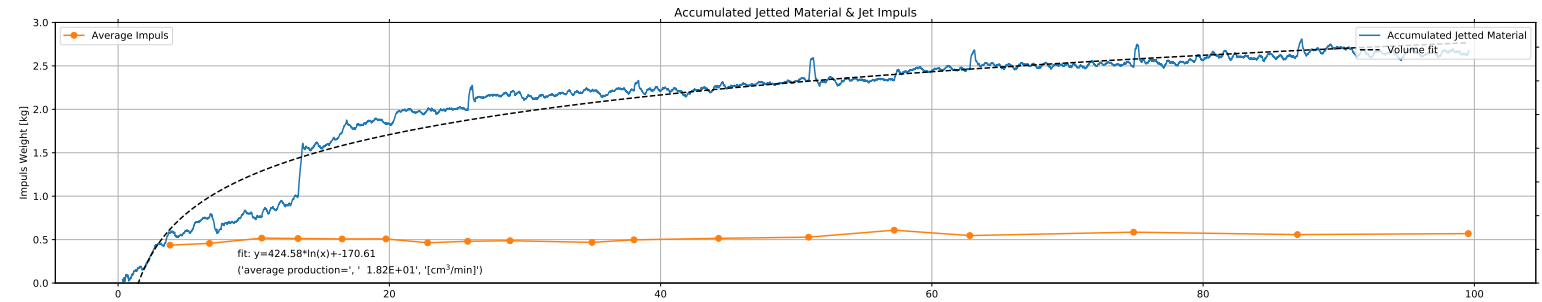

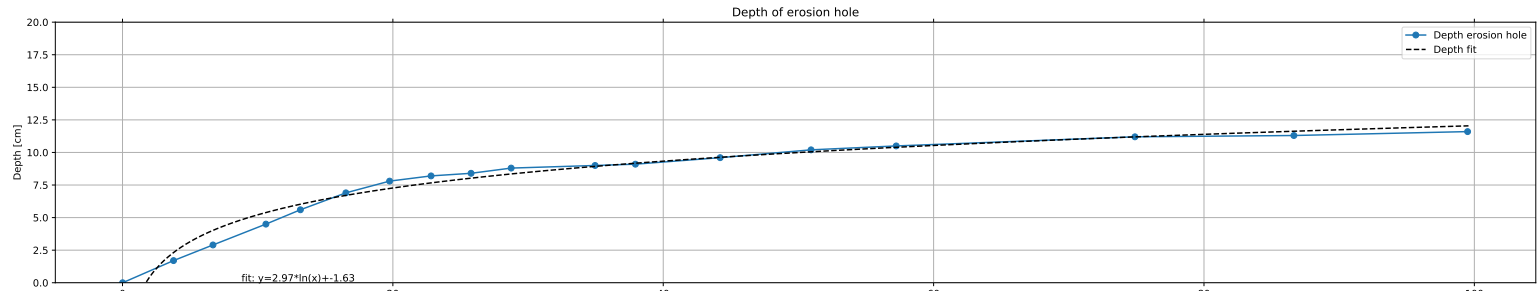

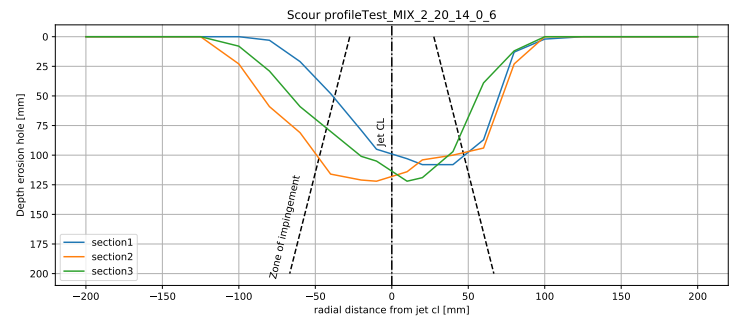

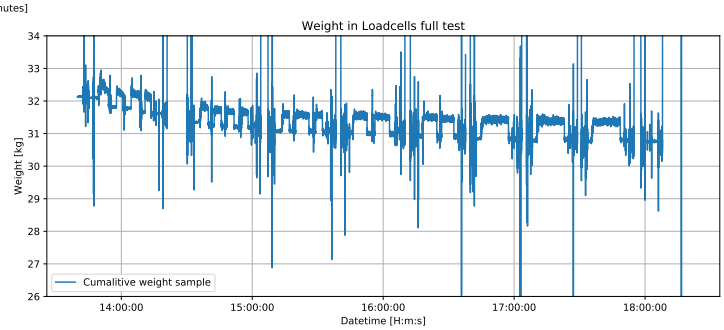

Table B.11: Test 10% Bent_15_0.6_1

TEST_10% Bent_15_0.6_1			pre-test	su	post-test				
							section 1	section 2	section 3
Date	04/09/19	dd/mm/yy		kPa	xo	mm	255	-	-
u_0	4.75	m/s	pocket vane 1	12.02	yo	mm	-	225	-
Q	1.25E-03	m³/s	pocket vane 2	11.59	$Z_{c,cl}$	mm	151	-	-
SOD	153	mm	post-test	su	$Z_{c,max}$	mm	151	-	-
D_n	20	mm		kPa	$r_{Zc,max}$	mm	0	-	-
SOD/D_n	7.7	-	pocket vane 3	8.96					
$p_{stag,0}$	7.50	kPa	pocket vane 4	8.53	V_t	1561	cm3	74.33	cm3/min
$p_{stag,0}/su$	0.73	-	field vane 1	9.00	V_{scale}	2765	cm3	131.65	cm3/min
t_{tot}	21	min	field vane 2	8.75	V_{water1}	2600	cm3	123.81	cm3/min
m_{sub}	31853	gram	CPT	-	V_{water2}	2670	cm3	127.14	cm3/min
Notes:	1 corner was softer, measured 8 kPa su								

Test_10%_Bent_15_0.6_1

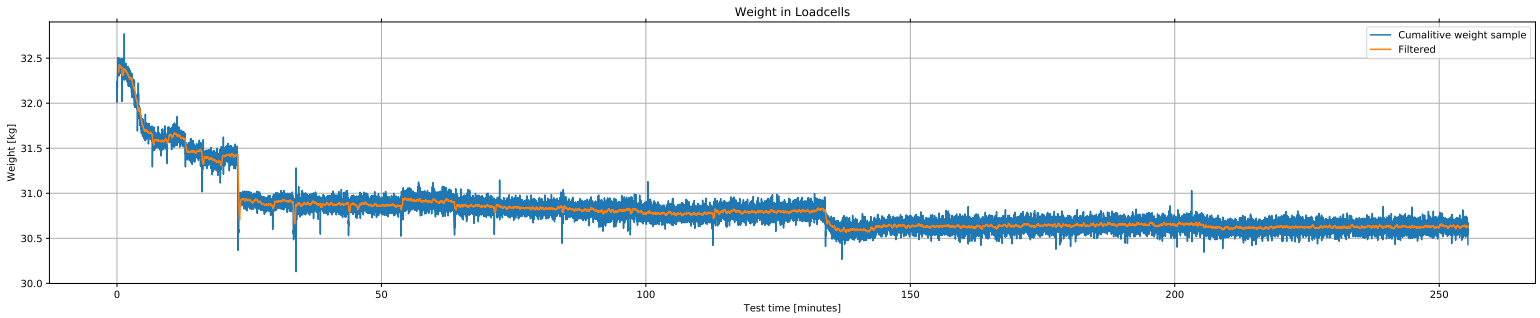

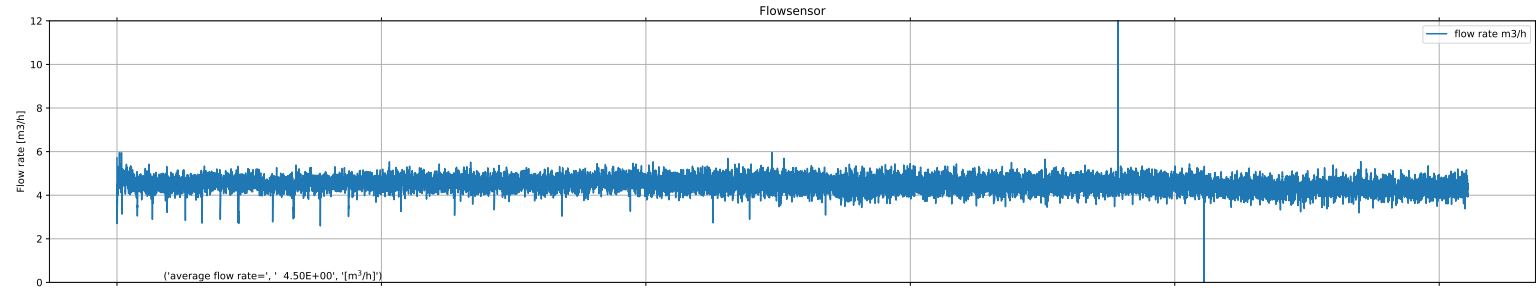

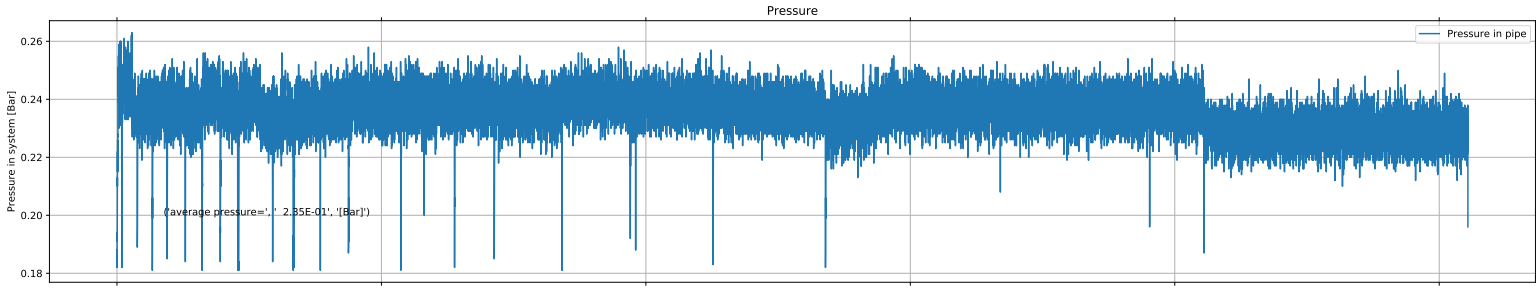

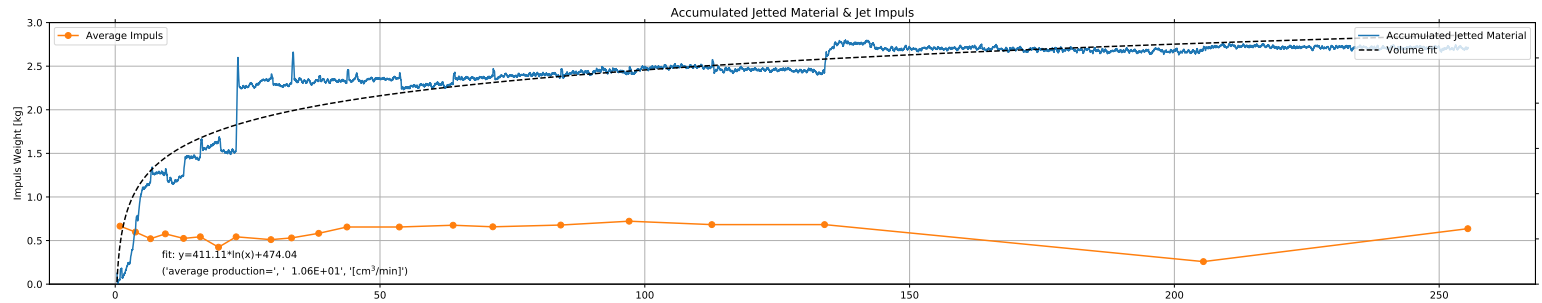

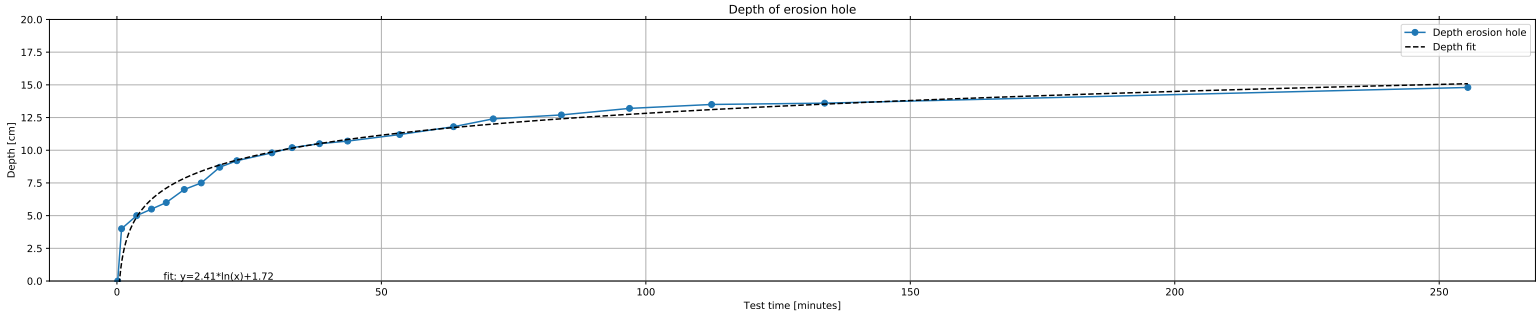

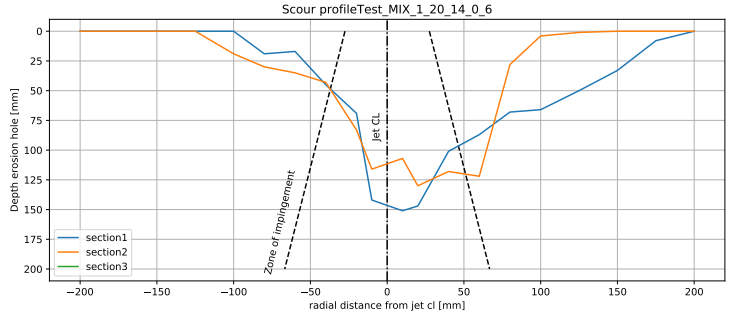

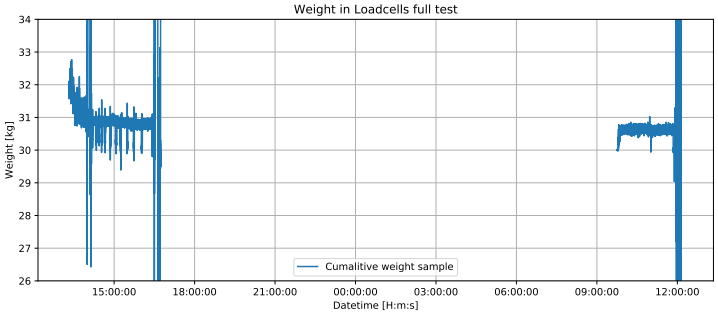

Table B.12: Test 15% Bent_15_0.6_1

TEST_15% Bent_15_0.6_1			pre-test	su	post-test		section 1	section 2	section 3
Date	10/24/19	dd/mm/yy		kPa	xo	mm	205	-	-
u_0	4.09	m/s	pocket vane 1	9.62	yo	mm	-	140	-
Q	1.07E-03	m³/s	pocket vane 2	8.53	$Z_{c,cl}$	mm	130	-	-
SOD	148	mm	post-test	su	$Z_{c,max}$	mm	132	-	-
D_n	20	mm		kPa	$r_{Zc,max}$	mm	10	-	-
SOD/D_n	7.4	-	pocket vane 3	7.43					
$p_{stag,0}$	5.50	kPa	pocket vane 4	6.56	V_t	1493	cm3	3.39	cm3/min
$p_{stag,0}/su$	0.61	-	field vane 1	9.50	V_{scale}	1765	cm3	4.01	cm3/min
t_{tot}	440	min	field vane 2	8.50	V_{water1}	2000	cm3	4.55	cm3/min
m_{sub}	32758	gram	CPT	14.00	V_{water2}	1850	cm3	4.20	cm3/min
Notes:	15% bentoninte, sample 11.								

Test_15%_Bent_15_0.6_1

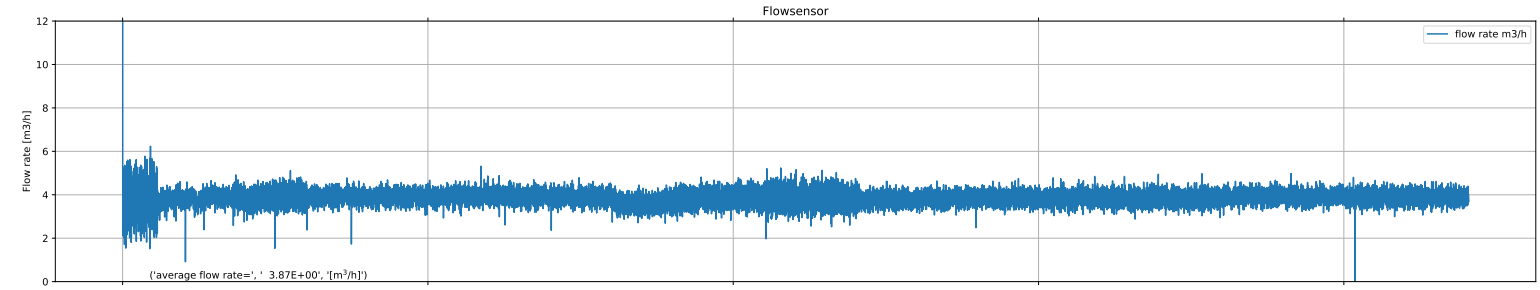

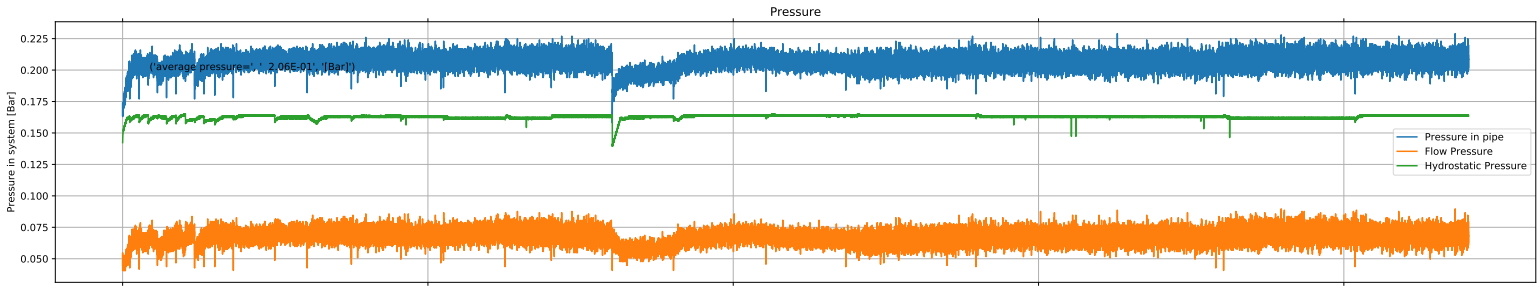

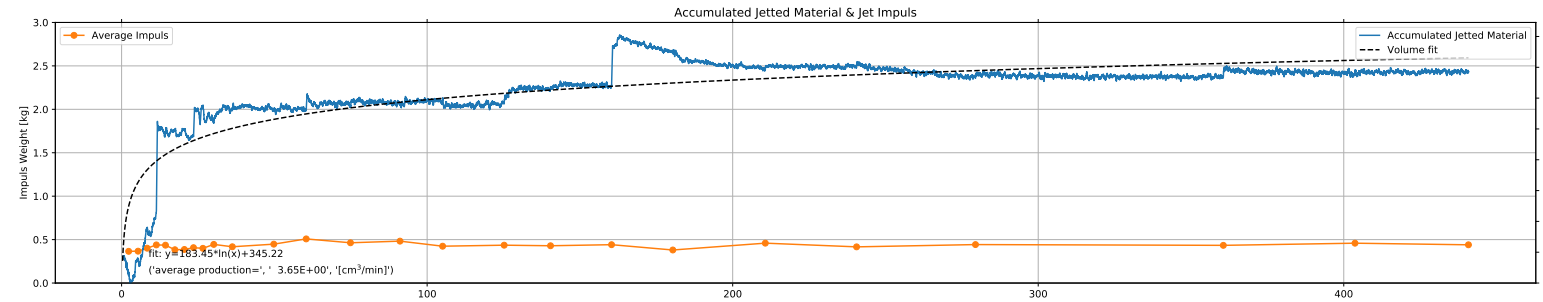

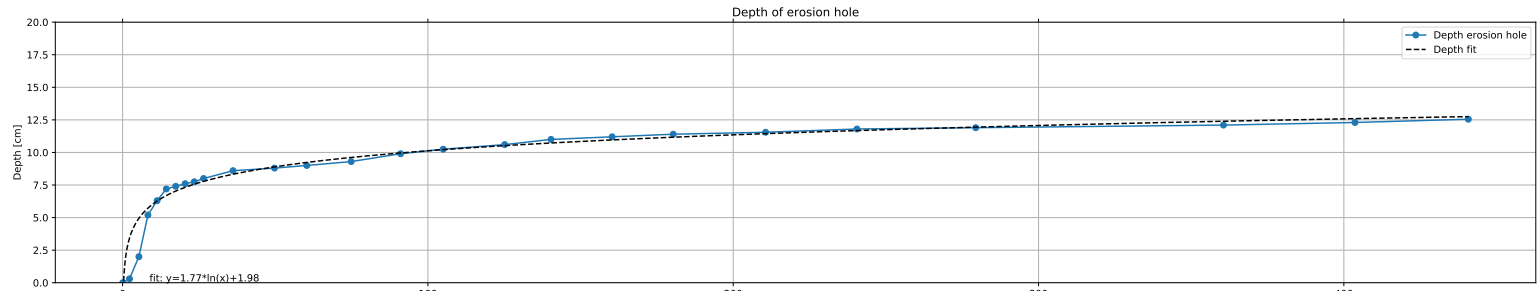

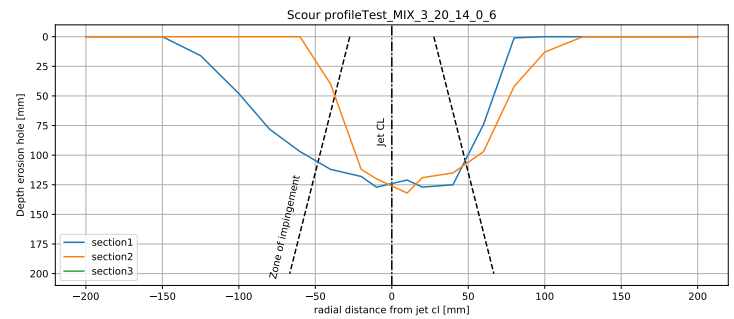

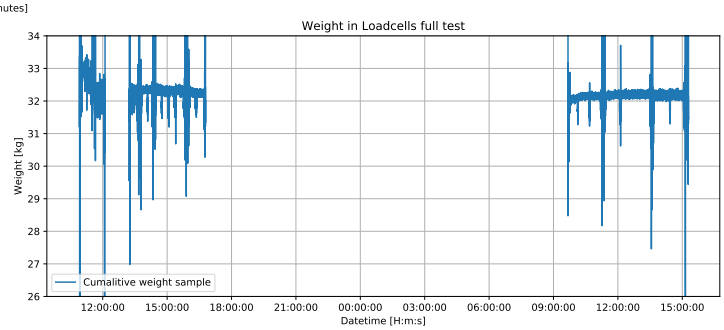

Table B.13: Test 15% Bent_15_0.6_2

TEST_15% Bent_15_0.6_2			pre-test	su	post-test		section 1	section 2	section 3
Date	11/20/19	dd/mm/yy		kPa	xo	mm	205	-	195
u_0	4.02	m/s	pocket vane 1	10.16	yo	mm	-	120	-
Q	1.05E-03	m³/s	pocket vane 2	8.09	$Z_{c,cl}$	mm	86	-	-
SOD	148	mm	post-test	su	$Z_{c,max}$	mm	169	-	-
D_n	20	mm		kPa	$r_{Zc,max}$	mm	65	-	-
SOD/D_n	7.4	-	pocket vane 3	9.40					
$p_{stag,0}$	5.50	kPa	pocket vane 4	7.21	V_t	2507	cm3	5.94	cm3/min
$p_{stag,0}/su$	0.61	-	field vane 1	8.50	V_{scale}	2515	cm3	5.96	cm3/min
t_{tot}	422	min	field vane 2	9.15	V_{water1}	2400	cm3	5.69	cm3/min
m_{sub}	33843	gram	CPT	18.00	V_{water2}	2500	cm3	5.92	cm3/min
Notes:	15% Bentonite, Sample 12								

Test_15%_Bent_15_0.6_2

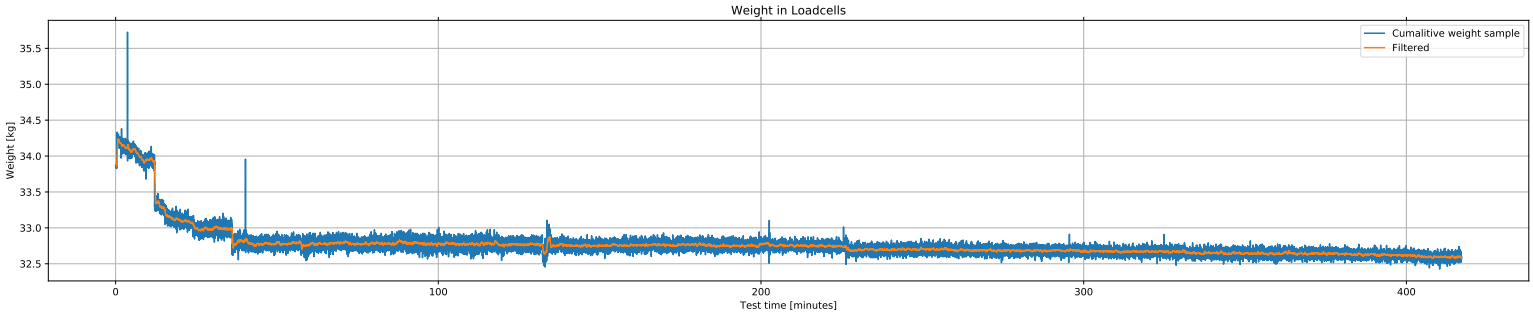

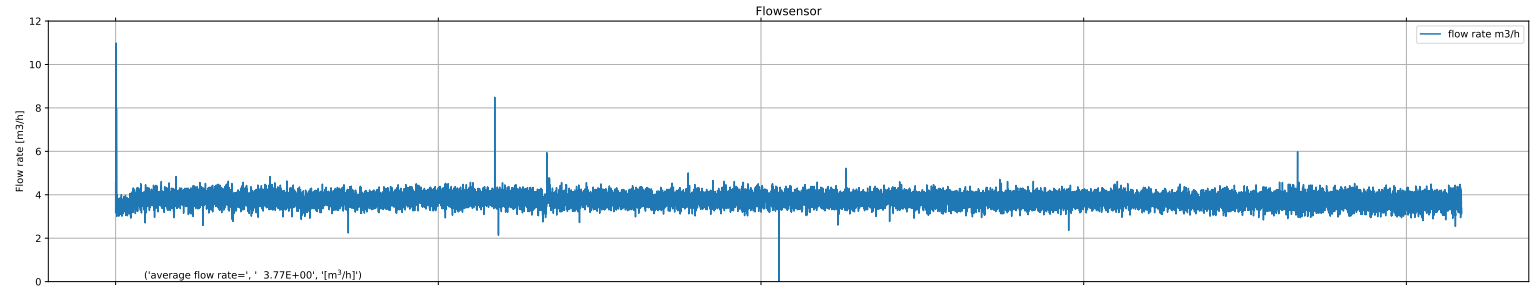

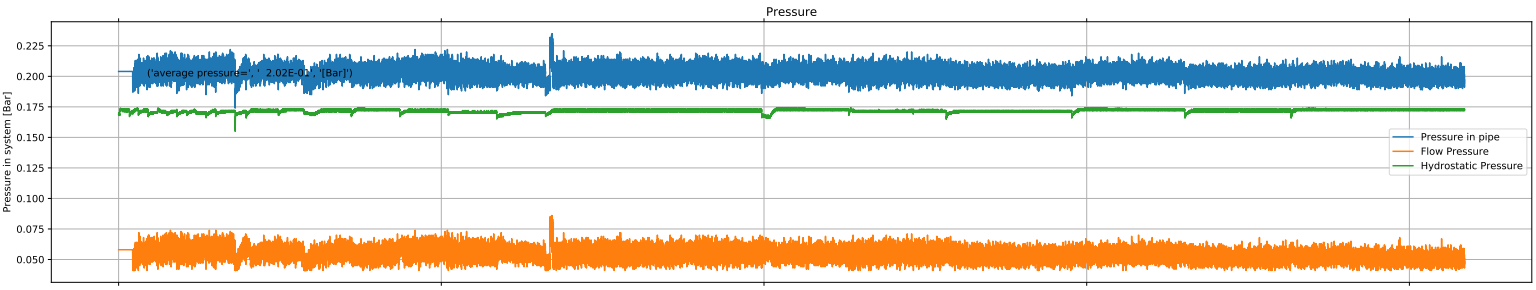

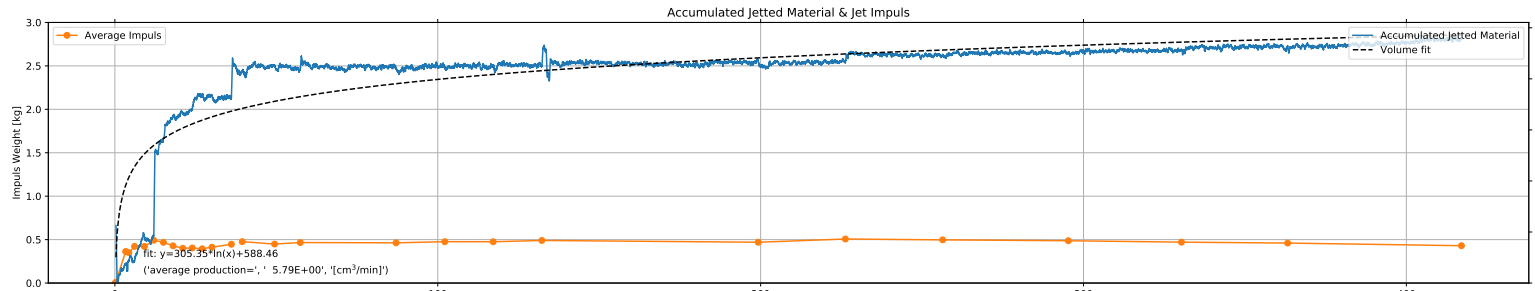

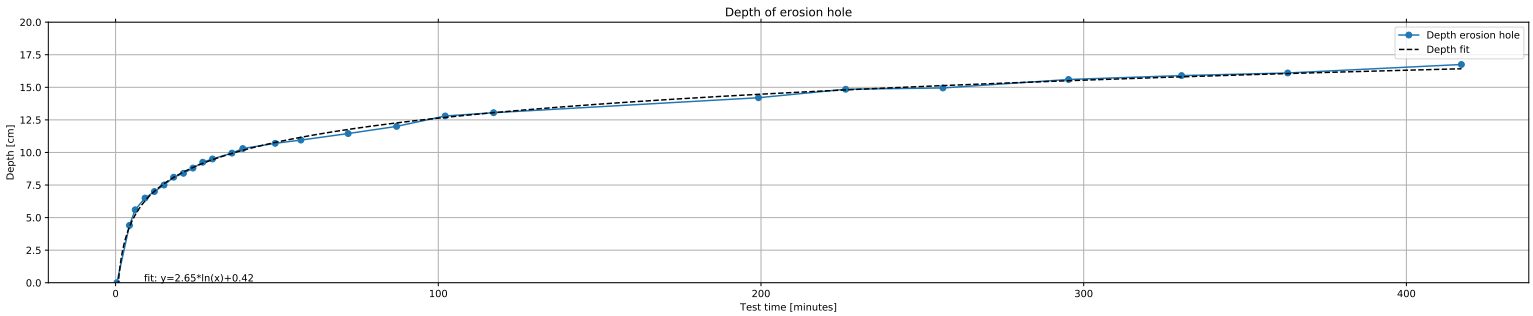

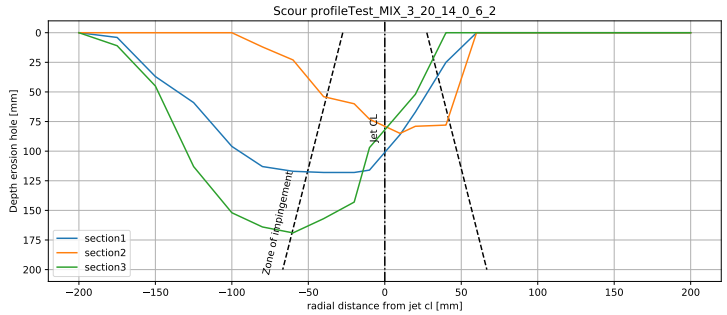

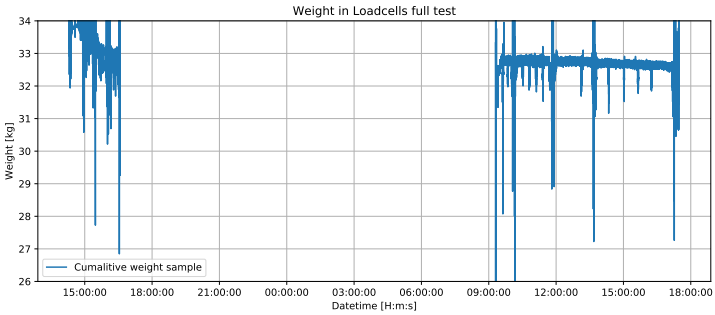

Table B.14: Test 25% Bent_15_0.6_1

TEST_15% Bent_15_0.6_2			pre-test	su	post-test		section 1	section 2	section 3
Date	10/29/19	dd/mm/yy		kPa	xo	mm	200	-	-
u_0	3.86	m/s	pocket vane 1	8.96	yo	mm	-	200	-
Q	1.01E-03	m³/s	pocket vane 2	7.87	$Z_{c,cl}$	mm	129	-	-
SOD	148	mm	post-test	su	$Z_{c,max}$	mm	131	-	-
D_n	20	mm		kPa	$r_{Zc,max}$	mm	0	-	-
SOD/D_n	7.4	-	pocket vane 3	5.47					
$p_{stag,0}$	5.02	kPa	pocket vane 4	5.90	V_t	2070	cm3	4.89	cm3/min
$p_{stag,0}/su$	0.63	-	field vane 1	7.00	V_{scale}	2071	cm3	4.90	cm3/min
t_{tot}	423	min	field vane 2	8.00	V_{water1}	2050	cm3	4.85	cm3/min
m_{sub}	34769	gram	CPT	10.0	V_{water2}	2075	cm3	4.91	cm3/min
Notes:	25% bentoninte, sample 15								

Test_25%_Bent_15_0.6

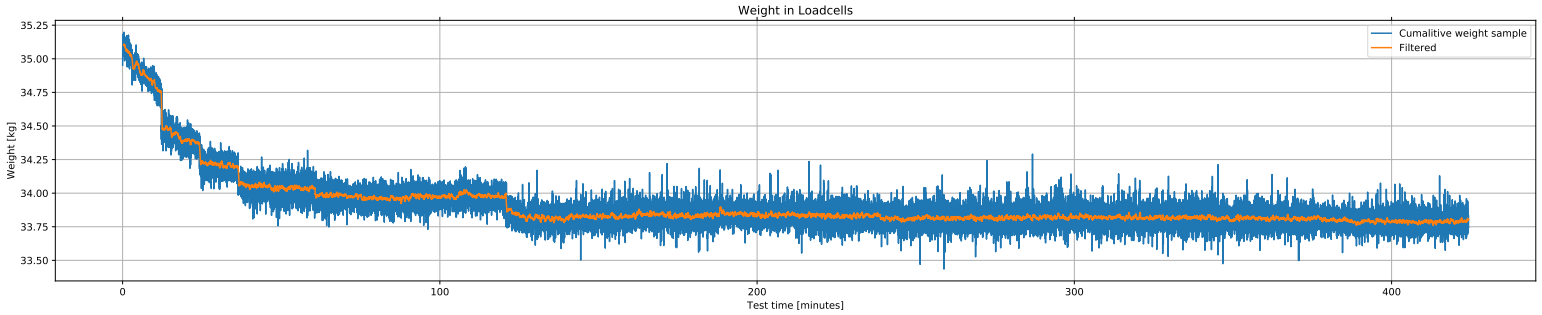

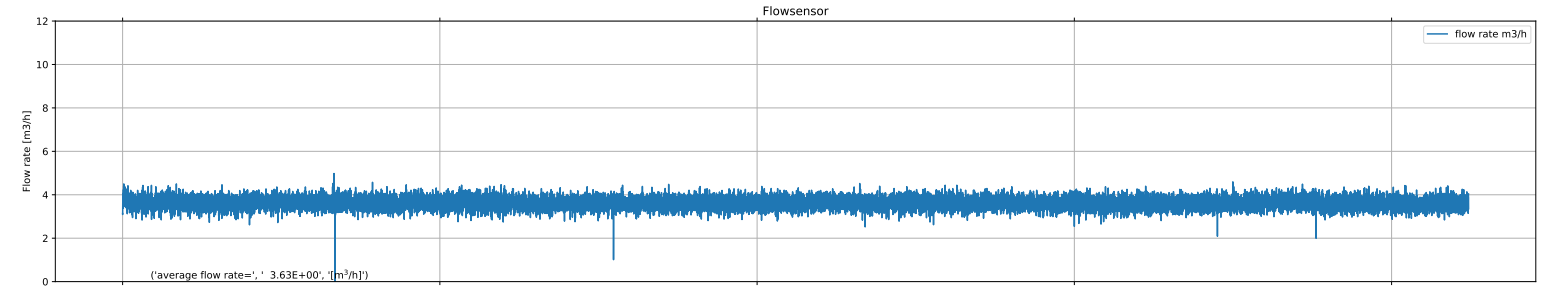

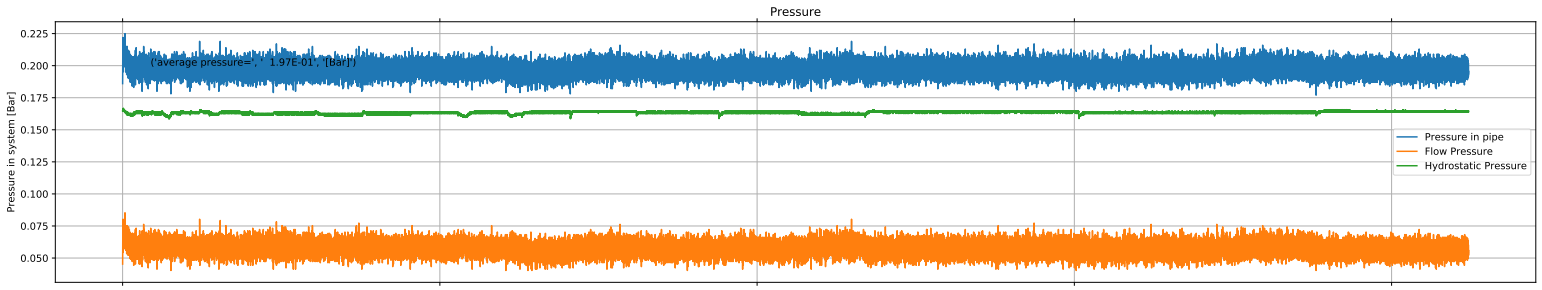

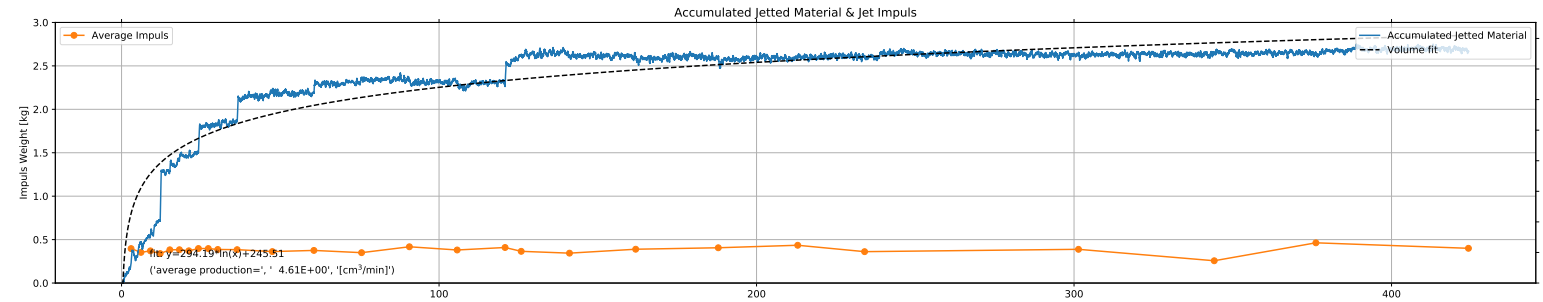

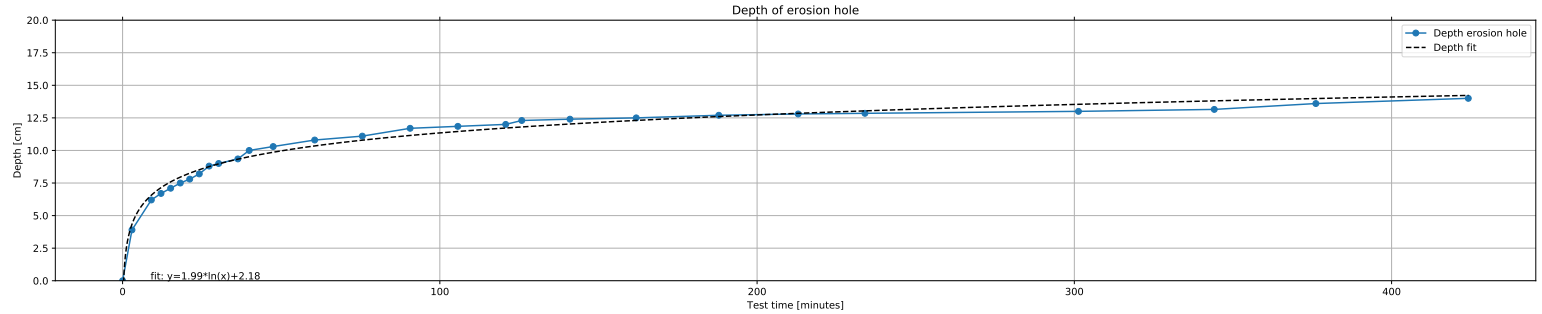

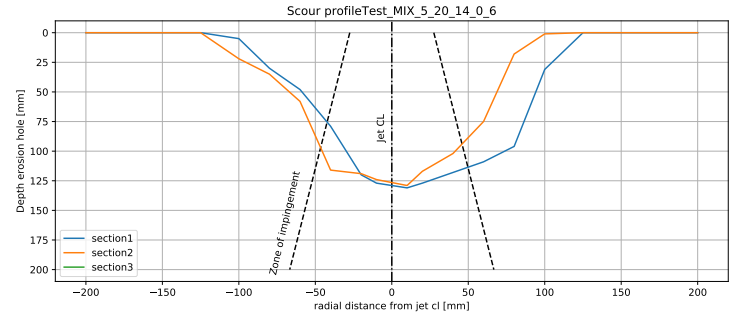

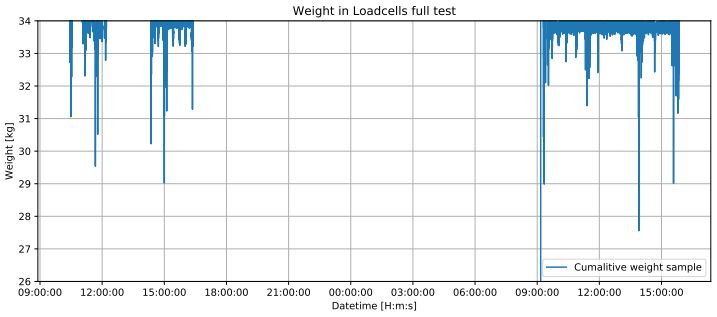

Table B.15: Test K_Sand_15_0.6_1

TEST_K_Sand_15_0.6_2			pre-test	su	post-test		section 1	section 2	section 3
Date	11/25/19	dd/mm/yy		kPa	xo	mm	140	-	-
u_0	4.06	m/s	pocket vane 1	9.18	yo	mm	-	160	-
Q	1.07E-03	m³/s	pocket vane 2	9.84	$Z_{c,cl}$	mm	168	-	-
SOD	147	mm	post-test	su	$Z_{c,max}$	mm	168	-	-
D_n	20	mm		kPa	$r_{Zc,max}$	mm	0	-	-
SOD/D_n	7.4	-	pocket vane 3	9.18					
$p_{stag,0}$	5.70	kPa	pocket vane 4	7.65	V_t	2238	cm3	21.32	cm3/min
$p_{stag,0}/su$	0.60	-	field vane 1	9.25	V_{scale}	2191	cm3	20.87	cm3/min
t_{tot}	105	min	field vane 2	10	V_{water1}	1800	cm3	17.14	cm3/min
m_{sub}	39130	gram	CPT	-	V_{water2}	1750	cm3	16.67	cm3/min
Notes:	Kaolin-Sand mix, Sample 17								

Test_Kaolin-Sand_15_0.6

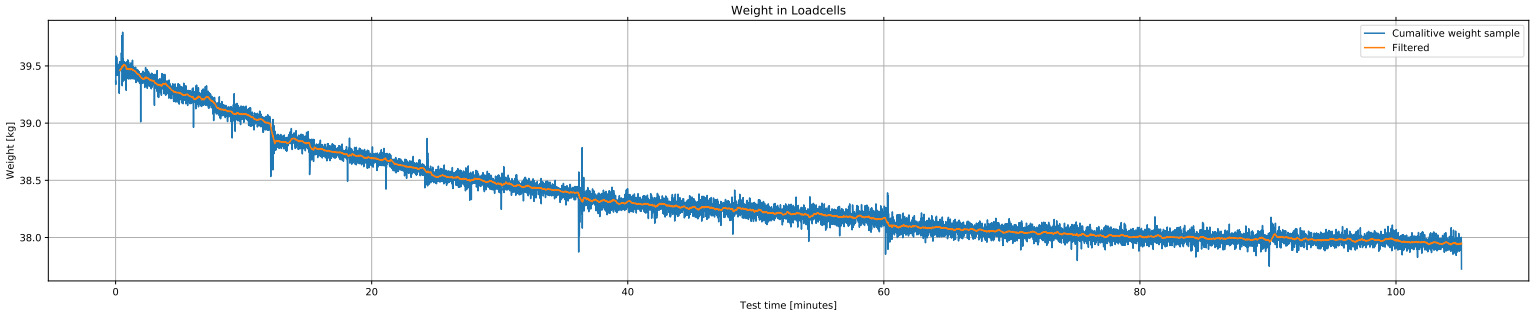

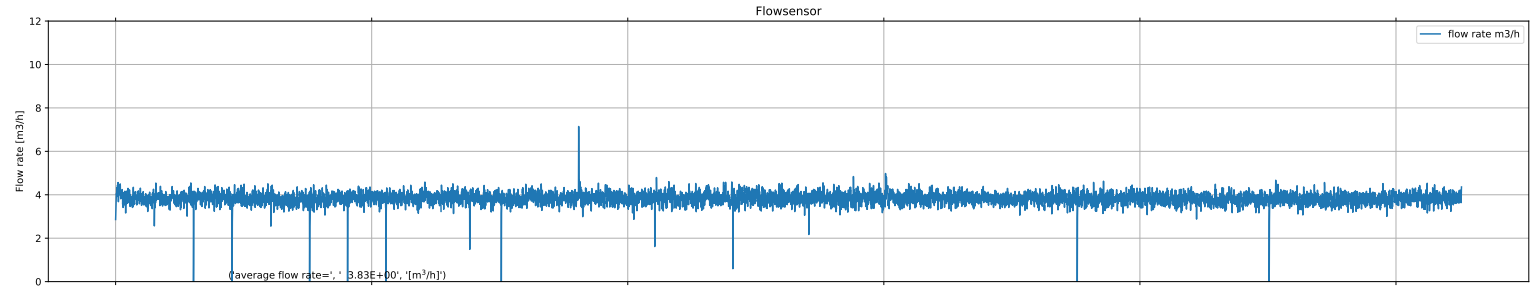

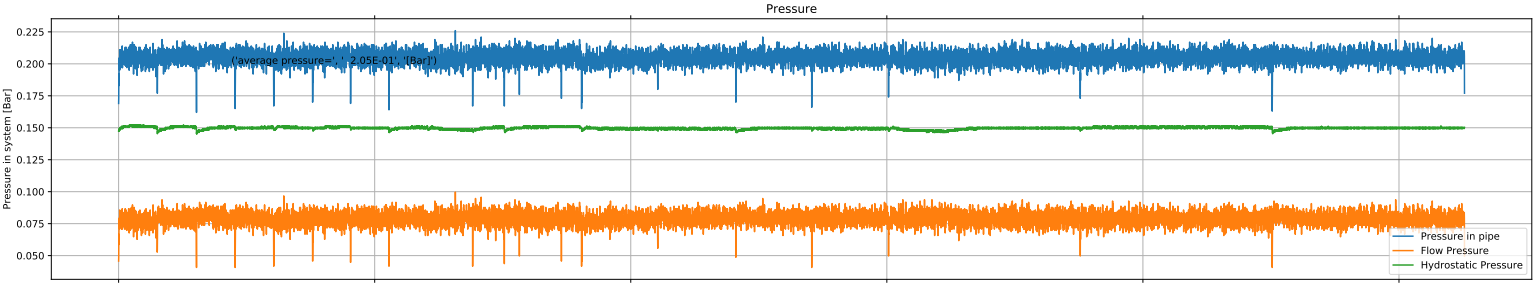

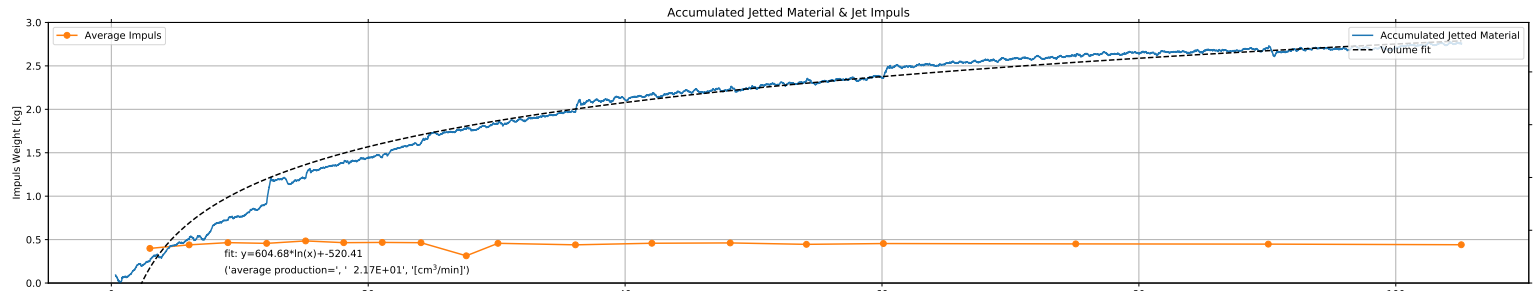

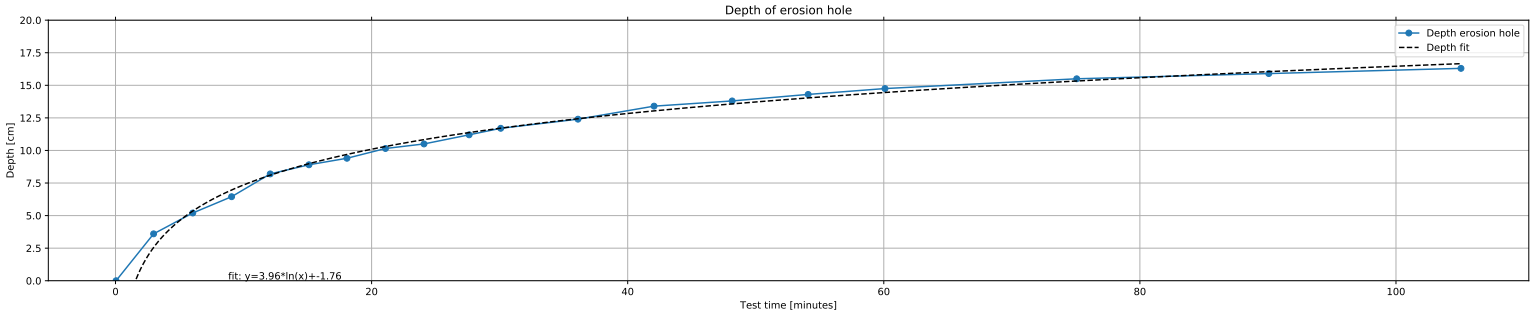

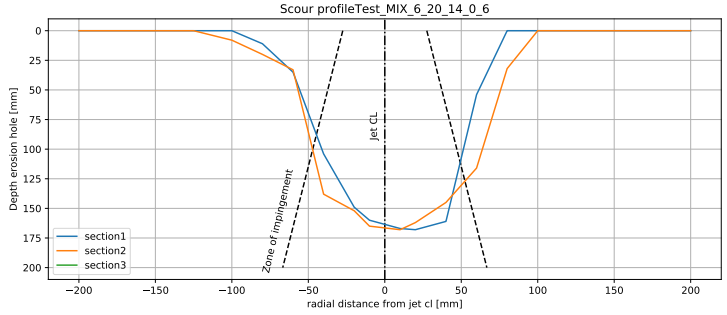

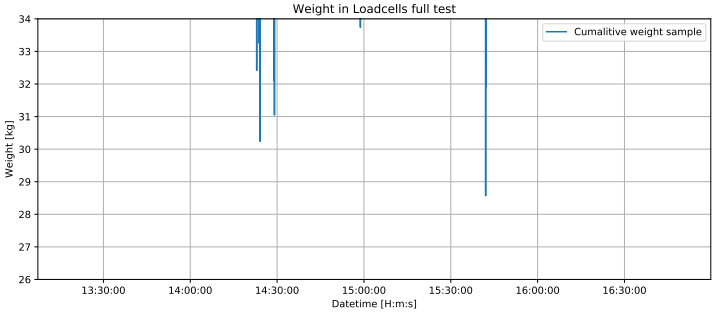

Table B.16: Test K_15_1.0_1

TEST_K_15_1.0_1			pre-test	su	post-test		section 1	section 2	section 3
Date	9/13/2019	dd/mm/yy		kPa	xo	mm	120	-	-
u_0	5.47	m/s	pocket vane 1	10.06	yo	mm	-	180	-
Q	1.43E-03	m³/s	pocket vane 2	10.27	$Z_{c,cl}$	mm	200	-	-
SOD	154	mm	post-test	su	$Z_{c,max}$	mm	200	-	-
D_n	20	mm		kPa	$r_{Zc,max}$	mm	40	-	-
SOD/D_n	7.7	-	pocket vane 3	9.84					
$p_{stag,0}$	10.20	kPa	pocket vane 4	9.40	V_t	3396	cm3	282.99	cm3/min
$p_{stag,0}/su$	1.04	-	field vane 1	9	V_{scale}	3121	cm3	260.12	cm3/min
t_{tot}	12	min	field vane 2	10	V_{water1}	3150	cm3	262.50	cm3/min
m_{sub}	30127	gram	CPT	18.5	V_{water2}	3175	cm3	264.58	cm3/min
Notes:	Kaolin test, due to localised hole depth measurement is incorrect from a depth of approx 155 mm (sample 5)								

Test_K_15_1.0_1

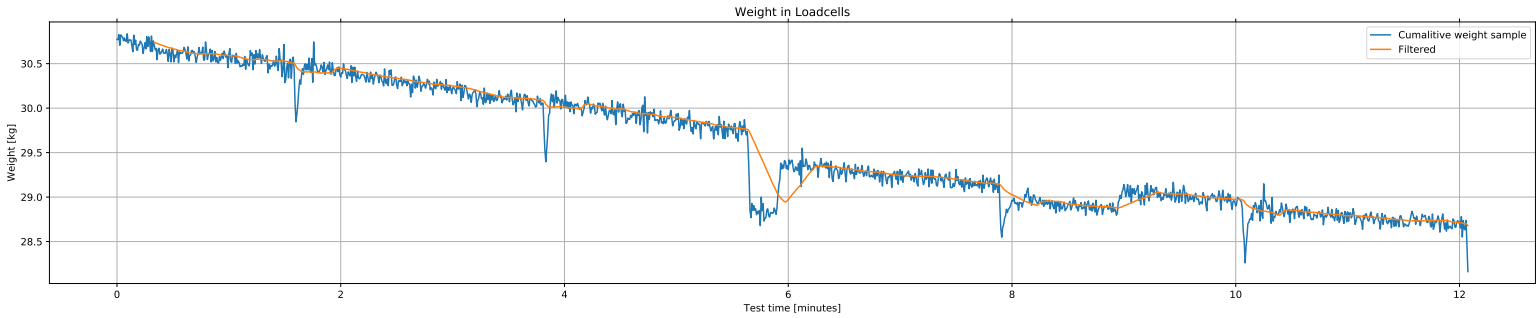
Weight in Loadcells
Cumalitive weight sample
Filtered
Weight [kg]
Test time [minutes]

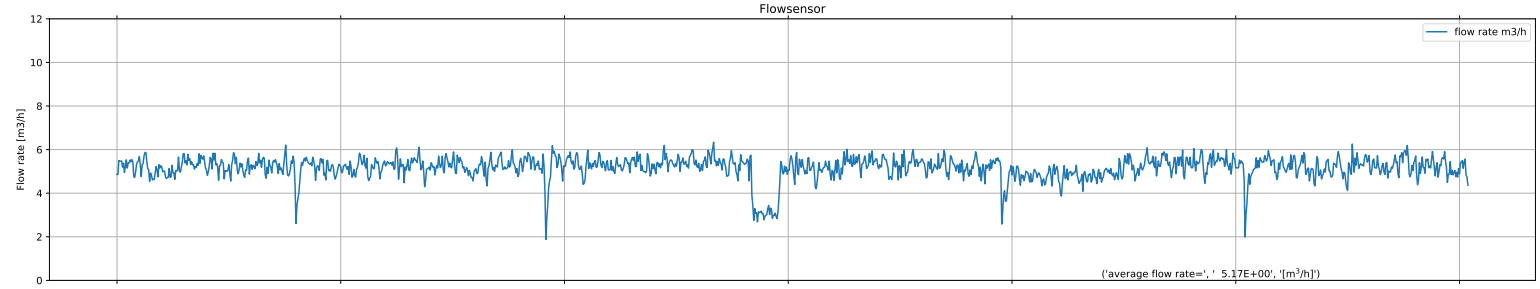
Flowsensor
flow rate m3/h
Flow rate [m3/h]
('average flow rate=', ' 5.17E+00', '[m³/h]')

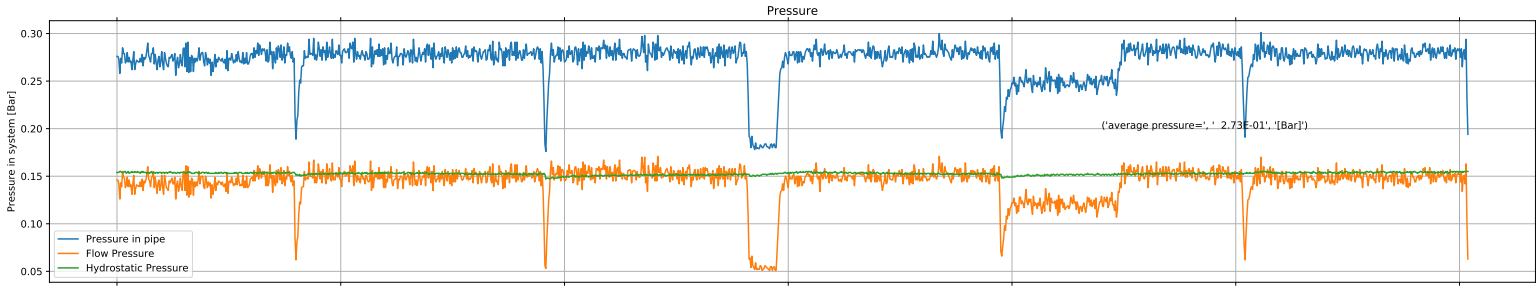
Pressure
Pressure in system [Bar]
('average pressure=', ' 2.73E-01', '[Bar]')
Pressure in pipe
Flow Pressure
Hydrostatic Pressure

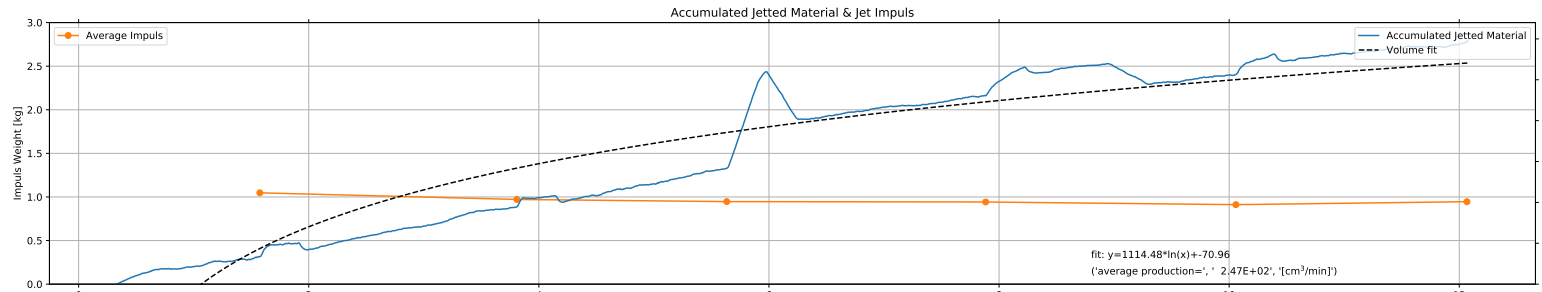
Accumulated Jetted Material & Jet Impuls
Average Impuls
Accumulated Jetted Material
Volume fit
Impuls Weight [kg]
Volume [cm3]
fit: y=1114.48*ln(x)+-70.96
('average production=', ' 2.47E+02', '[cm³/min]')

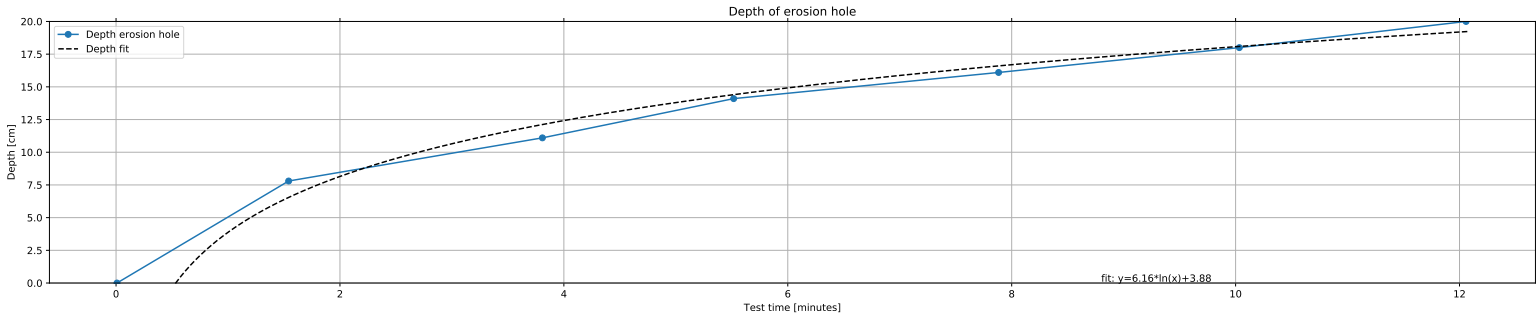
Depth of erosion hole
Depth erosion hole
Depth fit
Depth [cm]
fit: y=6.16*ln(x)+3.88
Test time [minutes]

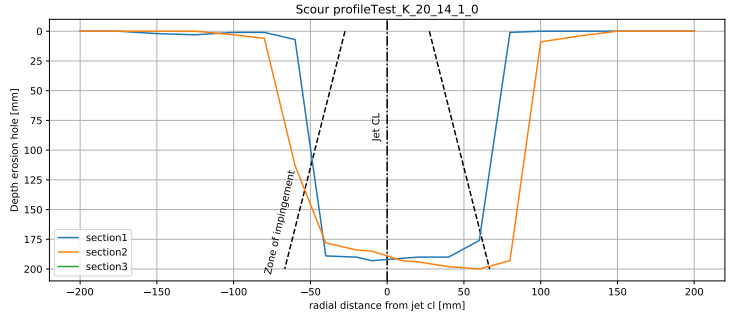
Scour profileTest_K_20_14_1_0
Depth erosion hole [mm]
Zone of impingement
Jet CL
section1
section2
section3
radial distance from jet cl [mm]

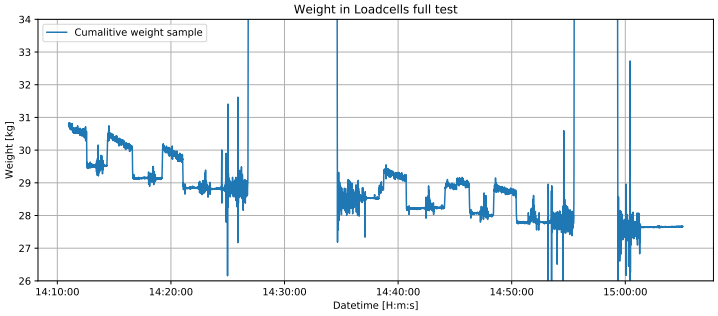
Weight in Loadcells full test
Cumalitive weight sample
Weight [kg]
Datetime [H:m:s]

Table B.17: Test 5%_Bent_15_1.0_1

TEST_5%_Bent_15_1.0_1			pre-test	su	post-test		section 1	section 2	section 3
Date	09/10/19	dd/mm/yy		kPa	xo	mm	255	0	-
u_0	5.85	m/s	pocket vane 1	12.02	yo	mm	-	250	-
Q	1.54E-03	m³/s	pocket vane 2	11.48	$Z_{c,cl}$	mm	200	-	-
SOD	152	mm	post-test	su	$Z_{c,max}$	mm	200	-	-
D_n	20	mm		kPa	$r_{Zc,max}$	mm	0	-	-
SOD/D_n	7.6	-	pocket vane 3	10.49					
$p_{stag,0}$	11.50	kPa	pocket vane 4	8.74	V_t	3304	cm3	45.89	cm3/min
$p_{stag,0}/su$	0.99	-	field vane 1	11.00	V_{scale}	3166	cm3	43.97	cm3/min
t_{tot}	72	min	field vane 2	11.75	V_{water1}	2900	cm3	40.28	cm3/min
m_{sub}	31578	gram	CPT	-	V_{water2}	2700	cm3	37.50	cm3/min
Notes:	5% bentonite, 1 softer corner 10.5 kPa, check density								

Test_5%_Bent_15_1.0_1

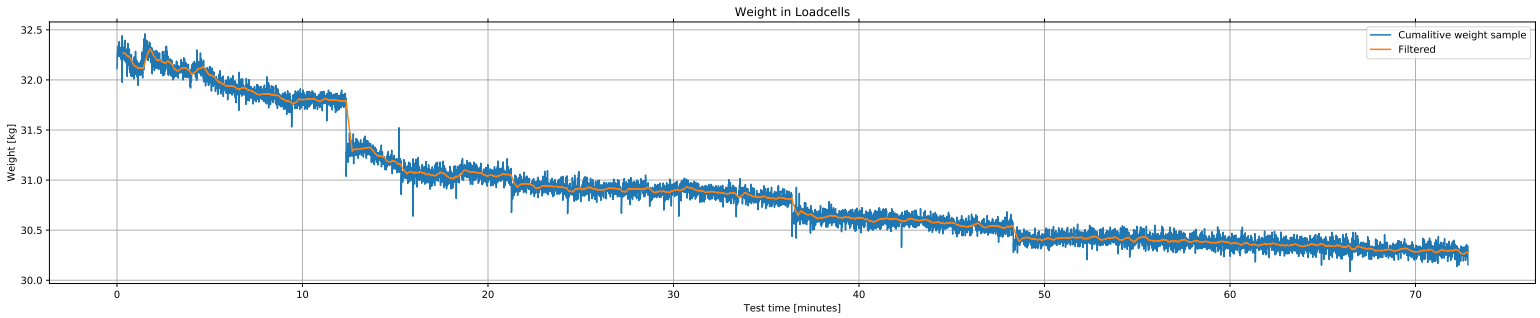

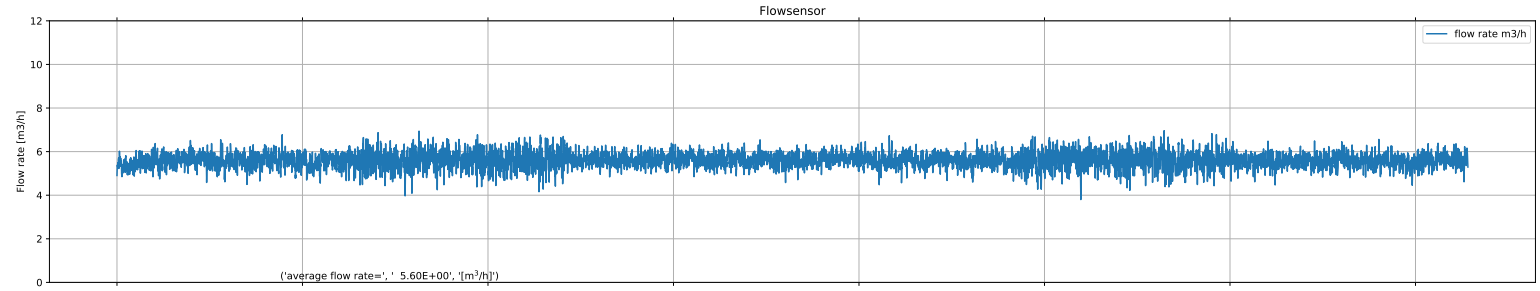

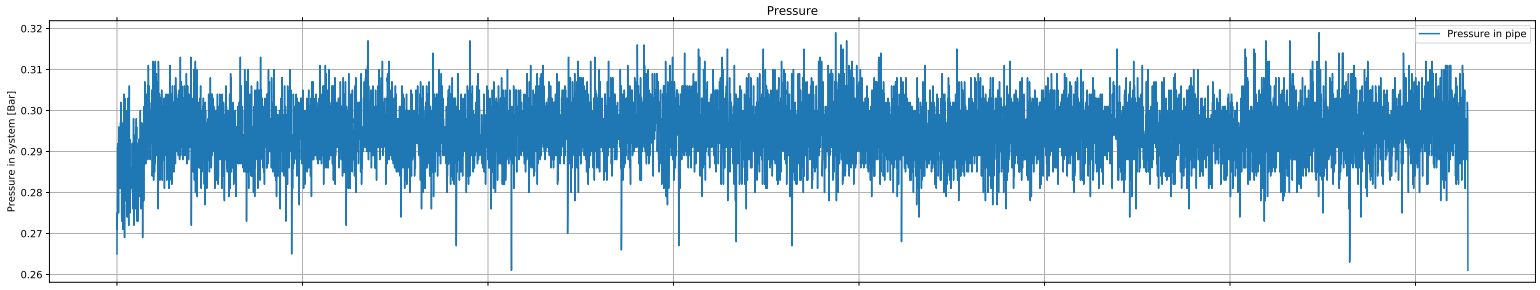

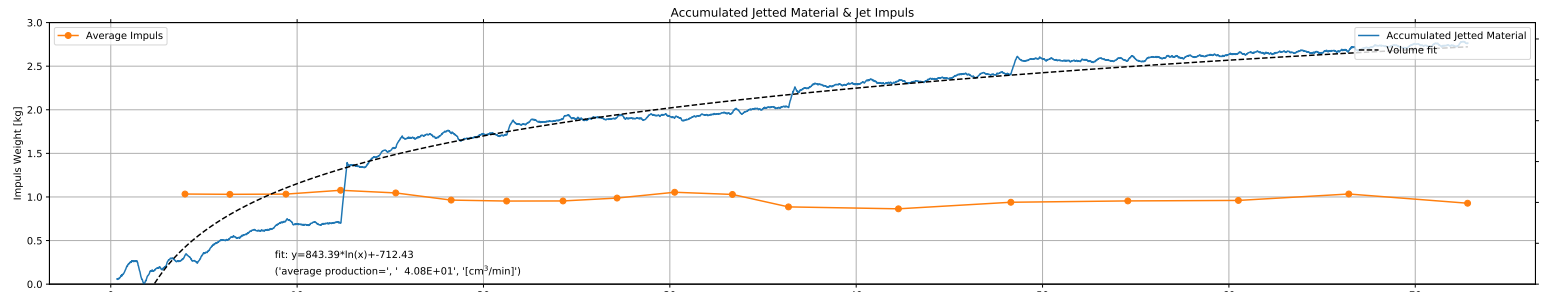

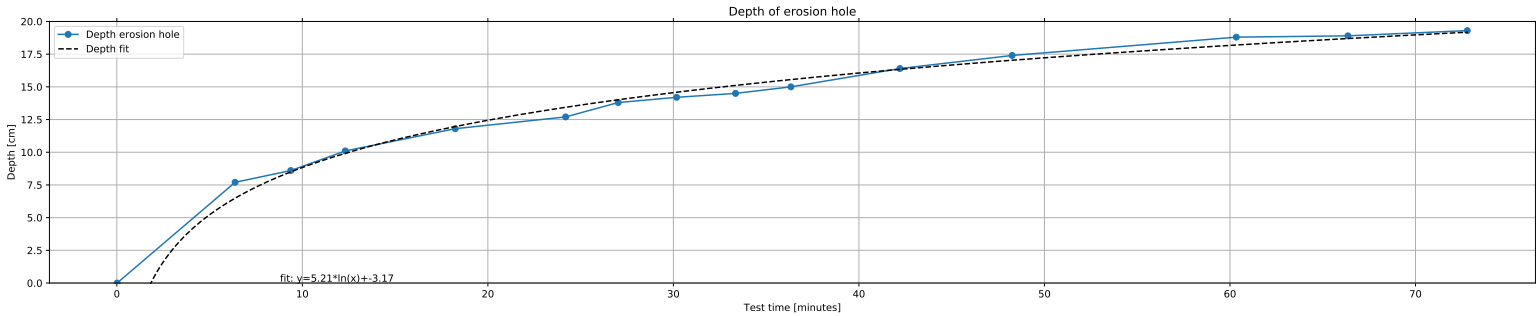

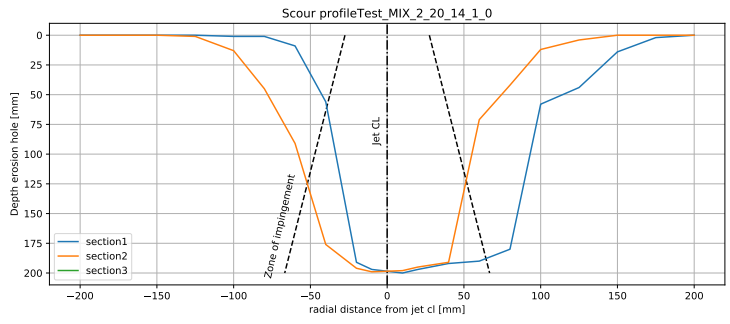

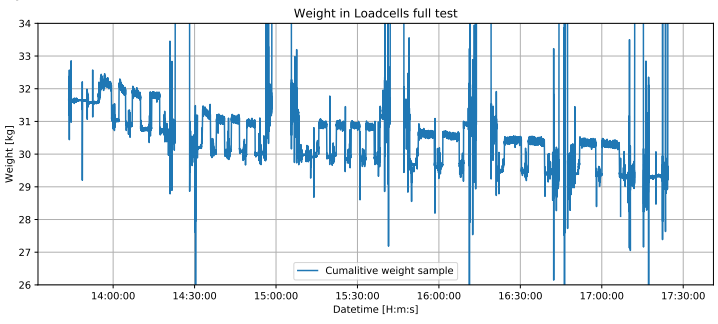

Table B.18: Test 10%_Bent_15_1.0_1

TEST_10%_Bent_15_1.0_1			pre-test	su	post-test		section 1	section 2	section 3
Date	09/18/19	dd/mm/yy		kPa	xo	mm	250	-	-
u_0	5.44	m/s	pocket vane 1	9.95	yo	mm	-	250	-
Q	1.43E-03	m³/s	pocket vane 2	10.93	$Z_{c,cl}$	mm	200	-	-
SOD	151	mm	post-test	su	$Z_{c,max}$	mm	200	-	-
D_n	20	mm		kPa	$r_{Zc,max}$	mm	0	-	-
SOD/D_n	7.6	-	pocket vane 3	7.65					
$p_{stag,0}$	10.40	kPa	pocket vane 4	8.09	V_t	4454	cm3	37.12	cm3/min
$p_{stag,0}/su$	0.96	-	field vane 1	12.00	V_{scale}	5971	cm3	49.75	cm3/min
t_{tot}	120	min	field vane 2	10.50	V_{water1}	4000	cm3	33.33	cm3/min
m_{sub}	31528	gram	CPT	21	V_{water2}	4200	cm3	35.00	cm3/min

Notes: 10% Bentonite; strongly deflected, High production wide hole, at the end filter was reached, therefore spike in the production at the end. Water volume measurements not accurate, water flows trough filter, scale weight is lower because measurement was done day after, therefore all the water was out of the filter therefore reducing the weight of the sample

Test_10%_Bent_1.0_1

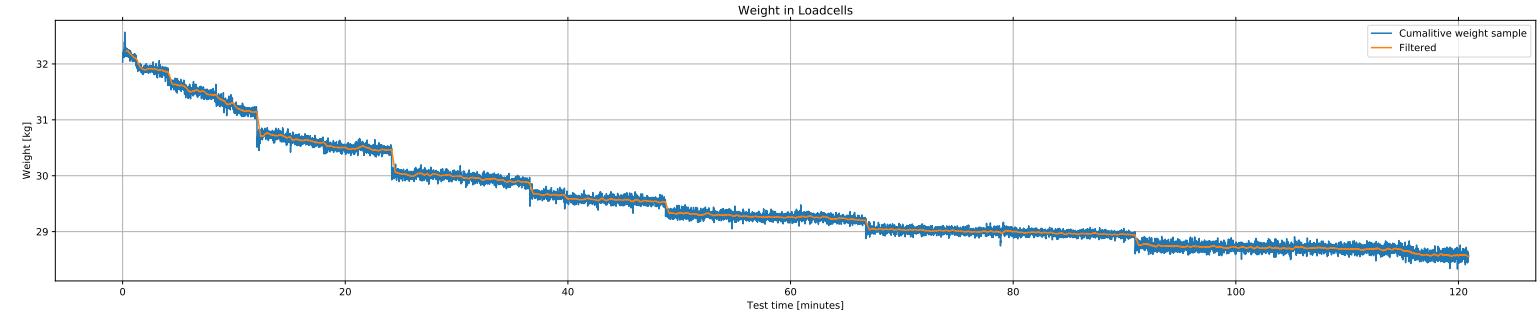

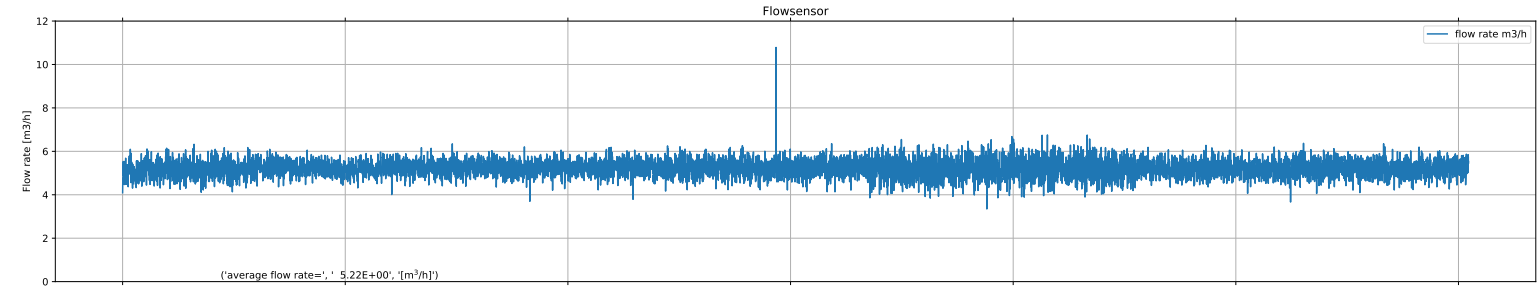

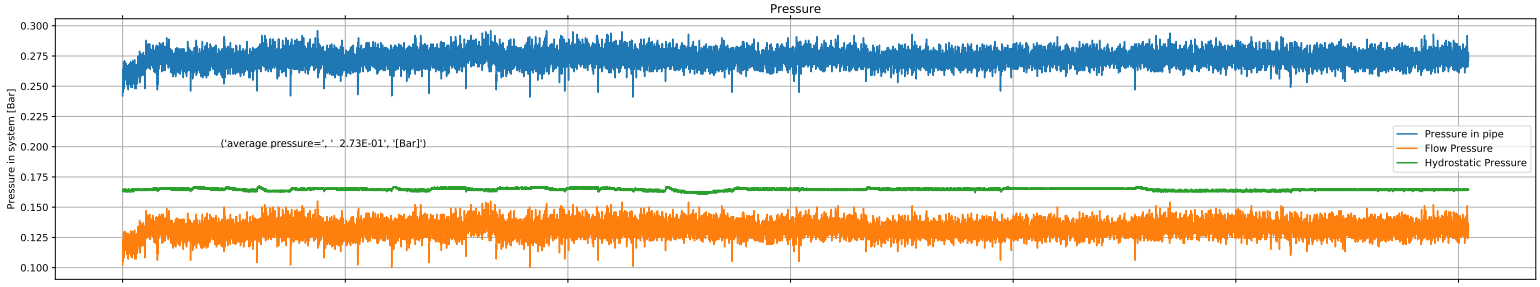

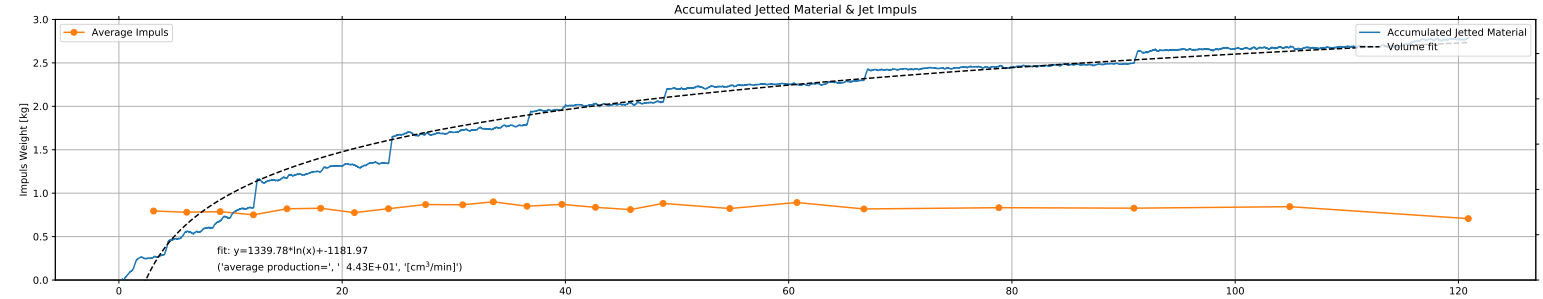

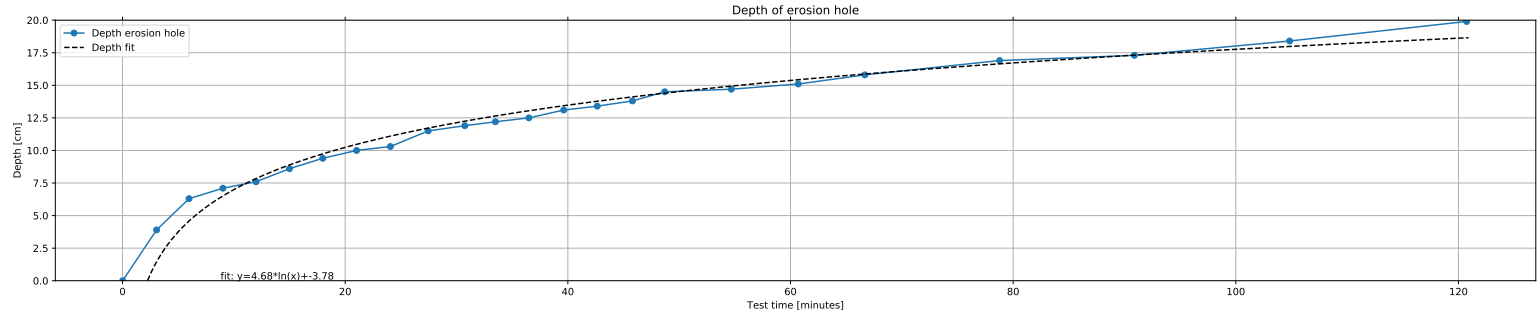

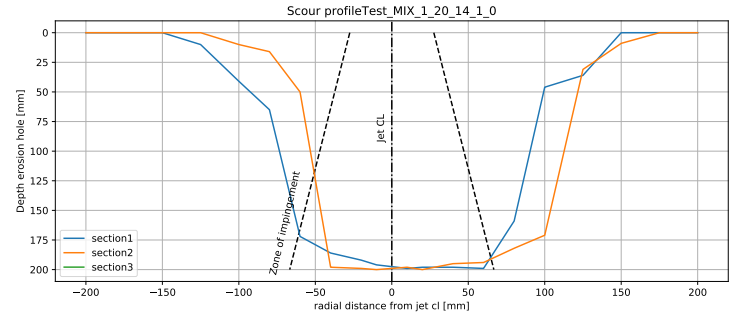

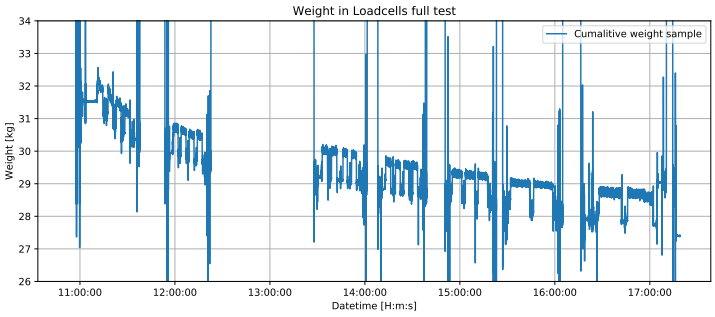

Table B.19: Test 5%_Bent_15_1.4_1

TEST_5%_Bent_15_1.4_1			pre-test	su	post-test		section 1	section 2	section 3
Date	10/02/19	dd/mm/yy		kPa	xo	mm	350	-	-
u_0	7.01	m/s	pocket vane 1	12.46	yo	mm	-	275	-
Q	1.88E-03	m³/s	pocket vane 2	12.46	$Z_{c,cl}$	mm	192	-	-
SOD	150	mm	post-test	su	$Z_{c,max}$	mm	192	-	-
D_n	20	mm		kPa	$r_{Zc,max}$	mm	0	-	-
SOD/D_n	7.5	-	pocket vane 3	11.48					
$p_{stag,0}$	17.50	kPa	pocket vane 4	9.84	V_t	7919	cm3	263.96	cm3/min
$p_{stag,0}/su$	1.42	-	field vane 1	12.75	V_{scale}	7604	cm3	253.45	cm3/min
t_{tot}	30	min	field vane 2	11.5	V_{water1}	7600	cm3	253.33	cm3/min
m_{sub}	32161	gram	CPT	19	V_{water2}	7620	cm3	254.00	cm3/min
Notes:	5% Bentonite, sample 6, wide hole at beginning jetting								

Test_5%_Bent_15_1.4_1

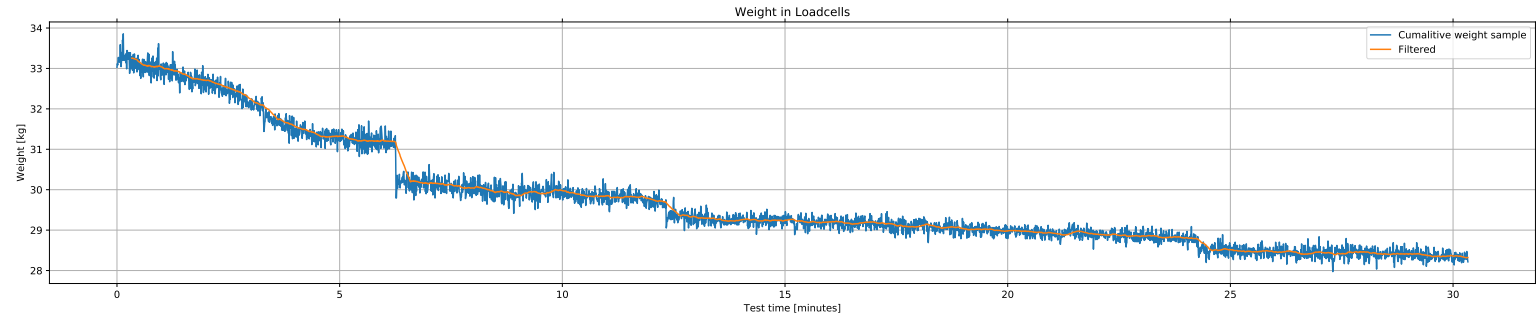

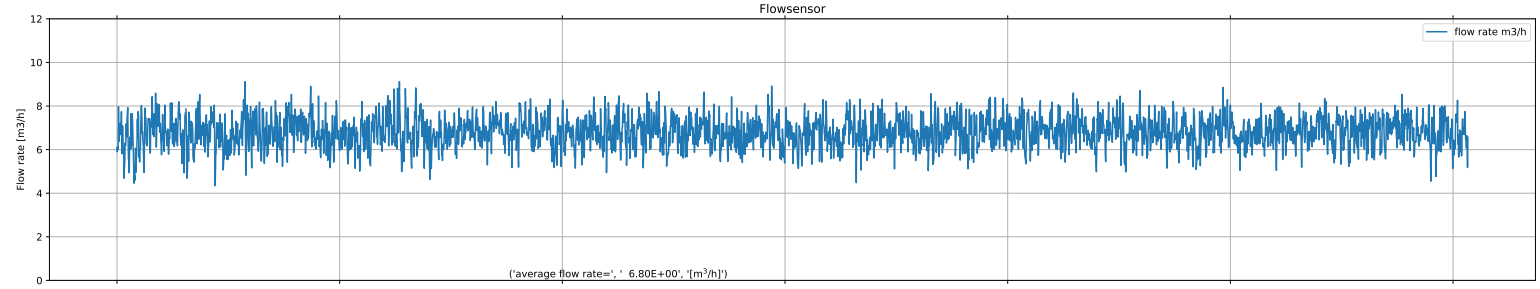

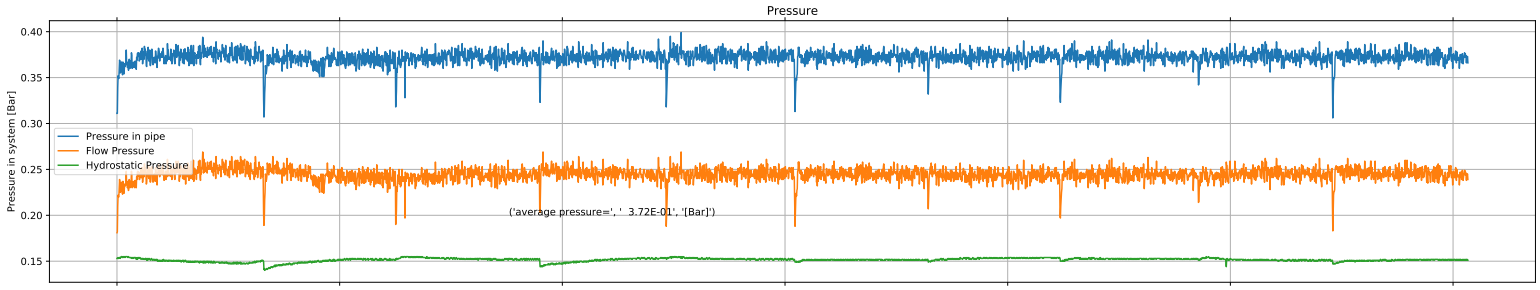

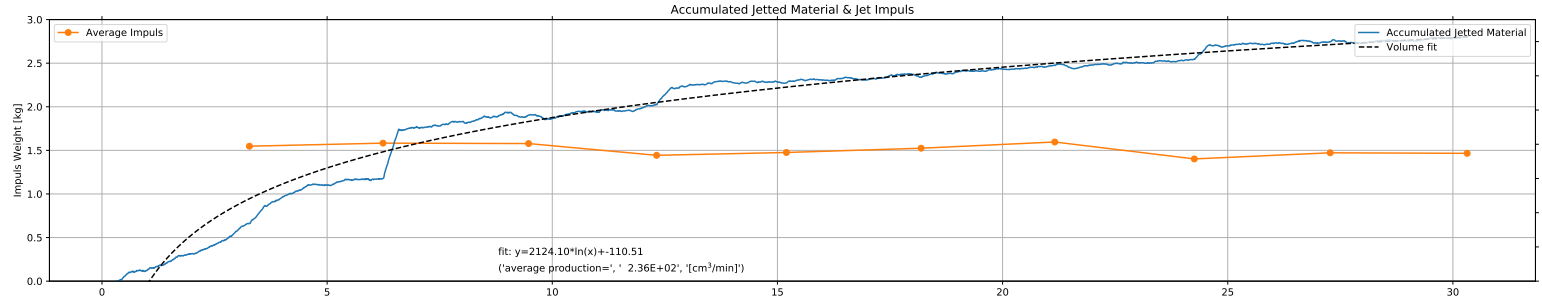

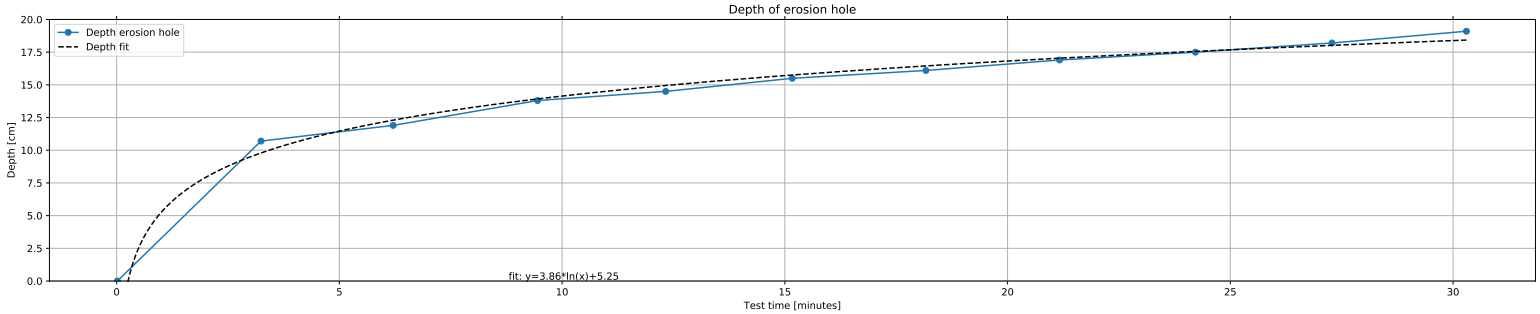

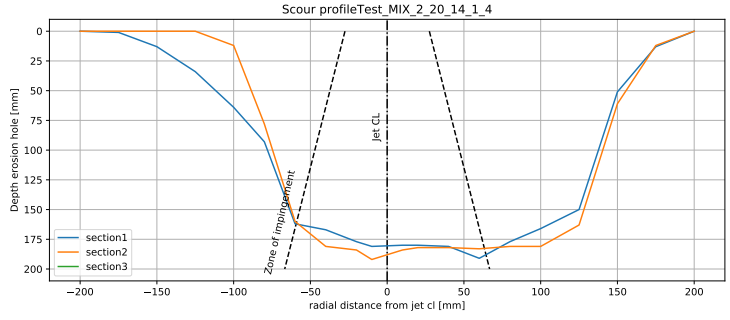

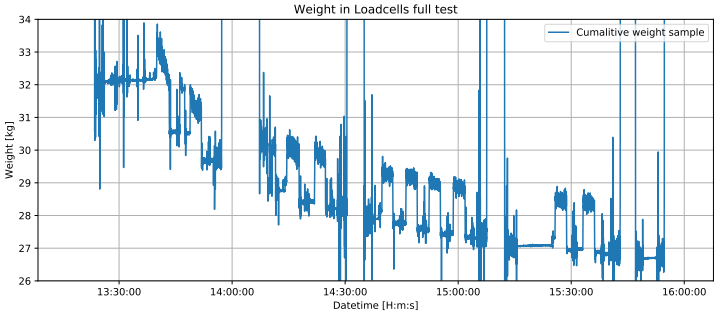

Table B.20: Test 10%_Bent_15_1.4_1

TEST_10%_Bent_15_1.4_1			pre-test	su	post-test				
							section 1	section 2	section 3
Date	10/09/19	dd/mm/yy		kPa	xo	mm	250	-	-
u_0	6.19	m/s	pocket vane 1	9.29	yo	mm	-	300	300
Q	1.65E-03	m³/s	pocket vane 2	9.73	$Z_{c,cl}$	mm	190	-	-
SOD	150	mm	post-test	su	$Z_{c,max}$	mm	200	-	-
D_n	20	mm		kPa	$r_{Zc,max}$	mm	20	-	-
SOD/D_n	7.5	-	pocket vane 3	8.31					
$p_{stag,0}$	13.30	kPa	pocket vane 4	9.29	V_t	5340	cm3	74.17	cm3/min
$p_{stag,0}/su$	1.46	-	field vane 1	8.50	V_{scale}	5206	cm3	72.30	cm3/min
t_{tot}	72	min	field vane 2	9.00	V_{water1}	4950	cm3	68.75	cm3/min
m_{sub}	33169	gram	CPT	17	V_{water2}	5150	cm3	71.53	cm3/min
Notes:	10% Bentonite, sample 7								

Test_10%_Bent_15_1.4_1

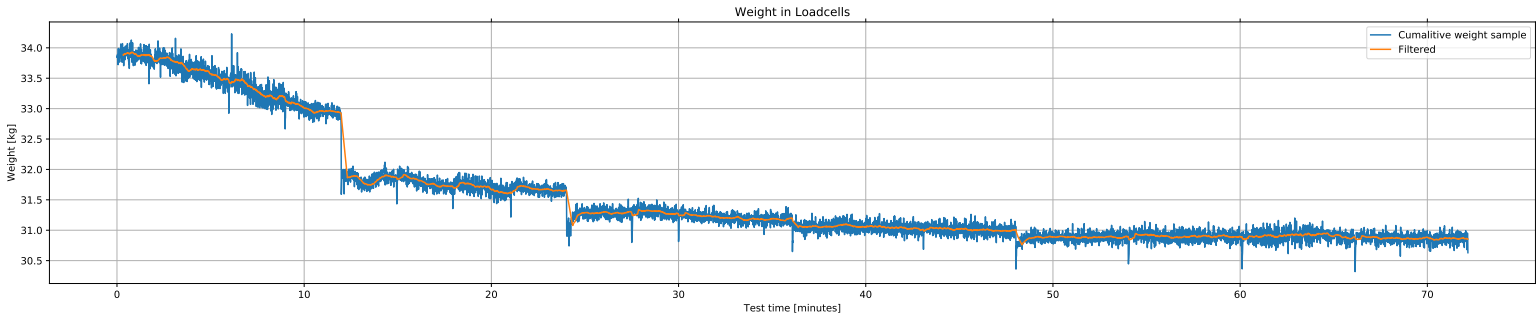

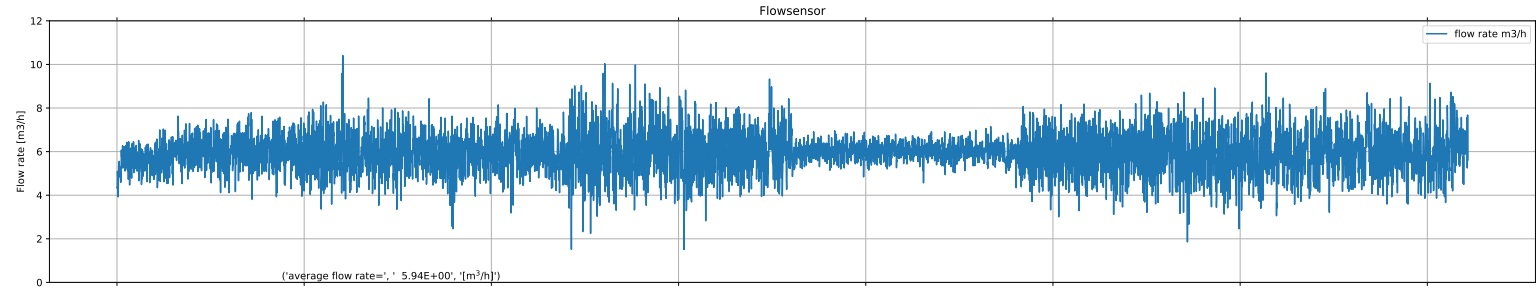

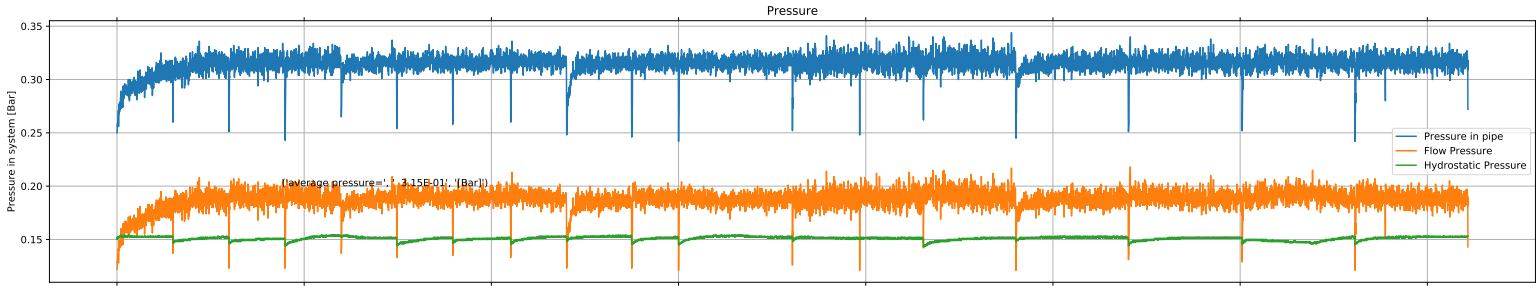

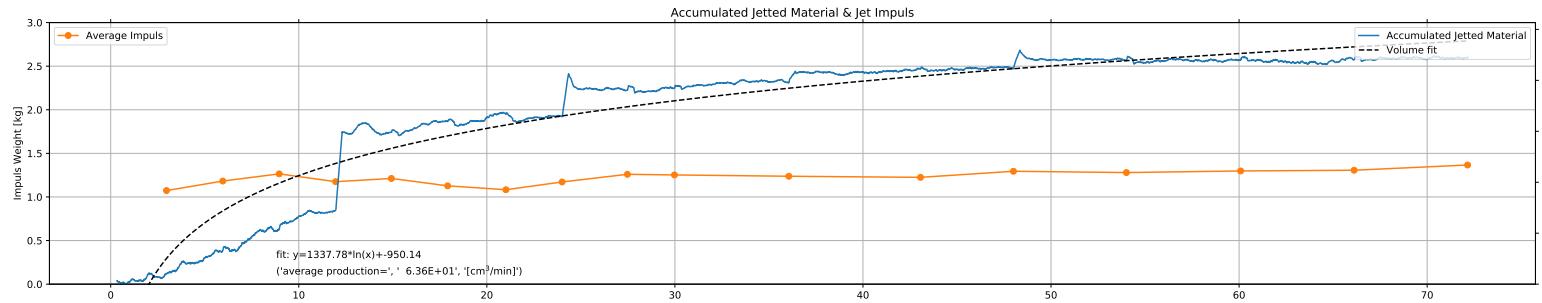

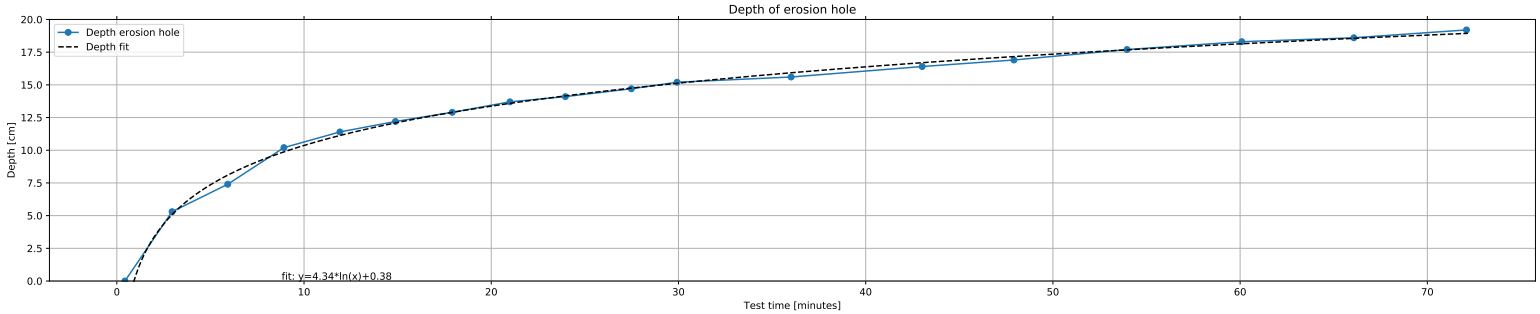

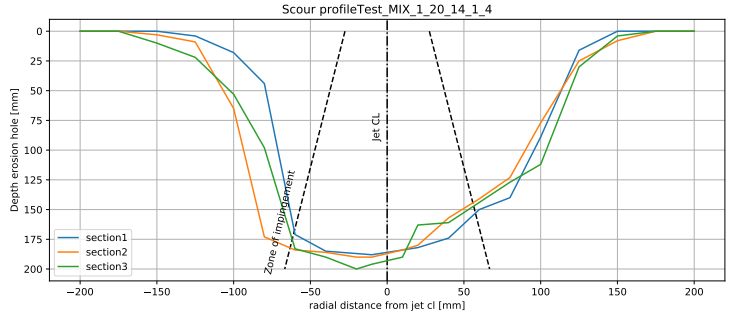

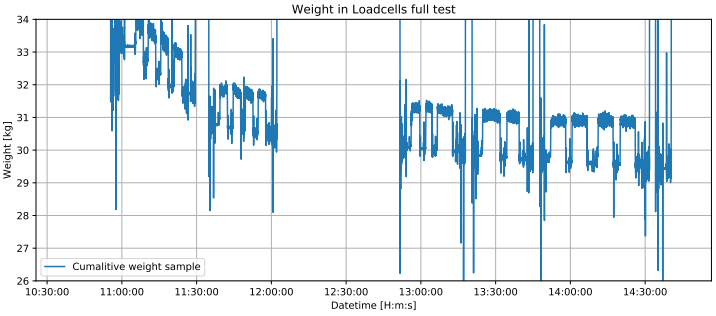

C

Individual soil parameter influence plots on scour depth at discrete time points

In this appendix the individual plots of the effects of a individual soil parameter on the scour depth at individual time points are given. At: 5, 15, 25, 35, 55, 75, 100, 200, 300, 400 min the data is analyzed. At the start of the test a higher resolution is taken, as the scour depth changes at a higher rate as later on in the test. The data-set is subdivided into a data-set that is obtained in this study and the study of Kerssens. And a data-set with all gathered data, which includes the data of Mazurek [22] (2001), Hedges [13] (1990), and Dong et al. [7] (2019). The data-set is split up in this manner because all the data obtained in this study and that of Kerssens is directly known and the test setup was largely similar. Whereas for the other tests different scales where used, some of the relevant parameters are not directly known, and different test setups where used. This combined could result in errors and worse results.

C.1. Consolidation Coefficient

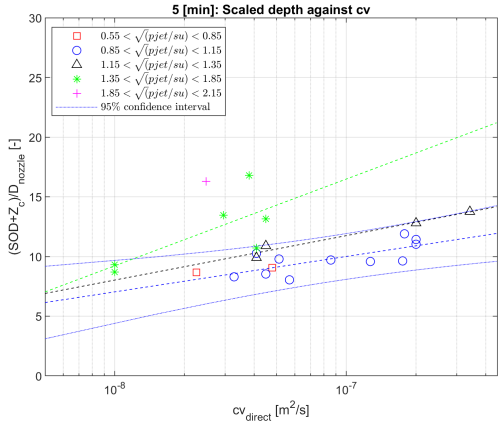

(a) Part of data-set: 5 min.

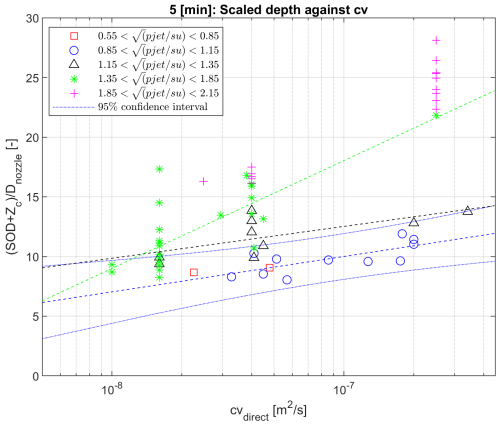

(b) Full data-set: 5 min

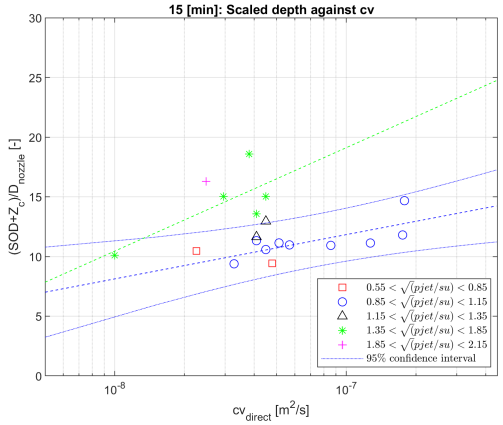

(c) Part of data-set: 15 min.

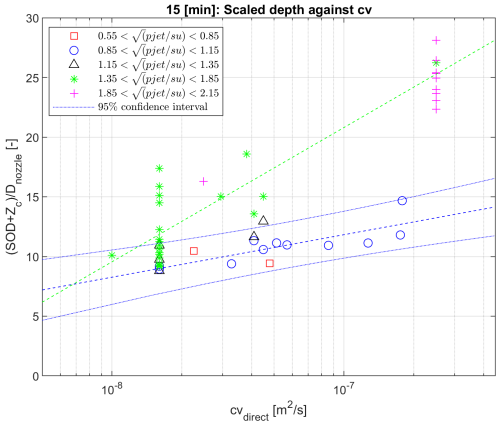

(d) Full data-set: 15 min

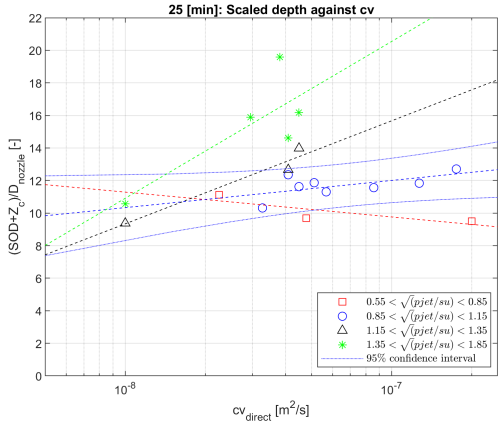

(e) Part of data-set: 25 min.

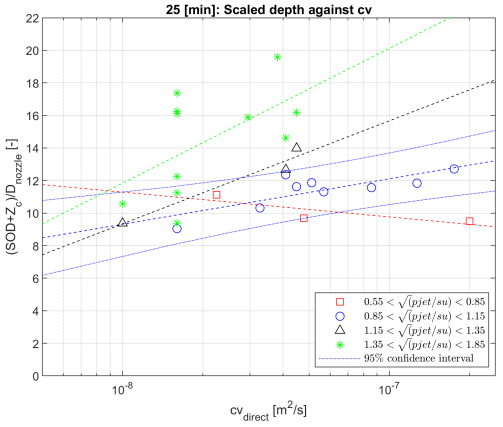

(f) Full data-set: 25 min

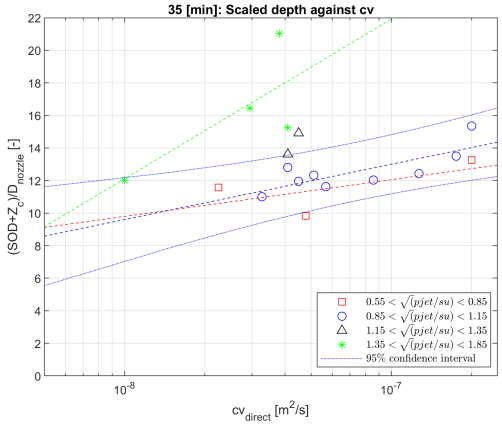

(g) Part of data-set: 35 min.

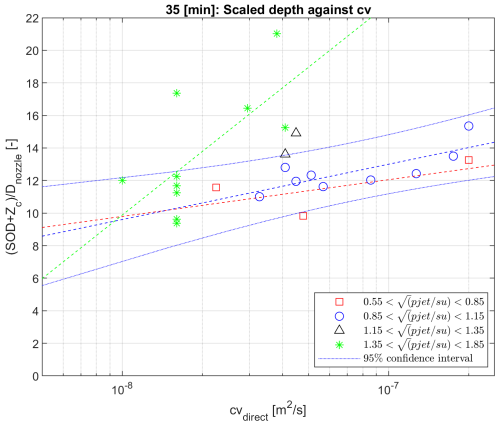

(h) Full data-set: 35 min

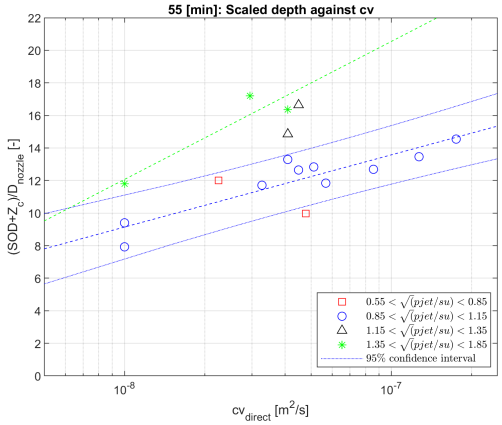

(i) Part of data-set: 55 min.

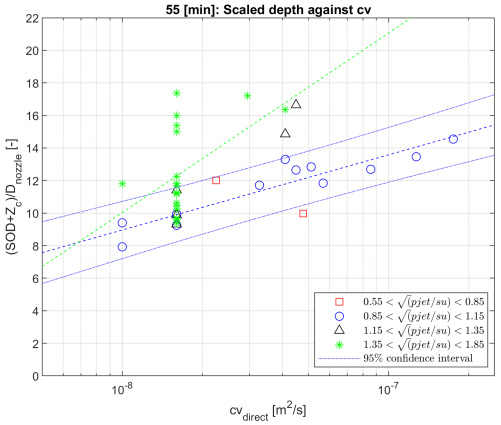

(j) Full data-set: 55 min

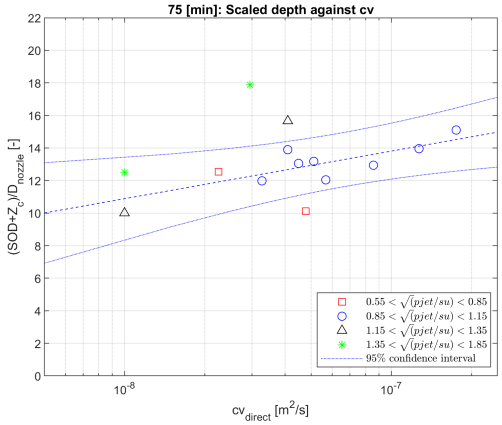

(k) Part of data-set: 75 min.

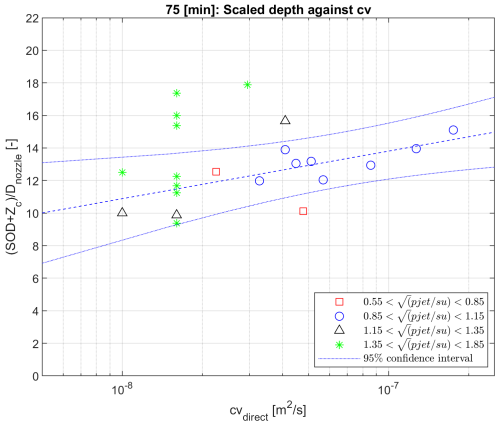

(l) Full data-set: 75 min

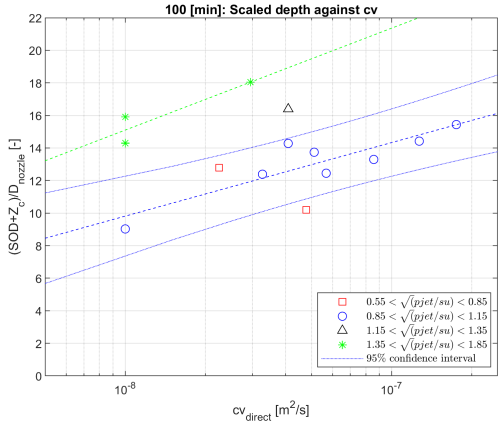

(m) Part of data-set: 100 min.

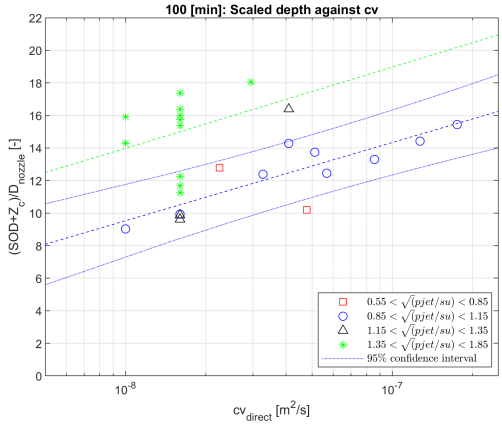

(n) Full data-set: 100 min

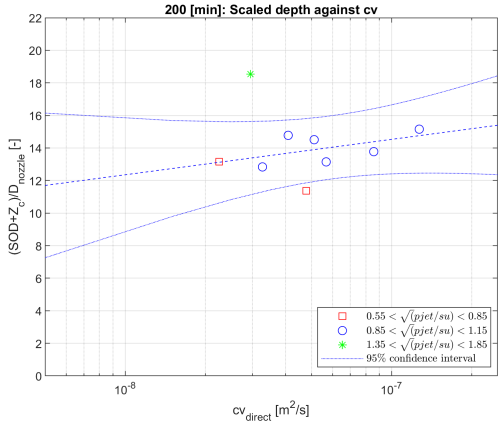

(o) Part of data-set: 200 min.

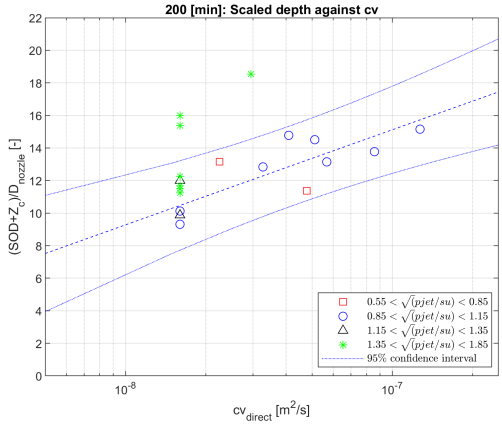

(p) Full data-set: 200 min

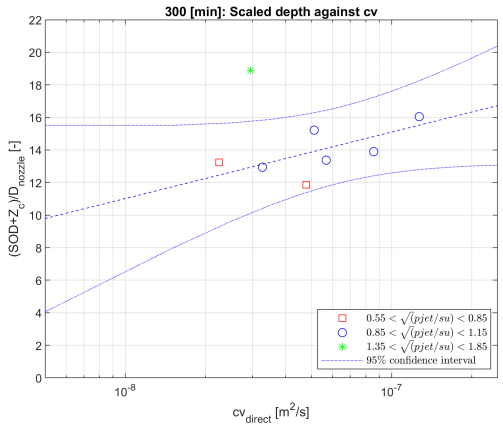

(q) Part of data-set: 300 min.

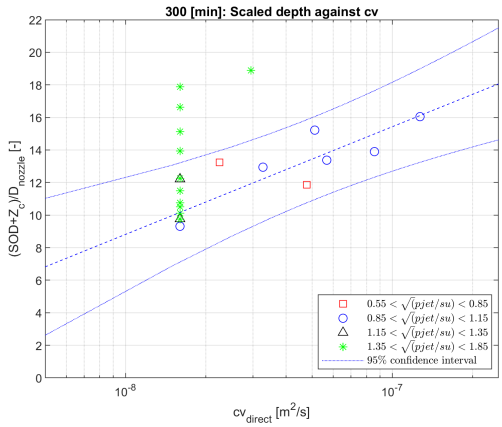

(r) Full data-set: 300 min

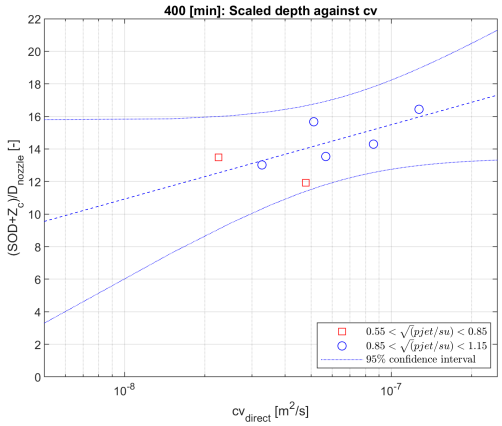

(s) Part of data-set: 400 min.

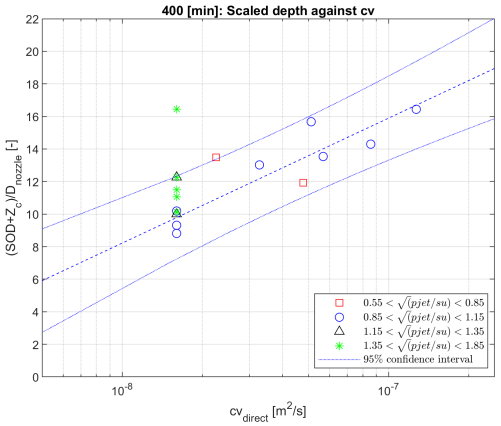

(t) Full data-set: 400 min

Figure C.1: Effect of the consolidation coefficient on the dimensionless depth of the erosion hole at different time points for part of the data-set and the complete data-set, including fit lines and 95% confidence interval

C.2. Plasticity index

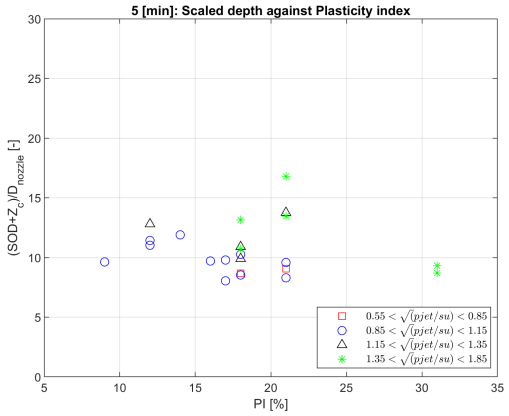

(a) Part of data-set: 5 min.

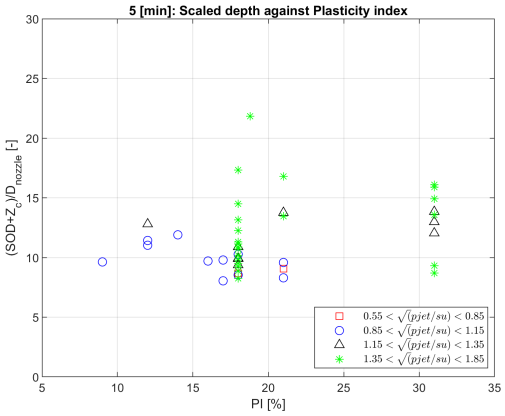

(b) Full data-set: 5 min

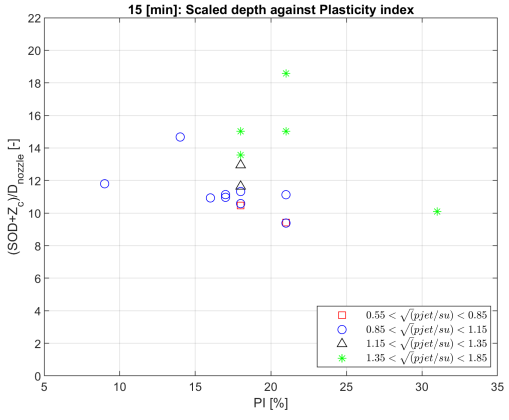

(c) Part of data-set: 15 min.

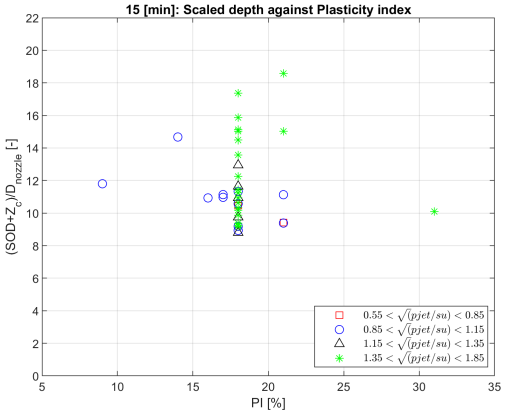

(d) Full data-set: 15 min

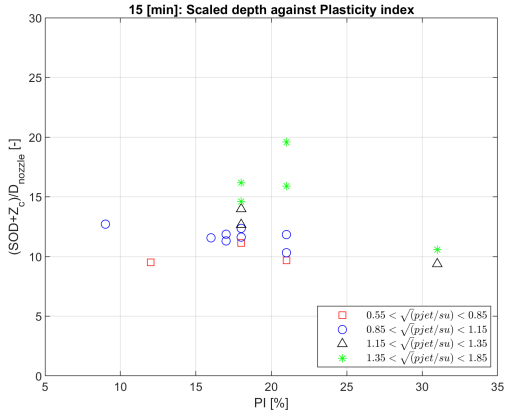

(e) Part of data-set: 25 min.

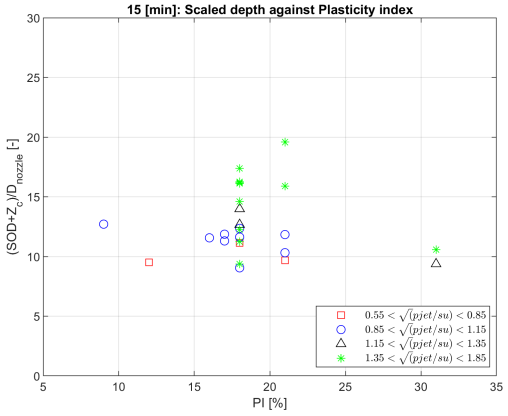

(f) Full data-set: 25 min

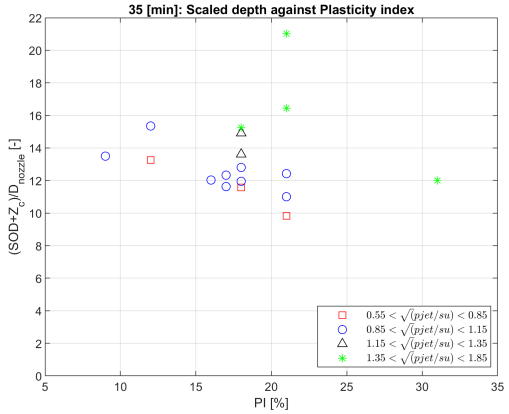

(g) Part of data-set: 35 min.

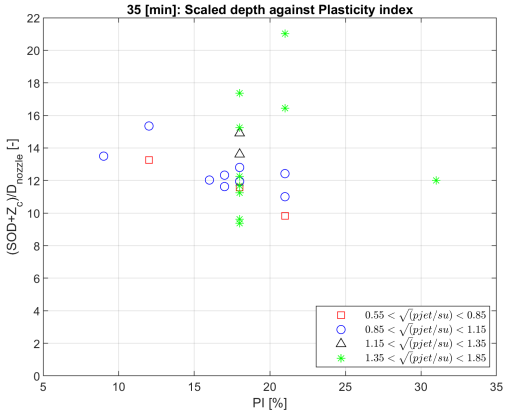

(h) Full data-set: 35 min

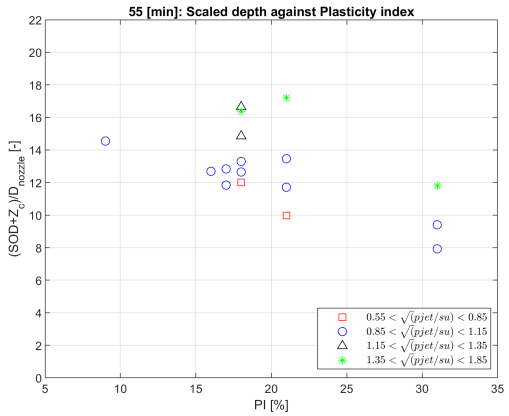

(i) Part of data-set: 55 min.

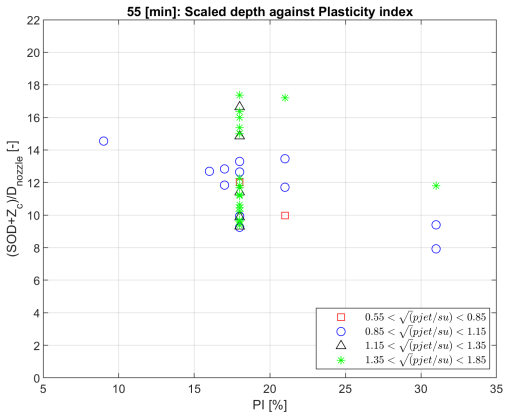

(j) Full data-set: 55 min

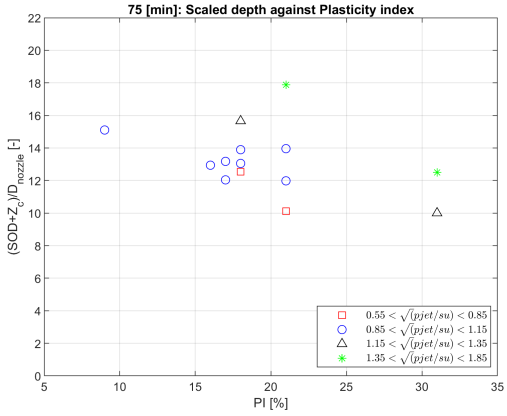

(k) Part of data-set: 75 min.

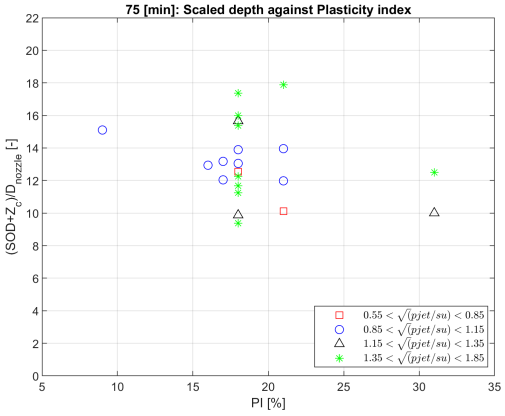

(l) Full data-set: 75 min

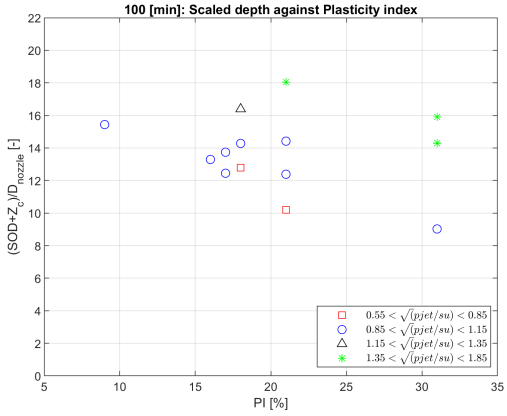

(m) Part of data-set: 100 min.

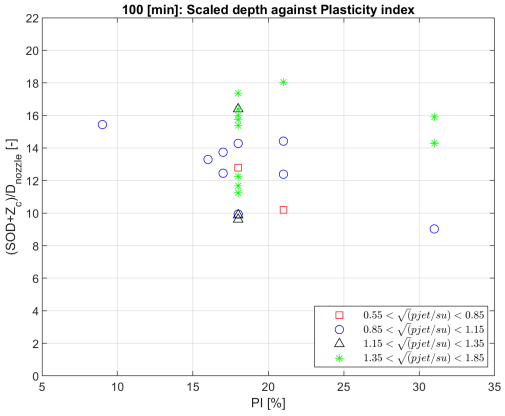

(n) Full data-set: 100 min

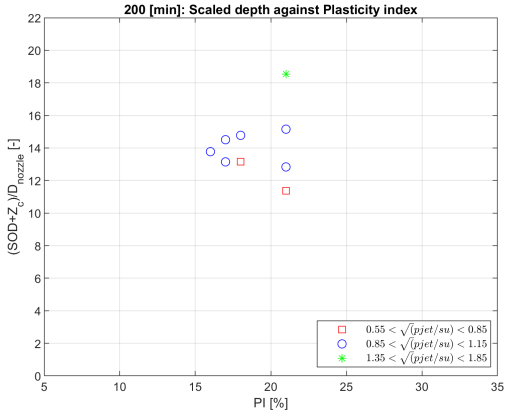

(o) Part of data-set: 200 min.

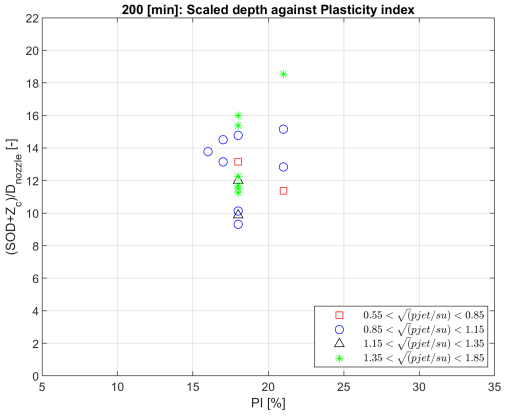

(p) Full data-set: 200 min

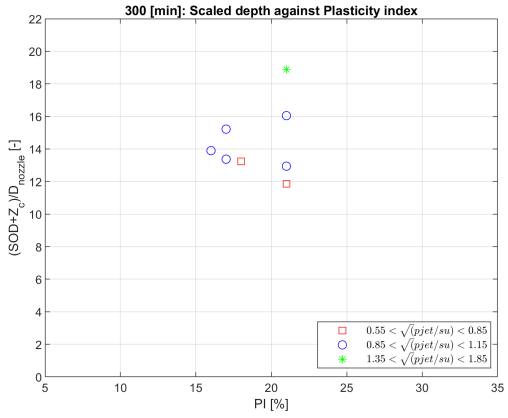

(q) Part of data-set: 300 min.

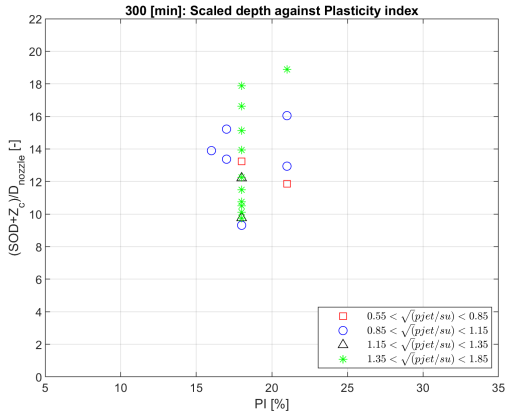

(r) Full data-set: 300 min

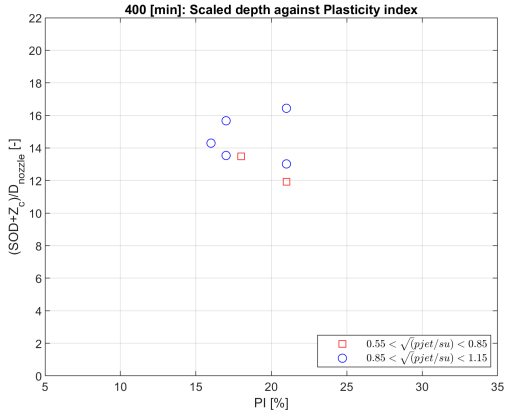

(s) Part of data-set: 400 min.

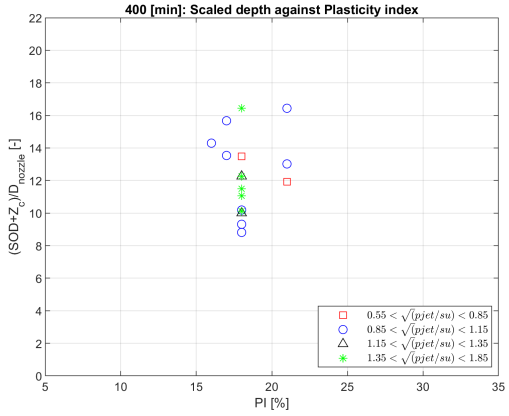

(t) Full data-set: 400 min

Figure C.2: Effect of the plasticity index on the dimensionless depth of the erosion hole at different time points for part of the data-set and the complete data-set.

C.3. Liquid limit

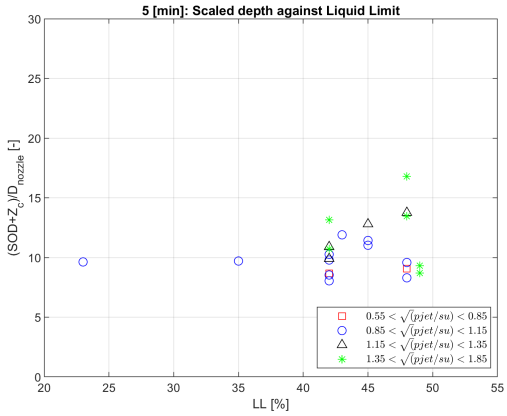

(a) Part of data-set: 5 min.

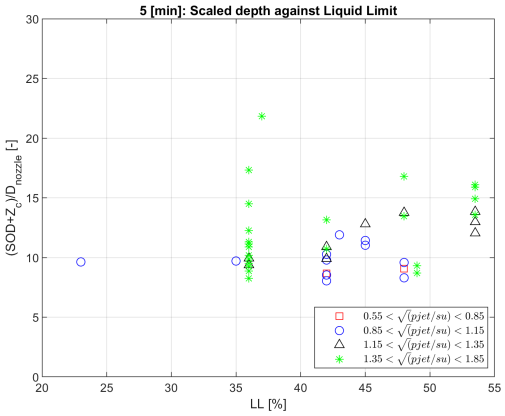

(b) Full data-set: 5 min

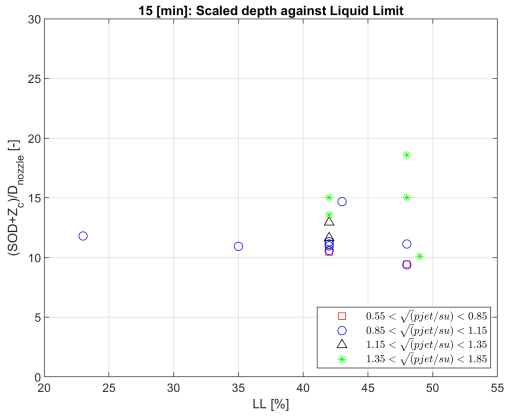

(c) Part of data-set: 15 min.

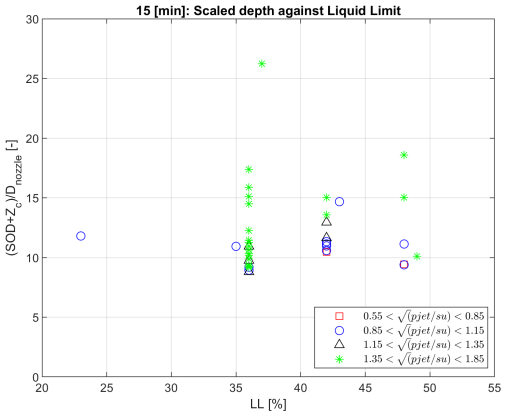

(d) Full data-set: 15 min

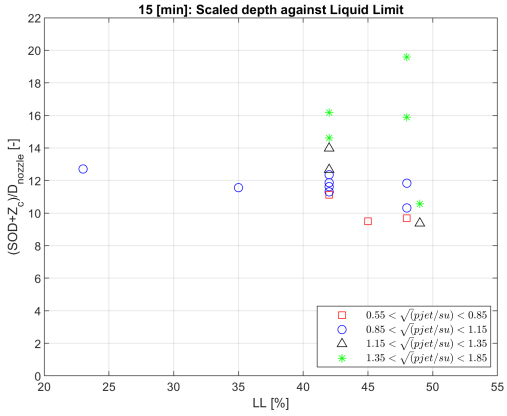

(e) Part of data-set: 25 min.

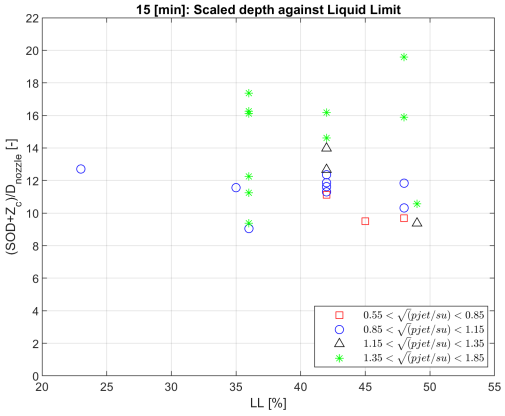

(f) Full data-set: 25 min

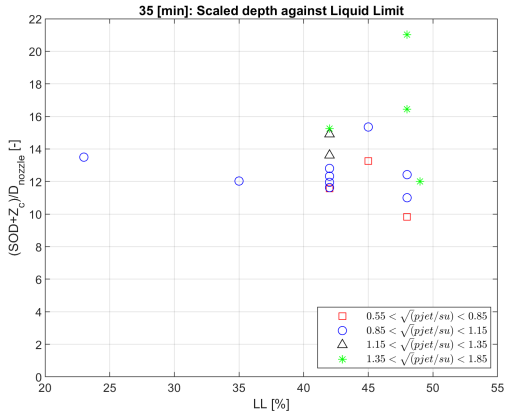

(g) Part of data-set: 35 min.

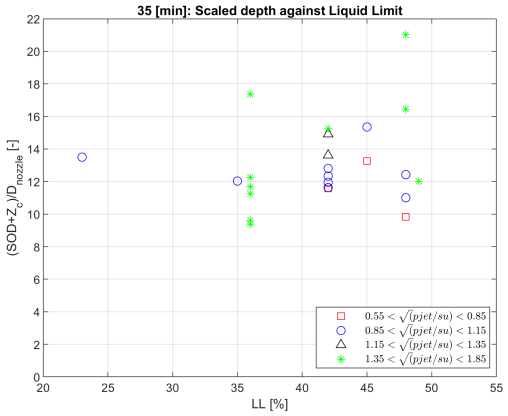

(h) Full data-set: 35 min

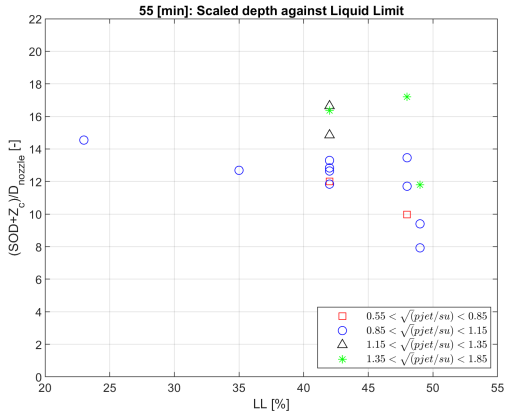

(i) Part of data-set: 55 min.

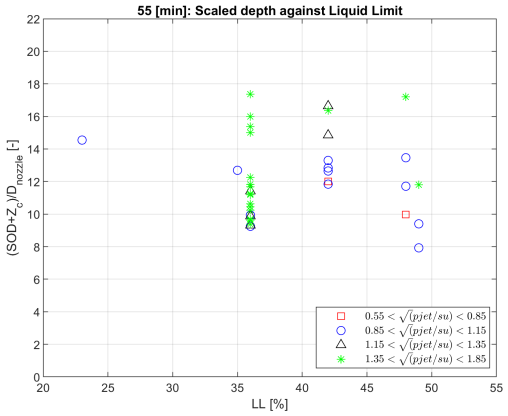

(j) Full data-set: 55 min

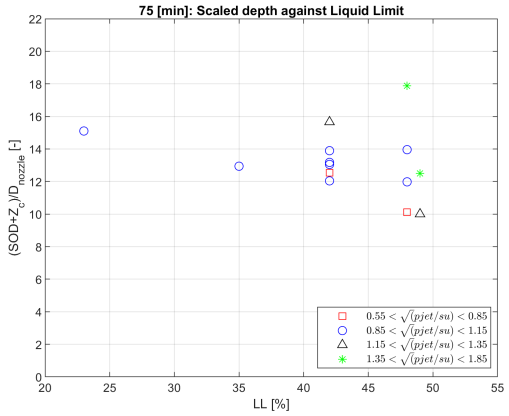

(k) Part of data-set: 75 min.

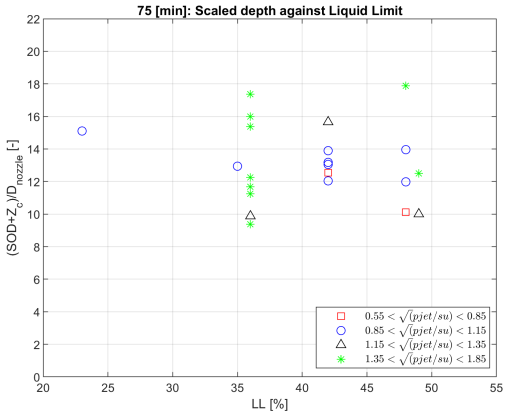

(l) Full data-set: 75 min

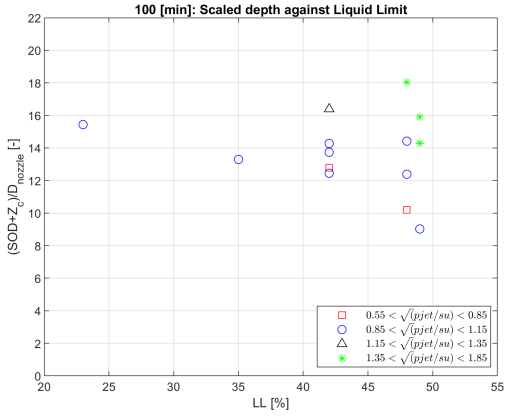

(m) Part of data-set: 100 min.

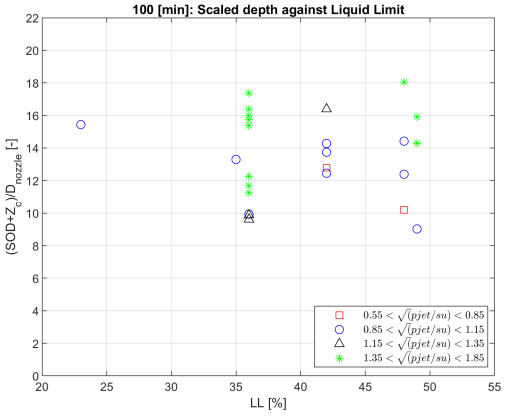

(n) Full data-set: 100 min

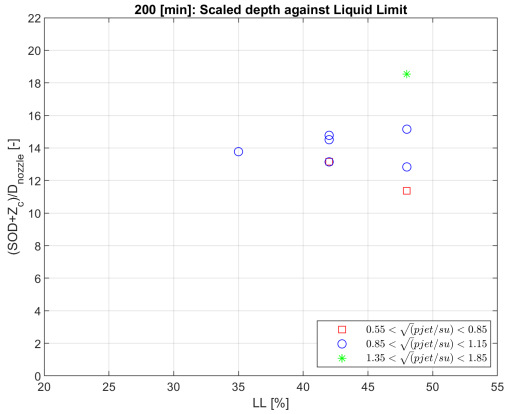

(o) Part of data-set: 200 min.

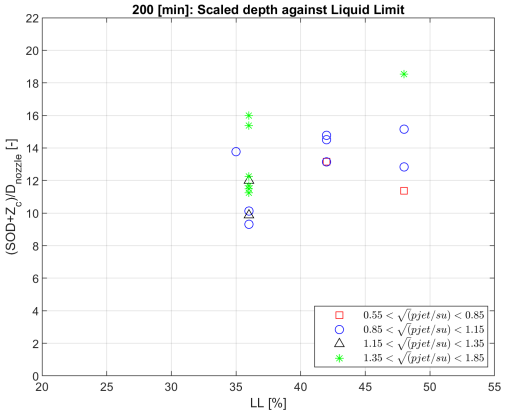

(p) Full data-set: 200 min

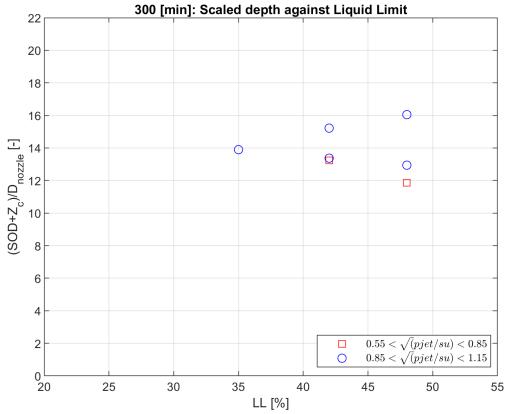

(q) Part of data-set: 300 min.

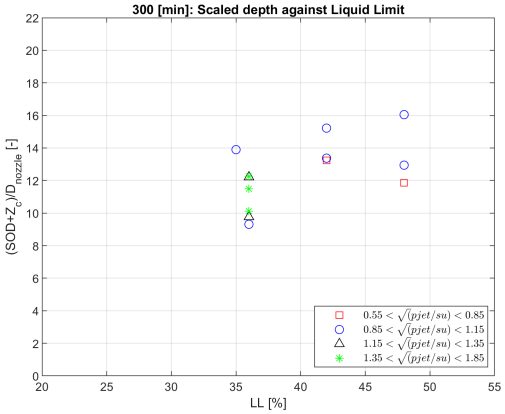

(r) Full data-set: 300 min

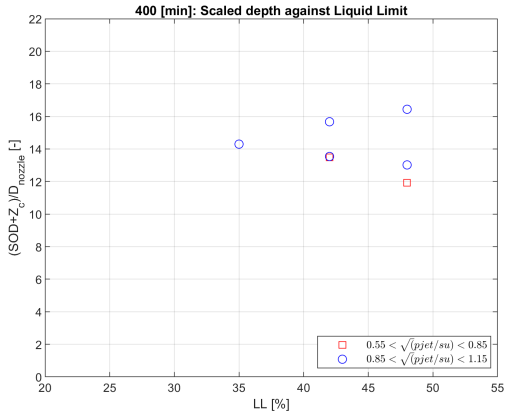

(s) Part of data-set: 400 min.

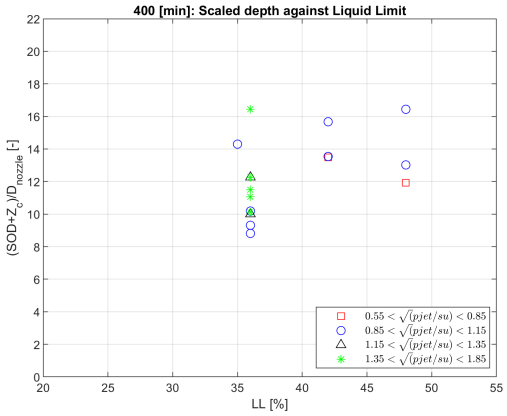

(t) Full data-set: 400 min

Figure C.3: Effect of the liquid limit on the dimensionless depth of the erosion hole at different time points for part of the data-set and the complete data-set.

C.4. Dimensionless water content

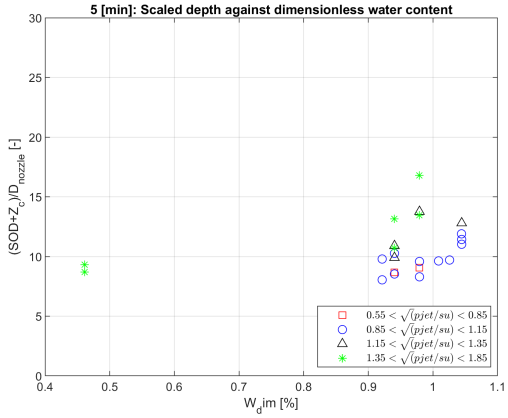

(a) Part of data-set: 5 min.

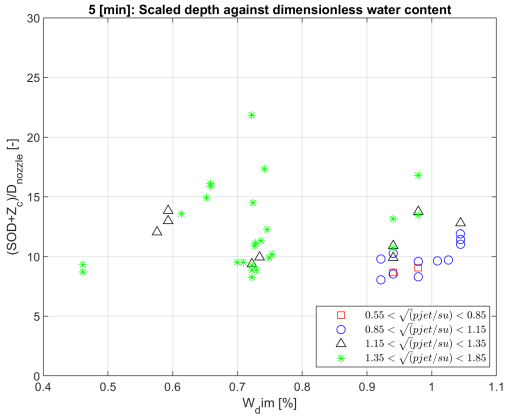

(b) Full data-set: 5 min

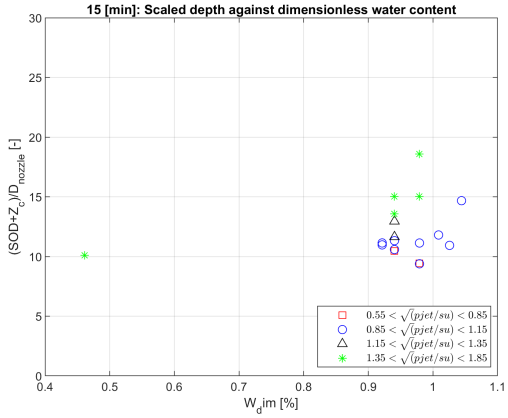

(c) Part of data-set: 15 min.

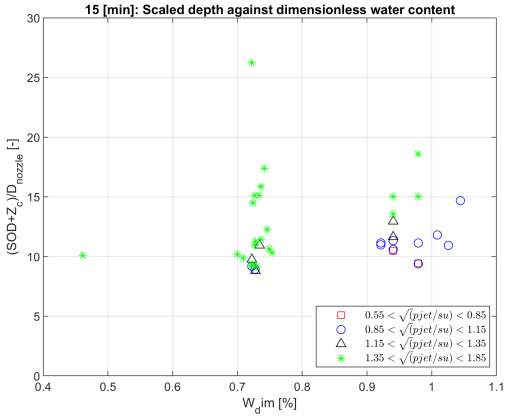

(d) Full data-set: 15 min

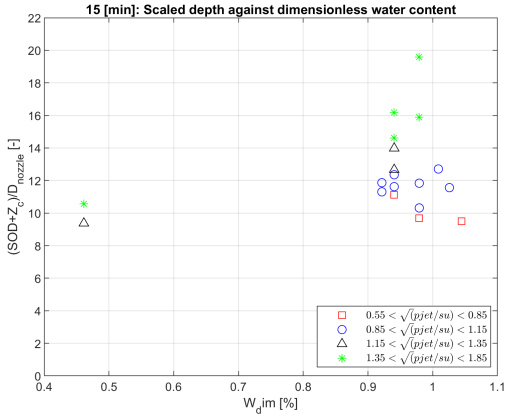

(e) Part of data-set: 25 min.

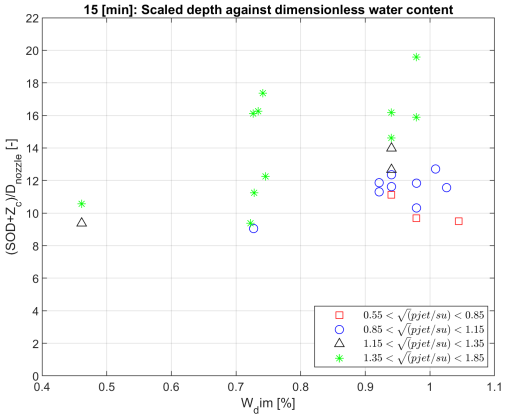

(f) Full data-set: 25 min

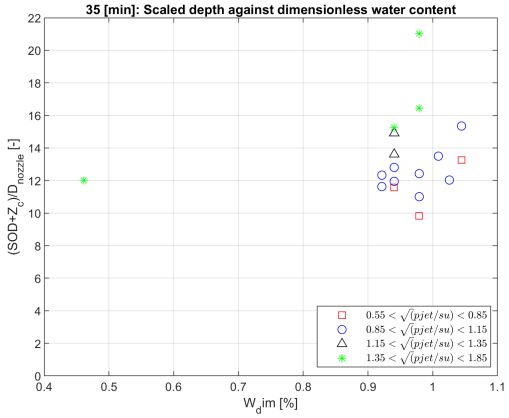

(g) Part of data-set: 35 min.

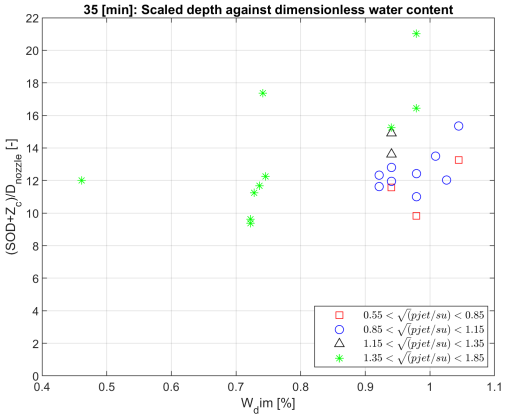

(h) Full data-set: 35 min

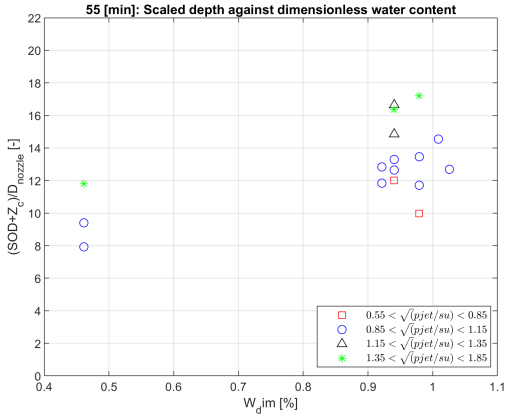

(i) Part of data-set: 55 min.

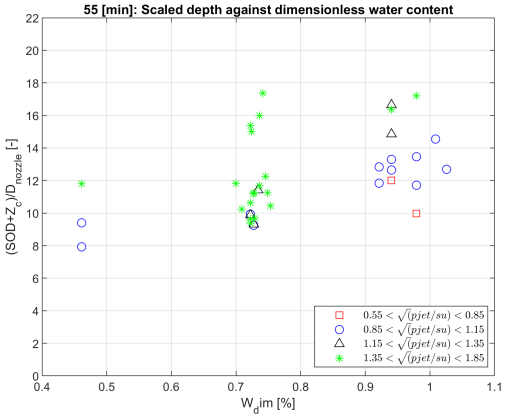

(j) Full data-set: 55 min

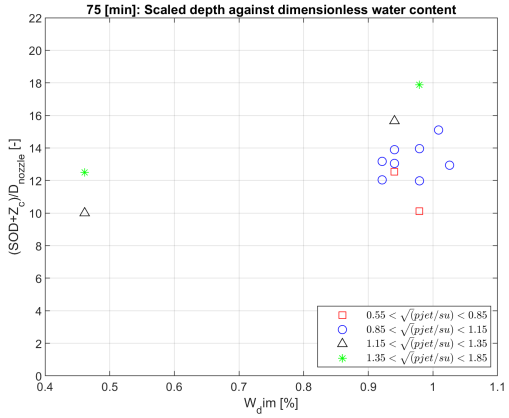

(k) Part of data-set: 75 min.

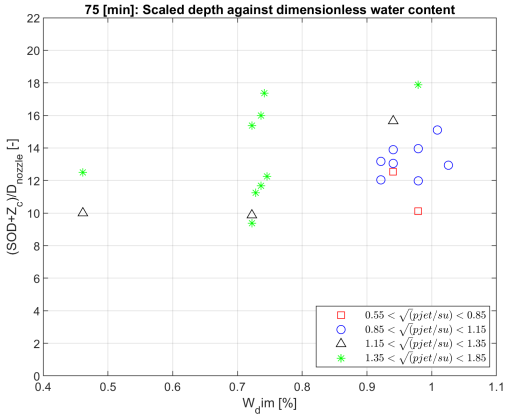

(l) Full data-set: 75 min

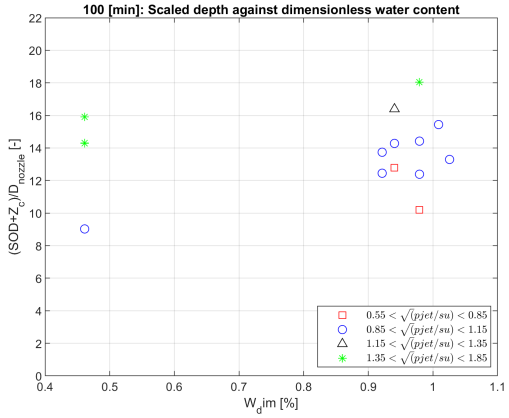

(m) Part of data-set: 100 min.

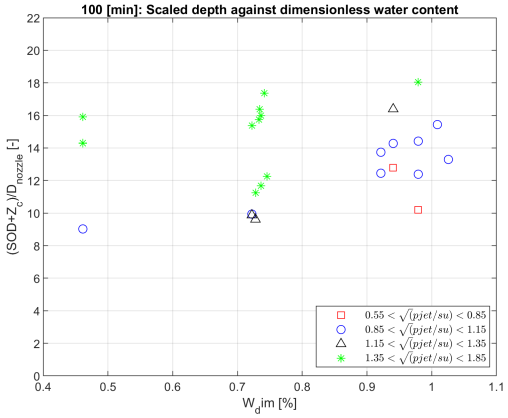

(n) Full data-set: 100 min

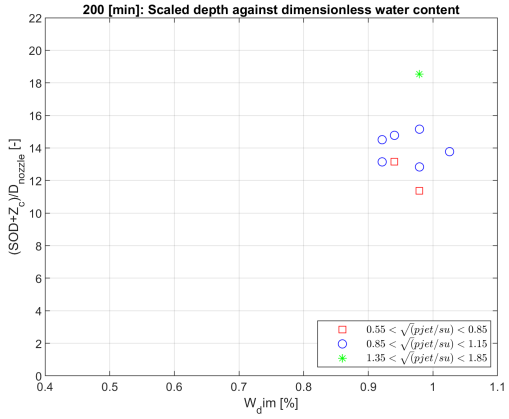

(o) Part of data-set: 200 min.

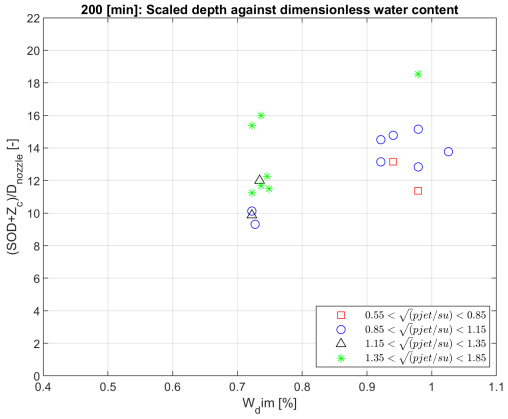

(p) Full data-set: 200 min

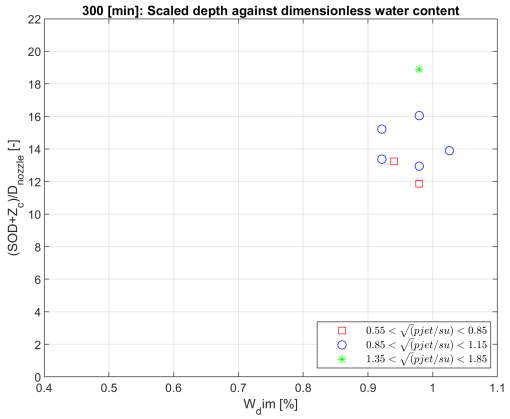

(q) Part of data-set: 300 min.

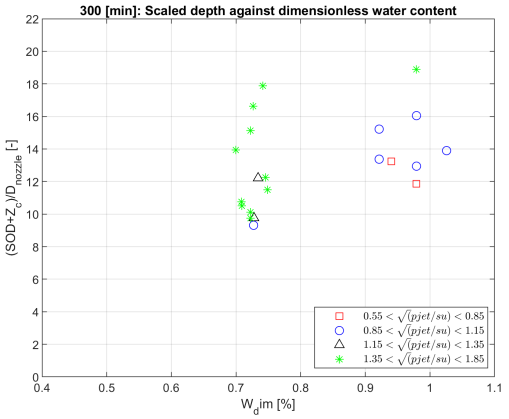

(r) Full data-set: 300 min

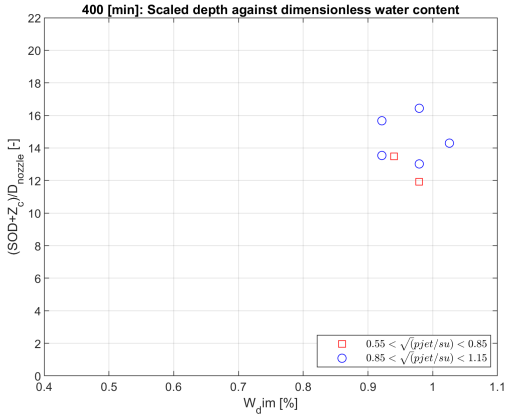

(s) Part of data-set: 400 min.

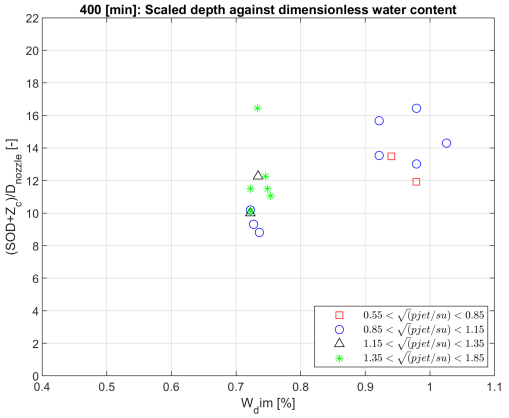

(t) Full data-set: 400 min

Figure C.4: Effect of the dimensionless water content (water content/ liquid limit) on the dimensionless depth of the erosion hole at different time points for part of the data-set and the complete data-set.

D

Soil Sample Characteristics

D.1. Soil sample characteristics tests

Boskalis
Environmental

Boskalis Environmental B.V.
Laboratory
Rosmolenweg 20
3356 LK Papendrecht
PO Box 76
3350 AB Papendrecht
The Netherlands

T +31 78 6969836
F +31 78 6969901

laboratorium@boskalis.com
www.boskalis.com/environmental

BBK BV - Central Business Support

attn. Mr. R. Janmaat
Rosmolenweg 20
3356 LK PAPENDRECHT

Subject

Clay Jetting

Your reference

Our reference

234278

Page

1 of 3

Attachments

1

Dear Sir,

We are sending you the report regarding "Clay Jetting, Boskalis afd. R&D".

Atterberg limits
We find the results contradictory for the Atterberg limits for sample 1, 2 and 3.
We expected that with the increase in the percentage of bentonite (it is a so-called "swelling clay") the Atterberg limits would also increase, but we constatate that they are decreasing.

Density
The measured situ and dry density are very indicative because it concerns stirred material.

Please do not hesitate to contact us if you have any questions concerning this report (+31 78 6969 836).

We trust to have informed you adequately.

Kind regards,

C. E. v. Bergeijk.

Chantal van Bergeijk

Boskalis Environmental

Project: Boskalis afd. R&D
Order: Clay Jetting
Order number:234278

Summary of results

Test	Unit	241317	241318	241319	241320	241321	241322
Moisture content	%	39,5	42,6	38,7	35,9	47,0	23,2
Dry matter content	%	71,7	70,1	72,1	73,6	68,0	81,1
Density (Situ)	Mg/m³	1,742	1,780	1,809	1,738	1,668	1,970
Specific gravity	Mg/m³	2,562	2,630	2,577	2,653	2,629	2,632
Plastic limit	%	23	25	23	20	27	15
Liquid limit	%	42	45	39	35	48	23
Plasticity index	%	18	20	17	16	21	9
Density (Dry)	Mg/m³	1,242	1,248	1,304	1,279	1,134	1,598

Test	Unit	241323
Dry matter content	%	69,0
Moisture content	%	44,9
Density (Situ)	Mg/m³	1,710
Specific gravity	Mg/m³	2,617
Plastic limit	%	28
Liquid limit	%	43
Plasticity index	%	14
Density (Dry)	Mg/m³	1,180

Nr.	Monsternaam
241317	01 sample 07
241318	02 sample 08
241319	03 sample 12
241320	04 sample 13
241321	05 sample 14
241322	06 sample 17
241323	07 sample 10

Sampling:

The samples were delivered to us on 11 December 2019.

Sample storage:

On 11 June 2020, the sample(s) will be removed from our storage. If a longer storage time is required, please notify us in time.

Boskalis Environmental

Project: Boskalis afd. R&D
Order: Clay Jetting
Order number:234278

Method/SOP information

TestType	Method	SOP-code
Density volume ring method (Dry)	NEN	W004
Density volume ring method (Situ)	NEN	W004
Liquid limit	ASTM	W021
Moisture content	NEN-ISO	W002
Plastic limit	ASTM	W021
Specific gravity	NEN-EN	W006

Boskalis Environmental

VOLUME OF AIR IN SAMPLE RING

Method:
own method

Order name : Clay jetting
Order number : 234278
Analist : cehe
Date : 17-Jan-20
Remarks : A value of 0% air volume is measured in samples 241318 and 241319. Based on the method we used, we would expect that there is always (a small part) air present in the prepared sample. We cannot find a specific explanation for these values. A possible cause may be the spread within the analyzes we performed.

Sample number	Sample name	V_{water} %	V_{air} %	V_{solids} %	V_{total} %
241317	01 sample 07	50.0	1.5	48.5	100.0
241318	02 sample 08	53.2	0.0	46.8	100.0
241319	03 sample 12	50.5	0.0	49.5	100.0
241320	04 sample 13	45.9	5.9	48.2	100.0
241321	05 sample 14	53.4	3.5	43.1	100.0
241322	06 sample 17	37.2	2.1	60.7	100.0
241323	07 sample 10	53.0	1.9	45.1	100.0

D.2. Sieve size analysis test for soil samples used in research of Kerssens (2017)

Boskalis Environmental

Project: Clay samples of thesis project test series
Labnumber: 202318
Projectnumber: RD13015-50
Method: Based on BS

206661 - 01 Soilsample Deltaris	
Sieve (µm)	Percentage through sieve
63	75%
47	73%
34	72%
24	71%
17	70%
8	70%
4	67%
2	64%
1	62%
D90	
D80	
D70	10
D60	
D50	
D40	
D30	
D20	
D10	
% > 2 mm	
DMF totaal	
D60/D10	

206662 - 01 Soilsample KaolinC	
Sieve (µm)	Percentage through sieve
63	100%
46	98%
33	96%
23	94%
17	89%
9	65%
5	41%
3	17%
2	3%
D90	17
D80	13
D70	10
D60	8
D50	6
D40	5
D30	4
D20	3
D10	2
% > 2 mm	
DMF totaal	7.5
D60/D10	4.0

Sieve (µm)	Percentage through sieve
D90	
D80	
D70	
D60	
D50	
D40	
D30	
D20	
D10	
% > 2 mm	
DMF totaal	
D60/D10	

Sieve (µm)	Percentage through sieve
D90	
D80	
D70	
D60	
D50	
D40	
D30	
D20	
D10	
% > 2 mm	
DMF totaal	
D60/D10	

Remarks:
A pretreatment was performed on the samples given above. The samples are soaked for at least 16 hours in peptisator to make sure particles detach more easily. "The mass percentages are based on the original material and not only the mineral component."

Boskalis Environmental bv.
Laboratory for Environmental and Geotechnical Research

File: 202318_20170704_cehe_V1_PSD
7/6/2017

Figure D.1: Sieve Size analysis of Kaolin and Deltares sample used in study of Kerssens

Boskalis
Environmental

Labnumber: 202318
Projectnumber: RD13015-50

Clay samples of thesis project test series

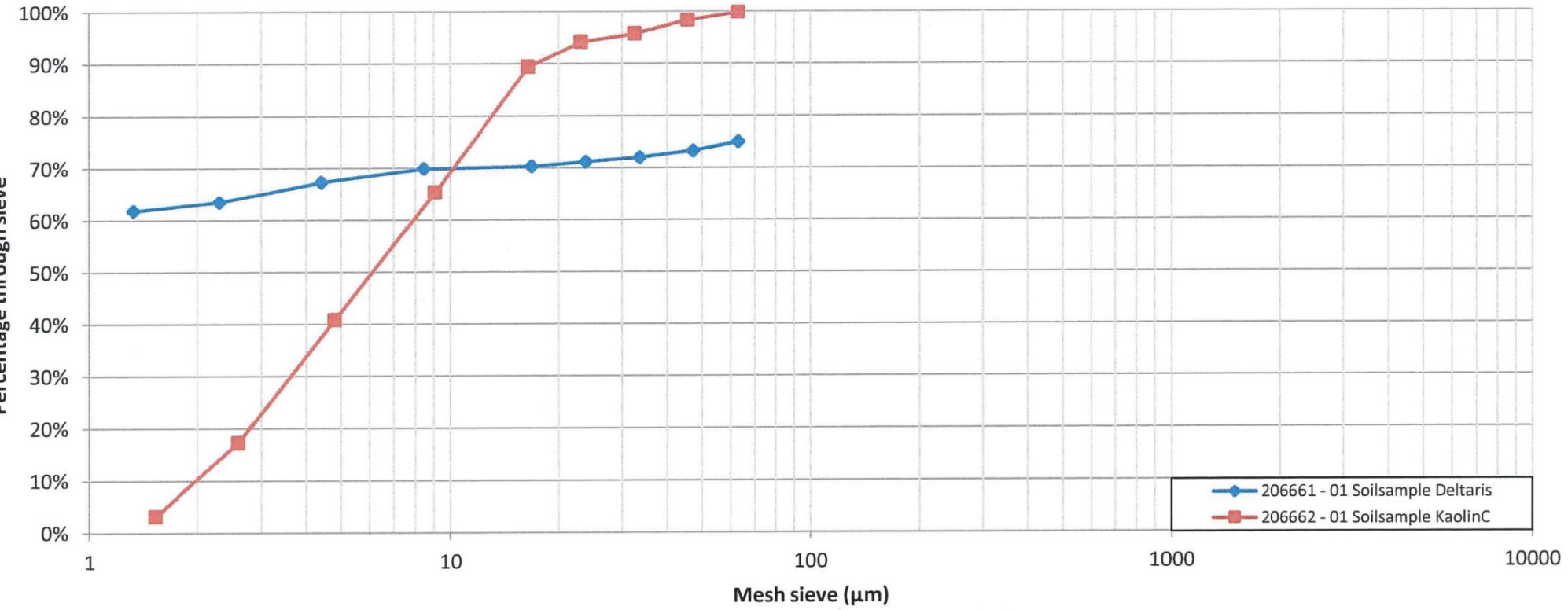

Sample:		D10	D20	D30	D40	D50	D60	D70	D80	D90	% > 2mm	DMF	D60/D10
Sieve	Name	µm	µm	µm	µm	µm	µm	µm	µm	µm		(total)	
1	206661 - 01 Soilsample Deltari							10					
2	206662 - 01 Soilsample KaolinC	2	3	4	5	6	8	10	13	17		7	4.0
3													
4													

D.3. Constant rate of strain tests for soil samples used in research of Kerssens (2017)

First results of the K0-CRS tests on Deltares clay and Kaolin sample
Dirk de Lange
22 December 2017
Project number 1210426.001

Deltares clay
Initial water content: 23.1 %
Sample height 22 mm
Sample diameter 63 mm
Initial sample weight 127.1 g

Phases

1. Loading phase 300 kPa
2. Unloading phase 60 kPa
3. Loading phase 600 kPa
4. Relaxation phase 16 hours
5. Loading phase 1200 kPa
6. Creep phase
7. Relaxation phase
8. Creep phase
9. Unloading phase

Applied strain rate: 0.6 µm/mm

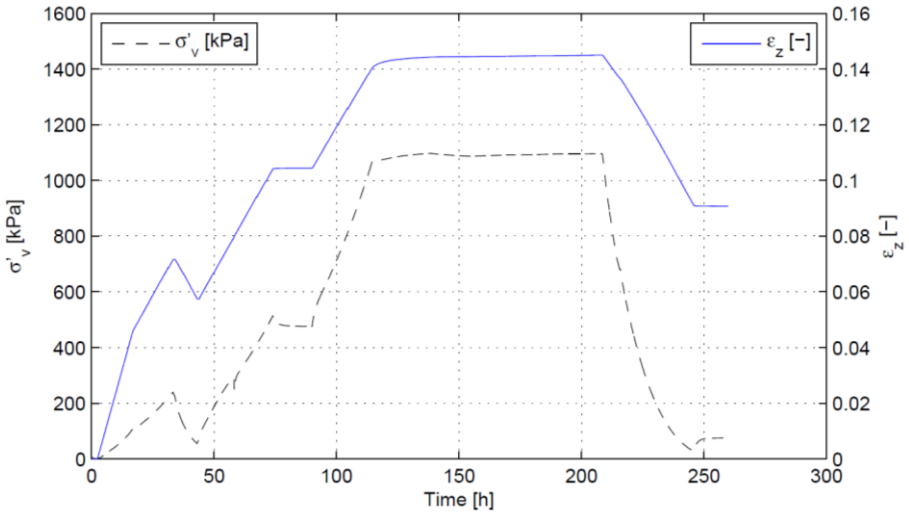

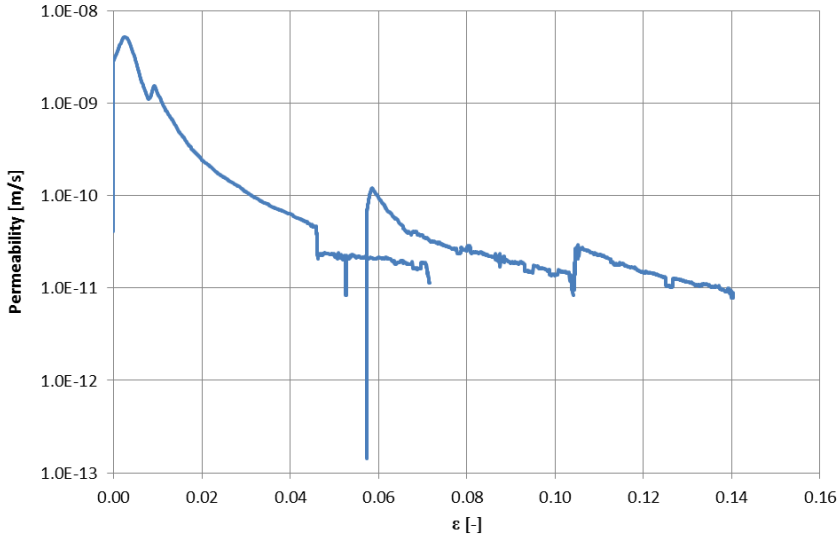

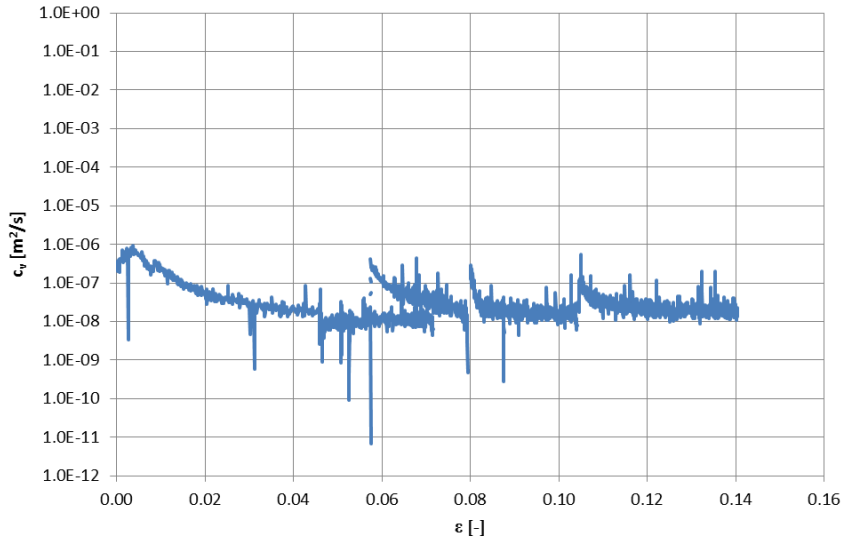

Kaolin
Initial water content: 50.9 %
Sample height 28 mm
Sample diameter 63 mm
Initial sample weight 140 g

Phases

1. Loading phase 35 kPa
2. Unloading phase 7 kPa
3. Loading phase 70 kPa
4. Relaxation phase 16 hours
5. Loading phase 140 kPa
6. Unloading phase

Applied strain rate: 12 µm/mm

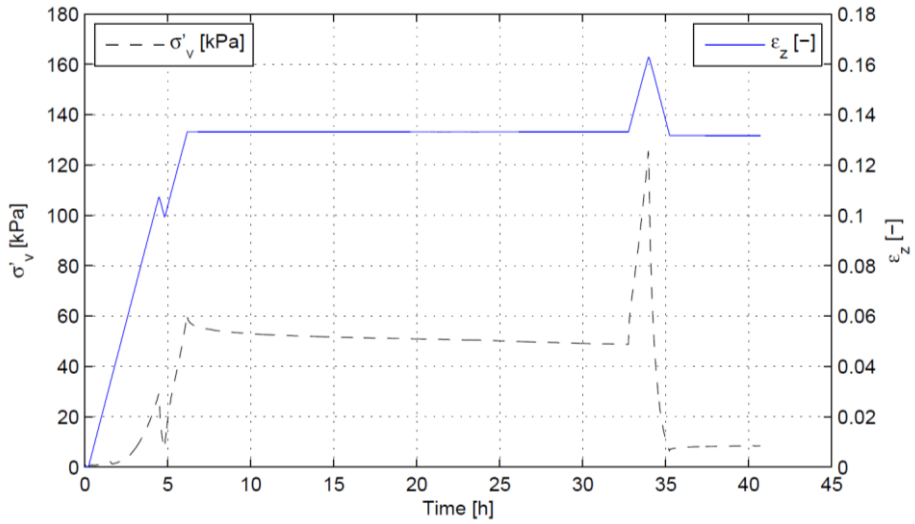
σ'v [kPa]
εz [-]
σ'v [kPa]
εz [-]
Time [h]

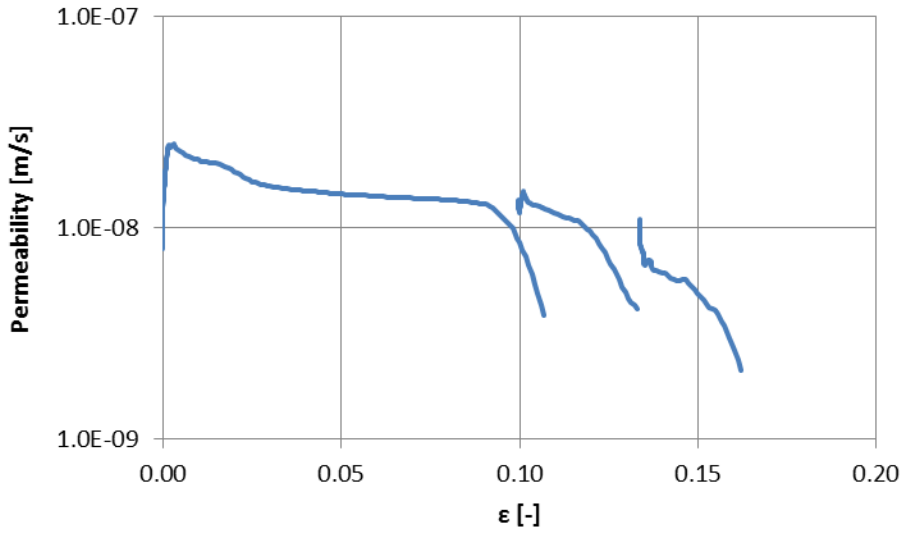
Permeability [m/s]
1.0E-07
1.0E-08
1.0E-09
0.00
0.05
0.10
0.15
0.20
ε [-]

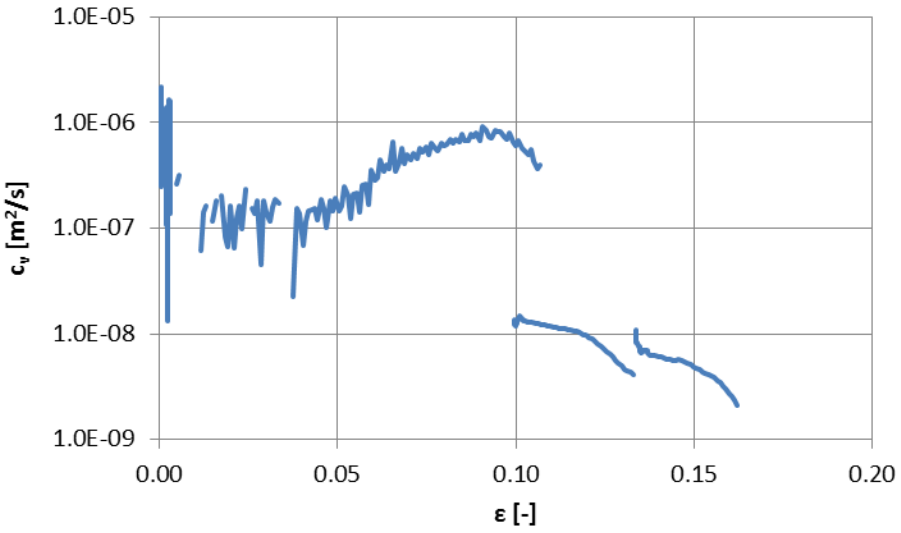
cv [m²/s]
1.0E-05
1.0E-06
1.0E-07
1.0E-08
1.0E-09
0.00
0.05
0.10
0.15
0.20
ε [-]

D.4. Approximation of consolidation coefficient of other used researches

The clay samples used by Mazurek where prepared using a vacuum extruder, which is the same preparation method as used by Kerssens. The consolidation coefficient c_v of the clay samples used by Mazurek is assumed to be approximately similar to the to the c_v value of the Deltares clay of Kerssens. The samples of Mazurek consisted of a mixture of kaolinite and illite. In table 2.2 the typical ranges for these minerals are given, therefore the c_v value could be in the range of $3 \cdot 10^{-9} \sim 9 \cdot 10^{7}$. Soil samples can be classified using the Unified Soil Classification System. Wallace and Otto [41] (1967), found that soils that can be classified as CL-CH the typical range of c_v is $1.6 \cdot 10^{-8} \sim 2.6 \cdot 10^{-7}$. In which CL is clay of low plasticity, lean clay and CH is clay of high plasticity, fat clay.
Taking these three arguments in consideration a value of $1.6 \cdot 10^{-8} m^2/s$ is assumed.

The consolidation coefficient of the clay sample of Hedges figure D.3 is used. Not much is known about the soil sample preparation used by Hedges. The clay is called Terra-cotta clay and is obtained from Trinity Ceramic Supply, Inc. in Dallas and has been pressed into a mold using a Cinva ram. The Virgin compression line is taken as a good approximation line for c_v value of the soil samples of Hedges, since it is not remoulded and has not been pre-consolidated. With a liquid limit of 37% the consolidation coefficient for the soil samples of Hedges is approximately $2.5 \cdot 10^{-7} m^2/s$.

The clay samples used by Dong are natural clay samples taken from Yangcheng Lake in China. All the samples are remoulded. Therefore the remoulded soil line upper bound is taken as a good approximation for the consolidation coefficient. With a liquid limit of 53.5% the consolidation coefficient for the soil samples of Dong is approximately $4.0 \cdot 10^{-8} m^2/s$.

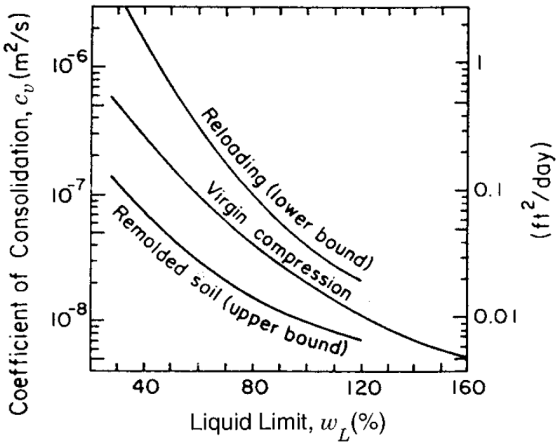

Figure D.3: Coefficient of consolidation as a function of liquid limit (NAVFAC [26], (1982)

E

Test setup and Protocols

E.1. Sample preparation and consolidation figures

(a) Sample containment frame wit filter on the bottom.

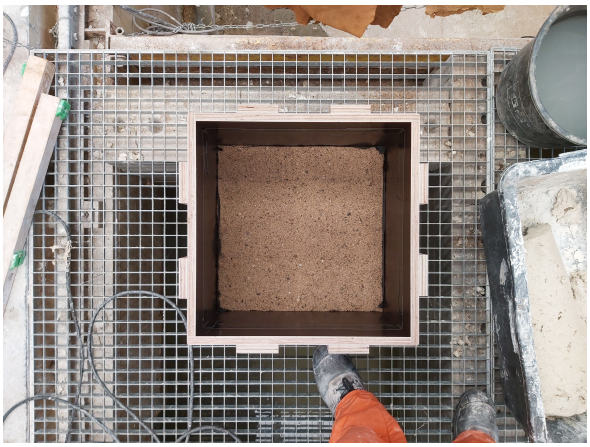

(b) Sample containment frame with a sand filter on the bottom of the sample.

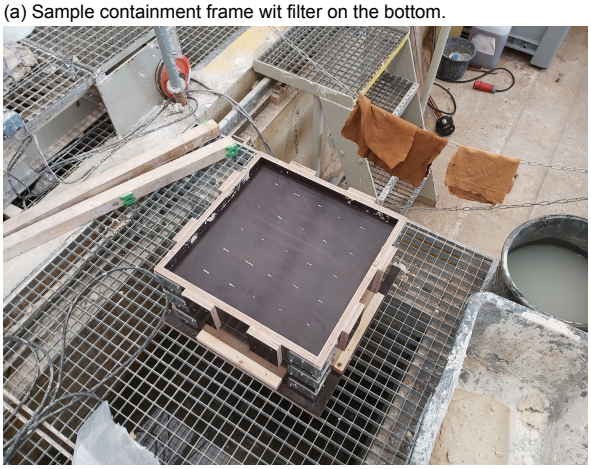

(c) Sample containment frame filled with the clay mixture and top plate positioned on top of the sample.

(d) Sample containment frame placed in the container filled with water. The sample is consolidated by the weight applied on top of the sample.

Figure E.1: Sample preparation and consolidation figures.

E.2. Oedometer setup figures

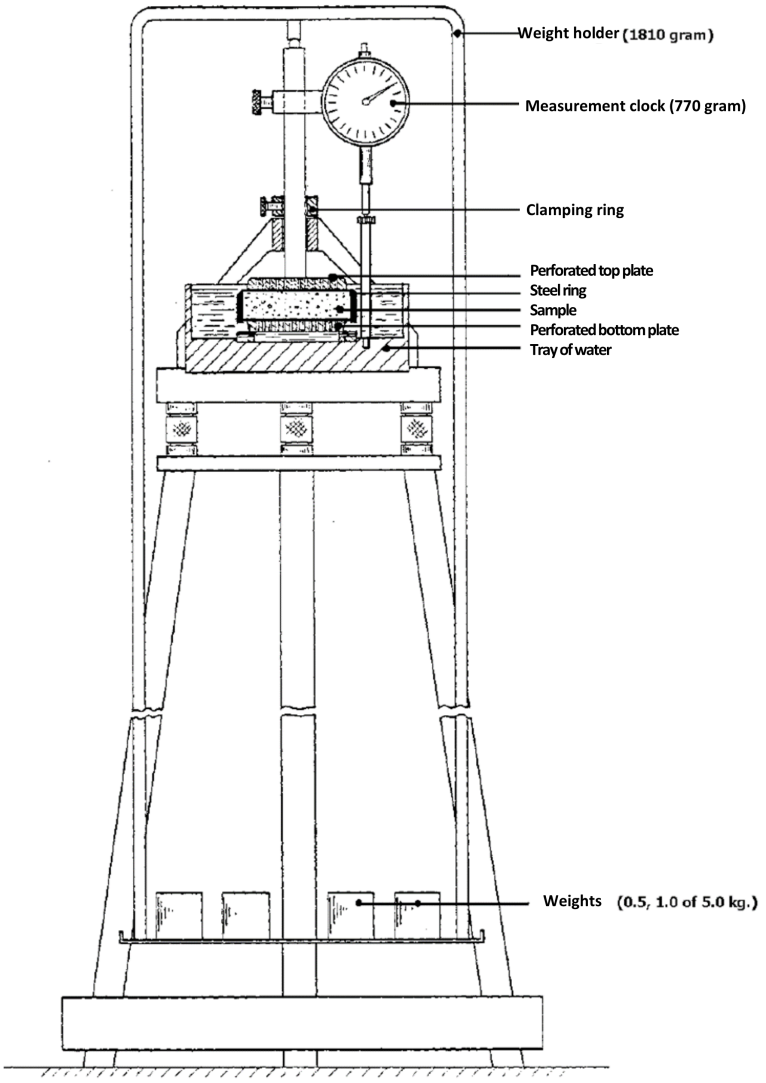

Figure E.2: Oedometer test setup including annotations (from CTB2000 Oedometer test book).

Figure E.3: Oedometer test setup picture.

E.3. Jet test setup figures

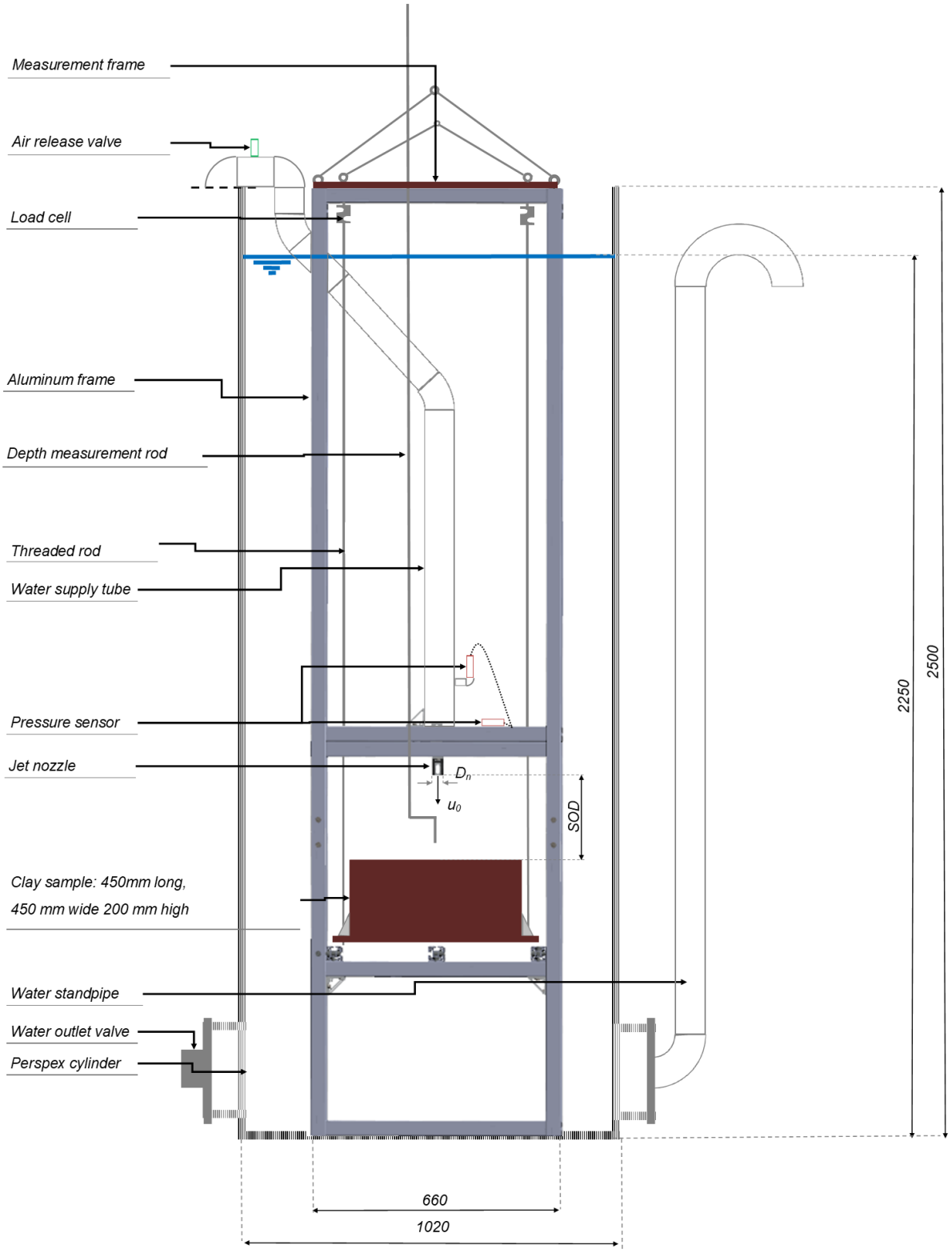

Figure E.4: Experimental test setup

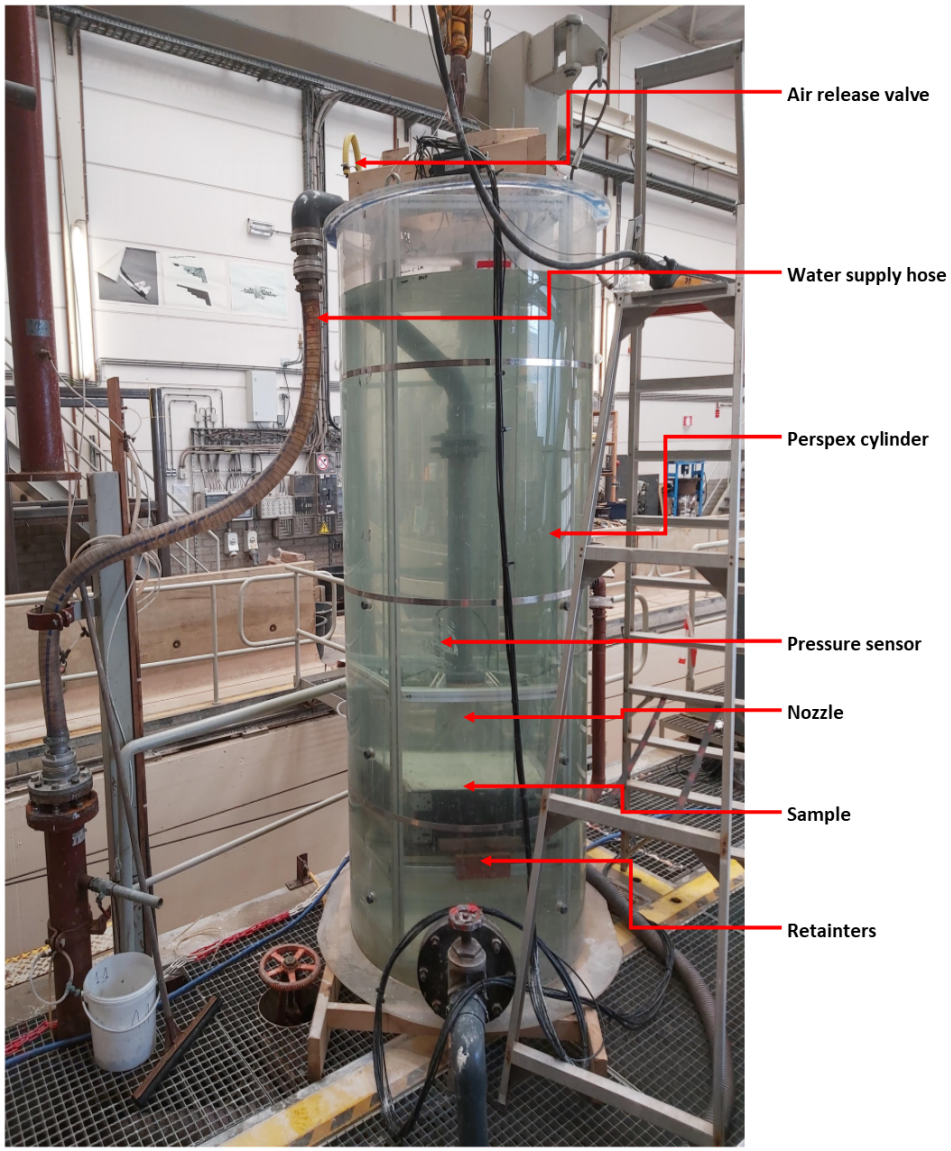

Figure E.5: Jet test setup. Measurement frame positioned in the water filled perspex cylinder.

Figure E.6: Jet test setup. Measurement frame positioned out of the water. Picture is taken after testing with the clay containment frame still hanging in the steel rods of the measurement frame. A jet scour hole can be observed in the middle of the sample.

(a) Pocket vane tester to measure the (undrained) shear strength of a soil.

(b) Field/hand vane tester to measure the (undrained) shear strength of a soil.

E.4. Direct consolidation protocol

1. Preparation

   (i) Sample is prepared with filter layers on the bottom and filter on the top.

   (ii) Close off sample with top betonplex plate.

   (iii) Clamp add-on edge on the sample containment frame using straps to prevent clay leaking out between add on edge and containment frame.

(iv) Hoist sample into container.

(v) Fill up the containter with water until the sample is fully submerged.

2. Testing - measurements

(i) Measure height between top of the sample (betonplex plate) and the top of the add on edge on the four corners of the sample, using the rear side of the caliper.

(ii) Hoist required amount of weight on the sample.

(iii) Note date and time of applying the weight on the sample.

(iv) Measure height on the four corners (consolidation) of the sample directly after applying the weight.

(v) Repeat the measurements of the consolidation and note the date and time, at the start of the test at high interval (after 1-,2-,5-,10-,20-,40-,60-,120- minutes) and later the time between measurements can increase, as the consolidation rate decreases.

(vi) Plot the average consolidation of the 4 measurements on the corner on the log(t) time scale and determine if the sample is fully consolidated.

E.5. Oedometer test protocol

1. Preparation

(i) Determine the inner diameter of the steel ring on two spots using a caliper.

(ii) Determine the height of the steel ring using a caliper.

(iii) Place the steel ring, with the sharp side up, in the consolidation apparatus.

(iv) Loosen the clamping ring and make sure the top perforated plate can be placed on the bottom perforated plate without effort.

(v) Put Vaseline on the inner side of the steel ring to reduce friction between the sample and the steel ring.

(vi) Put the sample on a glass plate, and push the steel ring, with the sharp side facing down, around the sample. Make sure the sample protrudes a few millimeters on both sides.

(vii) Remove the protruding parts of the sample using a wire saw and flatten the surface.

(viii) Put a moistened filter on the bottom side of the sample.

(ix) Put the sample, with the stub side down, on a mold in such a way the sample protrudes 0.5mm on the sharp side and remove the protruding part of the sample.

(x) Remove sample leftovers from the outside of the ring.

(xi) Put a moistened filter on the top side of the sample.

(xii) Moisten the bottom perforated plate of the consolidation apparatus.

(xiii) Place the sample (and ring), with the blunt side down, on the bottom perforated plate and make sure the sample is placed horizontally centric.

(xiv) Loosen the clamping ring, and lower the top perforate plate on the sample, make sure the top plate does not rest on the steel ring.

(xv) Fill the container with water.

(xvi) Make sure the measurement clock has enough space to measure the consolidation.

2. Testing

(i) Put the required amount of weights on the weight holder.

(ii) Note the begin value on the measurement clock and the begin time.

(iii) Place the weight holder on place and start the timer. Make sure the weight holder is hanging still on place (and therefore does not swing)

(iv) Read out the consolidation after 15-30 sec., 1-2-4-8-16-30 min. after the start when the load was applied.

(v) Plot the consolidation on the log(t) time scale and determine if the sample is fully consolidated.

(vi) Place extra weights on the weight holder for the next stage of consolidation measurements and repeat 2.(ii)-(v).

3. Post test

(i) Remove sample from the consolidation apparatus and dispose the sample.

(ii) Clean the test setup and the used materials.

E.6. Jet test protocol

1. Preparations - Before test

(i) Fill up perspex cylinder till desired water level.

(ii) Remove weight from consolidated sample.

(iii) Remove add on edge.

(iv) Cut the clay flush with the top side of the sample using a steel wire.

(v) Clean the sample containment frame.

(vi) Measure the undrained strength on two locations using a pocket vane.

(vii) Weigh the sample including the containment frame and hoisting equipment on a scale.

(viii) Hang off the sample in the measurement frame.

(ix) Hang the sample level and make sure the sample is positioned exactly in the middle of the measurement frame, in such a way the sample does not touch the position retainers.

(x) Measure standoff distance between nozzle and the top of the soil using laser measurement tool.

(xi) Turn on data collection.

(xii) Position the measurement frame inside the perspex cylinder.

(xiii) Check sensor data.

(xiv) Note the submerged weight of the sample.

(xv) Connect the water supply hose to the PVC tube on the measurement frame.

(xvi) Turn on pump at low RPM with the air release valve open and make sure all air is out of the system/flow.

2. Testing

(i) Start up pump and slowly and increase flow rate until required stagnation pressure on the soil.

(ii) Start timing at the same time the pump starts.

(iii) Stop pump at required interval.

(iv) Perform depth measurement by positioning the depth measurement tool near the jet centerline and lowering it, subsequently find the maximum scour depth by slightly rotating the tool.

(v) Note sample weight when jet is turned off as backup.

(vi) Restart at 2.(ii)

(vii) Repeat 2.(ii)-(vi) for required amount of intervals (3 times for the first 12 minutes).

(viii) Disconnect water supply hose.

(ix) Hoist measurement frame out of water.

(x) Take pictures of sample hole and jetted clay material.
(xi) Clean sample of jetted clay residue.
(xii) Lower sample in water and connect water supply hose.
(xiii) Note submerged weight with jet off.
(xiv) Restart at (ii).
(xv) Repeat 2.(ii)-(xiv) for required amount of times.
(xvi) Switch off pump and data-logging.
(xvii) Disconnect water supply hose and hoist measurement frame out of water.

3. Post test

(i) Collect sample from measurement frame.
(ii) Make photographs of the sample.
(iii) Weigh the sample including hoisting equipment on scale, make sure no water is remaining in the scour hole.
(iv) Perform scour hole dimension measurements at 2 or if required 3 sections using the laser measurement tool.
(v) Perform water volume measurements.
(vi) Measure undrained shear strength on 2 locations using a pocket vane, of which 1 is in the scour hole.
(vii) Measure undrained shear strength on 2 locations using a hand (field) vane.
(viii) Note particular observations if necessary.
(ix) Dispose the clay sample.